IMPERIAL COLLEGE OF SCIENCE
TECHNOLOGY AND MEDICINE
DEPARTMENT OF CHEMISTRY

P H D T H E S I S

submitted for the
Degree of Doctor of Philosophy
of Imperial College London

Defended by
Andreas Hadjimitsis

Three-dimensional Optogenetic Control of Gene Expression in *E. coli*

prepared at Imperial College London, Centre for Synthetic Biology

submitted on January 3, 2024

Supervisors : Guy-Bart Stan - Imperial College London
Rodrigo Ledesma-Amaro - Imperial College London
Claire Stanley – Imperial College London

Three-dimensional Optogenetic Control Of Gene Expression in *E. coli*

Abstract

Synthetic Biology has for a long time had the ambition of controlling biological behaviour, through the use of engineering principles. One of the most exciting realms of synthetic biology in this regard, is the ability to control the production of biomaterials. These materials can be produced by, and incorporate living organisms. Applications of biomaterials have been various, from wearable responsive biosensors for heavy metals, to biodegradeable plastics, to methods for the selective uptake and delivery of drugs. Within the area of biomaterial production, another important sector has been the ability to form the biomaterial in any shape desired, through technologies such as 3D printing. 3D bioprinting, as this discipline has been called, uses concepts from conventional 3D printing, such as extrusion. However, these techniques are limited in their geometric possibilities. More interestingly, light techniques such as stereolithography have been used for mammalian cell bioprinting, but their reliance on toxic photoinitiators has made them unsuitable for use with living cells. In this work, we devise a new method for 3D bioprinting, based on optogenetic control. We use optogenetically-equipped *E. coli* cells embedded in a solid matrix, and activate their gene expression in a localised manner. In this work, we express a fluorophore conjugate protein in 3 dimensions, as well as a bioplastic, and gradient expression of a digestive enzyme. This technique has the advantages of allowing full three-dimensional control, without any geometric or toxicity constraints.

Declaration

I hereby certify that everything included in this thesis is my own work, and in the instances where work has been used from other sources, it is acknowledged appropriately. The copyright of this thesis rests with the author. Unless otherwise indicated, its contents are licensed under a Creative Commons Attribution-Non Commercial 4.0 International Licence (CC BY-NC). Under this licence, you may copy and redistribute the material in any medium or format. You may also create and distribute modified versions of the work. This is on the condition that: you credit the author and do not use it, or any derivative works, for a commercial purpose. When reusing or sharing this work, ensure you make the licence terms clear to others by naming the licence and linking to the licence text. Where a work has been adapted, you should indicate that the work has been changed and describe those changes. Please seek permission from the copyright holder for uses of this work that are not included in this licence or permitted under UK Copyright Law.

Acknowledgments

Thank you to Guy for his supervision and support over the vast majority of my PhD. Thank you to Rodrigo and Claire for taking me on towards the very end and taking the daunting task of reading the chapters. Thank you to Connor for giving me access to the labs and providing helpful support with the engineering part. Massive thank you to Borut for the engineering work, heated scientific discussions and all the engineering and physical viewpoint into this work. Big thank you to all the GBS lab and the whole centre for their support through all these years. Thank you to George Taylor for his introduction to the centre, his support and the work on PHB and agarase, as well as Martin Todd. Extra thank you to the original B603 PhD students, Albert, Alice and Alicia for their friendship and support which made finishing this work actually possible. Thank you to Davina for being the best desk buddy ever. Finally, thank you to my friends and family for their support throughout this.

Σὰ βγεῖς στὸν πηγαιμὸ γιὰ τὴν Ἰθάκη,

νὰ εὔχεσαι νᾅναι μακρὺς ὁ δρόμος,

γεμάτος περιπέτειες, γεμάτος γνώσεις.

Contents

Page

List of Figures 10

List of Tables 14

1. Introduction **15**

1.1 Summary 15

1.2 Production by Living organisms 17

1.2.1 Motivation for designing biomaterials in synthetic biology 17

1.2.2 Materials produced by living organisms 18

1.2.2.1 Background and uses of biomaterials 18

1.2.2.2 Biosynthesis and properties of the most widely used Bioplastics 19

1.3 Optogenetics 22

1.3.1 History of Optogenetics 22

1.3.2 Optogenetic classes in bacteria 23

1.3.3 Optogenetic systems 23

1.3.3.1 Cph8/OmpR 23

1.3.3.2 YF1 23

1.3.3.3 EL222 24

1.3.3.4 CCaSR 24

1.3.3.5 BLADE 24

1.3.3.6 Opo-T7RNAPs 25

1.3.4 Applications of Optogenetics 26

1.4 3D Bioprinting 30

1.5 Aims and Objectives 34

2. Establishing a biological set up for optogenetically controlled 3D printing **36**

2.1 Introduction 36

2.2 Results and Discussion 46

2.2.1 Growth and gene expression in darkness 46
2.2.2 Comparison of CcaSR 2.0 and 3.0 under different light intensities 48
2.2.3 Choice of reporter 58
2.2.4 Choice of solid support medium 63
2.2.5 Choice of growth medium 68
2.2.6 Growth and response of cells in agarose hydrogel 71
2.2.7 Improving the dynamic range – Digitalizer 80
2.3 Conclusions 85
3. 3D Optogenetically activated gene expression under continuous illumination 87
3.1 Introduction 87
3.2 Results and Discussion 89
3.2.1 Localised optogenetic production on the surface of a Petri Dish 89
3.2.2 Optogenetic-induced gene expression on the surface of a 3D hydrogel 94
3.2.3 Visualising Optogenetic production inside a cuvette 96
3.2.4 Improving the visualisation and printing equipment 100
3.2.4.1 Improvement of imaging through a gel slicer and a gel scanner 101
3.2.4.2 Improvement of illumination through a custom rig 103
3.2.5 Shotgun experiments for 3D-controlled production 105
3.2.5.1 3D controlled production: Crossed lasers 105
3.2.5.2 3D controlled production: Rotation 111
3.2.6 Characterisation of a line of gene expression across the hydrogel 112
3.2.7 Combining red and green light to control gene expression in a voxel 119
3.3 Conclusions 129
4. Optogenetic control of gene expression using discontinuous illumination 130
4.3 Introduction 130
4.2 Results and Discussion 132
4.2.1 Discontinuous illumination can improve contrast 132
4.2.2 Discontinuous illumination for a line and a voxel in 3D 134
4.2.3 Periodic illumination to control photoreceptor ratios 139
4.2.4 Illumination of two voxels 142
4.2.4.1 Two voxels can be illuminated in the same z-plane 142
4.2.4.2 Alternating illumination 144
4.2.4.3 Concurrent illumination 149
4.2.4.4 Parallel illumination 155

4.2.5 A combination of illumination methods can print a double helix 160
4.3 Conclusions 166
5. Optogenetic control of biomaterial and enzyme production in 3D 168
5.1 Introduction 168
5.2 Results and Discussion 171
5.2.1 Combinatorial assembly of PHB pathway in *E. coli* 171
5.2.2 PHB production under optogenetic control in liquid media 173
5.2.3 PHB production under optogenetic control in solid media 184
5.2.4 Optogenetic control of PHB production with continuous illumination 189
5.2.5 Optogenetic control of PHB production: discontinuous illumination 194
5.2.6 Control of gene expression in the whole hydrogel 199
5.2.7 Production of tdFAST2 in a gradient in a whole hydrogel 200
5.2.8 Production of PHB in a whole hydrogel 204
5.2.9 Agarase gradient production 205
5.3 Conclusions 214
6. Conclusions and Future Work 215
6.1 Conclusions 215
6.2 Future Work 219
7. Materials and Methods 221
7.1 Materials 221
7.1.1 *E. coli* strains 221
7.1.2 Plasmids used in this work 221
7.1.3 Antibiotics 222
7.1.4 Inducers and dyes 222
7.1.5 Media and Buffers 223
7.1.5.1 M9 223
7.1.5.2 Terrific Broth (TB) 224
7.1.5.3 Solid Hydrogel Agarose medium 224
7.1.5.4 Pluronic- F127 medium 225
7.1.5.5 Sodium Alginate medium 225
7.1.5.6 SOB 225
7.1.5.7 SOC 225
7.1.5.8 TSS 225
7.1.5.9 PBS 226

7.2 Equipment 227
7.2.1 96-well plate 227
7.2.2 Mechanical apparatus 228
7.2.3 Hydrogel slicer 231
7.3 Methods 232
7.3.1 Molecular biology methods 232
7.3.1.1 Culturing cells 232
7.3.1.2 Competent cell preparation and transformation 232
7.3.2 General DNA manipulation 233
7.3.2.1 PCR 233
7.3.2.2 Start-Stop Assembly 233
7.3.2.3 Gibson Assembly 233
7.3.3 Assays, data collection and analysis 234
7.3.3.1 3D bioprinting experiments 234
7.3.3.2 Hydrogel slicing 235
7.3.3.3 Hydrogel image acquisition 235
7.3.3.4 Hydrogel image analysis 236
7.3.3.5 Plate reader timecourse assays 236
7.3.3.6 Food dye experiments 238
7.3.3.7 Bleaching experiments 238
7.3.3.8 Plate reader analysis 238
7.3.3.9 Flow cytometry assays 239
7.3.3.10 Material hardness assays 239
7.3.3.11 Plate digestion assay 240
7.3.3.12 Microscopy assays 240
7.3.3.13 Hydrogel absorbance assays 240
8. Bibliography 241
9. Appendix 252
8.1 Table of Sequences used 252
8.2 Table of Primers used 256
8.3 Derivation of Equation 2.1 257

List of Figures

		Page
1	PHA and PHB production	21
2	Schematic of the main optogenetic systems	26
3	Uses of Optogenetics	29
4	3D printing methods	31
5	CCaSR Optogenetic system	39
6	Activation and Inactivation of the CCaSR system	41
7	The Logic behind the 3D printing approach	44
8	Growth and Fluorescence intensity of CCaSR 2.0 and 3.0 in liquid media	48
9	96-well light plate	50
10	CCaSR 2.0 Illumination response (growth)	52
11	CCaSR 3.0 Illumination response (growth)	53
12	CCaSR 2.0 Illumination response (fluorescence)	56
13	CCaSR 3.0 Illumination response (fluorescence)	57
14	CCaSR 3.0 Illumination response (flow cytometry)	58
15	CCaSR 3.0 under anaerobic conditions	60
16	TdFAST2	61
17	Different tfLime concentrations	63
18	Light absorbance of unpopulated hydrogels	65
19	OD700 and fluorescence intensity of cell-populated hydrogels	67
20	Growth with different media	69
21	Fluorescence with different media	70
22	Fluorescence in agarose hydrogel	72
23	Growth in agarose hydrogel	73
24	Fluorescence intensity and OD700 after 300 minutes	75
25	Growth rate in agarose	76
26	Fluorescence Intensity normalised with OD700 in agarose	77
27	Fluorescence intensity in liquid media with tdFAST2	79

28	Schematic of the Digitalizer module	81
29	Induction of the Digitalizer with Methyl Benzoate	82
30	Fluorescence Intensity of cells harbouring the Digitalizer module	83
31	Comparing the Digitalizer with CCaSR 3.0	84
32	Optogenetic system and setup for 3D optogenetics	90
33	Optogenetically activated gene expression in a Petri dish	92
34	Hydrogels incubated in darkness for different periods of time	95
35	Cell death after 7 hours of illumination with 500 mW/m^2 green light	96
36	A localised voxel produced on the surface of a 3D hydrogel	97
37	Inactivation of tfLime by UV light	98
38	Injecting hydrogel into the cuvette	100
39	Method for slicing the hydrogel in a longitudinal fashion	102
40	Images of slices obtained using an NX70 cryotome	103
41	The gel slicer used	104
42	Samples obtained with optimised imaging method	106
43	Crossed laser illumination	107
44	Results of crossed laser illumination	109
45	Raw images of crossed laser illumination	110
46	Diffusion of dye in the cuvette	110
47	Rotation illumination hydrogel images	112
48	Raw data of a printed line	113
49	Analysed singles slices of a printed line	115
50	Characterisation of a line, analysed means	117
51	Cross sections of means across a slice	118
52	Normalised means of a line	119
53	Schematic of simultaneous green and red illumination	120
54	Hydrogel samples from green and red illumination	121
55	Analysed slices with green and red illumination	122
56	Normalised slices with green and red illumination	123
57	Contrasted slices with green and red illumination	124
58	Areas used for cross-sectional paths	126
59	Values across the green beam path	126
60	Values across the red beam path	128
61	Hill Function for active state photoreceptors	132

62	Setup for discontinuous illumination	135
63	Line of tdFAST2 with 4 different green intensities	136
64	Hybrid printing with and without red light	137
65	Discontinuous illumination with different red intensities	138
66	Printing with variable green period	140
67	Schematic of periodic illumination	141
68	Periodic illumination with different red light intensities	141
69	Arrangements of two voxels on the same plane	143
70	Setup for alternating horizontal illumination	145
71	Results for alternating horizontal illumination	145
72	Setup for alternating vertical illumination	146
73	Results for alternating vertical illumination	147
74	Setup for alternating diagonal illumination	148
75	Results for alternating diagonal illumination	149
76	Setup for concurrent horizontal illumination	150
77	Results for concurrent horizontal illumination	151
78	Setup for concurrent vertical illumination	152
79	Results for concurrent vertical illumination	153
80	Setup for concurrent diagonal illumination	154
81	Results for concurrent diagonal illumination	155
82	Setup for separate illumination	156
83	Slices for separate illumination	158
84	Cross-sections for separate illumination	159
85	Schematic of the double helix	161
86	Incident intensities used	162
87	Simulation of the double helix	163
88	Raw data for a double helix	163
89	Analysed data for a double helix	165
90	Schematic of PHB production in *E. coli*	172
91	PHB production under rhamnose induction	173
92	PHB production under optogenetic control	174
93	BP18 in liquid media	175
94	BP18 OD700 with different red light intensities in liquid media	176
95	BP18 fluorescence intensity	178

96	BP18 fluorescence intensity/OD700	180
97	Fluorescence Intensity change rate over time	182
98	BP18 flow cytometry	183
99	BP18 OD700 and fluorescence intensity in solid media	184
100	BP18 fluorescence intensity with different growth media	185
101	BP18 OD700 with different red light intensities in solid media	187
102	BP18 fluorescence intensity with different red light intensities in solid media	188
103	Contrasted printing slices for PHB	189
104	Analysed data of a PHB line	190
105	Plots parallel and perpendicular to a PHB line	191
106	PHB line with LB media	192
107	PHB line with low green light intensity	192
108	PHB voxels with different intensities of red	193
109	Cross sections of PHB voxels	194
110	PHB initial discontinupus illumination experiments	195
111	PHB changing green and red light voxels	196
112	PHB changing red light voxels at two different temperatures	197
113	Microscopy for PHB	198
114	Light plate for gradient experiments	200
115	TdFAST2 gradient	202
116	The effect of temperature on fluorescence	203
117	Production of PHB in whole hydrogel	204
118	PHB gradient	205
119	The beta-agarase reaction	206
120	Agarase diffusion in hydrogel	207
121	Food dye assessment of hydrogel concentration	208
122	Agarase OD700 over time	210
123	Agarase assay in 2D	211
124	Hydrogel hardness measurments	212
125	Young's modulus for hardness	213
126	Assembly of the Light plate	228
127	Bioprinting Illumination platform	231

List of Tables

		Page
1	Parameters used for CCaSR 2.0 and 3.0	43
2	Times of illumination for separate illumination	157
3	Parameters for enzymes involved in PHB production	176
4	Strains used in this study	222
5	Antibiotics used in this study	222
6	Dyes and inducers used in this study	223
7	Recipe for 2x M9	224
8	Excitation/emission for Tecan Spark plate reader	238
9	Table of sequences used	252
10	Table of primers used	256

Chapter 1

Introduction

1.1 Summary

Living organisms ubiquitously use light to interact with their environment, from sight, as is the case with most animals, to producing glucose like plants, algae and cyanobacteria, to altering their gene expression in response to light as a cue for the time of day or season (Baumschlanger & Khammash 2021; Darwin, 1859). Light offers an ideal stimulus for living organisms to respond to, as it is non-invasive, can be directed spatially and offers energy to the cells (Boyden et al., 2005). As a result, there are several molecules that are able to respond to light by changing their conformation, leading to responses ranging from hormone and physiological responses to alteration of gene expression (Molday & Moritz, 2015; Legris et al., 2019; Smith, 2000; Fushimi & Narikawa, 2019). Therefore, it comes as no surprise that the ability to control the properties and behaviour of living organisms using light has reached a prominent position in synthetic biology, precisely due to its non-invasive and spatiotemporal control abilities. Optogenetics has been defined as this ability to use optical input to achieve gain or loss of function of specific events in living organisms (Deisseroth, 2011). Specifically in microorganism synthetic biology, optogenetics has been used for a wide array of applications, such as spatial control of bacterial aggregation (Huang et al, 2019), production of fluorescent proteins (Tandar et al., 2019), self-healing (Wang et al., 2020) and even response to stimuli on biosensors (Wang et al., 2017). It has the unique property of allowing to control microorganisms embedded on a surface in a controlled area (Levskaya et al., 2005), and therefore is a unique asset in the toolbox of creating novel engineered living materials (ELMs), which combine living and synthetic components (Gilbert & Ellis, 2018).

A number of studies have shown the use of optogenetics in functionalising the surface of ELMs (Gilbert et al., 2021), and the power of optogenetics in conferring spatially localised production of

materials (Reshetnikov et al., 2022). Despite the two-dimensional abilities of optogenetics, however, little work has focused on their ability to functionalise ELMs in three dimensions. In this section, I aim to highlight the power of optogenetics in shaping materials in more than two dimensions. To this end, I discuss: i) progress in the generation of ELMs, ii) how optogenetics has been used to spatially control cell function and produce biomaterials in 2 dimensions and iii) approaches for 3D printing biomaterials in 3 dimensions, and where optogenetics can offer an advantage.

1.2 Production of useful materials by living organisms

1.2.1 Motivation for designing biomaterials in synthetic biology

A traditional goal of synthetic biology has been to use living organisms to deterministically recapitulate some of their desirable properties, or confer to them new properties (Benner & Sismour, 2005). Since the first cloning methods developed such as restriction enzyme digestion (Cohen et al., 1973), followed by Gibson and Golden Gate assembly (Gibson et al., 2009; Engler et al., 2008), the field has been opened to engineer cells such as bacteria and yeast to perform non-native task and to exhibit useful behaviours.

At the very basic level, genetic engineering leads to expression of proteins or metabolites which can be useful for humans. This has been happening since the use of microorganisms to make yoghurt in ancient times, but synthetic biology has allowed humans to design organisms for specific applications. Examples of metabolites that have been produced through genetic engineering of microorganisms include high value compounds such as limonene (Liu et al., 2021), drugs like insulin (Baeshen et al., 2014), vitamins like vitamin B6 (Liu et al., 2023), and chemicals like beta-lactam (Skatrud, 1992).

While natively different bacteria are able to produce different proteins, synthetic biology has also allowed the creation of microbial cell factories, by allowing the transfer and optimisation of genetic information from organisms that have useful properties to model organisms such as *E.coli* (Hedges, 2002). The use of *E. coli* specifically has been advantageous in both research and industrial applications, due to its quick doubling time, wide availability of genetic engineering methods, and ability to grow on low-salt media. Moreover, *E.coli* shows great bioproduction capabilities, allowing to produce up to 50% of dry cell mass in heterologous proteins (Blount, 2015).

Perhaps the most exciting use of microorganisms in synthetic biology is the ability to engineer biomaterials (Liu et al., 2022). Materials like wood, cotton and silk have been used for millennia by humans, but the properties of natural materials have been constrained by natural selection (Gilbert & Ellis, 2018). Synthetic biology instead, aims to create biomaterials from scratch, to meet these requirements. In this thesis I focus on the genetic engineering of microorganisms to produce biomaterials.

Advancements in materials produced by living organisms can roughly be split into two: i) materials and polymers produced by living organisms but which do not incorporate them in the material, or ii) materials which incorporate living organisms inside them, making them engineered living materials (Chen et al., 2015).

1.2.2 Materials produced by living organisms

1.2.2.1 Background and uses of biomaterials

In terms of materials that are merely produced by living organisms, advancements have been many and over a variety of applications. Some of the most exciting advancements in biomaterial production include the production of waterproof biomimetic materials, inspired by natural materials such as mussel foot protein and nacre (Wan et al., 2020; Wei et al., 2016). Excitingly, materials like spider silk have now been engineered for production by microorganisms, with the goal of their production in bioreactors in large scale for structural applications (Foong et al., 2020). Other processes that have found exciting applications include engineering urease production. *S. pasteurii* produces urease which is able to break down urea to produce CO_3- ions, which can then react with calcium to mineralised crystals, offering applications in bioremediation and self-healing materials (Ma et al., 2020).

Real-world uses of these biomaterials have been various, from the self-healing of surfaces (Ma et al., 2020) waterproof surfaces (Wei et al., 2016) and resistant wearables (Blamires et al., 2020). In addition, biomaterials have been used to replace artificial fur, and even as a starting point to replace synthetic plastics for the built environment. For the latter, research has widely focused on the ability of biomaterials to replace plastics, by creating biodegradeable polymers of bacterial origin (Luengo et al., 2003). These bioplastics offer advantages over synthetic plastics as they can be assimilated by many species, and can be largely non-toxic to the host, giving them biocompatibility, as opposed to synthetic products (Zinn et al., 2001).

Such bioplastics are generally formed from esters, and are therefore mostly lipid in nature (Madison & Huisman, 1999). Most of these bioplastics are accumulated in the form of storage, during periods of prolonged nutrient starvation and stress (Barnard & Sanders, 1989). The form of these bioplastics in cells is in amorphous granules, that vary widely in size and morphology depending on the producing organism and degree of production (Anderson & Dawes, 1990). These bioplastics are generally easy to observe in a microscope, as the granules are large and light-refracting, often changing the shape of the bacteria (Lee & Choi, 1999).

In terms of the more precise chemistry of bioplastics, they normally represent polymers of different oxidation intermediates of Acetyl-coA, such as 3-hydroxyacyl CoA (Steinbuchel & Fuchstenbusch, 1998). This is enzymatically polymerised through condensation of carboxyl groups in one monomer with thiol groups in the next one. Of course, bioplastics with different compositions exist, such as glutamic acid, which follows unique biosynthetic routes (Di Lorenzo & Silverte, 1999).

Currently, the main limitations for the bulk production of bioplastics, like most biomaterials, are their high production costs and scale. However, in the past years the yield has vastly improved (Gilbert & Ellis, 2018).

The first instance of a bioplastic in literature was Polyhydroxybutyrate, which was first mentioned by Lemoigne in 1926 (Lemoigne, 1926), describing its formation in *Bacillus megaterium* through an enoyl CoA hydratase pathway, leading to the dehydration and polymerisation of beta oxybutyric acid. However, it was not until the 1970s that the field of bioplastics underwent a resurgence, mainly due to the search of alternative fuels during the petroleum crisis, leading to the present day were members of more than 90 genera have been described to produce polyesters (Eggink et al., 1994). The most widely produced bioplastics to date include polylactic acid and polyhydroxyalkanoates (PHA), with PHB being the most prominent amongst them. In the rest of this section, I go over the properties and biosynthesis of some of the most prominent bioplastics, polylactic acid, polyhydroxyalkanoates (PHAs) and PHB.

1.2.2.2 Biosynthesis and properties of the most widely used Bioplastics

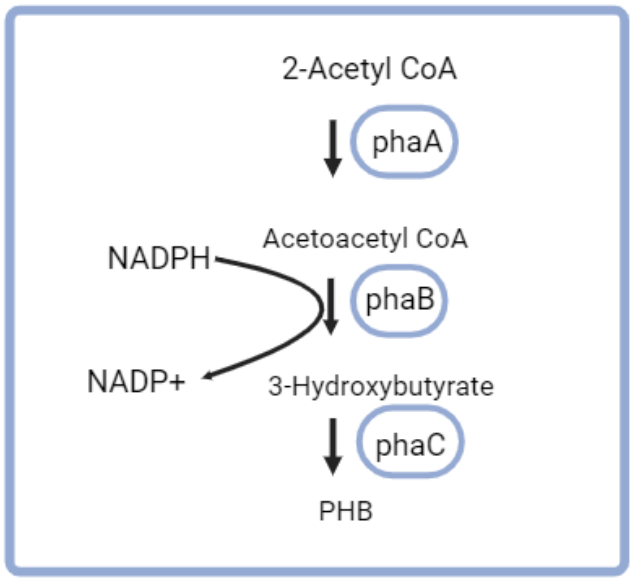
Polylactic acid is synthesised from 2-hydroxypropionic acid, through microbial fermentation, and then undergoes purification. (Juodeikiene et al., 2015), It was first produced in 1845, and shows a low molecular weight, and semi-crystalline appearance, with a melting point of around 130-150°C.

Polyhydroxyalkanoates are produced by *Pseudomonas oleovorans* and in *P. putida* I through mclPHA biosynthetic genes. Two polymerases are involved, PhaC1 and PhaC2, which catalyse the formation of PHA from 3-hydroxyacyl CoA derivatives (Huisman et al., 1991) (Fig.1.1). PHAs inside the cell are generally surrounded by a phospholipid monolayer envelope, which is believed to help avoid contact of PHAs with water, and therefore preventing the transition of PHA from an amorphous mass to a more crystalline form, as well as preventing toxicity to the cell (Sudesh et al., 2000).

PHB is natively found in *Cupriavidus necator,* where it is produced in periods of starvation from acetyl coA, through action of the phaCAB operon (Wang & Yu, 2007). This operon includes 3 genes:

phaA, encoding a 3-ketothiolase which catalyses the conversion of 2 molecules of acetyl-CoA to acetoacetyl-CoA; *phaB*, which encodes an NADPH-dependent acetoacetyl-CoA reductase, which produces 3-hydroxybutyl-CoA from acetoacetyl coA; *phaC*, which encodes poylhydroxyalkanoate synthase, which catalyses the polymerisation of 3-hydroxybutyl-CoA into PHB. phaC is very active towards monomers up to 5 carbon atoms, but tends to include small quantities of higher length polymers (Zinn et al., 2001). Interestingly, excess acetyl CoA suppresses PHB synthesis, while a reduction in acetyl CoA restores it under native conditions. This is a mechanism is to signal acetyl-coA use in other processes when nutrients are abundant, and is thought to happen, at least partly, through acetyl coA reducing the expression levels of *phaA* (Oeding & Schlegel, 1973) (Fig.1.1).

A



B

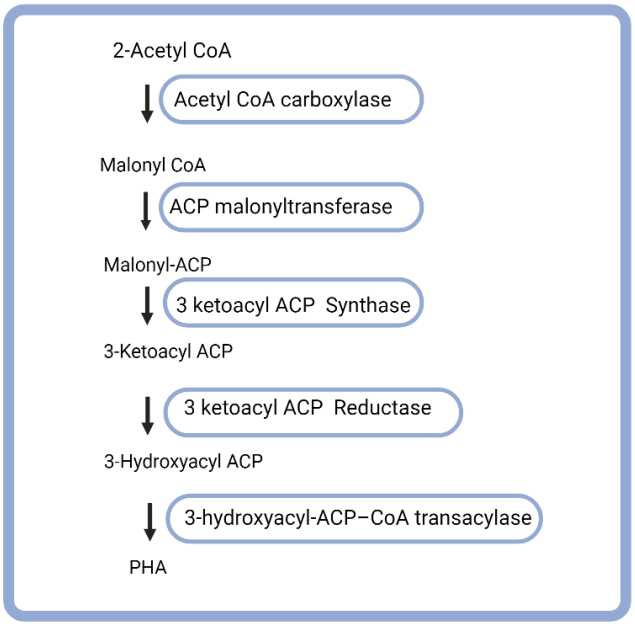


Figure 1.1: *A) Schematic of PHB production B) Schematic of PHA production*

In terms of properties, PHB has a tensile strength close to that of polypropylene, and a melting point temperature of 175°C. It is soluble in organic solvents such as chloroform and biocompatible with medical applications (Turco et al., 2021).

1.3 Optogenetics

1.3.1 History of optogenetics

All kingdoms of life, including animals, plants, fungi, bacteria and protozoa have ways to detect and respond to light (Banerjee & Mitra 2020). There are many uses of light-related properties, from energy conversion, to orientation and the regulation of developmental processes (Brautigam et al., 2004). Aside from photosynthesis, the study of photoreceptors and other molecules involved in bringing about the responses of living organisms to light has been going on for decades, since the first serendipitous observation of light-driven reaction on surface isolates of halobacteria (Oesterhelt & Stoeckenius, 1973). However, the first use of light-sensitive proteins to confer new functionalities to non-light responsive cells comes from the field of neurobiology in 2002, with the expression of *Drosophila* rhodopsin and its signalling proteins in neurons (Zemelman et al., 2002). The same year, channelrhodopsin was discovered in *Chlamydomonas*, which aided the acceleration of the field (Nagel et al., 2002), while the first artificial optogenetic system was created by using a yeast two-hybrid system to create light regulated transcription (Shimizu-Sato et al., 2002). Channelrhodopsin was first engineered into neurons in 2005 to equip them with light-responsive control of action potentials (Boyden et al., 2005). This was the first example of mammalian optogenetics – using light to control the response of living cells or organisms. Since then, optogenetics has been used in a variety of applications, from monitoring cell differentiation (Krishnamurthy et al., 2016) to gene editing (Nihongaki et al., 2015).

In bacteria, the first instance of heterologous optogenetics, that is conferring light responsiveness to cells that do not endogenously possess it, was also shown in 2005 by Levskaya and colleagues, when a cyanobacterial light sensor responding to red and far red light was fused to the *E.coli* EnvZ-OmpR two-component system. In this way, red light was used to spatially control *LacZ* expression by *E. coli*, creating high resolution photographs (Levskaya et al., 2005).

The advantages of optogenetics are various, due to the nature of light as an orthogonal, non-invasive, spatiotemporal stiumulus. At the same time, its accuracy allows control of signalling pathways and biological processes, in a way that has high control over interference. It is superior to pH and chemical cues due to the wave nature of light, which makes it non-diffusible, able to be applied and removed at will with no need for washing the culture medium (Glantz et al., 2016).

1.3.2 Optogenetic classes in bacteria

Since the first bacterial optogenetic system was used In *E.coli,* a number of optogenetic systems have been adapted or developed for microbial optogenetics. While mammalian optogenetics largely uses opsin-based molecules as the sensors, due to the native presence of opsins in mammals (Koyanagi et al., 2014), in bacteria there is a preference for non-opsin photoreceptors such as Light-Oxygen-Voltage (LOV) domains, GAF domains and PCD domains, present in phytochrome, cyanobacteriochrome and cryptochrome proteins (Baumschlager & Khammash 2020). In general, phytochromes were first identified in plant systems and are sensitive to red and far-red wavelength, while cyanobacteriochromes come from cyanobacteria and are sensitive to a wide range of wavelengths. Cryptochromes are found in plants and animals and respond to a variety of wavelengths as well, regulating largely circadian rhythms. Optogenetic function is brought about by light-sensitive domains changing conformation upon receipt of light at a certain wavelength. This effect is brought about by the presence of compounds, called chromophores, which are bound to light-sensitive domains and absorb energy upon sensing of light. Common chromophores include phycoviolobilin (PVB), phycocyanobilin (PCB), phytochromobilin (PFB), and biliverdin (BV), and they determine the wavelength sensed by the optogenetic system (Ikeuchi & Ishizuka, 2008; Ziegler & Moglich, 2015). Common response regulators, which can either be bound to the photoreceptor proteins, or independent entities, are transcription factors, which are activated by the photoreceptors to bring about gene expression. Some of the most popular and well known optogenetics systems in bacterial systems are explored further below. These include the YF1 system, the Cph8 system, EL222, the CCaSR system.

1.3.3 Optogenetic systems

1.3.3.1 Cph8/OmpR

The Cph8/OmpR system was the first one to be used in *E.coli* (Levskaya et al., 2005). Briefly, it was created through exploiting the modularity of two-component systems and phytochromes. A *Synechocystis* phytochrome, Cph1, which uses phycocyanobilin as the light sensitive molecule, but is natively not connected to a DNA binding domain was used as the sensor in this approach. As a response regulator, the *E.coli* EnvZ/OmpR two-component system was adapted. This is a well-characterised system which natively regulates gene expression in response to osmotic shock (Kenney & Anand, 2020). By fusing the sensor from the Cph1 to OmpR, the histidine kinase and the response regulator from EnvZ/OmpR, a one-component system was created. This system undergoes

autophosphorylation under red light, allowing activation of the transcription factor properties, while far-red light has phosphatase and therefore gene expression inhibitory effects (Fig 1.2).

1.3.3.2 YF1

YF1 was generated as a hybrid using the same logic as Cph8/OmpR. As a sensor domain, the LOV photosensory domain of YtvA from *Bacillus subtilis* was used, which is inactive under blue light and activated under dark. This was connected to a histidine kinase, FixL from *Bradyrhizobium japonicum* to create a two-component system (Losi et al., 2002). The signal polarity can be inverted to become inducible under blue light (pDawn) by incorporating a λ phage cI repressor at the downstream of the promoter (Fernandez-Rodriguez, 2017).

1.3.3.3 EL222

EL222 is a naturally evolved transcription factor that encompasses a photosensitive N-terminal LOV domain and a C-terminal DNA-binding domain. Its optogenetic properties are brought about by a dimerization reaction. In the dark, the DNA binding domain contacts to LOV domain, preventing DNA binding. Upon reception of blue light, however, a conformational change is brought which frees the DNA binding domain and allows it to homodimerize to bind a EL222 motif on the transcription factor of choice (Amoutzias et al., 2008).

1.3.3.4 CCaSR

The CCaSR system is a naturally occurring system that is found in *Synechocystis*. It comprises the transmembrane photoreceptor CCaS, and its response regulator CCaR. Upon sensing of green light, CCaS undergoes an autophosphorylation reaction, and then a phosphotransfer reaction to CCaR, which binds to its its cognate promoter to activate gene expression. Upon sensing of red light, phosphorylation of CCaS is inhibited, and rather a dephosphorylation reaction is triggered. Work has been performed on CCaSR, creating two new versions CCaSR 2.0 and CCaSR3.0. The former optimises expression levels of the proteins in *E coli* while the latter builds upon CCaSR2.0 to use a smaller version of the photosensor, and overall to increase its dynamic range by more than 100-fold from the native construct (Tabor et al., 2011; Olson et al., 2014; Ong & Tabor, 2018).

1.3.3.5 AraC Dimers in Escherichia coli (BLADE)

To create this system, the dimerization domain of AraC was exchanged with a blue light-controlled dimerization domain, Vivid (VVD), which has been widely used to control the dimerization of proteins (Wang et al., 2012). Dimerisation of the resulting construct, following illumination, allows

the DNA binding domains of AraC to bind to the I_1 and I_2 half sites of the P_{BAD} promoter and activate transcription (Romano et al., 2021).

1.3.3.6 Opto-T7RNAPs

This system uses the heterologous T7 RNA polymerase, originating from the T7 bacteriophage, and is highly selective for the T7 promoter, independent of native transcription (Baumschlager et al., 2017). The T7 RNA polymerase can be split at different points across its amino acid chain, and normal activity is reconstituted by heterodimerization. Therefore, by splitting the polymerase, and using engineered forms of VVD, termed Magnets, light-controlled dimerization allowed for light dependent control of gene expression from the T7 promoter.

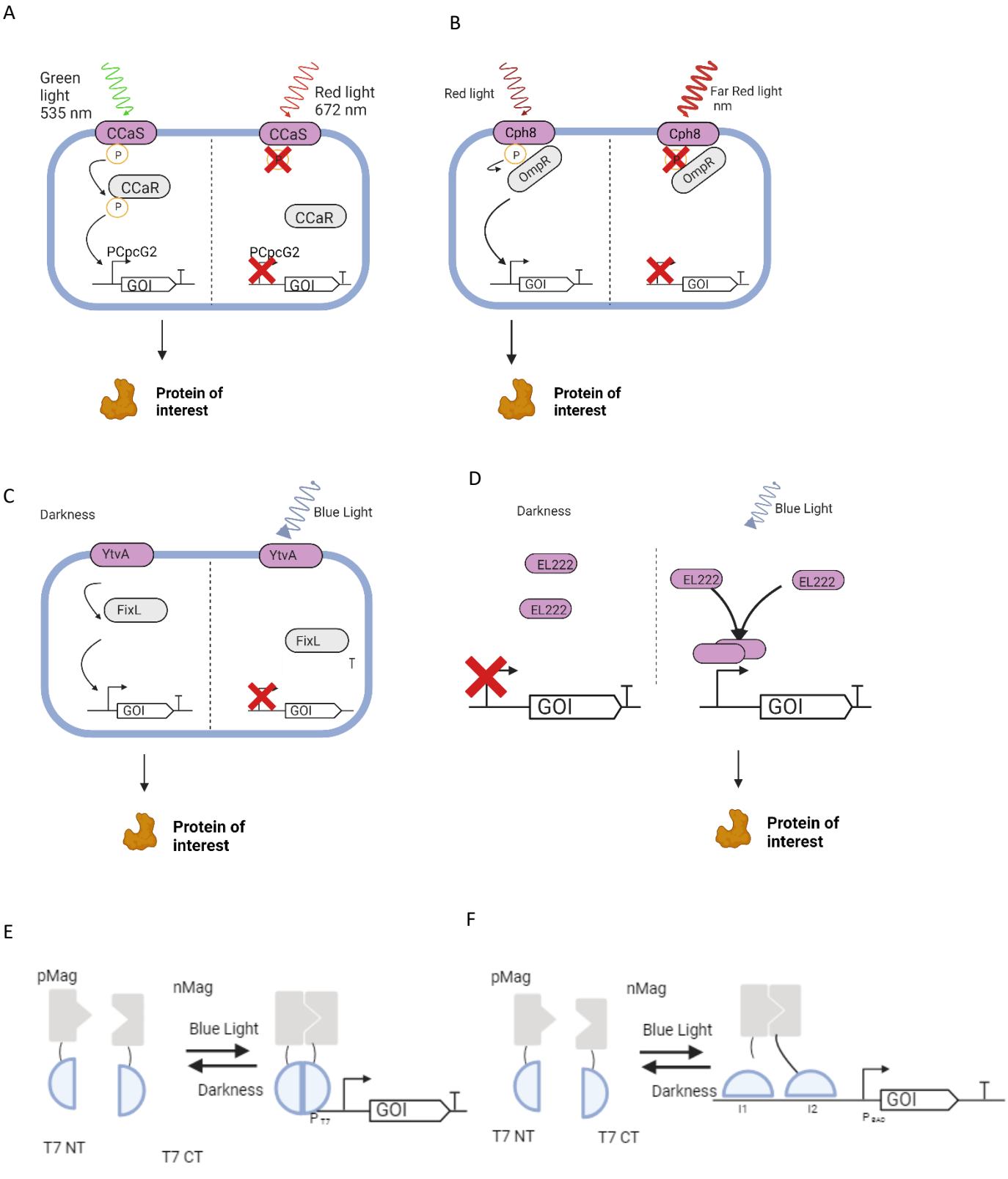


Figure 1.2: *Schematic for the main optogenetic systems. A) CCaSR B) Cph8/OmpR C) YtvA/FixL D) EL222 E) BLADE F) Opto-T7RNAPs.*

1.3.4 Applications of Optogenetics

The ability of optogenetics to control spatial gene expression is a unique one, and has been widely used in synthetic biology to show the ability to control production in 2D for many applications (Fig.1.5). Traditionally, optogenetics has been used in many medicinal applications, most notable in neurobiology, where the non-invasiveness of light inputs together with their spatial capabilities have been used to activate neurons in both mice and human brain cells, allowing the modulation of neural activity (Boyden et al., 2005; Deisseroth et al., 2005).

The first instance of an engineered optogenetic gene expression system in *E.coli* was developed in 2005, involved a photograph on a Petri dish through gene expression of a LacZ pathway in response to red light. This spatial approach was able to demonstrate how optogenetics can control bacterial production in 3D to bring about emergent responses (Levskaya et al., 2005).

Since this first synthetic optogenetic application in bacteria, optogenetics has been widely used in the patterning of ELMs in two dimensions. This technology and concept has been replicated many times, transferring it to different organisms, and printing different molecules in response to light (Tabor et al., 2011; Huang et al., 2018). Some of the most important applications of optogenetic patterning have been for the generation of patterns in 2-dimensional ELMs. For example, in a simple approach utilising the light sensitivity of photoreceptors, a permuted version of the outer membrane protein OmpX has been displayed on the surface of *E.coli* cells, with the other member of the pair immobilised on glass slides. Localised blue light illumination allowed the proteins to interact and localise the cells on the glass slide (Sun et al., 2022). Other technologies have used more traditional optogenetics, controlling gene expression of biofilm forming proteins (csgA), so that localised illumination allowed patterning of biofilms onto diverse surfaces, like textiles and ceramics (Moser et al., 2019). In an application of optogenetic-induced biofilm formation, *E.coli* cells were engineered to produce tryptophan constitutively, but csgA under light control. In this way, light was able to control biofilm thickness and tryptophan production (Hu et al., 2019) (Fig. 1.3).

Optogenetic creation of biofilms has also been used in other organisms, through the use of different signals. Huang and colleagues have managed to use optogenetics to induce biofilm formation by *Pseudomonas aeruginosa* cells on glass slides with an accuracy of 10µm. The cells were engineered to produce, upon illumination, c-di-GMP, a molecule that causes cellular aggregation. This molecule then started a signalling cascade which led to more biofilm formation in

areas of higher c-di-GMP, and the ability to pattern biofilm formation and gene expression of a reporter molecule (Huang et al., 2018) (Fig.1.3).

Light controlled biofilm formation has been coupled to a number of output modules, such as biomineralization, through the optogenetic control of the production of urease (Liu et al., 2022). In other studies, biofilms were patterned using optogenetics to control processes such as antibiotic resistance and the production of pollutant-degrading biofilms (Hu et al., 2019; Sheets et al., 2023).

Aside from biofilms, optogenetics has even been used in the control of autonomous ELM cocultures. More specifically, *S. cerevisae* have been used in coculture with *K. rhaeticus*, where *K. rhaeticus* produced bacterial cellulose sheets which trapped the yeast cells. By engineering the yeast to respond to optogenetic inputs, cocultures were able to be dynamically patterned (Gilbert et al., 2022). In another study, cooperative interactions in yeast communities have been engineered through optogenetic control of invertase production, using optogenetics to shift the behaviour of yeast cells between collaborators and cheaters (Morales et al., 2021).

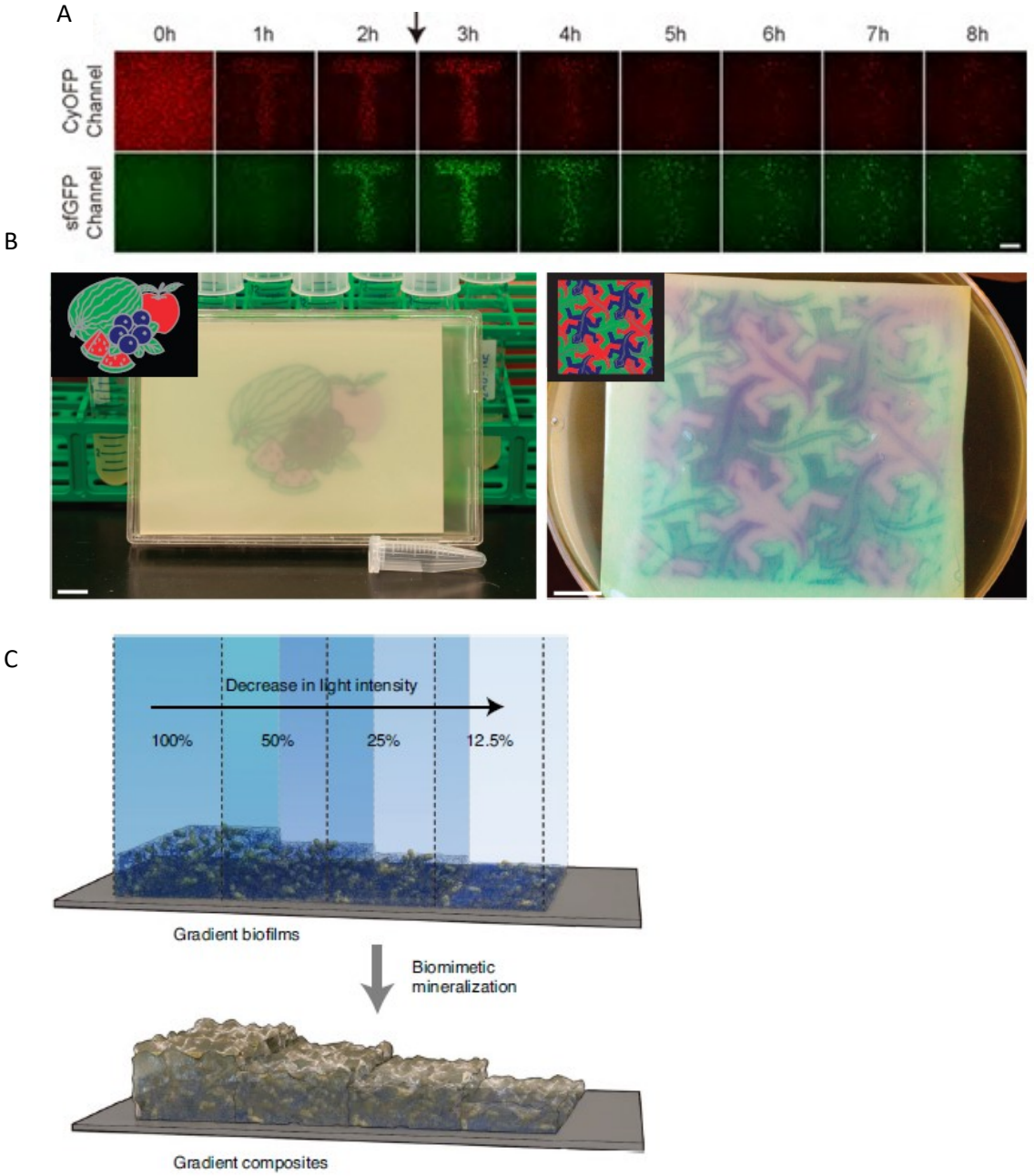


Figure 1.3: *Examples of uses of optogenetics to produce products in 2D as well as a gradient. A) Use of optogenetics to induce biofilm formation in Pseudomonas aeuriginosa, producing cyOFP and sfGFP (adapted from Huang et al., 2018). B) Use of trichromatic optogenetic control in E.coli, to produce living photographs (adapted from Fernandez-Rodriguez et al., 2017). C) Use of optogenetics to produce a biomineralization gradient on a surface (Figure adapted from Wang et al., 2020).*

Extensions to current optogenetic tools in 3D have included an *E. coli* strain that could respond to red, green and blue light inputs (Fernandez-Rodriguez et al., 2017), which was able to attach to fabrics or other surfaces, generating patterned sensors for light and chemical stimuli.

One current limitation of optogenetic systems in patterning cell behaviour, is that they have largely been limited to two dimensions and patterning cells and gene expression on surfaces. All spatial applications of optogenetics so far involve shining light on the surface of a solid culture, to create materials on the surface. The closest optogenetics has come to 3D biomaterials has been the printing of 3D biomineralization gradients. While this technique was still far from able to control precise production in 3 dimensions it showed how optogenetics can be used to guide gene expression beyond two dimensions (Wang et al., 2020). This allows optogenetics in synthetic biology to 3D. For this, it has come of age to incorporate optogenetics into 3d bioprinting.

1.4 3D Bioprinting

Additive manufacturing, commonly known as 3D printing, is the process of creating three-dimensional objects by adding and connecting materials in layers, instead of removing pieces from a whole or connecting parts together (Shahrubudin et al., 2019). It encompasses both traditional 3D printing, as well as bioprinting, which for this case is defined as the printing of biomaterials of microbial origin for the purposes or creating ELMs. Bioprinting has be performed using bioinks loaded with cells, or with bioinks alone that are seeded with cells afterwards (Gona et al., 2020).

Various 3D printing technologies exist. Of them, two are widely used in bioprinting for the creation of biomaterials: material extrusion and inkjet bioprinting. In addition, light based methods such as laser-based bioprinting, vat polymerisation and tomography are gaining popularity in conventional 3D printing, as well as in the 3D printing of organs, but have not yet been used in microorganisms for the printing of ELMs .

In material extrusion-based bioprinting, an ink is released from a nozzle onto the printing surface in a layer-by-layer manner, creating the desired shape in this way (Spiesz et al., 2019; Jiang et al., 2020). Most often, the ink is loaded into a syringe, which allows a computer to control pressure and positioning, therefore how much ink is released where. For extrusion bioprinting, the rheological and cell viability properties of the ink are very important, as a bioink needs to be viscous enough with shear-thinning properties to maintain its structure, but soft enough to allow extrusion, while maintaining viability of the cells (Fu et al., 2021). Advantages of extrusion-based printing include the uniformity and availability of cell loading, but it is a slow process, with low resolution and limited geometric options and cell viability.

Extrusion-based bioprinting is by far the most widely used method in 3D bioprinting of biomaterials. To this end, conventional existing 3D printers have been adapted to be able to extrude

alginate based hydrogels, creating cheap methods for the 3D printing of biomaterials (Lehner et al., 2017, Spiesz et al., 2019). In addition, hydrogels with antimicrobial activity for medical uses have also been printed using this approach (Ramesh et al., 2021) (Fig.1.4).

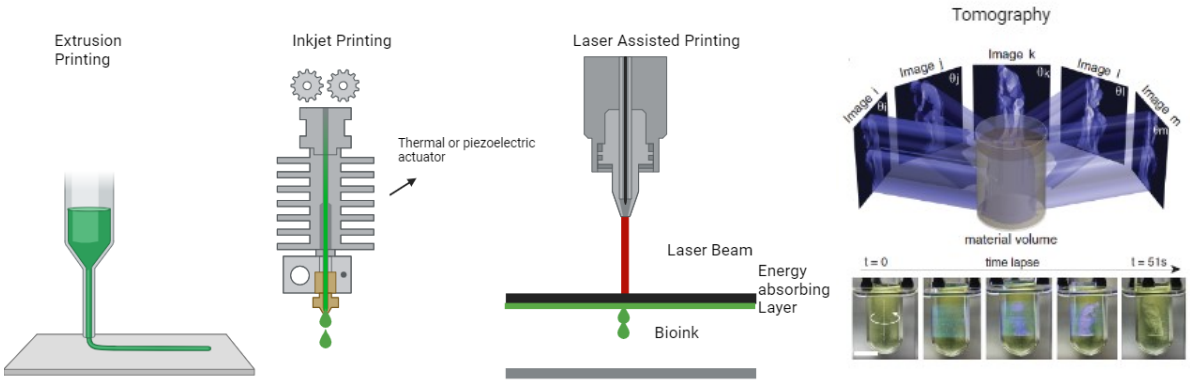


Figure 1.4: *3D printing methods with potential for 3D bioprinting.*

In terms of applications, regenerative photosynthetic ELMs have been created through the encapsulation of algae in an alginate matrix, followed by extrusion 3D printing, on a substrate of agar or bacterial cellulose, creating materials of only living origin (Balasubramanian et al., 2019). In addition, biofilms have been printed using extrusion-based methods, creating living materials with high stiffness and strong mechanical properties (Balasubramanian et al., 2019). Others have been able to combine functions of bacteria in the hydrogels. For example, through the use of bioinks composed of three biologically compatible polymers, phenol-degrading *Pseudomonas putida* was immobilised on a 3D lattice for the biodegradation of waste and bacterial cellulose-producing *Acetobacter xylinum* was printed in a 3D structure (Schaffner et al., 2017). In another study, researchers embedded *E. coli* cells and nanofibers into microbial ink, which can sequester toxic moieties, release biologics, and regulate its own cell growth through the chemical induction of rationally designed genetic circuits. The bioink itself, termed 'flink' which was able to form 3D shapes in arbitrary geometries upon extrusion. Other ways to improve bioinks used have also combined it with the materials printed, for example by using *G. xylinus* to print granular cellulose hydrogels which help to set a fluid bioink (Binelli et al., 2022).

Other research has focused on developing the shapes that can be printed, for example in developing robotic arms with 6 degrees of freedom in movement. Alternatively, research has focused on real-world applications. For example, for medical applications, dried *Lactobacillus rhamnosus* has been incorporated in bioinks for oral delivery of probiotics (Rosas-Val et al., 2023), while *Sporosarcina pasteurii* has been used for its biomineralization abilities to 3D print bone-like composites (Hirsch et al., 2023).

Inkjet printing is similar to extrusion printing in that it involves a nozzle extruding the material. However, in inkjet bioprinting the material is extruded in droplets, either through heat or acoustic means. The bioink needs to be more liquid than in extrusion -based printing, which has been achieved by using lower concentrations of cells and additives that affect the viability of cells. However, it is a cheap technology for 3D bioprinting (Zub et al., 2022).

Inkjet bioprinting has been used widely in the early days of bioprinting, for example to produce 2-dimensional shapes using biotin (Wilson & Boland, 2003). Alginate has also been a widely used hydrogel in inkjet bioprinting, although biomaterials printed through inkjet printing have been found to present hollow microstructures not seen with extrusion bioprinting, and relating to the droplet methods involved in inkjet printing (Axpe et al., 2016). However, despite its wide use in medical applications and the 3D printing in organ and tissue bioprinting, inkjet bioprinting has not found such wide success in bacteria, due to poor resolution and the requirements for clean-room facilities for fabrication of the bioinks (Lehner et al., 2017).

Another similar approach widely used for mammalian cells is laser-assisted bioprinting, where the bioink is deposited on a glass slide with a thin metal coating. Laser applied to the glass slide causes it to heat up, creating a bubble that extrudes the bioink on to the substrate. This method has been used for a variety of materials, and offers high resolution, precise deposition, and the ability to print bioink-free cells, but is expensive due to the inclusion of lasers (Dou et al., 2021). Cells printed using this approach include human dermal fibroblasts, muscle myoblasts, as well as graftskin substitutes (Douillet et al., 2022; Ostrovidov et al., 2019; Michael et al., 2013), indicating its importance in regenerative medicine. However, it has remained largely underused in bacterial biomaterial work due to the small size of bacteria, need for specialised media and high temperatures required, which would kill living organisms.

As opposed to layer-by layer approaches described above, Vat polymerization-based bioprinting, often referred to as stereolithography (SLA), involves using a laser to directly cause polymerisation of a liquid photopolymer in situ, to create a 3D object (Shaukat et al., 2022). These photopolymers typically consist of a monomer or oligomer starting liquid and a photoinitiator, that absorbs light to start the polymerisation process. Photoinitiators play a crucial role in driving polymerization upon exposure to specific wavelengths of light. Conventional vat polymerization in 3D printing entails illuminating a thin layer of polymer at the vat's surface, and then adding additional layers, through projecting an image or tracing a laser beam on the layer.

Bioinks used in vat polymerization-based bioprinting are photosensitive and solidify layer by layer through the projection of an image. Instead of UV light, which is used for bioink polymerization, visible light-based bioinks have been developed to minimize cell damage (Zheng et al., 2021).

A subset of vat polymerisation is dual wavelength polymerisation, where either polymerisation happens upon receipt of two different activating wavelengths of light, or one activating wavelength and one inhibiting wavelength. These techniques allow polymerisation anywhere within the volume rather than just near the surface, but specific photoinitiators and photoinhibitors are needed (Zhang et al., 2021).

In volumetric vat photopolymerization the whole object is polymerized simultaneously. One approach is tomographic reconstruction, where a hologram of the image is projected in 3 dimensions in different positions. Using this method, very accurate shapes have been printed in conventional 3D printing, with accuracies of up to 0.3 mm and within timeframes of 120 seconds (Kelly et al., 2019). In addition, optically tuned resins have been used for the printing of liver organoids (Bernal et al., 2022).

Despite the superiority of optical based 3D printing methods in conventional 3D printing in terms of timing, resolution and geometric capabilities, as well as their coming of age in organ bioprinting, light based bioprinting remains underused for the 3D bioprinting of microbial biomaterials and in the generation of ELMs. The main reason for this has been the traditional toxicity of photoinitiators and photoinhibitors, as well as lack of viability of microorganisms in many of the organ-based bioinks. However, despite the inherent or engineered ability of microorganisms to respond to light through optogenetics, surprisingly, no studies have attempted this in 3 dimensions.

1.5 Aims and Objectives

Optogenetics is a promising platform for the control of position and gene expression by microorganisms in 3 dimensions, for the purposes of controlling 3D printing of hybrid biomaterials and ELMs. It poses several advantages over conventional, inkjet-based 3D bioprinting methods, as it allows a suite of non-trivial 3D geometries to be achieved, is not limited by the availability of fluid bioinks that can support cell viability and also solid shapes, and allows for non-invasive control of production, even post-deposition of the cells in the desired shape. Moreover, optogenetics offers advantages compared to traditional light-based bioprinting, as it dispenses of the need for photoinitiators or light-responsive resins, which have posed problems for toxicity of cells.

Optogenetics studies have focused on improving the dynamic range and sensitivity of systems, combining systems together, and allowing optogenetic control of a wide variety of behaviours. With these in mind, the use of optogenetics in 2-dimensional bioprinting, as well as gradient biomineralization has paved the way for the use of optogenetics in 3 dimensions, by showing how optogenetics can be used to generate dynamic contrasts in gene expression of reporter molecules, as well as useful materials.

The overarching aim of this work, was therefore to **use optogenetics to control gene expression by microorganisms in a 3D hydrogel matrix.** From this aim stemmed 3 more specific objectives, which aimed, when and if achieved, to show how optogenetics can, as a proof of concept, be used to control gene expression in 3 dimensions, improving current 3D printing approaches, and with the potential to 3D print biomaterials and ELMs in the future.

Objective 1: Optogenetically control in three dimensions the expression of a visually quantifiable reporter molecule by cells embedded in a 3D hydrogel matrix. This should be such that expression of the reporter should be (a) able to be thresholded in a quantifiable way, such that the positions of 'production' of the reporter can be clearly distinguished from positions of non-production (b) produced in true three dimensions, such that positions of production are in the centre of the 3-dimensional volume and have no contact with either of the surfaces of the volume.

Objective 2: Optogenetically control in three dimensions the gene expression of a reporter molecule, such that a non-trivial 3-dimensional shape is produced by linking together all the thresholded production regions. This object should be produced without the need for support structures, and without the need for stacking of two-dimensional planes, therefore showing the superiority of the technique over conventional layer-by-layer 3D Bioprinting.

Objective 3: Use the concepts developed in achieving objectives 1-2, to control the production of biomaterials beyond fluorescent molecules in the 3-dimensional hydrogel matrix. These biomaterials can be hybrid biomaterials, incorporating living organisms with the matrix, as well as products of these living organisms, such as biologically produced plastics or enzymes that alter the appearance and properties of the matrix.

In achieving these 3 objectives, aims of the project also include some expected contributions. These are i) the characterisation of the optogenetic control of gene expression and growth of cells inside the hydrogel matrix; ii) the development of an illumination method suitable for optogenetic activation in three dimensions; iii) The development of a 3D bioproduction imaging system; iv) the generation of optogenetically-controlled biomaterials.

In this work, characterisation was done by Andreas Hadjimitsis. Borut Lampret was involved in making the illumination hardware, and developing the gcode programmes and simulations for 3D bioprinting, as well as deciding the light intensities and running a large number of the printing experiments. George Taylor and Martin Todd did a combinatorial library assembly of a pathway for PHB production *in E. coli*, while Albert Fabregas Flavia was involved in the initial cloning of tdFAST2 under optogenetic control.

Chapter 2

Establishing a biological set up for optogenetically controlled 3D printing

2.1 Introduction

The main goal of this thesis concerns the establishment of a system to control gene expression by microorganisms, in a 3-dimensional (3D) setting. Extrusion 3D printing is limited in the geometries and materials that can be printed (Jeong et al., 2020), therefore a light-based method was chosen for this technology. Optogenetics, i.e., the control of cell behaviour and gene expression using light, presents a technology that can control bacterial production in a non-invasive manner, without the need for toxic substances to act as photoinitiators. It also enables a greater variety of materials and geometries that can be printed compared to extrusion 3D printing. In this chapter, I focus on the development of the aspects of this 3D printing technology that pertain more to the cells and optogenetic systems used, rather than the illumination hardware. More explicitly, I focus on the strains, plasmids and optogenetic conditions used, as well as the culture conditions necessary for 3D bioprinting. In addition, I focus on choosing a molecule that could act as a reporter for the 3D control of gene expression, providing a proof of concept for the feasibility of the technology developed. Choices and measurements outlined in this chapter inform the printing setup and conditions used in the following chapters.

The development of this technology required several choices having to be made in order to optimise the printing platform, therefore increasing its performance in terms of materials printed and dynamic range and reducing parameters such as length of printing.

These choices were identified as:

1. The choice of chassis for the 3D printing. The organism that would be optogenetically engineered in order to act as the producing organisms for the required materials.
2. The optogenetic system used, to give a high dynamic range for accurate prints.
3. A solid support medium, which would be able to support the cells in a 3D volume, while allowing light to reach them with minimal scattering.
4. A growth medium that could be mixed with the solid support medium to allow the cells to be viable and grow in the 3D volume for the duration of the print, without affecting detection of the results.
5. A reporter molecule for the proof-of-concept print, that would be able to be accurately quantified spatially, in a non-invasive, optical imaging way.
6. Any genetic circuits that could be employed to improve the dynamic range of the optogenetic system, in order to increase print contrast.
7. Any other considerations that could improve the print.

For the first consideration, I wanted to choose a cellular chassis that would be easy to genetically modify and transform, to insert genetic modules coding for optogenetic components and material production. Secondly, the chassis should be well studied in terms of its bioproduction capabilities for down-the-line customisation of 3D printing and possible production of an array of materials. Thirdly, the chassis should be well studied, with several optogenetic modules available for easier troubleshooting. Finally, in order to reduce printing time, the chassis should have a short doubling time. *E. coli* fulfilled all these criteria, as it has a doubling time of around 30 minutes, and a suite of genetic modification tools available, with a large number of optogenetic and bioproduction studies showcasing its abilities (Taj et al., 2014).

The second parameter that needed to be chosen before the start of experiments was the optogenetic system used. There are many optogenetic systems available, with various advantages and disadvantages. The scope of this project was to provide a proof-of-concept for the 3D bioprinting platform, which would involve a number of optimisation processes and changes through the course of the project. Therefore, instead of doing a wide array of optogenetic system characterisations, I wanted to settle on a system to use from the beginning, which would allow me more time to work on optimising the printing conditions. The requirements for such a system included: (i) a large dynamic range, in order to obtain the necessary contrast, and (ii) a high sensitivity, to avoid using high intensities of light that could damage the cells. Finally, it would be beneficial for the optogenetic system to respond to multiple wavelengths of light, ideally allowing activation and inactivation, fine-tuning of production, or the potential for printing multiple materials.

A module that fulfilled all of these requirements is the CCaSR optogenetic system (Tabor et al., 2011). CCaSR is based upon a cyanobacterial 2-component system, that controls expression of the phycobilisome linker protein CpcG2 in the *Synechocystis* PCC6803 complementary chromatic adaptation pathway. It includes the CCaS transmembrane light sensor protein, which is a cyanobacteriochrome histidine kinase, and the response regulator, CCaR. CCaS comprises a putative N-terminal transmembrane region, a photosensitive phycocyanobilin (PCB)-binding GAF domain, two PAS domains and a C-terminal histidine kinase domain (Hirose et al., 2008). CCaS is produced in the green-absorbing, inactive ground state that has a low histidine kinase activity. Under green light at 532 nm, CCaS undergoes a conformational change to the active, red-absorbing state, which leads to an autophosphorylation reaction. CCaS autophosphorylation subsequently increases its histidine kinase activity and leads to phosphorylation of the response regulator, CCaR. Upon phosphorylation, the response regulator undergoes a conformational change which activates its transcription factor properties, allowing it to bind to the CpcG2 promoter, promoting gene expression. Under red light at 660nm, CCaS undergoes dephosphorylation, leading to deactivation of CCaR, and a reduction in gene expression (Hirose et al., 2008) (Fig 2.1).

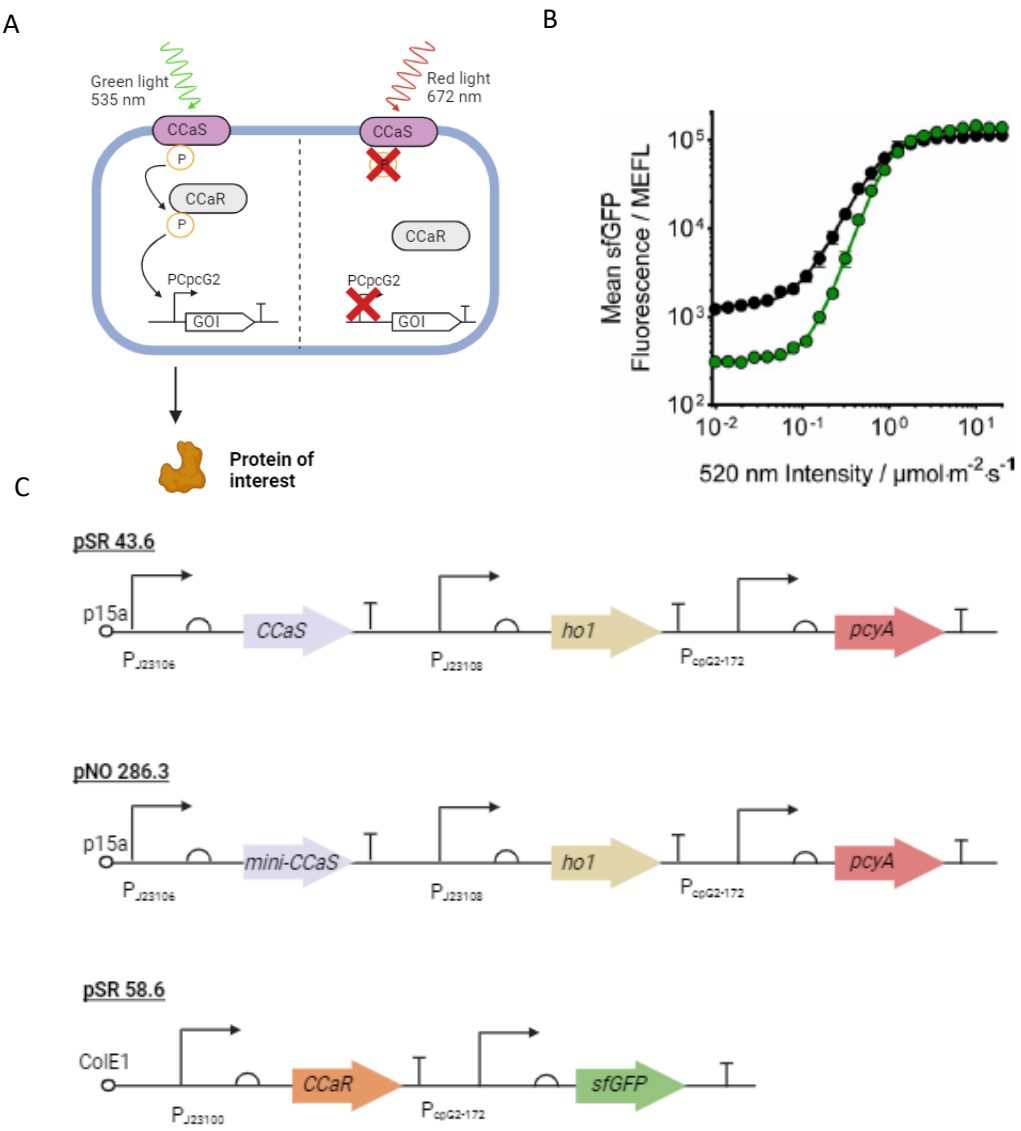


Figure 2.1: *A) Graphic depiction of the CCaSR 3.0 optogenetic system. Here, the locations of each of the two proteins in the cell are indicated, as well as the responses to green and red light. Under green light, a phosphorylation cascade leads to transcription of the gene of interest (GOI), through activation of the PcpG2 promoter. Under red light, CCaS is dephosphorylated, leading to reduced gene expression. B) Schematic of the Hill function for the response of CCaSR 2.0 (black line) and CCaSR 3.0 (green line) to green light at 520nm, according to Ong and Tabor (Figure taken from (Ong & Tabor, 2018)). 1 µml/m²/s corresponds to 230 mW/m². While both systems reach a similar fluorescence intensity at saturation, CCaSR 3.0 gains its higher dynamic range due to a lower fluorescence intensity in darkness and very low light intensities. C) Schematics of the genes involved in the CCaSR 2.0 and 3.0 versions. CCaSR 2.0 is made from plasmids pSR 43.6 and pSR 58.6, while CCaSR 3.0 is made from plasmids pNO 286.3 and pSR 58.6. ho1 and pcyA encode for auxiliary proteins, aiding in the production of PCB, a component of the active CCaS protein.*

The first use of CCaSR in *E.coli* was reported by Tabor et al., who optimised it by co-transforming *E. coli* with two plasmids: one containing the genes encoding for CCaS and CCaR, together with another plasmid containing Synechocystis PCC6803 *ho1* and *pcyA*, which encode correspondingly a heme oxygenase and a phycocyanobilin (PCB) / ferredoxin oxidoreductase, in order to enhance PCB production by *E. coli* (Tabor et al., 2011). In a second iteration of the system, CCaSR 2.0, libraries of synthetic ribosomes and promoters were used to optimise expression of each of the genes, giving a 170-fold dynamic range (Schmidl et al., 2014). The most recent iteration to date is CCaSR 3.0, where a truncated version of CCaS was used, leading to a reported dynamic range of over 590-fold (Ong & Tabor, 2018). Therefore, this optogenetic system fulfilled all the initial requirements, with a high dynamic range, a high sensitivity, with a response at 23 mW/m^2, and the possibility to use both green and red light for activation and repression accordingly.

In order to characterise the optogenetic system and obtain some confidence in the results, it was necessary to test both the CCaSR 2.0 and 3.0 systems. Under steady state, CCaSR follows Hill function dynamics in its activation, with a steady background expression that occurs in the dark, and in very dim lights below an activation threshold. This gene expression is thought to occur not through CCaS and CCaR activation, as these would be inactive in the ground state, but through off-target binding of other transcription factors to the promoter. Once the activation threshold is reached, gene expression increases with a higher intensity of green light, up to a point where maximum gene expression is reached. Therefore, increasing light intensity above the maximum threshold would also not have an effect on gene expression, beyond maximum expression. Olson and colleagues have modelled this system through time-course measurements in a light plate and flow cytometry, to infer activation and inactivation dynamics of the system, and to characterise parameters and draw equations around the function of the system (Olson et al., 2017). Measurements were taken under steady state, by observing cells in exponential phase. In order to understand how CCaSR works, and the parameters involved, this model is explored further here.

Theoretically, the model is based around the concept of the presence of photoreceptors in the system, representing sensor CCaS molecules. These are produced in the inactive, ground state, and become active upon absorption of green light, while red light deactivates the photoreceptors back to the ground state (Fig.2.2).

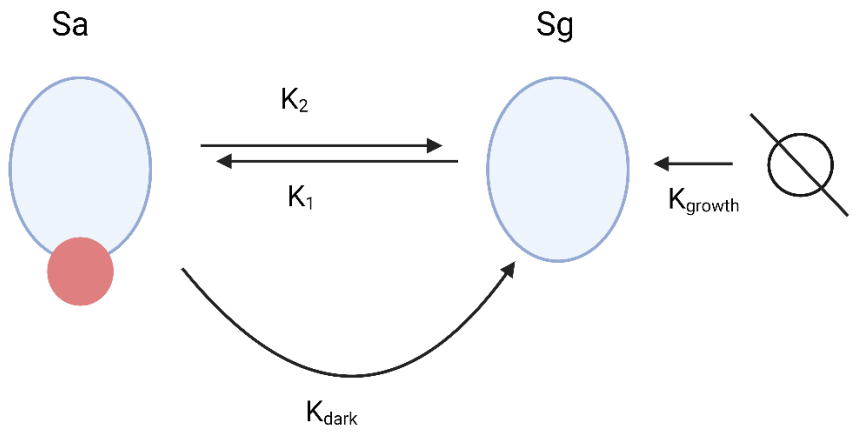


Figure 2.2: *Activation and inactivation of the CCaSR system photoreceptors, where S = Sg + Sa, Sg and Sa are the total, ground-state and active-state photoreceptor populations respectively,* k_{growth} *is the rate at which new photoreceptors are produced,* k_{dark} *is the rate at which active-state photoreceptors revert to the ground state in the dark. k1 is the rate at which green light converts ground-state photoreceptor to the active-state and k2 is the rate at which red light converts the active-state photoreceptors back to ground-state.*

Under steady state, the total photoreceptor population is proportional to the cell growth and therefore k_{growth} becomes the same as the cell growth rate. The dark reversion rate k_{dark} for CcaSR is be negligible (Rockwell et al., 2012), and can be set to zero.

The forward and reverse photoconversion rates both k1 and k2 are dependent on the wavelength of light, while the intensity of light affects the photoconversion rate as a product with k_i. Therefore, the parameters in fig.2.2 can be used to give an expression for the rate of production of active state photoreceptors, as a ratio of the total photoreceptors in the system (equation derived in appendix).

$$\frac{d\eta(t)}{dt} = k_1 - (k_1 + k_2 + k_{growth})\eta(t) \qquad \text{(Equation 2.1)}$$

Therefore, the total fraction of active photoreceptors becomes equal to

$$\eta(t) = \eta_0 + \left(\frac{k_1}{k_{sum}} - \eta_0\right)\left(1 - e^{-k_{sum}t}\right) \qquad \text{(Equation 2.2)}$$

If the K values are constant. Where η= Sa/S, η_0 is the initial fraction of active-state photoreceptors and k_{sum} equals the sum of all rates $k_{sum} = k_1+k_2+ k_{growth}$. Therefore, the steady state fraction of active photoreceptors is proportional to the activating photoconversion rate as a proportion of all rates.

If the photoreceptors are left in the dark, assuming no spontaneous activation and inactivation of photoreceptors ($k_1 = k_2 = 0$), then there are no active-state photoreceptors in steady state, as new ground-state photoreceptors are constantly produced, diluting any active state photoreceptors. As the growth rate of the cells increases, the fraction of active state photoreceptors also exponentially approaches zero.

If the photoreceptors are illuminated with only green light ($k_2 = 0$, $k_1>0$), then the steady-state fraction of the active photoreceptors depends on the intensity of light in relation to the rate of growth. Under no growth, the endpoint fraction of active photoreceptors would be 100% due to the activation of all photoreceptors, regardless of light intensity. However, due to cell growth and constant addition of ground-state photoreceptors, the intensity of the green light needs to overcome the dilution due to the addition of ground state photoreceptors. If the photoreceptors are illuminated only by the red light ($k_1= 0$, $k_2>0$), then the steady-state fraction of the active photoreceptors is zero, with the red light intensity only affecting the rate of deactivation of already active photoreceptors. If both green and red light are used, the steady state fraction of active photoreceptors will tend to a steady state, depending on the ratios of the constants used as well as k growth.

The fraction of active photoreceptors can be connected to the rate of gene expression by the system in steady state (exponential growth) through a Hill function:

$$Ex(t) = b + a\frac{R^n(t-\tau)}{K^n+R^n(t-\tau)} = b + ah(t) \qquad \text{(Equation 2.3)}$$

where b is the minimum gene expression rate, that can occur by leaky activation of the promoter. a is the maximum expression rate induced by all active photoreceptors, n is the Hill coefficient, R =Sa/Sg = $\eta/(1-\eta)$ is the ratio between active-state and ground-state photoreceptors, K, is the ratio Sa/Sg at which induced expression is at 50% and τ is the delay between the change of the state of photoreceptors and the change in reporter gene expression rate.

To determine the total gene expression density, the gene expression in each individual cell is multiplied by the number of cells: If growth is exponential, then the solution to the Hill function is also exponential. If gene expression rate and cell population are constant the solution to Eqn. 2.3 is a linear function of time. Of course, this model was devised by measurements in early exponential phase, and the relationships and values between parameters are only valid for exponential growth and not for states like lag phase, where metabolism would be different, largely affecting values such as a & b.

This model was parametrised using flow cytometry of CCaSR 2.0 cells in a liquid medium (Olson et al., 2017). At the same time, parameters for the Hill equation of CCaSR 3.0 have also been supplied in later iterations of the technology (Ong & Tabor, 2018). The constants for photoconversion and growth were not calculated for CCaSR 3.0, but time-variant measurements under green and red light showed similar results to CCaSR 2.0 therefore, allowing the hypothesis that the two constants were similar.

Parameter	Value CCaSR 2.0	Value CCaSR 3.0	Units
a	9.7	15.84	10^4 MEFL
b	0.165	0.00267	10^4 MEFL
N	2.11	2.74	-
K	0.319	0.43	-
K1	10.7	N/A	10^{-3} min^{-1} μmol^{-1} s m^2
K2	4.86	N/A	10^{-3} min^{-1} μmol^{-1} s m^2
k_{growth}	1.85	N/A	10^{-2} min^{-1}

Table 2.1: *Parameters used in CCaSR 2.0 and 3.0. MEFL stand for units of equivalent fluorescein. Units were used for the CCaSR version in use at any case when they were used. In the case of absent parameters for CCaSR 3.0 the CCaSR 2.0 parameters were used, except for kgrowth which was set at 0.96 x10² min⁻¹.*

The high dynamic range, multiple wavelengths available and availability of theoretical modelling of CCaSR, giving the values of several available parameters, allowed us to choose CCaSR as the system of choice with relevant confidence. Once the optogenetic system and chassis were chosen, a broad strategy for the 3D printing was devised. Similarly to tomographic 3D printing (Kelly et al., 2019), I envisioned the cells immobilised inside a 3D volume. In this case, for simplicity of function, instead of a light mask, activation would occur with targeted light focusing optogenetic activation in specific 3D locations. In a theoretical print, gene expression and protein production is observed in locations where the light exceeds the threshold for activation. This occurs in specific ‘dots’, or ‘voxels’ of

activation, in 3D locations. A 3D shape is therefore created through the joining up of multiple voxels, in continuous locations (Fig. 2.3).

With the optogenetic system, organism of choice and a theoretical printing framework in place, the rest of the considerations were assessed experimentally, to obtain values and timeframes for the activation and inactivation of gene expression as well as the growth of cells. Once the optimal set of conditions was decided, the system was characterised with those conditions.

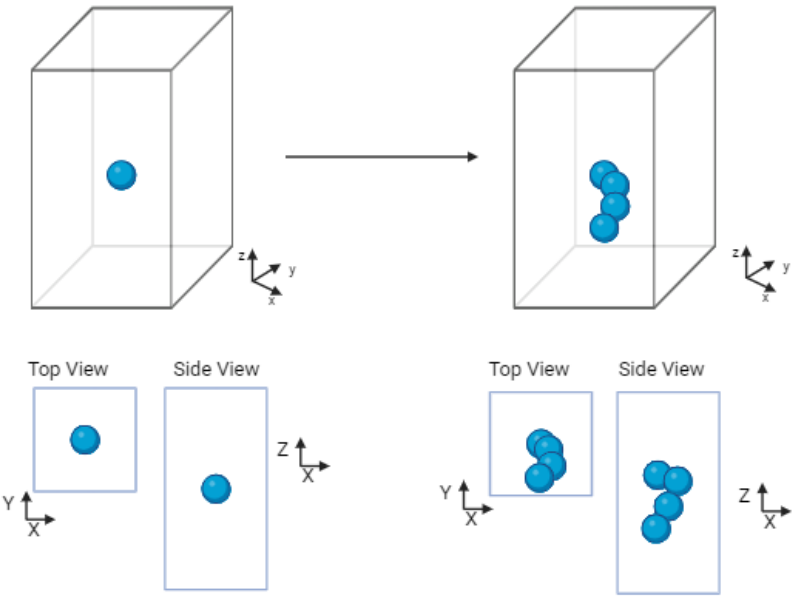


Figure 2.3: *Schematic of the logic behind the 3D printing approach. On the left a single dot (voxel) is printed in a 3D volume. On the right, a series of voxels are printed independently, together making a 3-dimensional shape in the volume.*

Overall, in this starting chapter, I obtain initial results with the aim of identifying a 3D bioprinting biological system that could be optimised to respond to localised optogenetics. Once this system was identified, it was characterised both experimentally and computationally, and the requirements for a 3D printing result 'proof of principle' were designed. The protocol, characterisation and 3D printing goals stemming from results of this chapter, is used in the following chapters, which attempt to print in 3D using the identified system.

Objectives for Chapter 2

- Characterise growth and gene expression of cells harbouring either version of CCaSR in liquid
- Decide which version of CCaSR to use

- Decide which molecule to use as a reporter
- Decide which solid support medium to use
- Decide which growth medium to use
- Characterise the optogenetic system with the chosen parameters under different light intensities
- Identify ways to improve the dynamic range of the system

2.2 Results and Discussion

2.2.1 Growth and gene expression in darkness

The first step in understanding the optogenetic system was to verify growth and gene expression by CCaSR 2.0 and CCaSR 3.0-transofmed *E. coli* cells, in liquid media under darkness. The goal was for printing to be performed during the early stages of growth, so that the optical density would be low enough to avoid scattering, and fluorescence intensity by cells in darkness (background) would not interfere with detection of fluorescence from activated cells (signal).

For this reason, I obtained the CCaSR 2.0 and 3.0 plasmids from the Tabor lab, which include an output plasmid encoding superfolder green fluorescent protein (sfGFP), and a helper plasmid containing auxiliary genes for optogenetic gene expression. These plasmids were transformed into TOP10 competent cells (Thermo Fisher Scientific). In order to perform these darkness growth measurements, cells were grown in dark conditions overnight in liquid M9-glucose media supplemented with the necessary antibiotics, and then inoculated in the same media with glucose-M9 media at a starting OD700 of 0.005, into a 96 well plate (Materials and Methods 7.3.3.5). OD700 was used instead of OD600, because OD600 is in the red light spectrum, and would interfere with the optogenetic system. In the 96-well plate, the CCaSR 2.0 and 3.0 strains of *E. coli* were then grown overnight in darkness with shaking, recording both their OD700 and fluorescence intensity of sfGFP (the latter using excitation/emission wavelengths of 485/535 nm respectively). Performing tests in a 96-well plate format enabled each experiment to use 78 replicates therefore obtain reliable data about the growth and gene expression of the cells over time. The experiments were repeated on multiple days (n=4).

The growth and fluorescence curves documented below (Fig. 2.3) indicate that both strains were able to grow and express *sfGFP* under darkness. Growth was similar for both strains, following standard bacterial growth kinetics. There was an initial early lag phase of low OD700, followed by an exponential phase lasting until roughly 350 minutes, after which growth seems to slow down (Fig.2.4 A).

Plotting the growth rate of the cells per hour indicates that the growth rate continuously increased in a linear manner for the cells in the first 350 minutes, followed by about 60 minutes of steady growth and then a decline in the growth rate (Fig. 2.4 B). The growth rate curves for both strains

were almost identical, as is also apparent in the OD700 graph. The final OD700 for both strains was similar, with CCaSR 2.0 plateauing at 0.37 arbitrary units (AU), while CcaSR 3.0 was at 0.41 AU after 500 minutes (t=1.118, p=0.3314). Similarly, the maximal growth rate was 0.06 AU/hr for CcaSR 3.0 and 0.067 AU/hr for CCaSR 2.0, reached for both after 360 minutes of growth. This result was expected, as both strains encode for very similar proteins in their plasmids and have a similar chassis due to the similar structure of the plasmids and the nature of the encoded proteins in the two strains. The only difference between them is the size of the CCaS protein, which is smaller in CCaSR 3.0. For both strains, the growth curve indicated that cells were at an actively dividing phase from the beginning of incubation until 300 minutes, offering a wide timeframe for optogenetics experiments to be performed.

In contrast with OD700, the measured fluorescence intensities differed largely over time for the two strains, in accordance with results reported in the literature about background fluorescence of the CCaSR 2.0 and 3.0 (Fig.2.1 C, Fig. 2.4 C; Ong & Tabor, 2018). CCaSR 2.0 showed a higher starting fluorescence, despite the same concentration of the initial inoculant. The lag phase, in terms of fluorescence intensity, for CCaSR 2.0 was around 100 minutes, after which the fluorescence intensity increased steadily to reach 1000 AU after 500 minutes. In comparison, CCaSR 3.0 fluorescence intensity maximum was 400 AU after 500 minutes, less than half that of CCaSR 2.0 (t=13.569, p=0.0034). The lag phase was found to be ca. 1.5 times longer, with a visible increase in fluorescence intensity appearing after 140 minutes.

In Fig. 2.4 D I studied the rate of change of fluorescence Intensity per hour. For both strains there were significant fluctuations, with a peak in the rate of change of fluorescence intensity around 460 minutes for both. The longer lag phase was also apparent in CCaSR 3.0, as fluorescence intensity change rate only started to increase after about 100 minutes.

Overall, CCaSR 2.0 and 3.0 showed similar growth kinetics, with an active dividing phase lasting over 300 minutes. With regards to fluorescence, CCaSR 2.0 showed more than double the background fluorescence of CCaSR 3.0. It also entered an active production phase earlier than CCaSR3.0, at 60 minutes rather than 100 minutes. Because of the lower fluorescence intensity under darkness of CCaSR 3.0, it was considered that it would be a more attractive candidate than CCaSR 2.0, as it would allow for lower background gene expression under darkness.

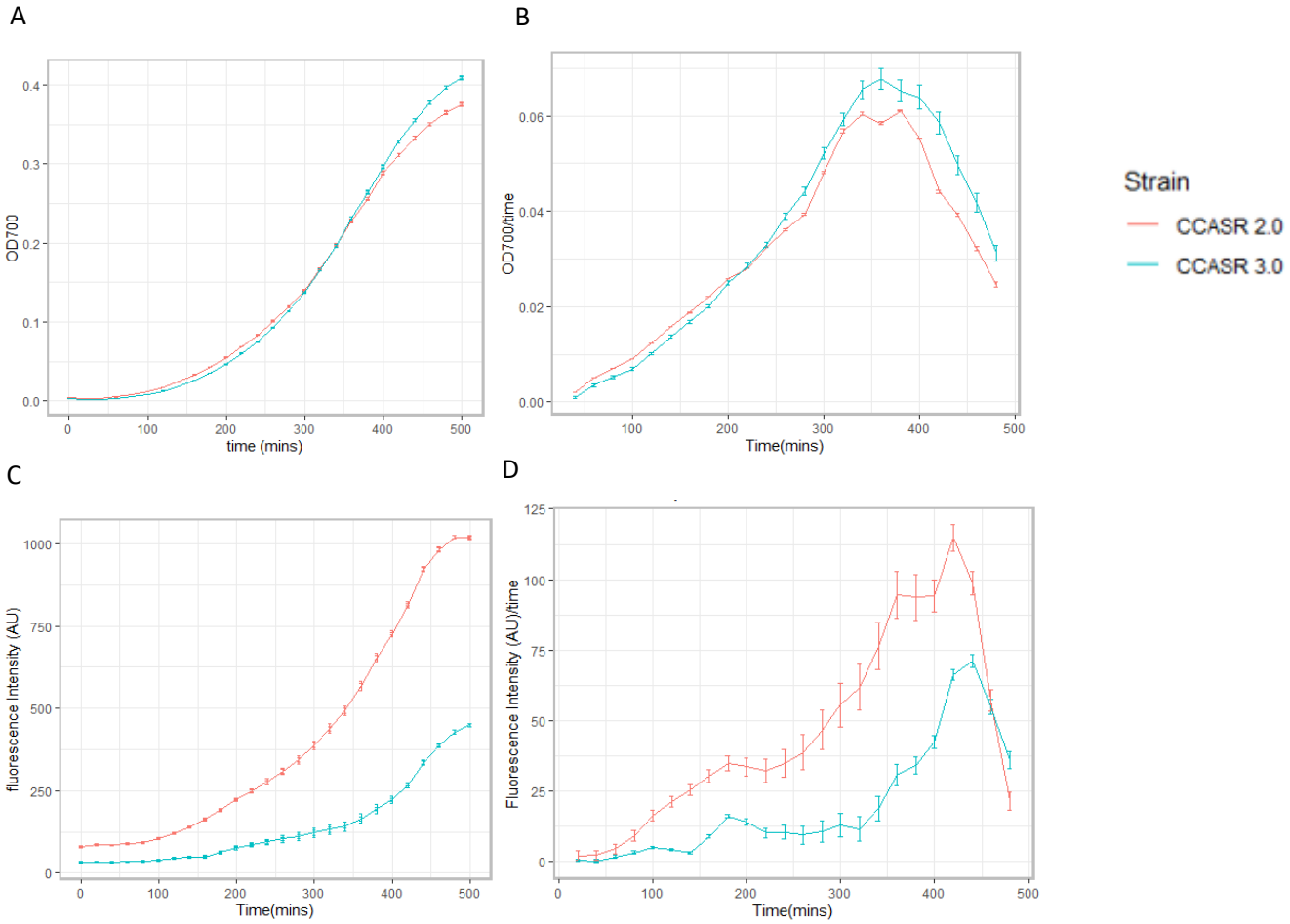


Figure 2.4: *Growth and fluorescence intensity of CCaSR 2.0 and 3.0 under dark conditions in liquid media. A) OD700 for CCaSR 2.0 and 3.0. Both strains grow and start reaching saturation about 500 minutes after initiation of incubation. The OD700 is largely similar for both the CcaSR 2.0 and 3.0 versions, and can be split into the three main regions: A 'delay' period that happens within the first 60 minutes, and where no or very little growth occurs. This is followed by an exponential growth phase, which begins to slow down around 400 minutes, reaching a stationary phase around 500 minutes. B) Growth rate for the two strains per hour. C) Fluorescence intensity for the two strains. CcaSR2.0 has a higher fluorescence intensity in darkness (higher background gene expression) than CcaSR 3.0, owing to a shorter lag phase. D) Rate of change of fluorescence Intensity per hour. (n= 4, error bars represent standard error).*

2.2.2 Comparison of CcaSR 2.0 and 3.0 under different light intensities

Having established the growth rate and background gene expression of the two systems, it was then deemed necessary to obtain parameters for their response to actual optogenetic activation by

different intensities of green and red light. Instead of doing this characterisation in 3D from the beginning, I envisioned performing these tests in two dimensions, in order to obtain an initial idea for the potential dynamic range of the two systems, and to choose which one would be more suitable for printing. While a lower background is desirable, what is also desirable is high gene expression upon activation, to ensure the ability to obtain accurate printing results.

Further to dynamic range, I wanted to understand the response dynamics of the systems: the minimum light intensity for which a response is observed, and after how long, as well as the interplay between green and red light. According to the model by Olson and colleagues (Olson et al., 2017), green light affects gene expression at very low intensities, while active photoreceptors remain active for the duration of the print. However, because in 3D printing, we would have to deal with cells enclosed in a volume, we have to look at the total response of the population. In this case, dilution of active photoreceptors due to cell growth becomes a confounding factor. Hysteresis only applies to the photoreceptors already produced, and to maintain the ratio of active to inactive photoreceptors, newly produced photoreceptors need to be activated during the duration of the print. In addition, the observations by Olson and colleagues were made under steady state, while in our case we had to deal with a continuously growing population, going from lag phase to early exponential, which might affect the results. Furthermore, understanding the dynamics of inactivation by red light was important to understand how the two wavelengths can possibly be combined in 3D printing.

Performing light illumination experiments in batch posed difficulties in that it required a mass illumination equipment that could give customisable light intensities and wavelengths to individual samples. Since the format of batch darkness experiments was the 96-well plate, I envisioned a 96-well illumination equipment that could be used together with 96 well plates. Ideally, each well could be illuminated with different intensities of red and green light and combinations of the two wavelengths.

Some commercially available light plates were identified. However, most of them were either prohibitively costly, required large amounts of electrical technical knowledge to prepare or could not control individual wells. Instead, I identified a 96 LED printed circuit board, with red, green and blue LEDs arranged in the conformation of a 96-well plate, and the ability to control each LED individually through an Arduino interface. The 96-well light board and a power board were obtained (Maplebear Electronics, USA) (Baillargeon et al., 2017) and combined with an Arduino UNO

(Arduino, USA). The components were connected and fitted together to create a 96 well light plate that was capable of illuminating individual wells independently at high throughput (Materials and Methods 7.2.1). In order to ensure homogeneous illumination of the wells, an empty 96-well plate and translucent tissue were fitted over the setting (Fig. 2.5). The whole system was placed inside a 37 °C dark incubator.

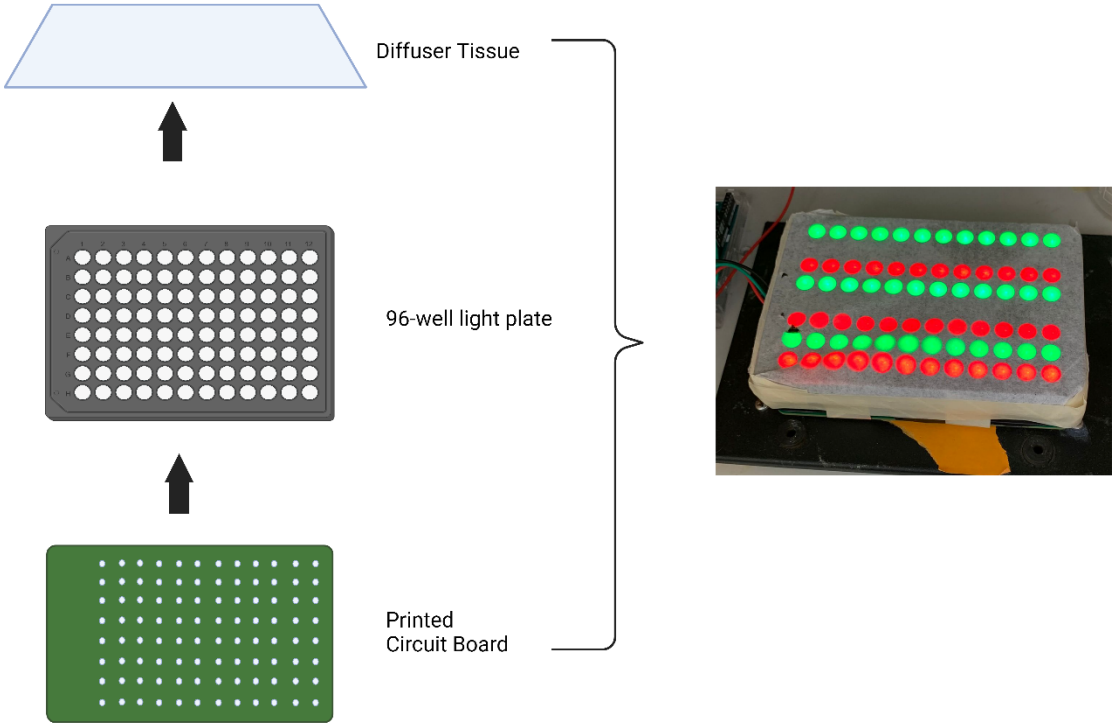


Figure 2.5: 96- well light plate. *The light plate was created by overlaying a Printed Circuit board (Maplebear electronics, USA) with an empty 96-well black flat-bottom plate (Greiner Bio-One). A Kimberly-Clarke Professional Kimwipe (Thermo Fisher, UK) was secured on top to ensure proper diffusion of the light and consistent lighting through all the wells (Materials and Methods 7.2.1). This set-up allows a 96-well Greiner plate containing each experiment can fit comfortably on top, ensuring that each well receives light from one LED. Distance between adjacent LEDs was* 2.04 mm.

The set-up of a 96-well light plate inside an incubator meant that cells could not be kept in the plate reader for the duration of experiments, which prohibited automated timepoint measurements. Instead, frequent timepoints were taken by moving the plate quickly in darkness to the plate reader, and then back to the illumination setup. In this manual way, a limited number of time points could be taken, requiring physical presence. Informed by the initial background experiments, I decided to spread these manual timepoints over the duration of active growth and division of the cells, over 300 minutes. In addition, since both OD700 and fluorescence intensity increased exponentially over

time, the time points focused on periods after the first 120 minutes of incubation, when the bulk of gene expression occurred. I decided that in that period, a reasonable period between timepoints would be 30 minutes, similar to the doubling time of the cells, enabling a representative number of time points to allow comparisons. This light plate was therefore used to assay the growth and response of CCaSR 2.0 and 3.0 to different intensities of light over 300 minutes.
Results are displayed in Fig. 2.6-2.9. For each of these conditions, different lines represent red and green light intensities of 0, 50, 100, 200, 400, 600 and 1000 mW/m^2. In figs. 2.6 -2.9 A-D, I display results under 4 different conditions: 1000mW/m^2 green light with different red light intensities, 1000mW/m^2 red light with all green intensities, no green light with all red intensities and no red light with all green intensities. The results are correspondingly for: OD700 for CCaSR 2.0 (Fig.2.6), OD700 for CCaSR 3.0 (Fig.2.7), Fluorescence intensity for CCaSR 2.0 (Fig.2.8) and for CCaSR3.0 (Fig.2.9). For completion, growth rate figures (Figs. 2.6-2.7 E-J) show all of the combinations of red and green light intensities.

In CCaSR 2.0, growth under all different red and green intensities exhibited similar dynamics as that under darkness, with a linear increase in the growth rate throughout the duration of the experiment, from 0.03 to about 0.06 units/hour (Fig. 2.6). This suggests initial slow growth for the first 60 minutes, followed by gradually faster growth. Final OD700 after 300 minutes was between 0.15-0.17 AU for all conditions tested, indicating consistency of growth. It was expected that samples under green light would grow slower, due to increased metabolic burden from the higher degree of induction, and samples under red light faster, due to reduced gene expression. However, growth did not correlate with red or green light intensity, indicating no effect of metabolic burden in this case.

For CCaSR 3.0, a similar growth profile was observed (Fig. 2.7), with the only difference being that the cells grew a bit faster, reaching an OD700 of 0.16-0.2 after 300 minutes. However, the difference between this and the OD700 of CCaSR 2.0 was not significant ($t=1.373, p=0.2051$). Similarly to CCaSR 2.0, there was no correlation between growth and illumination. Growth rate increased in a linear fashion for all illuminations. For both strains, the fact that cells, and fluorescence were present in all wavelengths and intensities, even at 1000 mW/m^2, showed that there was no danger of photobleaching of the fluorescent protein or the cells with high light intensities, or extreme burden due to gene expression.

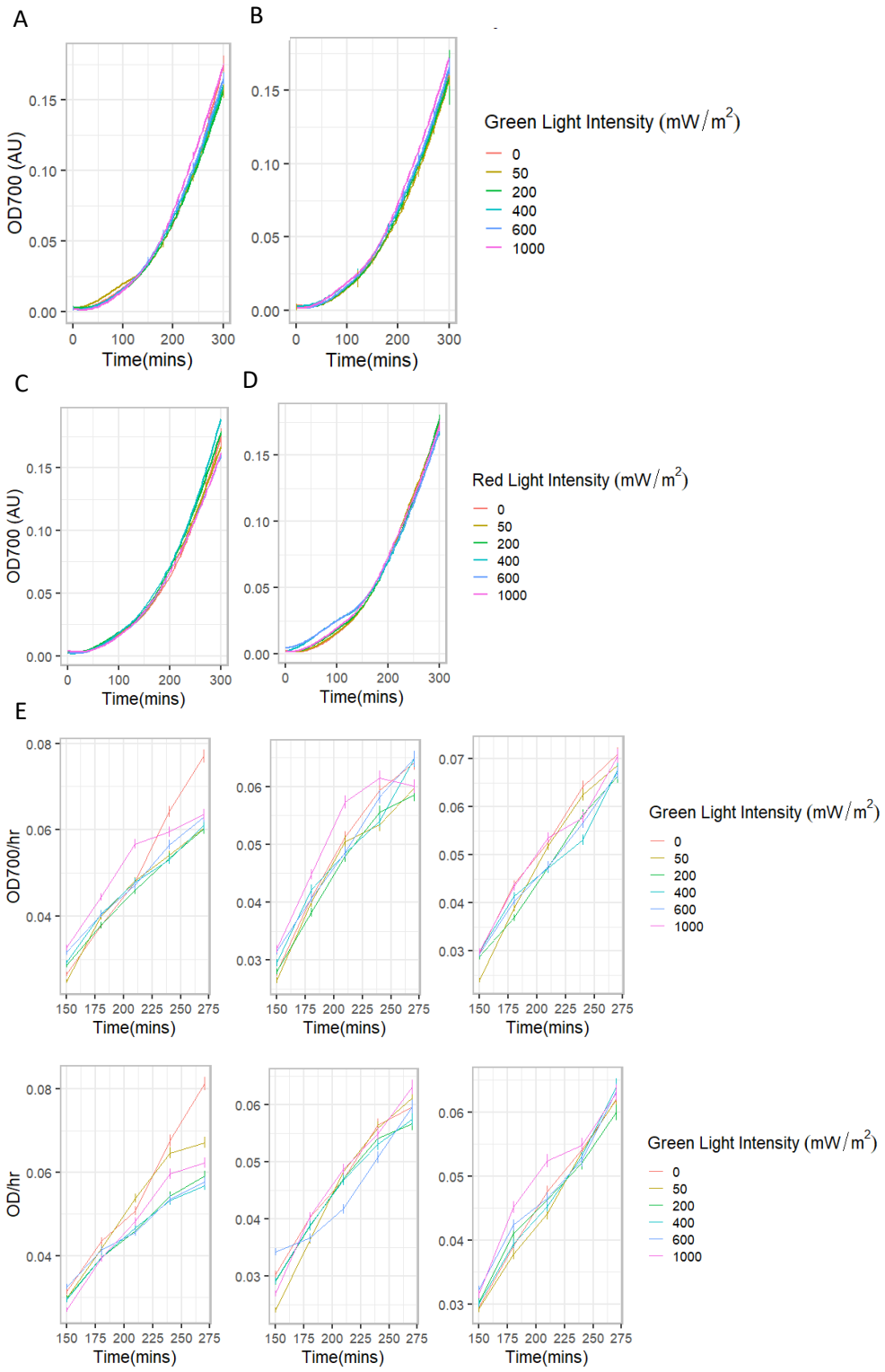


Figure 2.6: *OD700 and growth rate for CCaSR 2.0 with different intensities of green and red light A) no red light. B) Red light at 1000mW/m². C) No green light D) Green light at 1000 mW/m². Growth parameters are similar as with as the darkness measurements, with about 100 minutes of slow growth followed by entry to exponential phase. E) Growth rate of the cells, per hour, for red light intensities starting from 0, 50, 200, 400, 600 and 1000 mW/m², from left to right. (n= 4, error bars represent standard error).*

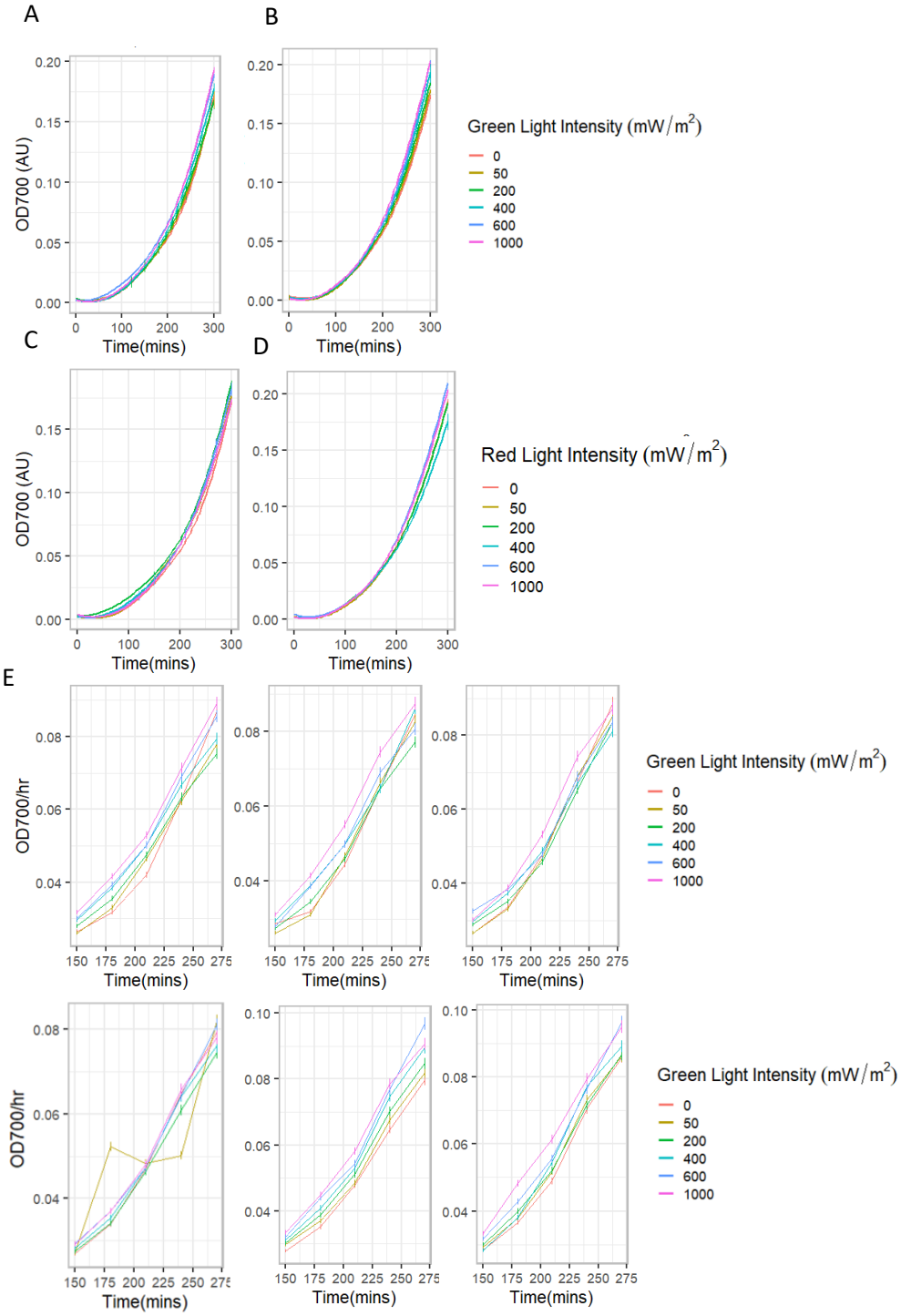


Figure 2.7: *OD700 and growth rate for CCaSR 3.0 with different intensities of green and red light A) no red light. B) Red light at 1000mW/m². C) No green light D) Green light at 1000 mW/m². E) Growth rate of the cells, per hour, for red light intensities starting from 0, 50, 200, 400, 600 and 1000 mW/m², from left to right. A steady growth is observed following an initial flat segment. Final OD700 reached is 1.13x higher than that of CCaSR 2.0 (n= 4, error bars represent standard error).*

Having studied the OD700 of the two strains, the slight increase in growth in the CCaSR 3.0 strain could potentially be attributed to the smaller size of the CcaSR 3.0 protein, perhaps allowing the cells to grow faster over the initial segment.

In CcaSR 2.0, the dynamics of fluorescence intensity over time were again similar to those observed in darkness (Fig.2.8). There was an initial period of slower increase in fluorescence intensity over the first 2 hours, followed by faster increase until 300 minutes. Under darkness, fluorescence intensity was 1000 AU, which was impressively reduced 4-fold by red light at 1000 mW/m^2. Even a faint red light of 50 mW/m^2 was capable of reducing fluorescence at 300 minutes by 25%, indicating high sensitivity of the system to low intensities.

Conversely, at a green light of 1000 mW/m^2, fluorescence intensity was 15-fold higher than in darkness, indicating the high activating effect of green light and the dynamic range of this system. In addition, no intensity of red light could reduce fluorescence under strong green light. This indicates that while red light was effective at converting active state photoreceptors back to the ground state, green light at the same intensity was more effective at activating the same photoreceptors (k1>k2), leading to net activation.

Under no red light (Fig.2.8 D), increasing the green light intensity gives more information on the sensitivity of the system. At 50 mW/m^2, green light was capable of increasing fluorescence intensity 5-fold compared to darkness, while the difference in fluorescence intensity between 1000 mW/m^2 and 400 mW/m^2 green light was only 2500 AU, or 16.7% of the maximum intensity. Therefore, an especially intense green light was not necessary in order to achieve high expression. These results agree with modelling from Olson and colleagues (Olson et al., 2017), which show that even faint light is enough to activate a large amount of the photoreceptors under steady state. In fact, the discrepancies seen here between different green light intensities can largely be attributed to the non-steady state conditions of this experiment, with cell division and dilution of active photoreceptors, which are replenished faster under more intense light.

Under maximum red light (Fig. 2.8 C), the effects of the interaction between green and red can be observed. As observed in the previous figures, red light is most effective under darkness, essentially reducing fluorescence to 1.6% of maximal fluorescence intensity under green. Red light is inefficient under equal intensity green light, however. Under lower intensities of green, the effectiveness of red light is proportional to the difference between the intensities. For green light of 50 mW/m^2, red light reduces fluorescence intensity 5-fold compared to darkness. For green at 200 mW/m^2, red only reduces fluorescence intensity by 35%, while for higher green intensities red is virtually inefficient.

Therefore, as a rule of thumb it was considered that red should be at least 5 times more intense than green in order to observe a reduction.

For CcaSR 3.0 (Fig 2.9-2.10), the trend observed with fluorescence intensity under different illumination regimes is similar to those of CcaSR 2.0. The maximum fluorescent intensity was a bit higher than CcaSR 2.0, with 15500 AU instead of 14500 under CCaSR 2.0, but the fluorescence intensity under darkness was also higher in this specific experiment, with 1500 instead of 1000, giving a dynamic range of 10.3x. The discrepancies with the apparent lower fluorescence intensity of CCaSR 3.0 under darkness in Fig 2.4 can be potentially explained by the different method of taking the readings in the light plate.

For CCaSR 3.0, red light appeared to be more effective than CcaSR 2.0, reducing the background intensity 12-fold compared to darkness and by 99.1% compared to maximal activation. In addition, even lower intensities of red were able to reduce fluorescence intensity under darkness to under 250 AU, which was not possible with CcaSR 2.0. Even in combinations of 1000 mW/m^2 red and 50 mW/m^2 green light, fluorescence intensity was reduced by 5% more compared to CcaSR 2.0.

Due to the higher fluorescence intensity observed with just green, as well as the higher dynamic range when red intensity is taken into account, I decided to proceed with CcaSR 3.0. This was because it was foreseen that higher fluorescence intensity would be useful in imaging the cells in a 3D matrix, while the impressive red light reduction of fluorescence was foreseen to be used to reduce background.

Consequently, as a means of better characterising gene expression by CcaSR 3.0 flow cytometry was performed with these cells, after illuminating for 5 hours with red or green light, or keeping in darkness (Fig.2.9E). Responses of individual cells could thus be observed and means of the fluorescent populations plotted. Interestingly, for each of the experiments, there was a large number of cells that remained not fluorescent, while a higher green light intensity led to more and more cells being activated by the light. The non-fluorescent cells might be due to loss of the optogenetic plasmids following culturing. The same effects as those seen on the plate reader could be observed, with cells under green illumination showing 3x the fluorescence intensity of cells in darkness and 12x fluorescence intensity of cells in red light. Under flow cytometry, the two intensities of red and green light used showed very similar results, indicating the sensitivity of the system to very low light intensities. The discrepancies observed with the plate reader results, where different intensities seemed to have a larger effect, can be explained by the fact that under flow cytometry and looking at individual cells, the effects of photoreceptor dilution due to cell division

and growth are removed, compared to looking at a batch population. There were no specific effects of photobleaching observed with the intensities used.

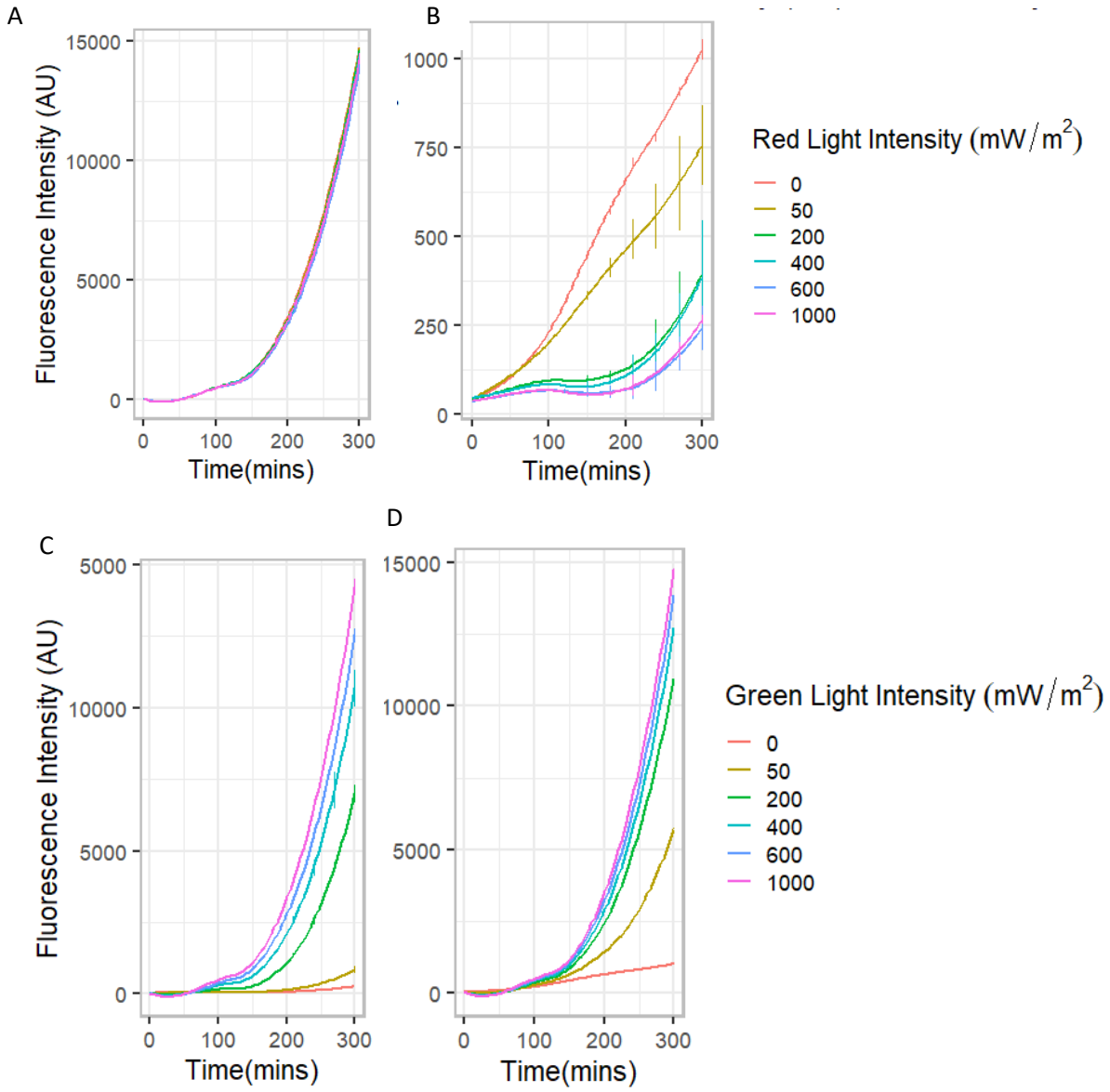


Figure 2.8: *Fluorescence intensity for CcaSR 2.0 under different light intensities over time. A) Green light at 1000 mW/m². B) No green light. C) Red light at 1000mW/m². D) No red light. At high green light intensities, red light does not affect gene expression. On the contrary, under equal red and green light the green light is more effective at activating the cells. Without red light, green light is quite effective in activating to about 13-fold, which becomes about 30-fold under intense red light (n= 4, error bars represent standard error).*

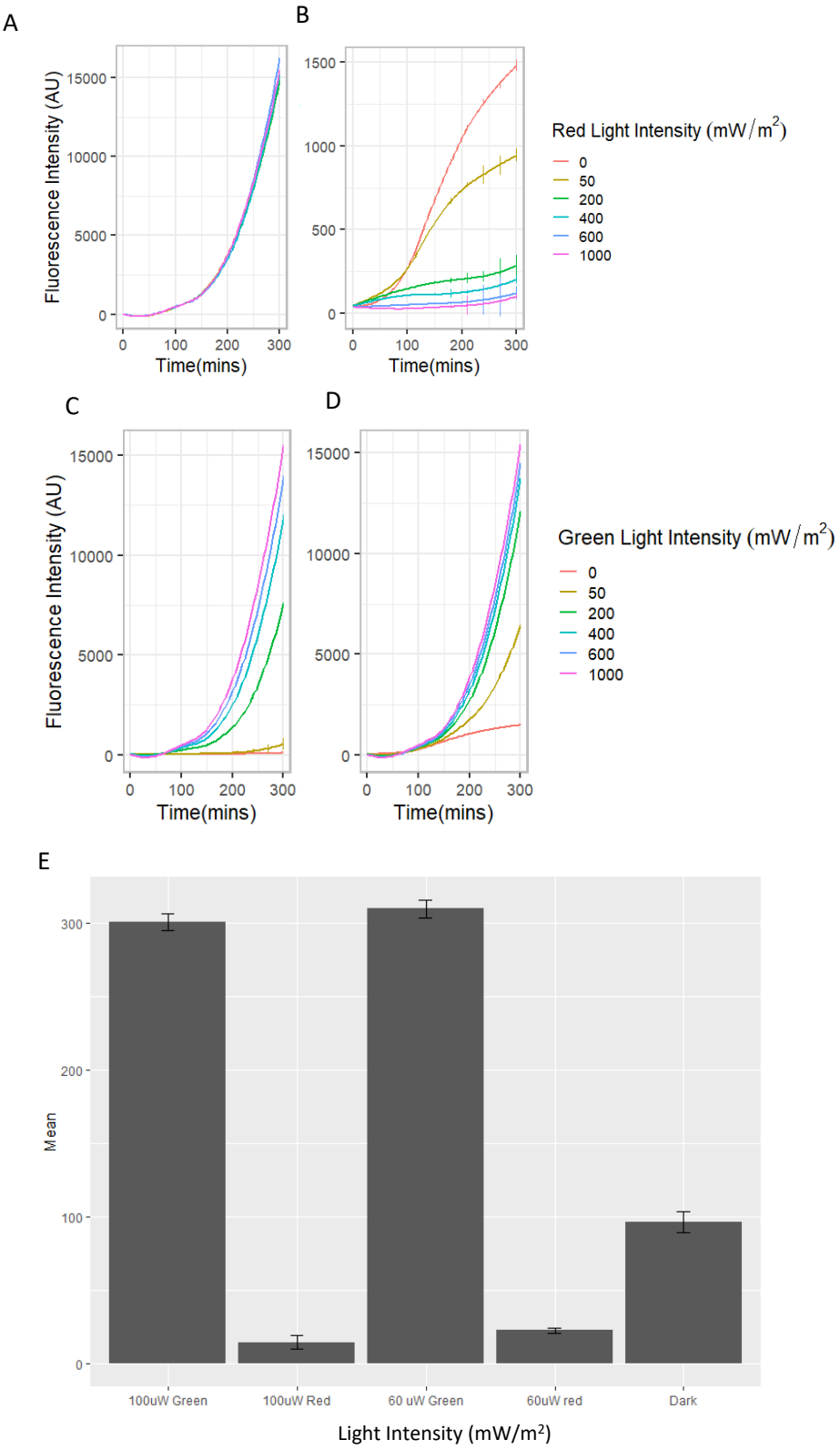


Figure 2.9: *CCASR 3.0 fluorescence Intensity over time under different light intensities. A) Green light at 1000 mW/m². B) No green light. C) Red light at 1000mW/m². D) No red light. E) Flow cytometry of CCaSR3.0 cells in liquid media, showing the geometric mean for fluorescence intensity by each of the conditions. (n= 4, error bars represent standard error).*

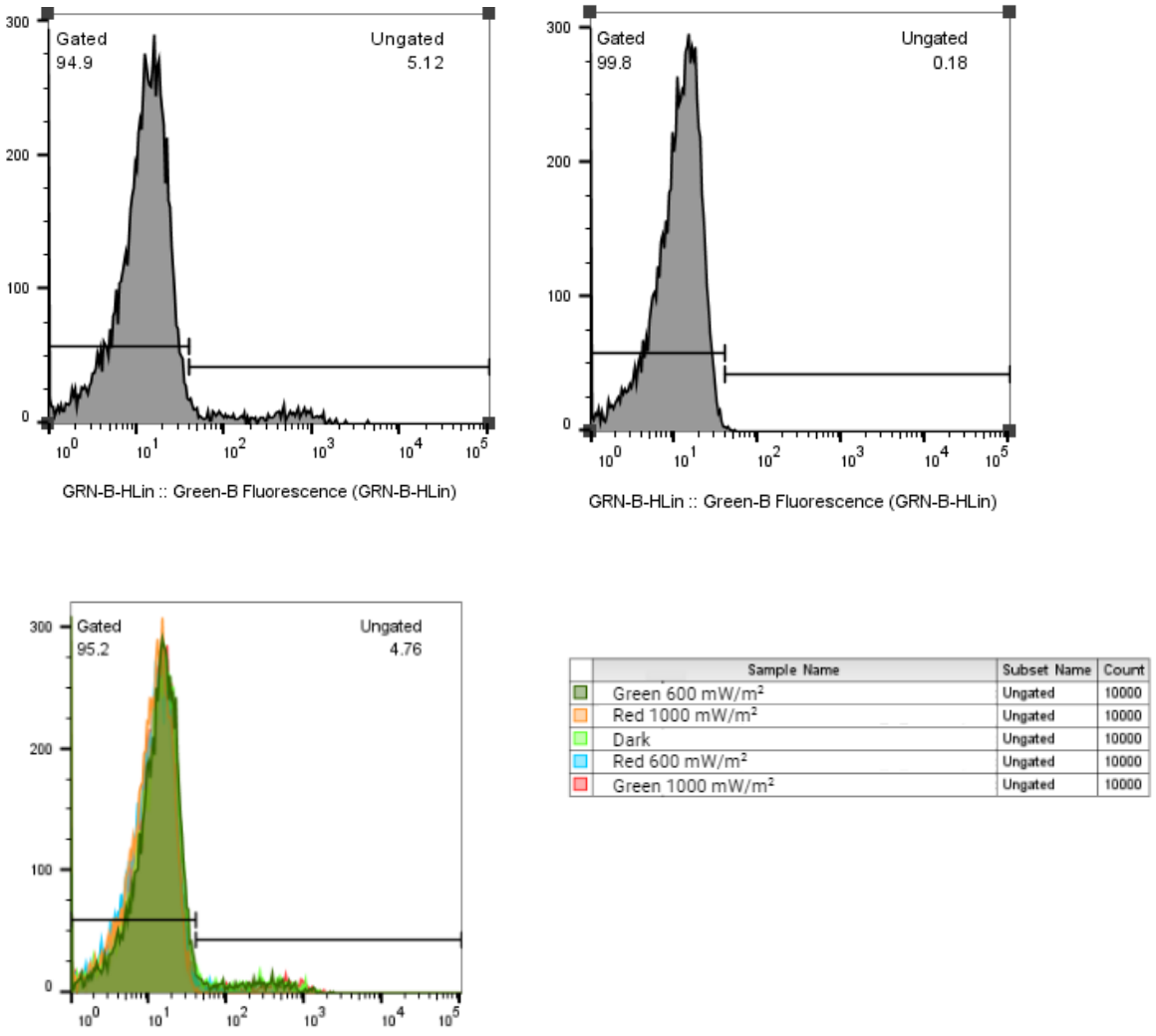


Figure 2.10: *A) Control of cells with and without dye, from left to right, showing the position of gating. B) Overlay of the 5 conditions, with the gate shown and percentage of cells on either side of the gate. (n= 4, error bars represent standard error).*

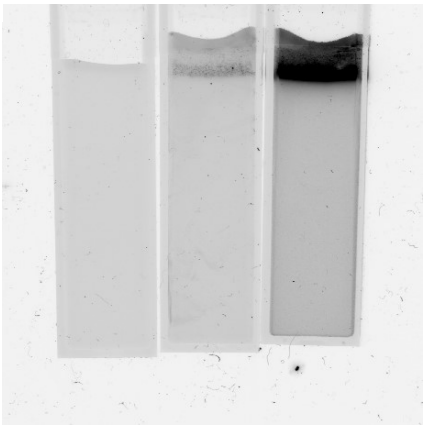
2.2.3 Choice of reporter

In order to perform 3D optogenetics, the system designed included a plastic cuvette, containing cells suspended in a solid hydrogel matrix as a solid support medium, mixed with a growth medium. This set-up required considerations of anaerobic growth and gene expression. As GFP and its derivatives require oxygen for maturation (Remington, 2011), it was hypothesised that it would not be ideal for these experiments. This was verified in two ways, first by using paraffin oil to cover the plate wells, and by using an agarose hydrogel in a cuvette and well plate to show gene expression under anaerobic conditions.

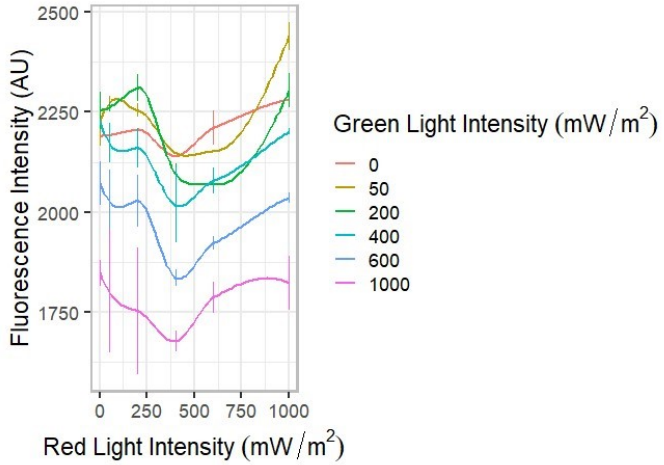
Briefly, I prepared an agarose-M9 hydrogel containing CCaSR 3.0 cells with the necessary antibiotics, poured it inside a cuvette and incubated for 15 hours, so that only the top part of the cuvette was exposed to oxygen (Materials and Methods 7.3.3.1). At the end of the 15 hours, I imaged the hydrogel for fluorescence using an Amersham Typhoon gel scanner (Amersham, UK, see Materials and Methods 7.3.3.3). I observed that fluorescence was detectable only on the surface of the hydrogel despite cells being present throughout. It was therefore hypothesised that only in an area with access to oxygen could any GFP produced fold and fluoresce (Fig.2.11 A).

This was verified by performing a light plate experiment in which CcaSR 3.0 cells were mixed with the hydrogel media and poured in wells of a 96 well plate. Each well was then covered with Paraffin oil to prevent contact with air (Materials and Methods 7.3.3.5), and an optogenetic characterisation was performed. Under a green intensity of 1000 mW/m^2, a fluorescence intensity of only 1750 AU was observed for all different light intensities, almost 10 times lower than maximum fluorescence in liquid state (Fig.2.11B) ($t=45.04$, $p= 6.14x10^{-7}$). This result indicated that sfGFP was unsuitable as a reporter, due to its low folding and fluorescence in anaerobic conditions.

A



B



C

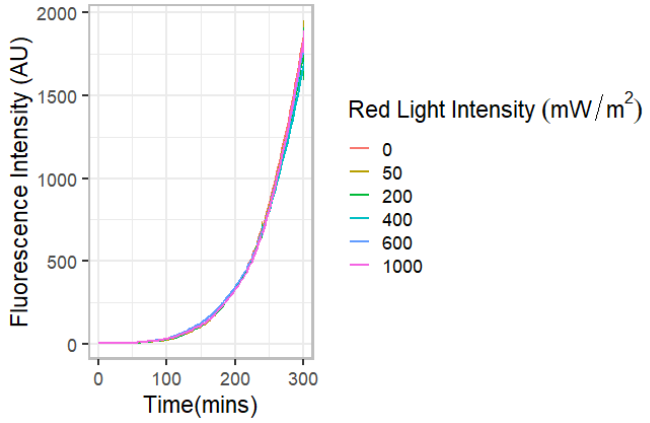


Figure 2.11: *Fluorescence Intensity by CcaSR 3.0 in anaerobic conditions. A) Cuvettes incubated without cells (left), with cells for 5 hours (middle) and with cells for 15 hours (right). B) Fluorescence intensity for CCaSR 3.0 cells with different red and green light intensities after 5 hours. C) Fluorescence Intensity for CCaSR 3.0 under 1000 mW/m² green light. Maximum fluorescence intensity is at least 6.8 times lower than in liquid, indicating that a lack of oxygen has a significant effect on the folding of the GFP. In addition, the dynamic range observed in the previous figures is diminished, indicating that GFP is unsuitable to be used in the bioprinting experiments (n= 4, error bars represent standard error).*

In order to obtain easily quantifiable results in an anaerobic environment, I wanted to stay within the realm of fluorescent molecules, as they offer easy, non-invasive and quantitative detection of production, which is especially necessary if performing experiments in 3D. Looking for a molecule that would be unaffected by the anaerobic environment, I came across research done on Fluorescence Activated and Absorption-Shifting Tags (FASTs) (Plamont et al., 2016). These are proteins which fluoresce when bound to a cell-permeant and non-toxic ligand. These proteins can offer reversible and specific fluorescence even in anaerobic environments. In particular, I was interested by tdFAST2, a tandem dimeric anaerobic FAST (Tebo et al., 2018), which can specifically bind a variety of dyes with unique excitation/emission spectra, allowing to change the desired excitation/emission by simply changing the conjugate dye (Fig.2.12). Of these dyes, tfLime in particular has an excitation/emission of 480/541nm, which is very close to that of sfGFP, and allows accurate assessment of gene expression in anaerobic conditions. For this reason, *tdFAST2* was cloned by Albert Fabregas Flaviá in place of *sfGFP* in the CCaSR 3.0 pSR 58.6 plasmid, and co-transformed with pNO286.3 to give BP16, a strain that expresses *tdFAST2* under CCaSR 3.0 optogenetic control.

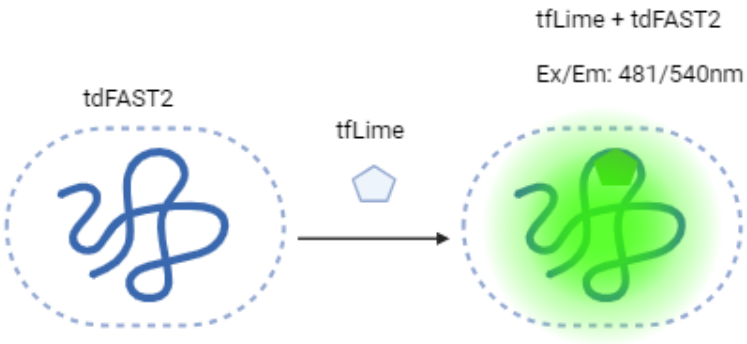


Figure 2.12: *Diagram of the binding principles behind tdFAST 2 and tfLime. The dye ligand tfLime binds tdFAST2 specifically. tfLime has an excitation/emission at 480/541 nm, a molar absorption coefficient of 41,000 $M^{-1}cm^{-1}$, and a quantum yield of 23%, giving bright fluorescence in a similar spectrum as that of sfGFP .*

It was possible to compare between different concentrations of the dye, to identify the best one for use. There were two considerations: the first one was brightness, as the dye needed to be bright enough to be detected even at very low light intensity and gene expression. The second consideration was uniformity of response, as the dye should be sensitive at low levels of the protein and not be a limiting factor at higher tdFAST2 levels. For both of these considerations, optimising the concentration also has economical implications, as the dye had to be commercially acquired.

While the recommended final concentration of the dye is 2.5 µM, different concentrations around this were tried at different light intensities over 300 minutes, and the fluorescence intensity recorded was assayed once at 300 minutes, in order to understand how the different dye concentrations respond to either a very low amount of protein at low light intensities, or to higher amount at high light intensities.

It was found that as expected, the higher the dye concentration the higher the fluorescence intensity, with the 10 µM concentration showing a 4x higher fluorescence intensity than the 1 µM concentration (Fig.2.13A). However, no saturation was observed at high light intensities, and even at the lowest dye concentration it was possible to detect fluorescence under no green light.

To verify this, the fluorescence ratio between darkness and the highest illumination used was compared for the three dye concentrations (Fig.2.13B). Since the ratio was very similar for all concentrations, it was concluded that at the illumination intensities and concentrations used, there was no significant reason to prefer one dye concentration over another. For economy purposes, the recommended 2.5 µM concentration was decided to be used, as it is an in-between concentration that would ensure good response even at higher light intensities.

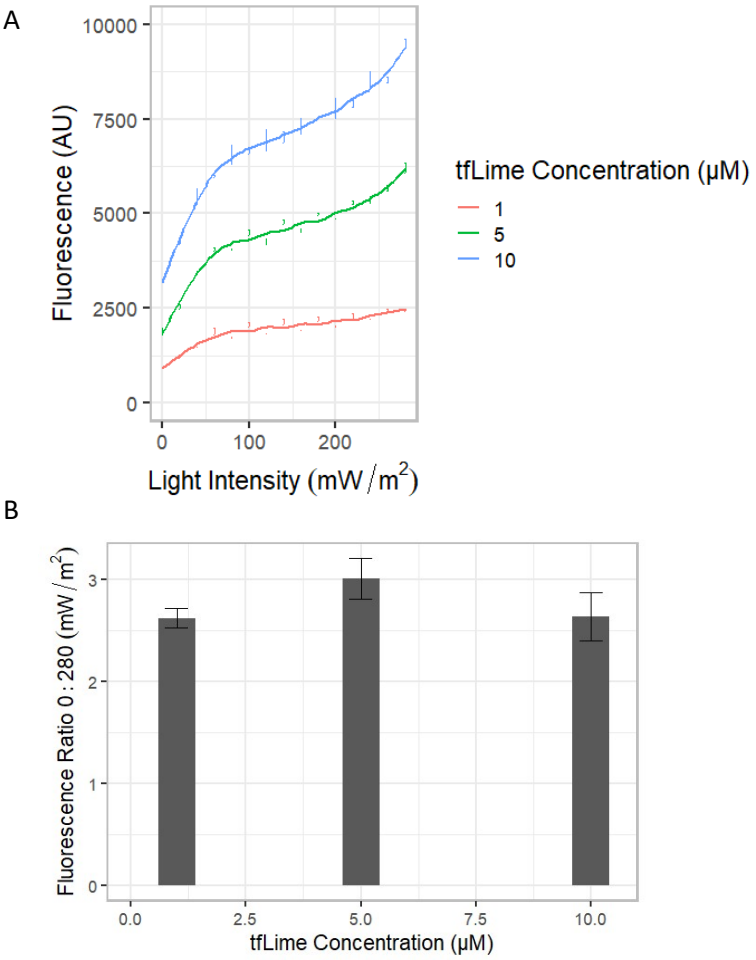


Figure 2.13: *A) Fluorescence with different tfLime concentrations under different green light illumination intensities. All dye concentrations show a 2.5-3x increase with higher intensity light. B) The ratio of fluorescence increase with light intensity from 0:280 mW/m². This ratio is similar for all dye concentrations and follows a similar trend, indicating no saturation dynamics (ANOVA test F value = 2.254, p = 0.186) (n= 4, error bars represent standard error).*

2.2.4 Choice of solid support medium

Once the reporter was chosen, it was necessary to choose a solid support hydrogel and growth medium. Several solid support media have been reported over time to be able to support growth of cells, and indeed several have been used in optogenetics and 3D bioprinting independently. In optogenetics, the requirements for a solid support medium were for it to enable cell growth and viability, but not interfere with light through scattering or spectral aberrations. Therefore, a solid medium should be as transparent as possible. Widely used media in this realm include agarose and LB agar, although the latter has a yellow-brown tint. In terms of traditional 3D bioprinting, the requirements of the colour of the media are less stringent. What has been more important is that

the solid media are soft enough to be extruded with a nozzle, but can solidify over time or upon demand. Such media include Pluronic F-127 and Sodium Alginate (Muller et al., 2015; Song et al., 2011).

For the purposes of optogenetically activated 3D bioprinting, the media need to be transparent, but also with a high focus on light permeability and cell viability. As a result, I considered the hydrogels mentioned above, including agarose, Sodium alginate, LB agar and Pluronic F-127. Of these, LB agar and Sodium alginate were rejected because the resulting hydrogel was not fully transparent and without colour, thus distorting the wavelengths of light used and precluding any possibility to perform targeted optogenetics, while also making visualisation harder.

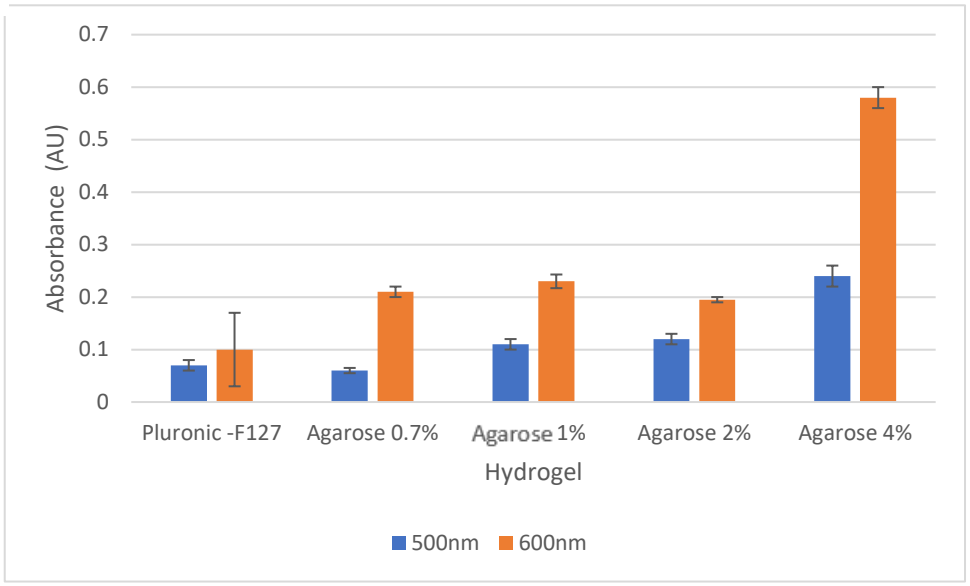
Pluronic F-127 appeared promising, due to its transparency and wide use in mammalian 3D printing. In addition, it has a property of being liquid at 4 °C but solidifying at 37 °C. This would be a useful property for 3D printing, offering an easy way to remove the medium once a solid material is produced inside it, leaving behind only the product. Finally, agarose dissolved in water was considered, as it has no colour tinge visible to the naked eye, has been shown to support cellular viability and can easily be produced in a variety of different concentrations. More specifically, low-gelling agarose (ThermoFisher, UK) was chosen, as it has a melting point at 37 °C instead of 42 °C, allowing it to be mixed and manipulated at lower temperatures that do not impact the viability of the cells.

Therefore, I set out to compare agarose in different agarose concentrations (0.5%, 1%, 2%, 4%) as well as Pluronic F-127 (20%), in terms of transparency and ability to support *E. coli* growth and gene expression (Fig.2.14-2.15). The hydrogels were mixed in a 1:1 ratio with 2x M9-glucose media, effectively halving the hydrogel and media concentration. Higher concentrations of agarose were not used as it was hard to liquefy and manipulate, even at higher temperatures than 37 °C. On the other side, lower concentrations were still too soft to manipulate.

The transparency of the hydrogels without cells, to green light ~500 nm and red light ~600 nm was assayed in a spectrophotometer, blanked with water. Pluronic F-127 was the most transparent hydrogel of all, reaching a transmission of 0.05 and 0.1 AU for 500 nm and 600 nm light respectively. For agarose hydrogels, absorbance increased with gel concentration, going up to 0.23 AU for 500 nm light and the agarose 4% hydrogel, and 0.8 AU for 600 nm in the same hydrogel. The 4% hydrogel showed at least double absorbance compared to the other hydrogels for both 500 nm and 600 nm light, and was therefore discarded.

As a second test, absorbance at 532 nm and 600nm was compared for 2% agarose and Pluronic-F127, after a day of incubation with BP16 cells. Interestingly, Pluronic-F127 showed a much lower absorbance after a day of incubation with cells, which suggested higher transparency (Fig.2.14 B).

A



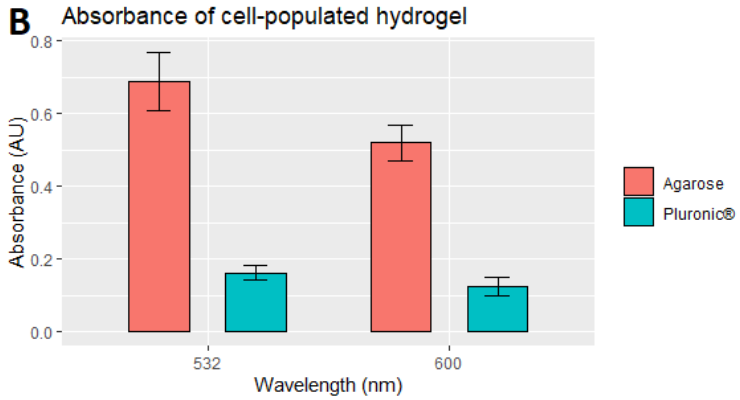


Figure 2.14: *The light absorbance of the hydrogels was assayed in order to choose one with low absorbance. A) Absorbances of the pure hydrogels are assayed in 500 nm and 600 nm light, to roughly test for red and green light absorbance, blanked with water. Pluronic F-127 had the lowest absorbance for red light, while agarose 0.7%-2% all had similar absorbance around 0.2 AU. Agarose 4% showed 0.6 absorbance for 600 nm. Fore 500 nm light, agarose 0.7% had the lowest absorbance, followed by Pluronic F-127 and then the other agarose hydrogels, in order of concentration. B) Absorbance of the 2% agarose and Pluronic F-127 with M9-glucose after an overnight incubation with cells is measured. For both 532 nm and 600 nm agarose has a higher absorbance than Pluronic F-127 (n=4, errorbars represent standard error).*

Having established the transparency of both hydrogels, and perplexed by the very high transparency of Pluronic-F127 after a day of incubation with cells, viability and fluorescence intensity in the different hydrogels were assayed in more detail (Fig.2.15). All mixtures were placed in a 96-well plate and the growth and fluorescence intensity assayed over time at 37°C. Growth for agarose hydrogels was inversely proportional to agarose concentration, with cells in lower agarose concentrations reaching a higher OD700. Cells in 2% agarose reached an OD700 23% lower than cells in 0.5% agarose. Pluronic F-127 had the lowest final OD700 with 0.23 AU. All samples settled to an OD700 of between 0.23 and 0.3 after 500 minutes, with two visible groups, agarose 0.5% and agarose 1% reaching OD700 closer to 0.3 AU, and Pluronic F-127 and agarose 2% closer to 0.23 AU. Differences between the two groups started to appear around 380 minutes, therefore only being effective in the late exponential phase. In the first 300 minutes of incubation, growth is still slower for Agarose 2% and Pluronic F-127, but the difference in absolute terms was less than 0.05 AU and not significant ($t=1.6038$, $p=0.1841$).

For fluorescence intensity, all agarose hydrogels performed similarly, showing similar lag phase, followed by exponential phase dynamics reaching fluorescence of 2500 AU after 400 minutes. However, during the exponential growth phase, higher agarose concentrations showed a slightly higher fluorescence, the opposite trend as the one seen for OD700. Pluronic F-127 stood out for fluorescence, showing consistently 20% lower fluorescence and a standard error of about 1000 AU.

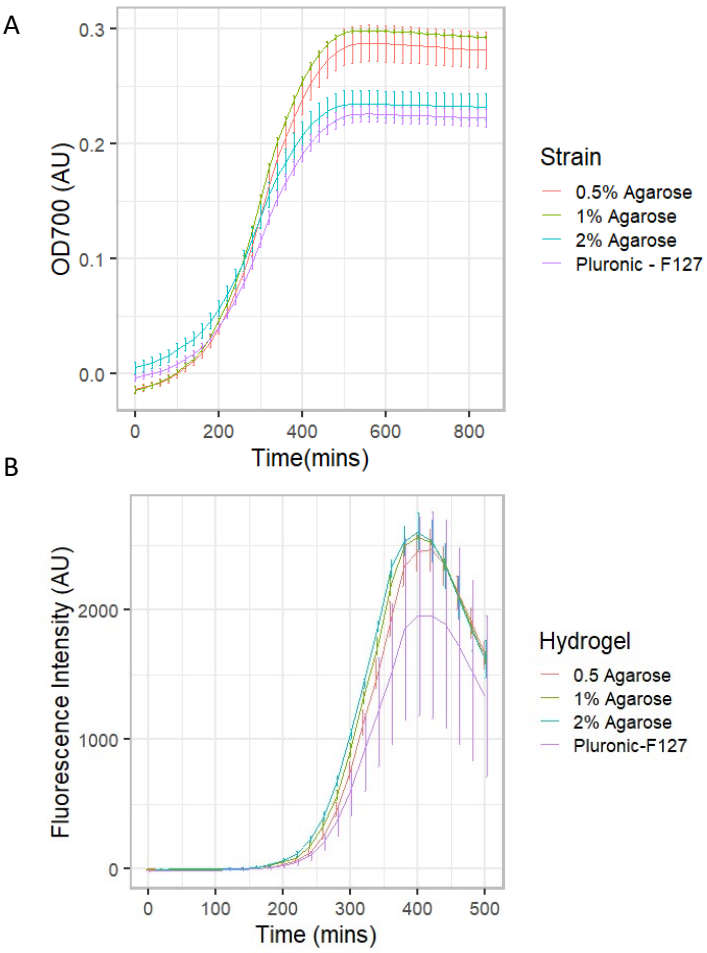


Figure 2.15: *OD700 (A) and fluorescence intensity (B) of different hydrogels. OD700 was higher for concentrations of agarose between 0.5%-1% after 300 minutes, reaching 0.3 AU. For Pluronic F-127 and 2% Agarose, final OD700 was 0.23 AU. Fluorescence is highest for 2% agarose, peaking at 2500 AU. However, it is very similar for all agarose concentrations, while Pluronic F-127 showed 20% lower peak fluorescence (n= 4, error bars represent standard error).*

In addition to transparency and ability to control cells, the ability to handle the hydrogels was also assayed by trying to insert a spatula in the gels to assay for hardness. It was observed that Pluronic F-127 failed to fully solidify at 37°C when mixed with media in 1:1, leaving a semi-liquid gel that was hard to manipulate properly. For this reason, a higher concentration was used, of Pluronic F-127:M9 in a 4:1 ratio. Growth and gene expression in this hydrogel medium was minimal at the required timeframe, indicating how it was not a suitable hydrogel to be used. Therefore, judging on a balance of the ability to support growth and fluorescence of cells in a hydrogel, solid support and ability to cast and handle the hydrogel, the 2% agarose was chosen as it offered the maximal gene expression by cells, a relatively lower growth indicating less light interference, and a solid gel that could be

manipulated easily. Due to the higher gene expression, ease of handling and relative transparency, 2% agarose dissolved in water was chosen as the solid medium of choice.

2.2.5 Choice of growth medium

After having chosen a hydrogel, a growth medium that could support cell growth and gene expression was considered. There were three obvious candidates that are widely used in bacterial growth: (i) Lysogeny Broth (LB), which is nutrient rich, complete and has been widely used in many bacterial growth experiments (MacWilliams et al., 2006), (ii) M9 minimal media supplemented with glucose, which offers slower growth of bacteria but is also commonly used for fluorescence measurements (Paliy et al., 2007) and (iii) Terrific Broth (TB), a broth even richer than LB that has been used for high-yield production by bacterial cells (Krause et al., 2010). In addition to these, LB was also tried with a double concentration, to observe the effect it might have on growth rate. It is worthy to note that the initial characterisation experiments up to this point were performed in M9, as it is the one most commonly used for fluorescence intensity measurements.

These four media were mixed with 2% agarose, to give final concentration of 1% agarose media. For example, in order to test the double concentration of 2x LB, 4x LB was mixed with 2% agarose, giving a final concentration of 1% agarose and 2x LB. OD700 and fluorescence intensity were measured under darkness, two different intensities of green and one intensity of red light, over time. The ideal results expected would be a medium that gives high fluorescence under all conditions, as well as a consistent growth of bacteria.

Surprisingly, all media showed similar growth for most illumination conditions, with LB and TB showing some outliers in certain conditions (Fig.2.16). This was postulated to be due to the mixing of the media with the hydrogel. M9 showed the most consistent growth, with small error bars and cells under all conditions reaching about 0.1 AU.

In the fluorescence measurements, fluorescence intensity observed with M9 was higher than with other media under all illumination conditions (Fig.2.16). This was postulated to be because of the lower autofluorescence of M9. TB and LB appeared to show a higher dynamic range, but this could also be attributed to higher autofluorescence, which would have an outsize effect on dynamic range, masking lower fluorescence intensities. To verify this, the background fluorescence of the media was compared, blanked with water, in samples without any cells (Fig.2.17 E), verifying the fact that M9 had lower fluorescence than the other media. As the focus of these experiments were to minimise autofluorescence in the media and maximise perceived fluorescence, so M9 was chosen.

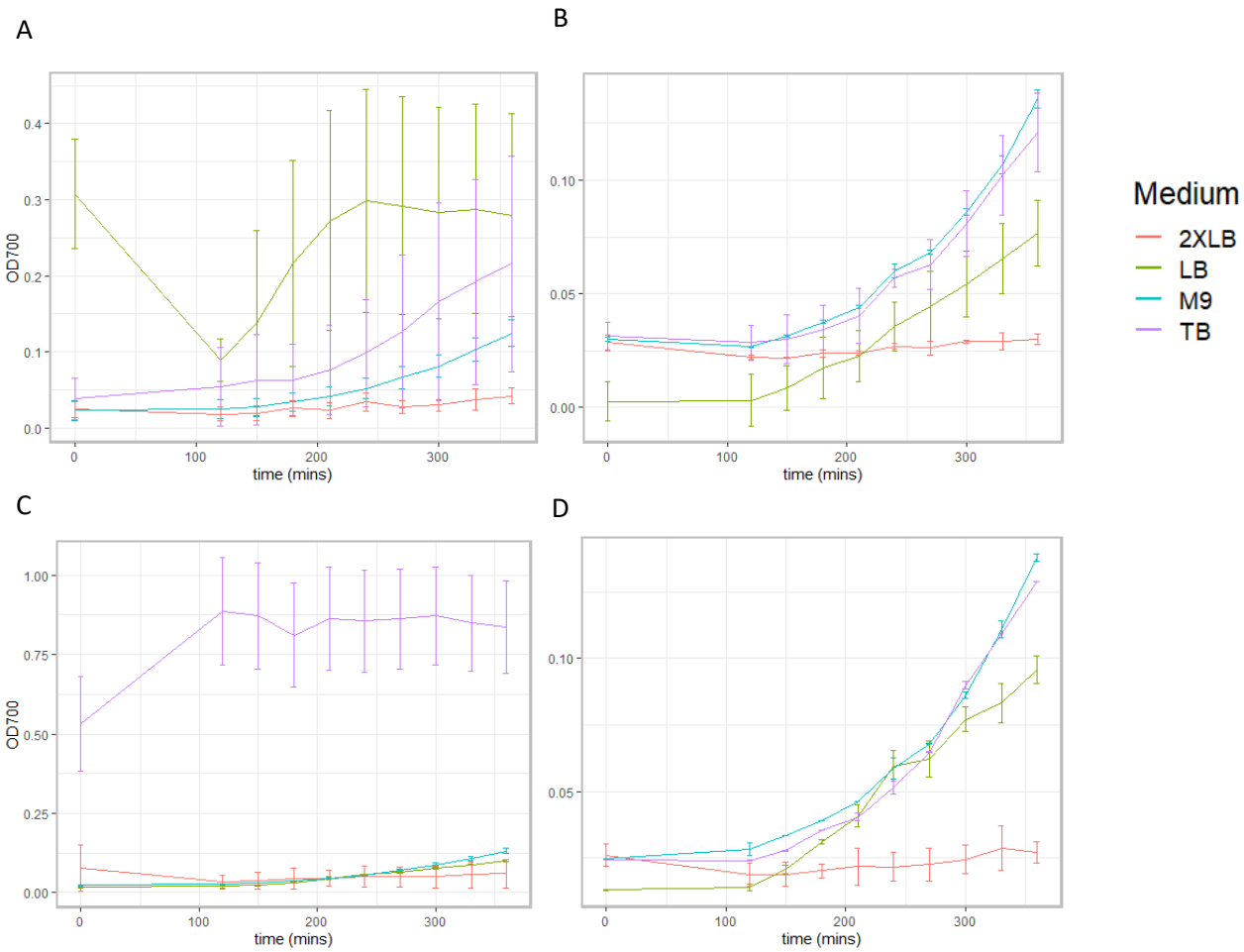


Figure 2.16: *Growth of cells over time in different media, under different light conditions. A) Darkness. B) 300 mW/m² green light. C) 1000 mW/m² green light. D) 1000 mW/m² red light. 2X LB supported very little growth of cells under any conditions, staying around 0.025. LB and TB showed similar growth to M9 in the medium green concentration as well as red light, but had very anomalous fluorescence intensity under darkness and high green intensities. The most consistent growth was in M9 media, which reached about 0.1-0.15 after 300 minutes (n= 4, error bars represent standard error).*

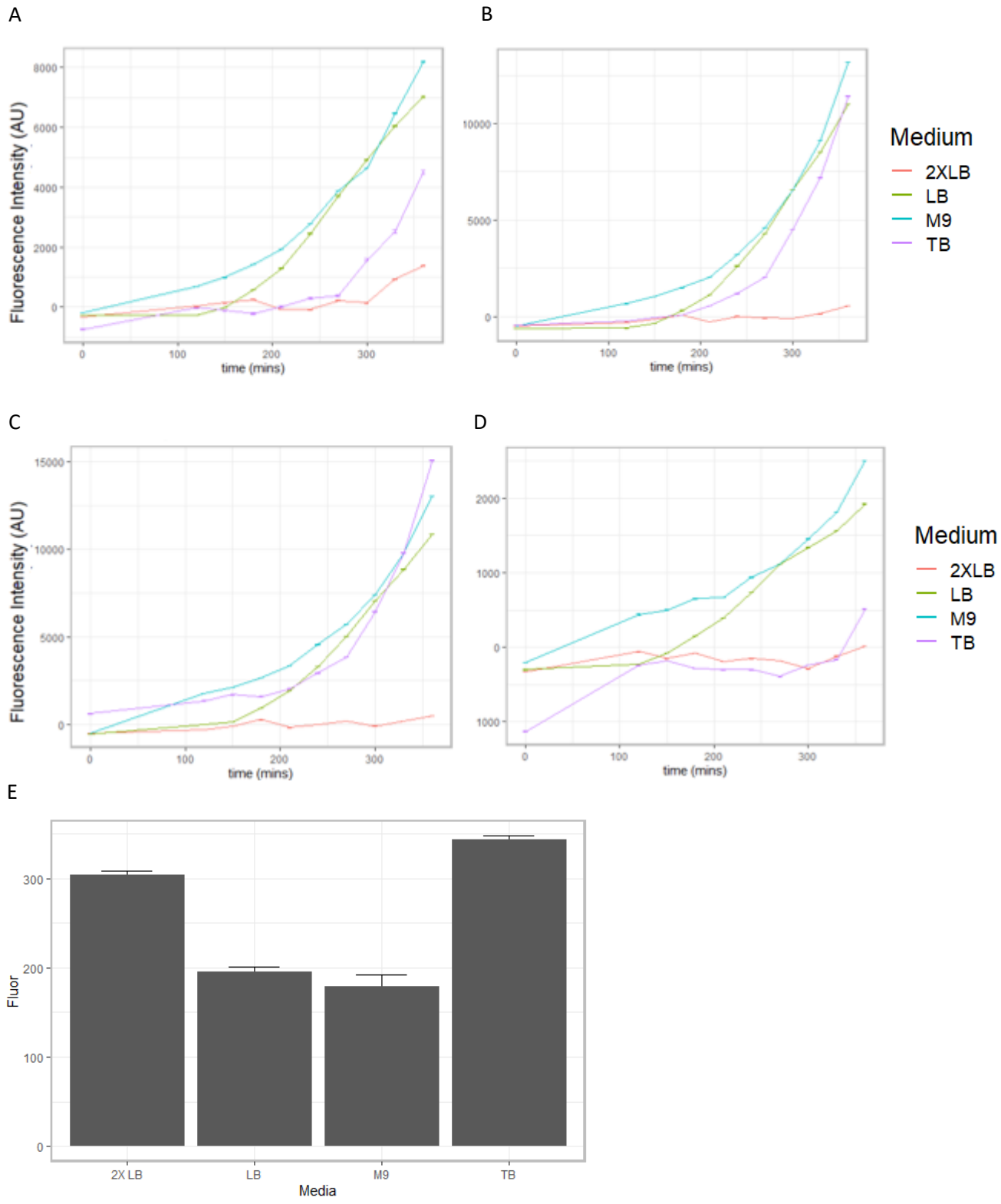


Figure 2.17: *Fluorescence under different liquid media. A) Darkness. B) 300 mW/m² green light. C) 1000 mW/m² green light. D) 1000 mW/m² red light. E) Autofluorescence of only media. A first look of the fluorescence over time graphs indicates that TB had the highest dynamic range (30x) after 360 minutes, followed by M9 (5.4) and LB (5.25). 2X LB showed very little response to the light. (n= 4, error bars represent standard error).*

2.2.6 Growth and response of cells in agarose hydrogel

Having identified an optogenetic strain, reporter and medium, I wanted to quantify the response of the system to different intensities and wavelengths of light in the chosen conditions. This was necessary in order to get a clear idea of how the whole system would behave in a 3-dimensional print.

The response of the cells expressing tdFAST2 under CCaSR 3.0 control (BP16) to light was assayed (Fig.2.18). Similar to the observations made for the sfGFP constructs under liquid conditions, red was capable of reducing fluorescence when its intensity was much higher than that of green light. Fluorescence intensity was similar to what was observed with sfGFP and liquid conditions, while the fold difference between the highest fluorescence under green and the lowest fluorescence under red was about 7.5x.

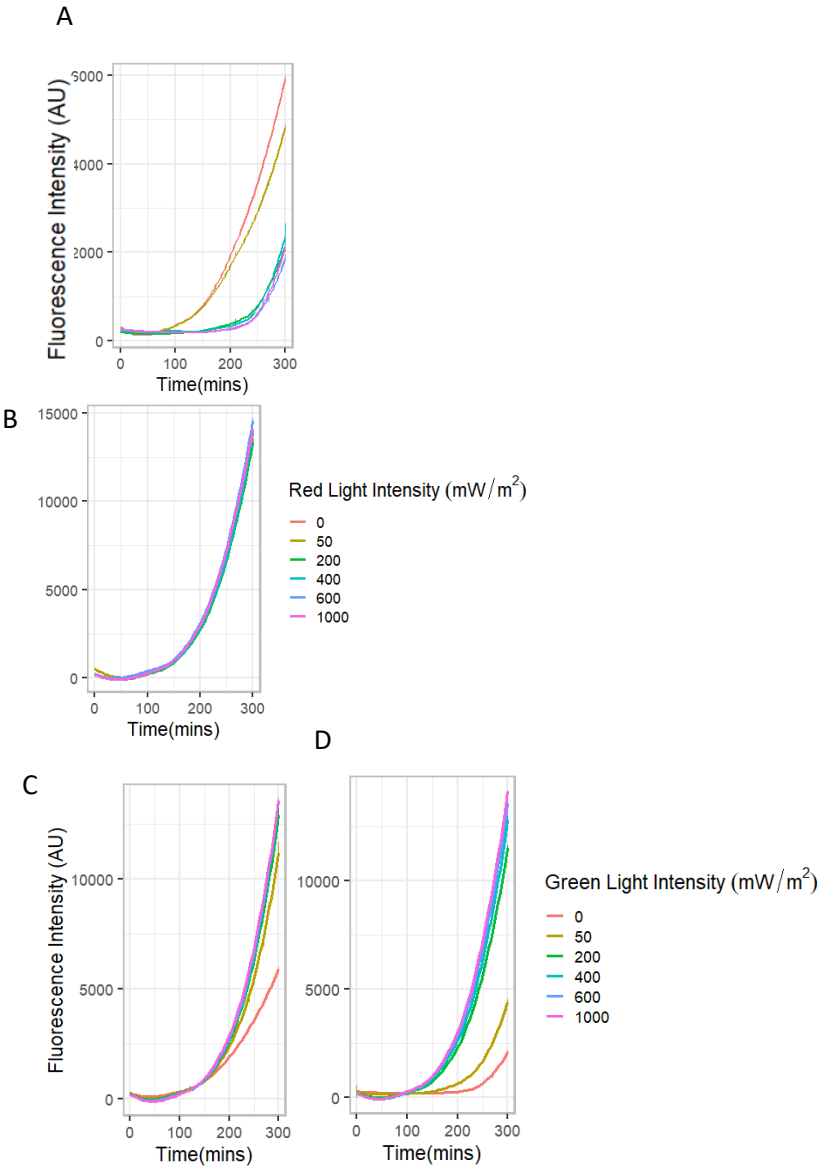


Figure 2.18: *Fluorescence intensity of tdFAST2 CCaSR 3.0 in 2% Agarose. A) No green light B) Green light at 1000 mW/m². C) No red light. D) Red light at 1000mW/m². Similar to the characterisation of the system in liquid, red light is needed in higher intensity than green to affect gene expression. The dynamic range between maximum fluorescence intensity under green and minimum under red light is 7.5x. In no green light, light intensity of over 50 mW/m2 has the same effect on fluorescence intensity, while in no red light, any green light from 50 mW/m² and above is enough to elicit the same response (n= 4, error bars represent standard error).*

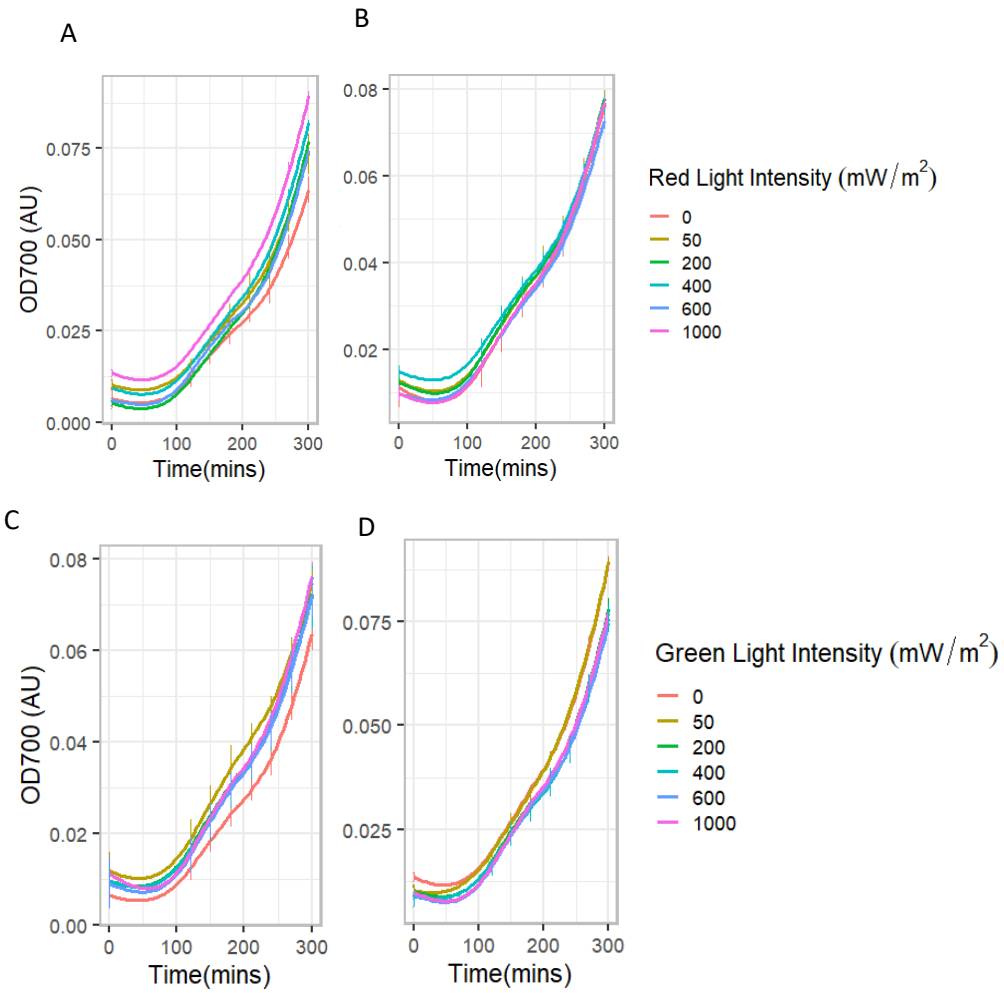


Figure 2.19: *OD 700 of tdFAST2 in CCaSR 3.0 in 2% Agarose. A) Green light at 1000 mW/m². B) No green light. C) Red light at 1000mW/m². D) No red light. Under no green and at maximum red light, the growth of the cells is inversely proportional to the induction, with cells inhibited using red light, or activated least by green growing faster. Under high green intensity, as all the strains had similar gene expression, no difference in growth is observed, while under no red light, cells in darkness grew slower than other samples (n= 4, error bars represent standard error).*

In order to understand the behaviour of the system a bit better, results were accompanied by plots of fluorescence intensity and OD700 at 300 minutes, at the end of the experiment. (Fig 2.20). In the fluorescence intensity image, the interplay between green and red light becomes apparent. Under no green light, fluorescence intensity was low levels at very low intensities of red. On the contrary, under 50mW/m² green light, fluorescence intensity was at similar levels only at intensities of red light higher than 200mW/m², while higher green light intensities maintain their gene fluorescence intensity regardless of red light intensity. In this way, it became clear how the red light was much more efficient in suppressing gene expression on its own, than in the presence of green light too.

The OD700 plots also show the effect of this interplay on OD700 (Fig.2.19 and 2.21). While in lower red light intensities all green light intensities reach the same OD700, under stronger red light, lower green light intensities reach higher OD700. This was postulated to be due to the reduction in gene expression by those samples, which led to lower burden.

By looking at the growth rate for the cells under different intensities of light, this burden hypothesis is confirmed (Fig.2.20): at low red light intensities there is little difference in the growth rate of the cells under different green light. as red light is intensified however, cells under lower green are able to grow faster. Interestingly, from the growth rate plots, the growth rate is lower for all samples between 150 and 200 minutes, followed by an increase in growth rate up to 300 minutes, which was thought to be because of the hydrogel affecting growth of the cells.

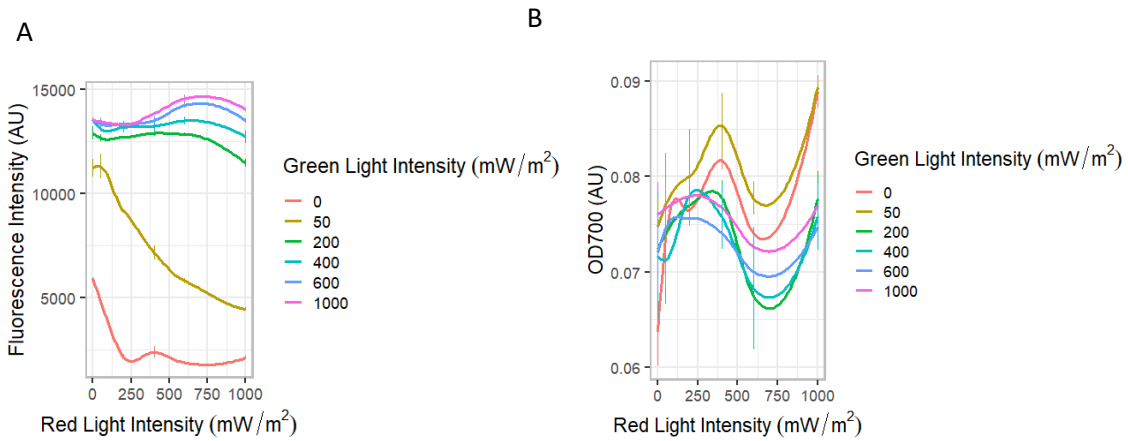


Figure 2.20: *Fluorescence Intensity (A) and OD700 (B) at 300 minutes for tdFAST2 in CCaSR 3.0. The fluorescence plots show that green light intensities of 200-1000 mW/m2 are largely unaffected by red light up to 1000mW/m2, as they remained relatively constant around 13000 AU. Under darkness, red light of 200mW/m2 is capable of reducing fluoresence to below 2500 AU, while cells in green light of 50mW/m2 show a steady decrease in fluorescence as red light intensity is increased. In terms of OD700, at lower red light intensities all green light intensities reach the same OD700, but as red light is increased to 1000 mW/m2 the samples under lower green light intensity are able to reach a higher OD700 (n= 4, error bars represent standard error).*

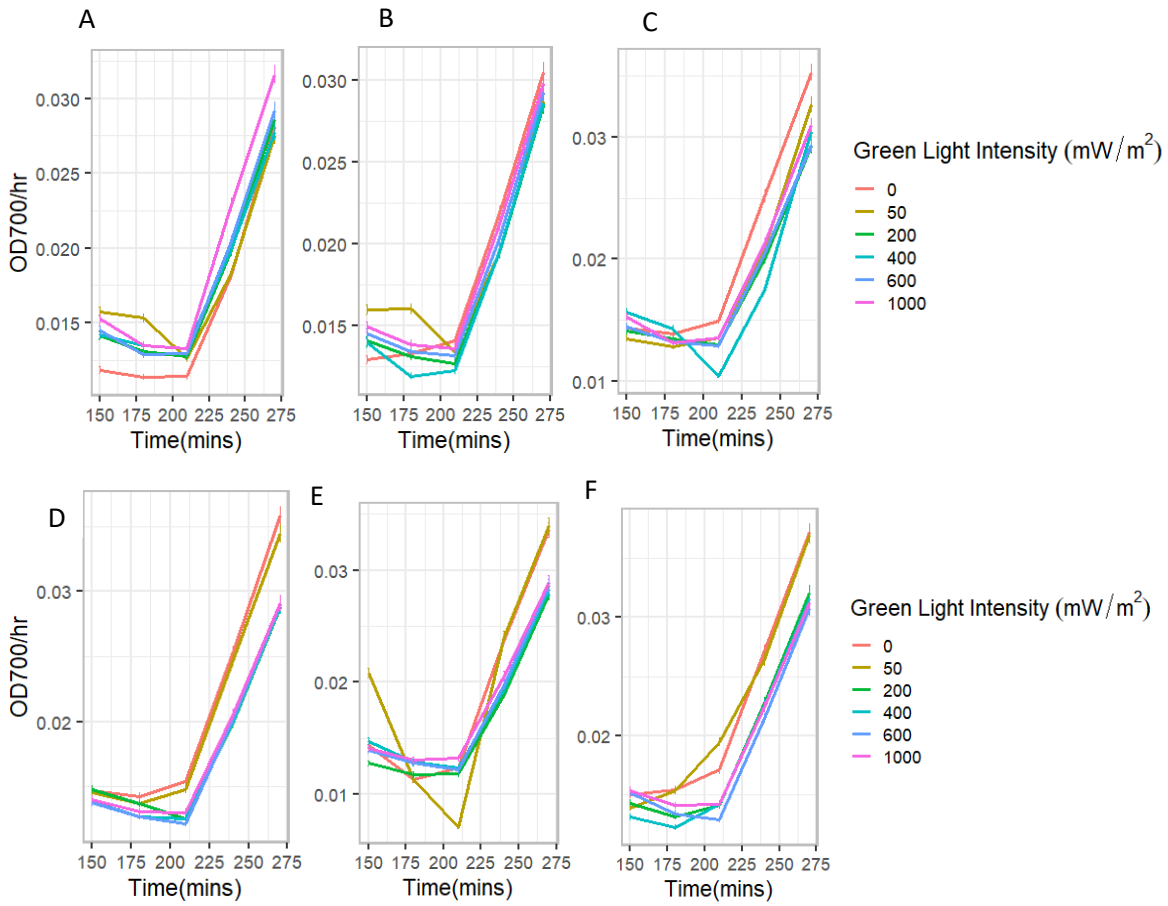


Figure 2.21: *Growth rate of tdFAST2 in CCaSR3.0 in agarose. (A-F) Growth rate of the cells, per hour, for red light intensities starting from 0, 50, 200, 400, 600 and 1000 mW/m², from left to right. Unlike previous characterisations, growth rate appears to be lower and stationary under all conditions in the first 200 minutes of incubation, linearly increasing after that. While under red light intensities from 0-50 mW/m2 all intensities show similar growth rate, at higher red light intensities, samples that were exposed to green light from 0-50mW/m2 had a higher growth rate than those exposed to higher green intensities (n= 4, error bars represent standard error).*

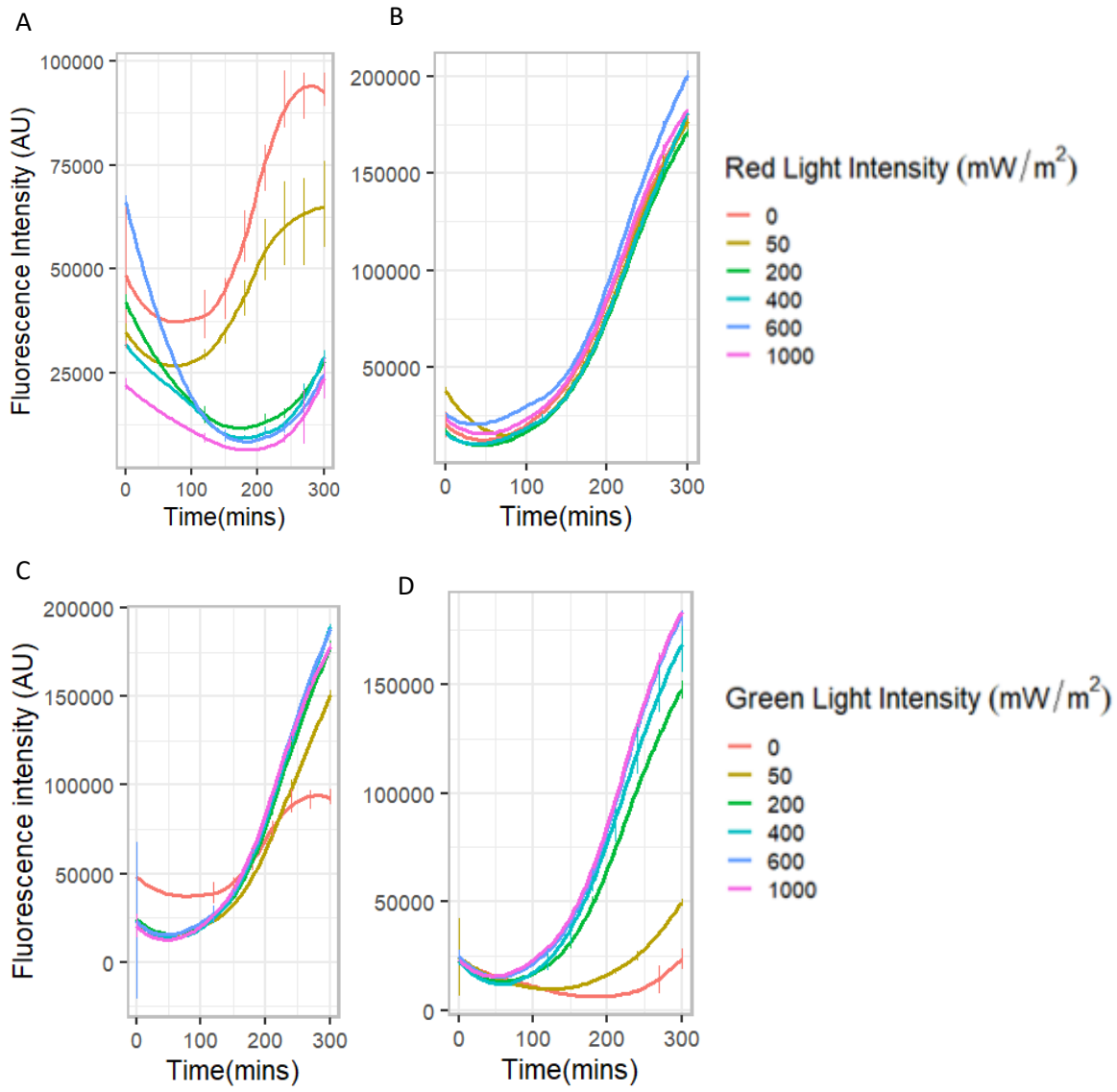


Figure 2.22: *Fluorescence intensity normalised with OD700 for tdFAST2 in CCaSR 3.0. A) No green light. B) Green light at 1000 mW/m². C) No red light. D) Red light at 1000mW/m². Under high red light intensities and low green intensities, a reduction is seen in fluorescence/OD, due to the production of new inactive photoreceptors, the inactivation of currently active ones by red light, and the dilution of active photoreceptors due to cell growth (n= 4, error bars represent standard error).*

In order to further elucidate the gene expression and behaviour of cells under different conditions, fluorescence intensity was divided by OD700 in order to understand the interplay of growth and gene expression in different conditions (Fig.2.22). In most of the plots, fluorescence/OD700 is similar to the trends observed for fluorescence, except for the conditions under no green light. Interestingly, there, for higher red light intensities, fluorescence/OD700 was reduced over time. This is suspected to be due to two factors: First, any photoreceptors activated during the overnight incubation of cells would be inactivated over time through the action of red light. Secondly, any new

photoreceptors in dividing cells would be produced in the inactive state, and maintained that way by the red light, therefore leading to areduction in the apprent fluorescence/OD700 over time.

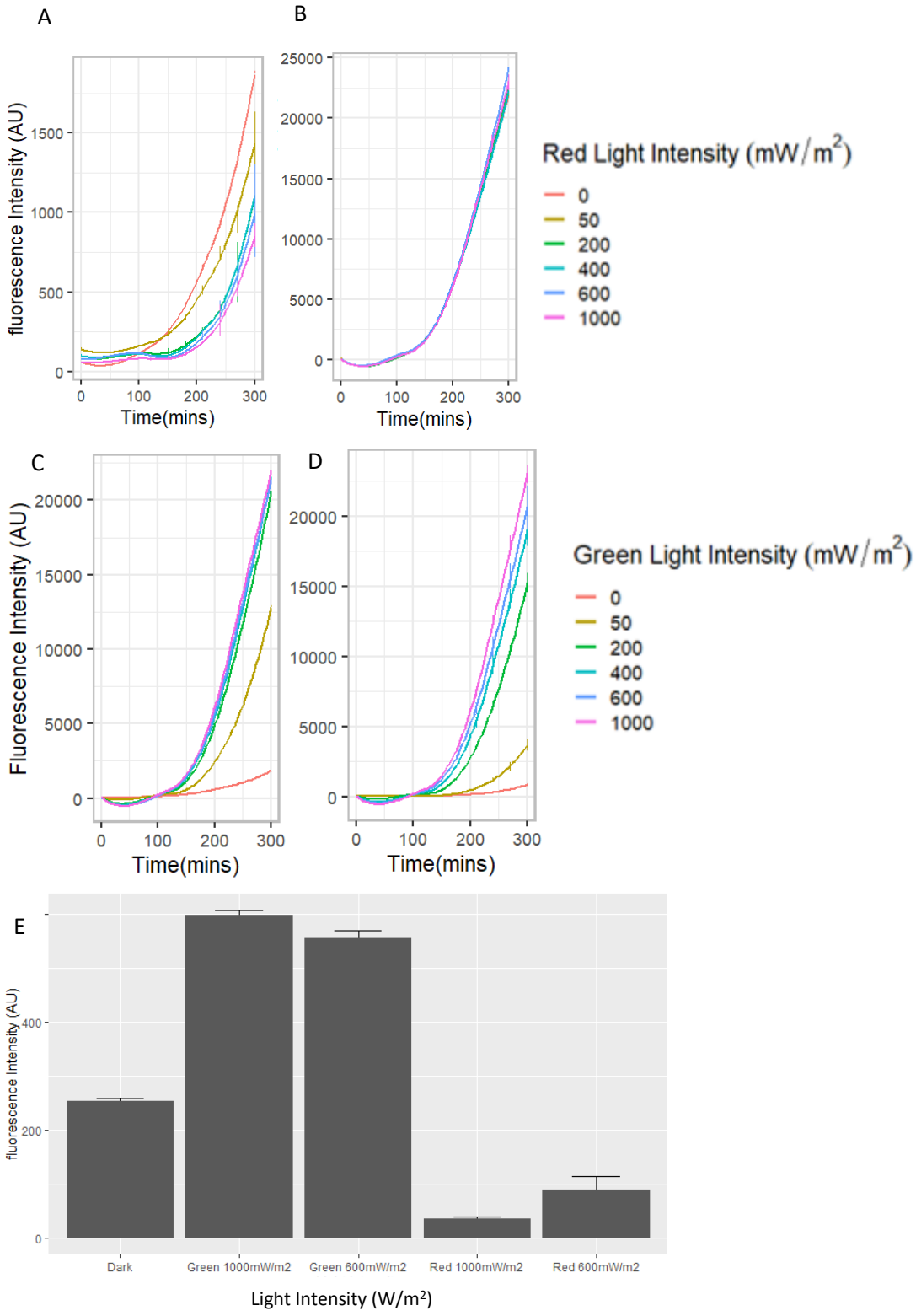


Figure 2.23: *tdFAST2 fluorescence intensity in liquid media. A) No green light. B) Green light at 1000 mW/m². C) No red light. D) Red light at 1000mW/m². E) Flow cytometry of cells in liquid media. Both the OD700 and fluorescence reach higher levels than in hydrogel, while the fluorescence dynamic range is also higher. Flow cytometry shows that a high dynamic range and behaviour by individual cells (n= 4, error bars represent standard error).*

This characterisation was repeated but in liquid media, in order to compare the full system in the hydrogel vs. in liquid media (Fig.2.22). As expected, OD700 at 300 minutes was higher in the liquid media, due to the lower spatial constraints present to the cells. In addition, fluorescence intensity was overall higher. However, fluorescence intensity/OD700 was similar for both experiments, indicating the similarity in gene expression both in liquid and in solid media. Flow cytometry showed similar results as with sfGFP, indicating a dynamic range of around 12.5x from maximum green to the maximum red light intensity used.

2.2.7 Improving the dynamic range - Digitalizer

While the results on the green and red efficiency of the optogenetic system were satisfying, I wanted to attempt to improve the dynamic range of the system even further. In the literature, multiple ways exist to improve dynamic range, including using multiple inputs, inhibitors and degradation tags. As a technique that would work with 3D printing however, I considered a toggle switch as the optimum way to improve the dynamic range, by reducing gene expression in the 'OFF', dark and red light locations, and activating gene expression only on the 'ON' green light (Gardner et al., 2000). The requirements for such a toggle switch were simple: It should allow for high activation with strong positive feedback to maintain hysteresis, but show quick reversal upon switching to the OFF state. The OFF state should be the least leaky possible, and the inhibitory mode should be as inactive as possible in the ON state.

Calles and colleagues have recently published a 'digitalizer' module, working largely as a toggle switch in Gram-negative bacteria, using sRNA dynamics for a genetic toggle switch (Calles et al., 2019). Briefly, for the ON state, an inducer activates the transcription factor that leads to expression of two genes under the same promoter: the gene of interest and a repressor that represses expression of an sRNA molecule. In its turn, the sRNA molecule represses the RBS upstream of the gene of interest and the repressor. As a result, under induction, the gene of interest and repressor are expressed in high quantities, giving the required output and repressing the expression of sRNA. Once induction stops, reduction in the levels of the repressor leads to sRNA expression and inhibition of repressor and gene of interest transcription, creating two opposing feedback loops.

The system's RNA dynamics promised to show the quick kinetics I was looking for in such a system, while the reported leakage under no induction was practically zero, making it a tempting system to try. As outlined in Figure 2.23, however, the success of the system when moved to a different

induction system would depend largely on the expression of the repressor, and how strongly repression of the sRNA could be achieved.

For the purposes of optogenetics experiments, the digitaliser was obtained and cloned downstream of the CCaSR 3.0 constructs, and sfGPF replaced with tdFAST2, to create a strain termed BPD.

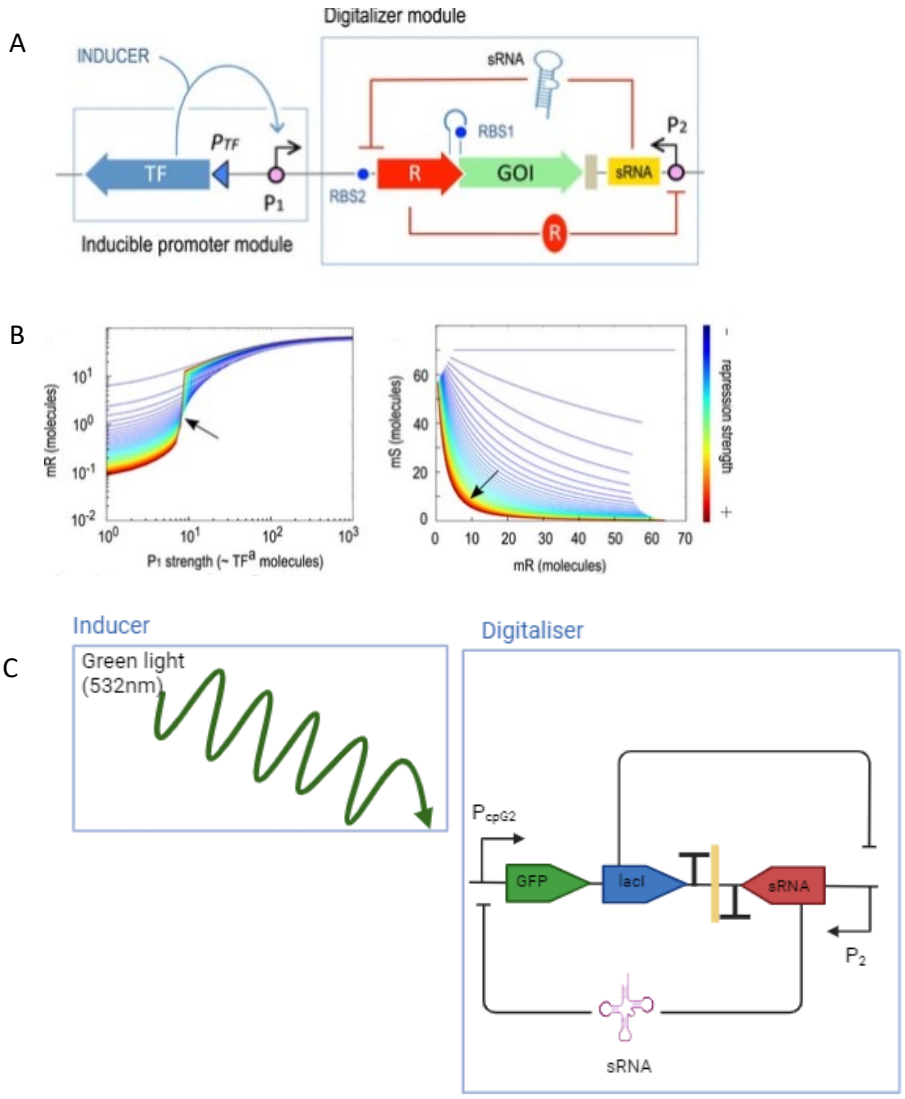


Figure 2.24: *A) Schematic of the architecture of the Digitalizer toggle switch. B) Figure indicating the dependence of the digitalizer on the strength of the promoter,and repression depending on mRNA moeclules. Both these parameters can be tuned with genetic engineering of the system. C) Schematic of the optogenetic implementation of the digitalizer. Figures adapted from (Calles et al., 2019).*

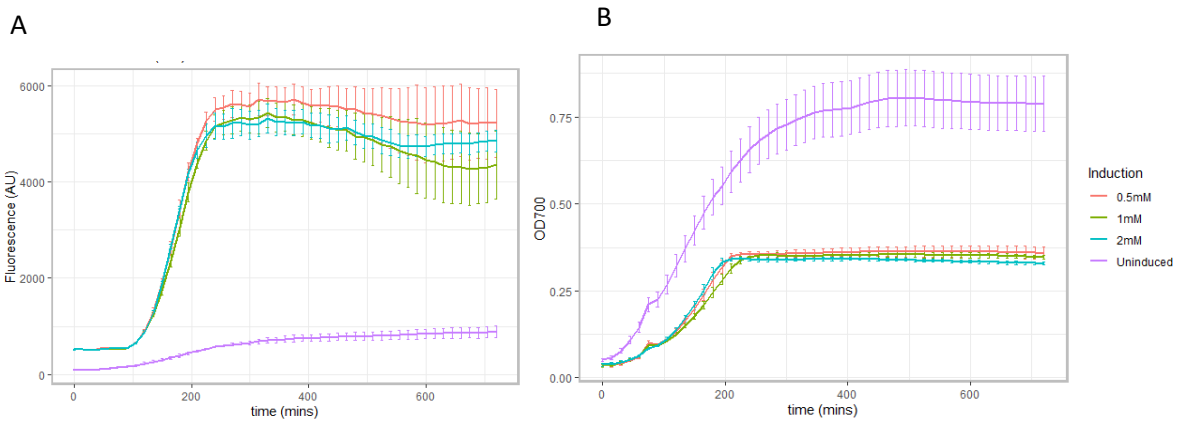


Figure. 2.25: *Fluorescence Intensity (A) and OD700 (B) of the Digitaliser upon induction with Methyl Benzoate. Induced strains showed much lower growth than uninduced ones, indicating a level of toxicity by the inducer. Induction levels of 0.5-2mM showed a similar induction level in terms of fluorescence, achieving a dynamic range of around 5x (n= 4, error bars represent standard error).*

Before testing the optogenetic construct, the performance of the original digitaliser was verified with methyl benzoate induction. It was found that the uninduced strain did indeed show very low fluorescence, and there was a 7-fold activation upon addition of methyl benzoate (Fig.2.24). Therefore, I proceeded to test whether the digitaliser would also work with the optogenetic constructs (Fig.2.26-2.27). As the fluorescence intensity and fluorescence/OD700 data show, the digitaliser worked in this case by reducing both the fluorescence during induction with green and during suppression with red, therefore effectively dimming fluorescence in the whole system. This indicated to me that the digitaliser as it worked at the moment was not able to improve printing contrast in 3D. In order to make such a toggle switch useful in the context of the optogenetic constructs, the promoters involved as well as the optogenetic system would have to be tweaked in future work, to shift the system to the position range where a small difference in activation makes a large difference in output fluorescence intensity. Therefore, in this case I decided to continue with the original design.

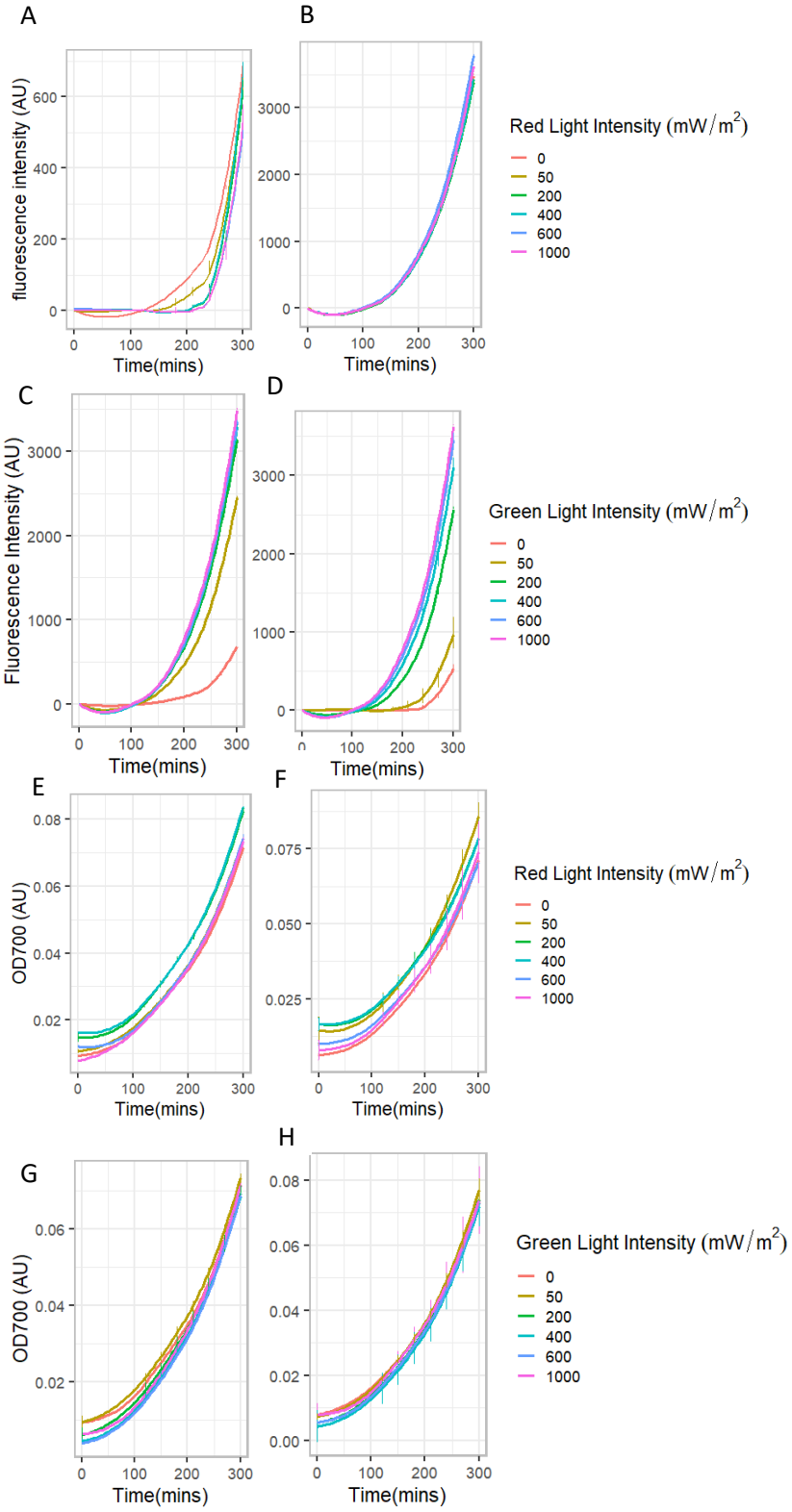


Figure 2.26: *Fluorescence intensity (A-D) and OD700 (E-H) of cells harbouring the digitaliser under different light intensities. From left to right: no green light, green light at 1000 mW/m², no red light, red light at 1000mW/m² (n= 4, error bars represent standard error).*

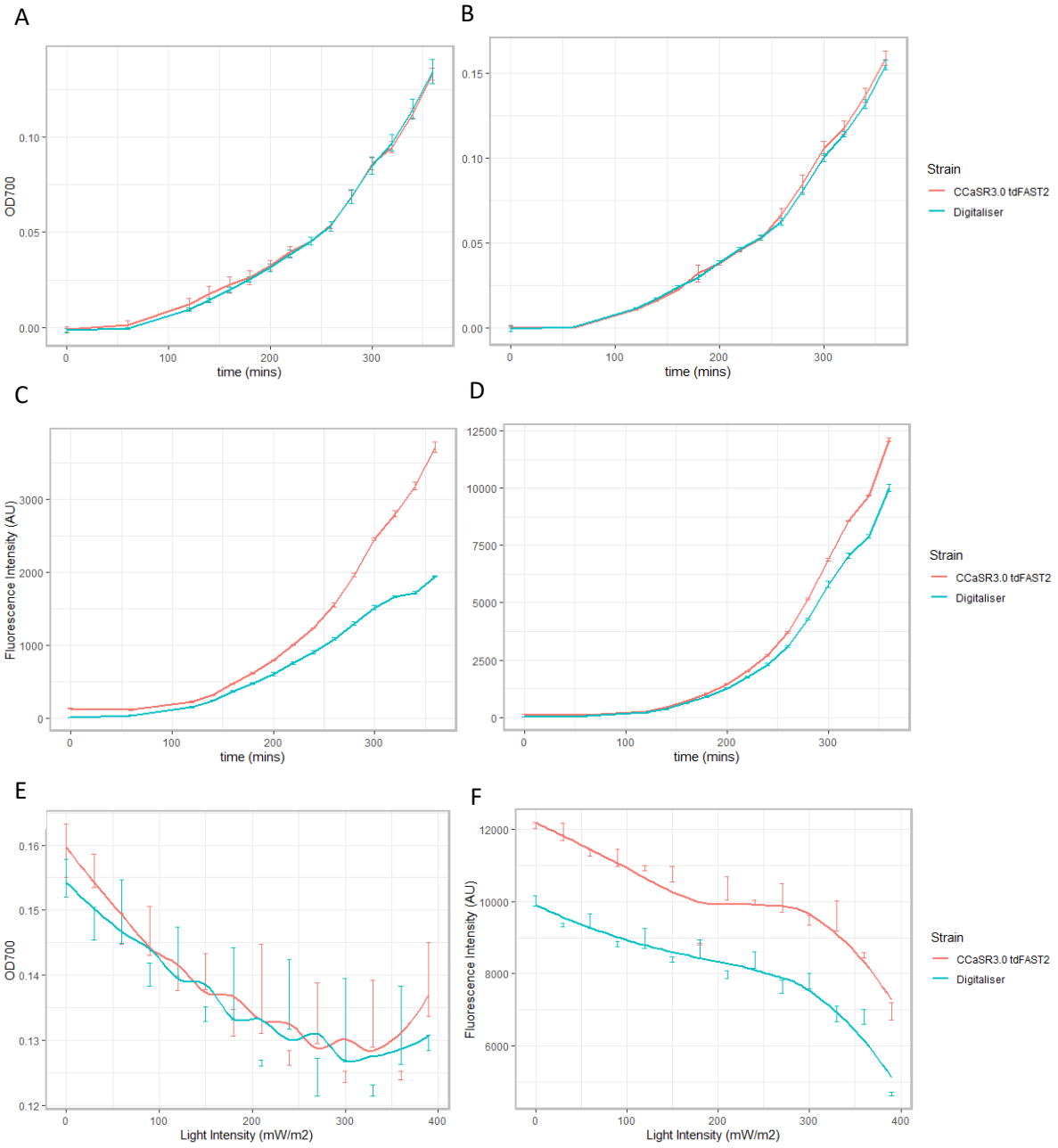


Figure 2.27: *Direct comparison of the digitaliser with CCaSR 3.0 harbouring tdFAST2. A-B) OD700 over time in green light (A) (800Mw/m²) and darkness (B). C-D) Fluorescence intensity over time time in green light (C) (800Mw/m²) and darkness (D). E) OD700 at 360 minutes with different green light intensities. F) Fluorescence intensity at 360 minutes with different green light intensities. OD700 does not significantly differ between the two strains, but fluorescence is lower for the digitaliser under all conditions of illumination. The difference remains roughly the same throughout all green intensities, indicating that the digitaliser does not truly increase the dynamic range, but lowers all gene expression under activation or not (n= 4, error bars represent standard error).*

2.3 Conclusions

In this chapter, I started from defining a goal for the project, that of optogenetically controlling production in 3D. I developed a theoretical set up for this 3D optogenetic production, based upon localised laser activation in points within a volume of hydrogel-embedded *E. coli* cells. Starting from this theoretical tenet, I then moved on to define the initial biological requirements for the project. These included an optogenetic system with high dynamic range, the media on which cells grow and the reporter to detect fluorescence.

I addressed these concerns individually and sequentially, through the use of a plate reader and a custom-made light plate for illumination. I picked 2 versions of an optogenetic system that showed a high dynamic range, activation and suppression wavelengths, and verified gene expression by both versions.

Following verification of gene expression I tested the two versions under different lights and determined the one that showed the highest dynamic range, CCaSR 3.0. Following this, I chose a reporter that could work well in an anaerobic environment, tdFAST2, optimised its conjugate dye concentration and characterised the responses of the system with the new reporter.

In terms of media, I characterised growth and gene expression of cells in a variety of different solid hydrogels and concentrations, while also characterising the optical properties of the hydrogel themselves. I chose 2% agarose, as it was a hydrogel that was easy to handle, offered consistently high fluorescence while being largely transparent. In terms of liquid media, I also assayed a number of media and concentrations, picking M9-glucose as it offered the lowest background fluorescence. Having picked all of the components of the biological setup for 3D production, I tested the system in 2D on the light plate, and verified that it worked. Finally, I attempted to improve the dynamic range of the system through the use of a toggle switch.

During these characterisation and optimisation experiments, a few properties of the system became apparent, in line with the characterisation and modelling of the system that had been performed before. Firstly, the system is highly sensitive to low intensities of green light, which are enough to activate gene expression. Secondly, in combination of red and green light, the red light needs to be at least 5x stronger than the green light in order to effectively supress expression. These results are supported by experiments in this chapter, as well as previous theoretical work indicating the reliance of the system on the proportion of active photoreceptors, and how these photoreceptors

are diluted with growth. The timeframe of the experiment was identified, as cells reach peak growth rate up until about 300 minutes, meaning that any 'printing' would have to take place before that.

The contributions of these chapter are useful in two ways: First, I optimise the biological 'hardware' that will employed throughout this project to achieve the first 3D optogenetic-activated optogenetic gene expression by *E. coli* cells. Then, I develop a cheap and easy to use optimisation hardware through the light plate, as well as experiment process and analysis, based on which any further characterisations and optimisations were performed. Thirdly, I offer an initial understanding of how the system works, which is important in designing 3D production. Finally, I offer a promising avenue in future work, in terms of improving the dynamic range through an optimised toggle switch.

In the next chapters, I use the biological setup as well as insights identified in this experiment to progressively move to optogenetically-activated production within a 3D volume, by first ensuring production in 2 dimensions, followed by increasingly accurate production in a spatial and temporal manner. I also use the analytical protocol identified here to improve measurements on some of the production parameters by the cells and identify their response to non-steady state illumination.

Chapter 3

3D Optogenetically activated gene expression under continuous illumination

3.1 Introduction

In the last chapter, I chose and optimised the biological part of the setup for optogenetically-induced production by living organisms in a 3D matrix. Further, I devised a theoretical framework on which 3D printing would be based, through the connection of individual voxels (Fig.2.2).

In this chapter, I use the set-up developed in Chapter 2 to start working towards 3D optogenetic production. In order to achieve 3D printing through the connection of individual voxels, I decided to start by assessing the feasibility of producing, through gene expression, a single voxel of the desired molecule, in this case tdFAST2, in the centre of a 3D volume. 2-dimensional (2D) cellular production using optogenetics has been performed several times, using multiple optogenetic systems, cellular chassis and molecular outputs (Baumschlager & Khammash, 2021). However, production of such a voxel in 3D would be a significant advancement in the field, allowing optogenetic control using bacteria in 'true' three dimensions, as opposed to the surface of a 2D culture. Once a single voxel is produced, optogenetically induced production of arbitrary shapes becomes an exercise of producing multiple such voxels in a temporally and spatially separate manner.

Herein, I document the progress towards producing and characterising a single voxel in the 3D volume, under continuous illumination and using tdFAST2 as the reporter molecule. I start by testing localised optogenetic gene expression by the BP16 strain, on the surface of a Petri dish, across two dimensions. Following this, I move on to attempting gene expression in 3D by illuminating a specific location on cell-laden hydrogel inside a 1x1x5 cm cuvette and perform experiments to visualise and quantify production in the middle of a hydrogel. I also attempt to improve the visualisation possibilities by using UV light to cure the cells post-printing, as well as developing a new optical hardware and imaging setup.

With a new hardware setup in order, I attempt to test the limits and capabilities of the system by trying two methods of inducing gene expression in 3D and quantifying the results. Following these, a more systematic characterisation in 3 dimensions in the cuvette is performed using one green light beam, as well as a split red beam. Finally, the combination of red and green lights led to a new method to achieve production in a single localised voxel. Different light intensities and their effects were also characterised and assessed.

This chapter constitutes the first step to achieving full optogenetic control in 3-dimensions for the generation of multiple shapes, serving as an initial proof of concept and starting point to printing multiple voxels. The contributions of this chapter amount to taking the optogenetic characterisation performed in 2 dimensions in the previous chapter, and using the cells, characterised light intensities and timeframes, to build up to 3D optogenetic control, while at the same time establishing the tools to quantify 3D production, and understanding the intricacies introduced to the system by adding a third dimension. This chapter culminates in the ability to induce gene expression, and characterise fluorescence intensity, in a single voxel in a 3D solid volume.

Objectives

- Develop hardware to illuminate a cuvette in 3 dimensions
- Develop a method to visualise production of the fluorescent reporter in 3 dimensions
- Activate production of a voxel on the surface of a 3D volume
- Activate production of a voxel in the centre of a 3D volume, under continuous illumination

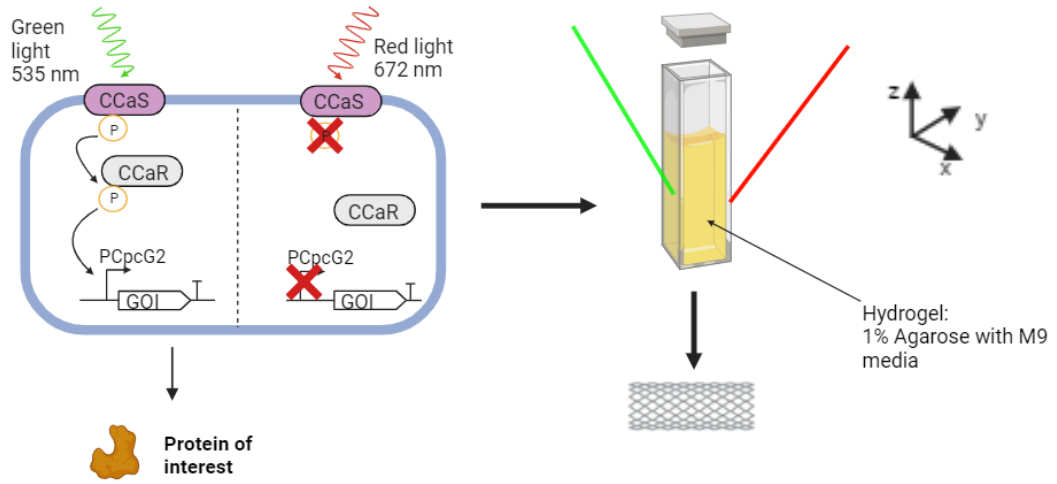
3.2 Results and Discussion

3.2.1 Localised optogenetic production on the surface of a Petri dish

As a first test of the spatial capabilities of the optogenetic system, I attempted inducing expression in a 2-dimensional area within a flat Petri dish. The purpose of this experiment was to optically distinguish maximal production by the cells against background in a 2-dimensional setting. This ability depended on three parameters: the dynamic range of the system in the timeframe tested, and the illumination and imaging tools available.

The first parameter that was established in preparation for the experiment, was the illumination and visualisation equipment. A setup was devised, where cells embedded in a 3D hydrogel matrix inside a container would be illuminated with laser beams, activating and deactivating expression in particular locations (Fig 3.1A). In order to achieve this, an initial optogenetic activation rig was built (RS, UK; Materials & Methods 7.2.2), which consisted of a base, on which a platform was based that could move in the X, Y and Z directions for the sample to rest. Besides the sample there were two holds for individual collimated (parallel) lasers (ThorLabs, UK). The lasers obtained were green lasers at 532 nm, with a maximum power of 0.9 mW and a beam diameter of 3.5 mm (93.5 W/m^2 maximum intensity). These lasers were fitted with Neutral Density (ND) Filters (ThorLabs, UK) with ND ranging from 1.0 to 2.0, therefore allowing for intensities to a minimum of 935 mW/m^2 (3.1B). The visualisation equipment at this stage was primitive, consisting of a Dark Reader Blue Transilluminator by Clare Chemical Research and a standard gel scanner consisting of a BioRad Chemidoc imaging system camera.

A



B

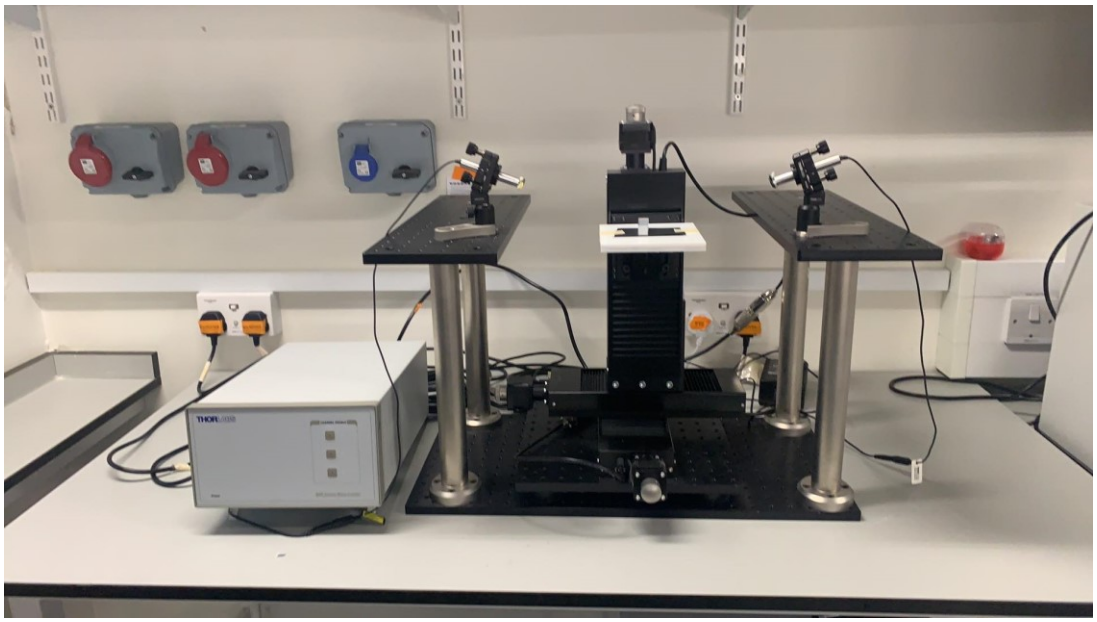


Figure 3.1: *(A): Schematic of the use of optogenetic system for 3D activation and inactivation. Cells harbouring CCaSR 3.0 are suspended in a solid matrix inside a cuvette. Red or green light is delivered in the form of a laser beam o particular locations in the hydrogel, inhibiting or activating gene expression correspondingly. Depending on the positions on which the laser is applied, different 3D shapes can be produced. (B) Set up for initial 3D optogenetics experiments. The sample is placed on the platform (white level, in the middle), which can move up and down. The lasers are placed on either side, with filters stuck on the surface of the laser. The entire apparatus is used in darkness.*

In order to achieve gene expression on a Petri Dish with this setup, I prepared a cell culture of BP16 in the hydrogel (hydrogel with cells), with a starting OD700 of 0.005 and a volume of 10 ml (Materials and Methods 7.1.5.3) and poured it on to an empty Petri dish to give a hydrogel of 5 mm thickness. I then left the hydrogel in a fridge at 4 °C for 30 minutes to solidify. Following that, I

incubated the Petri dish in a dark room overnight (10 hours) at 37 °C. Two different lasers were used at different locations (Fig.3.2). On the left, the ND = 1 filter was used, giving a light intensity of 9.35 Wm^2. On the right, an ND = 2 filter was used, giving 935 mW/m^2. These intensities were chosen in order to achieve maximum induction of gene expression. Similarly, the incubation time was 10 hours because, as the experiment was done in two dimensions, it was considered scattering due to high OD700 would not be an issue, and a longer incubation time could give higher contrast.

After 10 hours, I removed the Petri dish from the dark room and cooled it down in a fridge at 4 °C for 1 hour, followed by imaging. The image of the Petri dish indicated that the illuminated areas of the Petri dish (Marked with a black circle) had a higher fluorescence than the surrounding areas. In the area on the left, where the light intensity was 10x higher, the diameter of the activated area, where higher fluorescence was observed, was 4 nm, 4x larger than the area on the left, and also 4x larger than the diameter of the incident beam. This can be attributed to the Gaussian Nature of the beam (Kogelnik & Li, 1966; Materials and Methods 7.2.2), which means that the light intensity of a collimated laser beam decreases in space following a Gaussian distribution. Therefore, at a higher intensity, a larger area of the laser would be at a high enough intensity to activate the cells, leading to a wider activated spot. Alternatively, this phenomenon could be attributed to instabilities in the illumination equipment and small movements overnight, or to light scattering by cells, even in this small volume. Scattering could occur both during illumination as well as imaging.

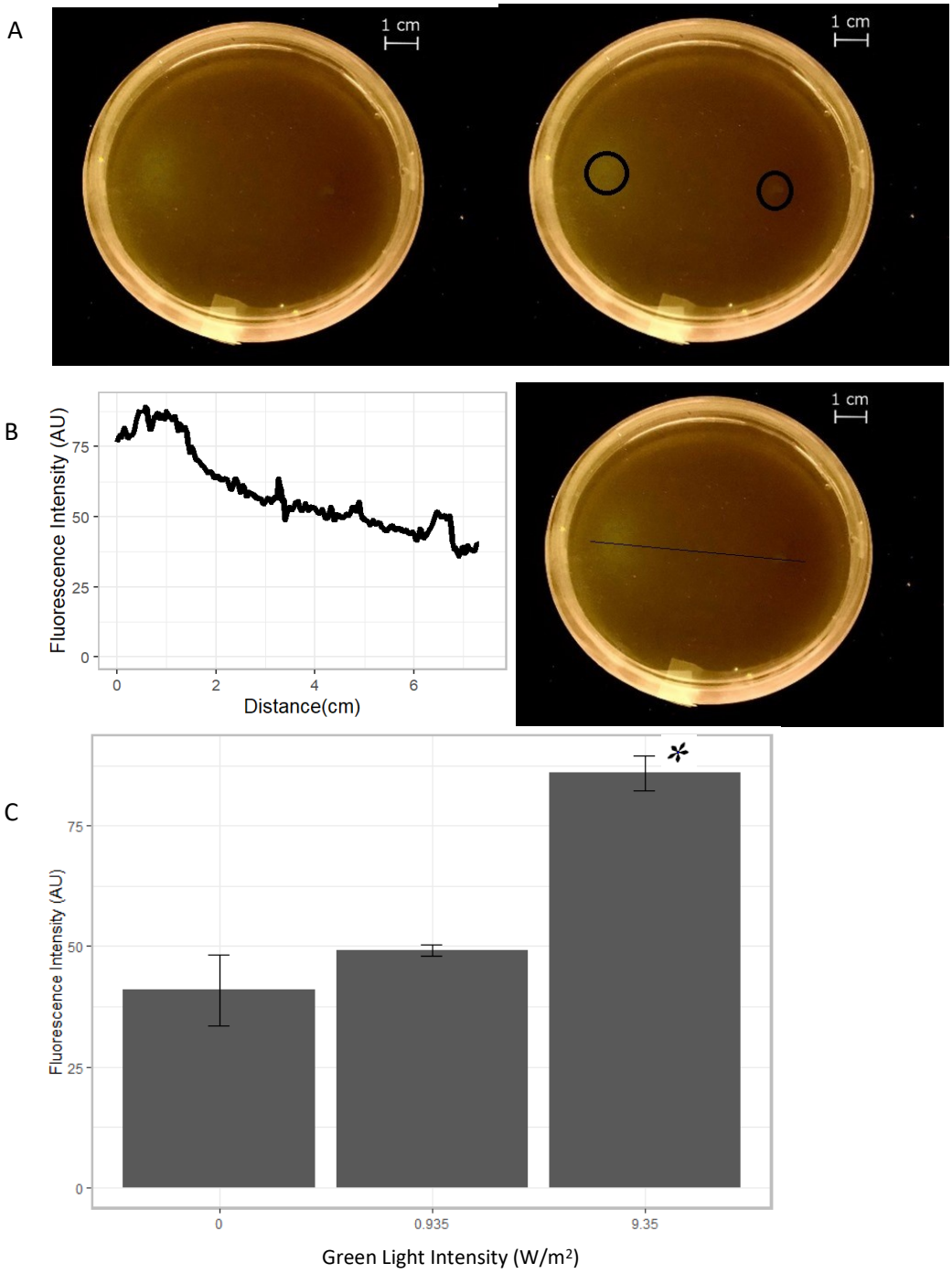


Figure 3.2: *(A) Optogenetically activated gene expression in a Petri dish. The Petri dish was illuminated for 10 hours with two different intensities of light. On the left (circled area), green light intensity was 9.35 W/m², and on the right 0.935 W/m². The left activated area was ca. 154 mm², while the activated area on the right was ca. 30 mm². (B) Fluorescence intensity across a line from the activated area to the edge of the Petri dish, as shown in the panel on the right. A sharp decrease is observed in the Petri Dish. (C) Fluorescence Intensity in twenty, 2 mm² -sized points the activated areas compared to twenty, 2mm² points spread across the inactivated area (n=3, error bars represent standard error).*

To better quantify these results, a line was plotted starting from the non-activated area on the left, to the activated area on the right, (Fig. 3.2B), and fluorescence intensity across the line was plotted. In the graph of fluorescence intensity across the distance of the line, there was a wide peak in the activated area on the left (9.35 W/m^2), but then a steady drop in the measured fluorescence intensity over distance, with another, smaller peak corresponding to the activated area on the right (0.935 W/m^2). The higher fluorescence intensity where higher illumination was used, was expected, corresponding to a higher degree of photoreceptor activation and less dilution due to growth.. However, the drop in fluorescence intensity across the Petri dish was unexpected. This could again be attributed to scattering, activation from the Gaussian nature of the beam, or inaccuracy in the imaging equipment.

Twenty square-shaped regions of interest (each 2 mm^2) were sampled from each activated area, as well as the surrounding areas, and the average fluorescence intensity and standard deviation plotted across different repeats (Fig 3.2 C). While the background was highly variable, it was consistently lower in fluorescence intensity than the 9.35W/m^2 activated area, with an average of 40% lower fluorescence. It was also generally lower than the 0.935 W/m^2 activated area, by 10% on average. Both activated areas also showed much more consistent fluorescence. This Petri dish experiment therefore worked as a proof-of-concept in two dimensions, indicating that it was possible to activate a particular region in an area using optogenetics.

There were several limitations in the experiment, however. The dynamic range in fluorescence intensity in the Petri dish was lower than what was expected, about 1.25x between darkness and 935 mW/m^2, compared to almost 3x observed in the plate reader experiments with similar intensities (Fig. 2.23). At the time, this was attributed to scattering by the cells, and the shape of the laser beam. It is possible that scattering of light, as well as any internal reflections in the Petri dish could reach areas across the whole area of the Petri dish over 10 hours, leading to uneven activation and an overall apparent reduction in dynamic range. In addition, the 10-hour growth period might have also led to uneven responses to activation, as the cells would enter stationary phase, reducing their responsiveness to optogenetic stimuli and therefore the dynamic range. Furthermore, even though the Petri dish was sealed with film for the duration of the experiment, differences in aeration might also have played a role in gene expression.

Overall, in this section, I used a localised beam of green laser light to activate expression of *tdFAST2* on the surface of a Petri dish. Two different intensities of light gave different fluorescent intensities and sizes for the activated area, indicating the potential influences of scattering, as well as limitations in the illumination and imaging equipment.

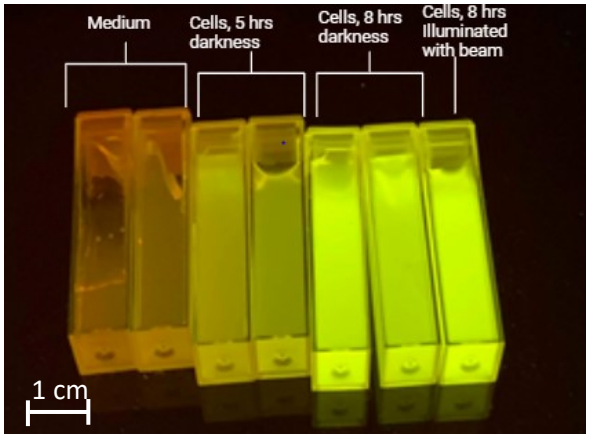
3.2.2 Optogenetic-induced gene expression on the surface of a 3D hydrogel

As the ultimate goal of this experiment was to control production in 3D, the next experiment in this regard was to transfer the illumination experiments to a 3D volume. As a container for this volume, a plastic cuvette (BetterEquipped, UK) was chosen as it represented a small volume where production can be controlled. The dimensions of the cuvette (10x10x50 mm), and thin (1 mm) transparent walls, meant that light could easily pass through the cuvette to the hydrogel volume without a large amount of scattering and attenuation, and also enabled easy and quick preparation of the experiments at low volumes.

The first attempts at printing with the cuvette employed 10-hour overnight illumination again, which resulted in no localised fluorescence (not shown here). Similarly with the 2D experiment, this was postulated to be due to three reasons: first, the 3-dimensional nature of the cuvette made it harder to distinguish differences in fluorescence in particular locations, as they would be masked by the accumulated background over the depth of the cuvette. In addition, scattering by the cells at high OD700 (around 0.2 AU after overnight incubation) would also affect the apparent light intensity in a specific location. Finally, cells entering stationary phase would not react in a predictable manner to illumination, affecting the results.

In order to investigate the increase in background expression and loss of contrast over time, several cuvettes were filled with the solid culture and incubated for different periods of time. As a control, 2% agarose with M9 glucose and tfLime was prepared (Media control) and incubated in a cuvette without cells. For the test samples, hydrogel with cells was prepared. Two of these cuvettes were kept in darkness for 5 hours, and 2 were kept in darkness for 8 hours. Finally, one cuvette was illuminated with 935 mW/m^2 laser for 8 hours. In the end of the incubation, all the samples were imaged together. While fluorescence for the media control was minimal, there was an increase in fluorescence in all the cell-laden cuvettes according to time. As a result, any background in the 8-hour exposed cuvettes was extremely bright, and expression in the activated part, if any, could not be distinguished (Fig. 3.3). It thus became apparent that shorter incubation times were necessary to distinguish gene expression in the induced areas from background.

A



B

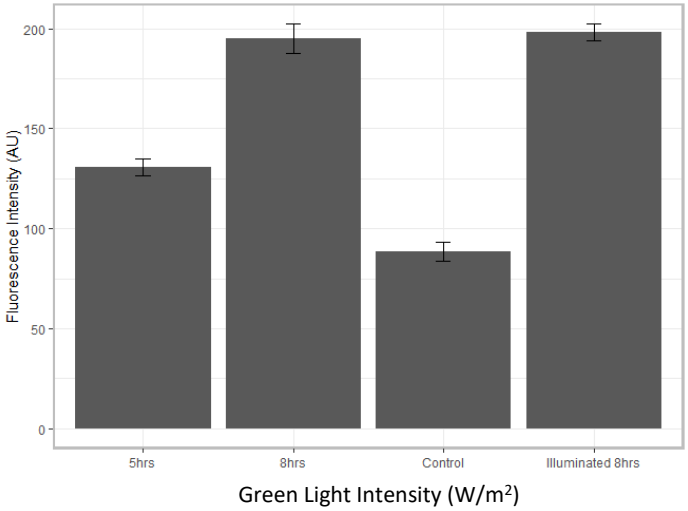


Figure 3.3: *Hydrogels incubated in darkness for different periods of time. (A) From left to right, 2 cuvettes containing only agarose/M9-glucose with tfLime, 2 cuvette incubated for 5 hours in darkness, 2 cuvettes incubated for 8 hours, and one cuvette incubated for 8 hours and illuminated 1 cm from the base with a 935 mW/m² green light beam. Even under darkness, background fluorescence builds up over time in these cuvettes, leading to overly high fluorescence intensities and inability to distinguish expression. (B) The fluorescence intensity of 20 2 mm² areas from the cuvettes were measured for each condition, and results plotted. Fluorescence intensity was about 50% higher than control after 5 hours of incubation, and 120% higher than control after 8 hours of incubation. There was no visible difference between the illuminated and non-illuminated cuvettes after 10 hours of incubation (n= 4, error bars represent standard error).*

Therefore, the next goal, was to increase contrast, by increasing induced expression and reducing background expression. To achieve this, I reduced illumination times to 3 hours, within the range characterised in Chapter 2 where cells would be in early exponential phase and background production would not be high. In order to maximise gene expression, I attempted this with a high

green light intensity, without the use of the ND filter (93.5 W/m²). After 3 hours of illumination with that intensity, it became clear that the light was damaging to the cells, with a round area of no cell growth appearing at the position at which the laser was hitting the cells (Fig.3.4). This is thought to be due to the accumulation of light energy having bactericidal effects (Kim et al., 2013.).

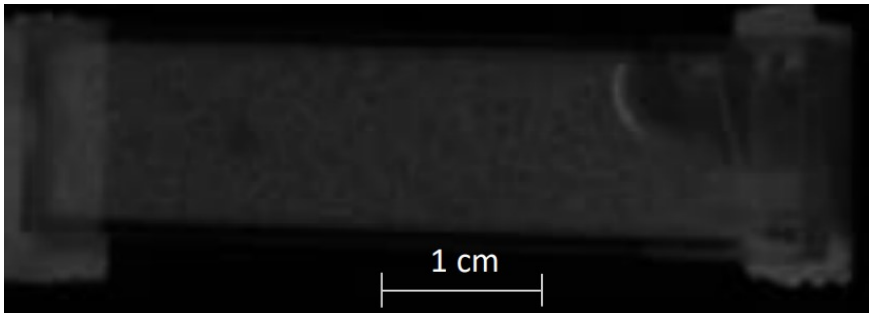


Figure 3.4: *Cell death after 7 hours of illumination with 500 mw/m² green light. A dot is seen about 1cm from the base, where there are no cells (black dot on the left side of the cuvette, shown by arrow).*

To avoid cell death, I decreased the illumination intensity to 935 mW/m² of continuous illumination for 3 hours. This time, upon imaging of the cuvette, a voxel of higher fluorescence intensity was visible at the point of illumination where fluorescence was higher than the surrounding areas (Fig. 3.5). A line across the cuvette was quantified and plotted, indicating an area with diameter of approximately 1.3 mm where fluorescence was at least 15 AU or 10% higher than surrounding areas. This constituted a first proof-of-concept that it was possible to achieve and measure localised optogenetic activation on the surface of a 3D volume. However, imaging was performed along the direction of the laser beam. Any attempts to image the cuvette from other directions did not show any differences in fluorescence (not shown here). Therefore, it was impossible to understand whether the observed difference in fluorescence corresponded to a line of any depth inside the hydrogel, or simply a dot on the surface of the hydrogel.

In this section, I performed the first proof-of-concept control of gene expression on a 3D cuvette, I started by using incubation times and green light intensities that were too high, resulting in saturation of the whole hydrogel or bleaching of the cells. By fine-tuning these two parameters I was able to achieve gene expression in a localised area on a 3D hydrogel.

3.2.3 Visualising Optogenetic production inside a cuvette

In order to be able to better quantify fluorescence intensity post-illumination, there were several obstacles that I had to overcome. The first one, following the inability to establish whether the voxel observed in Fig. 3.5 was a line or not, was the ability to image fluorescence inside the hydrogel and not just by looking at its surface. This problem arises because scattering of light by the hydrogel and cells would prevent both the laser to reach deep inside the cuvette, and the visualisation of the centre of the cuvette.

An initial hypothesis to solve this issue was that visualisation could be eased by killing the cells post-print, therefore reducing cell-caused scattering to allow for easier visualisation. First, to test the possibility of visualising fluorescence with tfLime after UV bleaching of cells, I needed to address the tolerance of tfLime to UV light. I prepared 1 ml of M9-glucose (liquid media) containing only the tfLime, liquid media with cells but without the tfLime and liquid media with the cells and the tfLime, and incubated them in the dark, in Eppendorf tubes for 3 hours. I imaged the Eppendorf tubes after the 3 hours. After the this first imaging, I incubated the tubes for 20 minutes under UV light this using UV light from a UV light box (Thermo Fisher, UK).

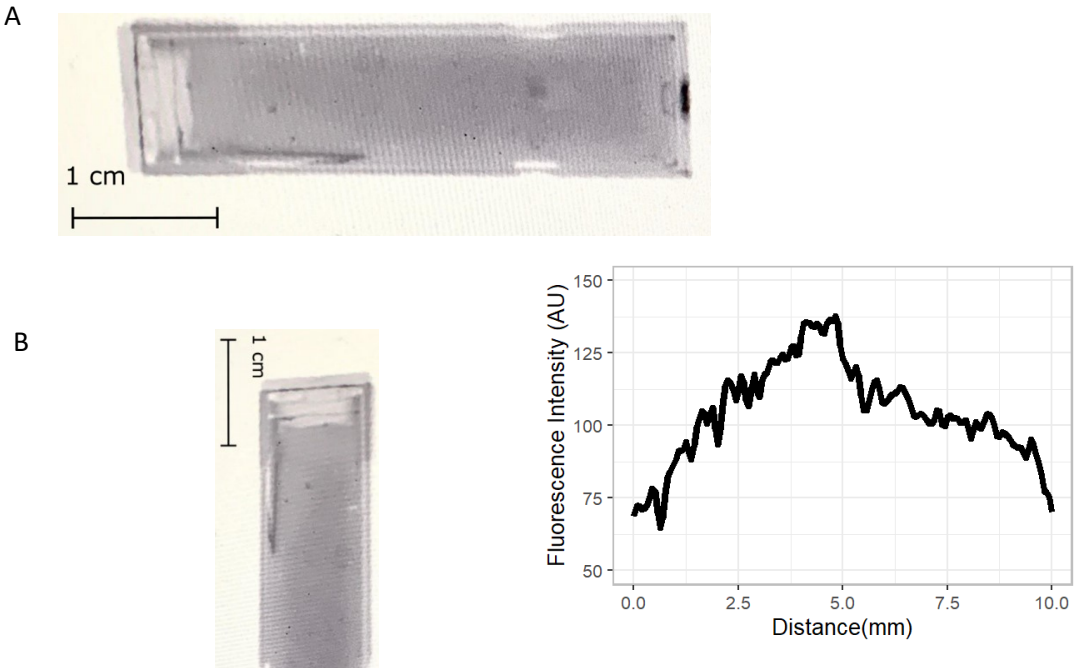


***Figure 3.5**: (A) A localised voxel produced on the surface of a 3D hydrogel, about 1 cm from the base (right) of the cuvette. (B) Plot of fluorescence intensity over distance across a line for the cuvette, in the line indicated on the left panel. The baseline fluorescence intensity across the cuvette increases around the central point.*

Post-UV treatment, fluorescence intensity was no longer detectable, indicating that the UV light was affecting either tfLime itself, tdFAST2, or the binding of the two (Fig. 3.6). Therefore, UV treatment was ruled out as a method to make the hydrogel more transparent, and the presence of cells in the 3D volume was noted as a limitation in imaging.

With this limitation in mind, I wanted to assess the possibility of visualising the centre of the cell-laden hydrogel. I designed a two-part experiment to test the possibility to optogenetically activate and visualise cells in the centre of the cuvette, but not in a *bona fide* 3D optogenetically inducible system. In the first part, I injected 20µl of blue food dye into a 1% agarose-only hydrogel, and visualised it, indicating that a) injecting into the hydrogel was possible, and b) that the hydrogel itself could be visualised in 3D (Fig.3.7.B)

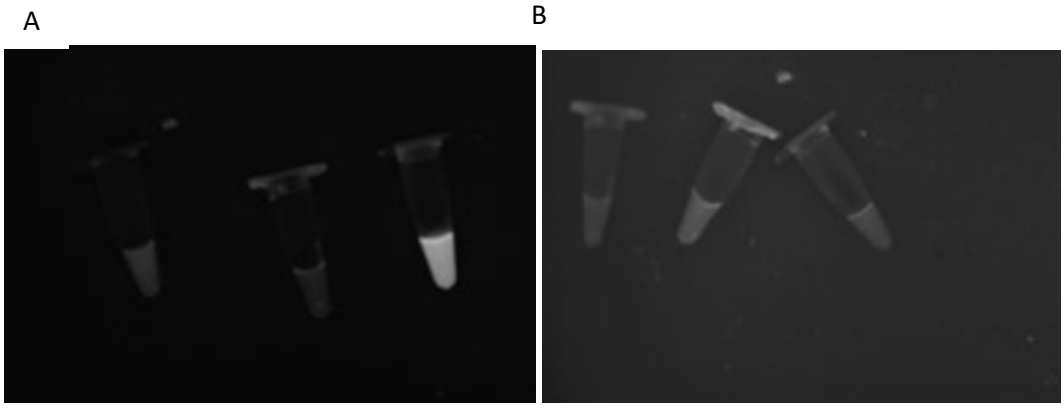


Figure 3.6: *Inactivation of tfLime by UV light. A) 3 containers are visible. From left to right, these contain: Cells with no tfLime in liquid M9-glucose, M9-glucose with tfLime and no cells, and cells with tfLime in M9 glucose. Cells were incubated at 37C for 3 hours. B) The three containers after a 20 minute exposure to UV light. Any fluorescence intensity in the tube containing tfLime + cells disappeared following exposure to UV light.*

As a second part of this experiment, I prepared a hydrogel with M9-glucose, agarose and cells, but without tfLime, and used it to fill a cuvette, therefore creating a hydrogel with cells that would scatter light, but not be involved in increasing fluorescence intensity. After about 10 minutes, just before the hydrogel in the cuvette set, I injected into the centre of the volume 20 µm of the same hydrogel mixture but this time also containing tfLime. In this way, light illuminating the centre of the volume would activate cells in across the path of the light, but only the injected area in the centre, where tfLime was present, would be able to fluoresce. I put the whole cuvette in the fridge at 4 °C for 1 hour, and after solidification incubated the cuvette under 935 mW/m² green laser

illumination for 3 hours. After 3 hours, I could clearly see fluorescence in the illuminated area of the injected cells, but not in the surrounding areas of the hydrogel that did not have tfLime (Fig. 3.7.C). In addition, control cuvettes where either the injected cells were kept in the dark, or cells without tfLime were also injected, showed no detectable fluorescence.

These results indicated that it was possible to activate optogenetically equipped cells through a cell-laden hydrogel in the centre of the required volume, and that it was also possible to visualise them using the current equipment and setup, if the contrast is high with the surroundings. Therefore, the problem in correct visualisation was about ensuring contrast between the background and activated production.

The result of this experiment was not a true optogenetic activation of a voxel in 3D, as the volume through which the light passed to activate the cells was not capable to respond to optogenetics to achieve detectable fluorescence. Instead, this result was more similar to traditional, additive 3D bioprinting, where cells responsive to a stimulus were localised in a 3D location through an injection in a hydrogel, before applying the stimulus, in this case light, to activate them. What would make this 'true' 3D optogenetic bioprinting is if the cells were not placed in the specific location through injection, but were homogeneous in the volume, and localised gene expression was controlled through optogenetics.

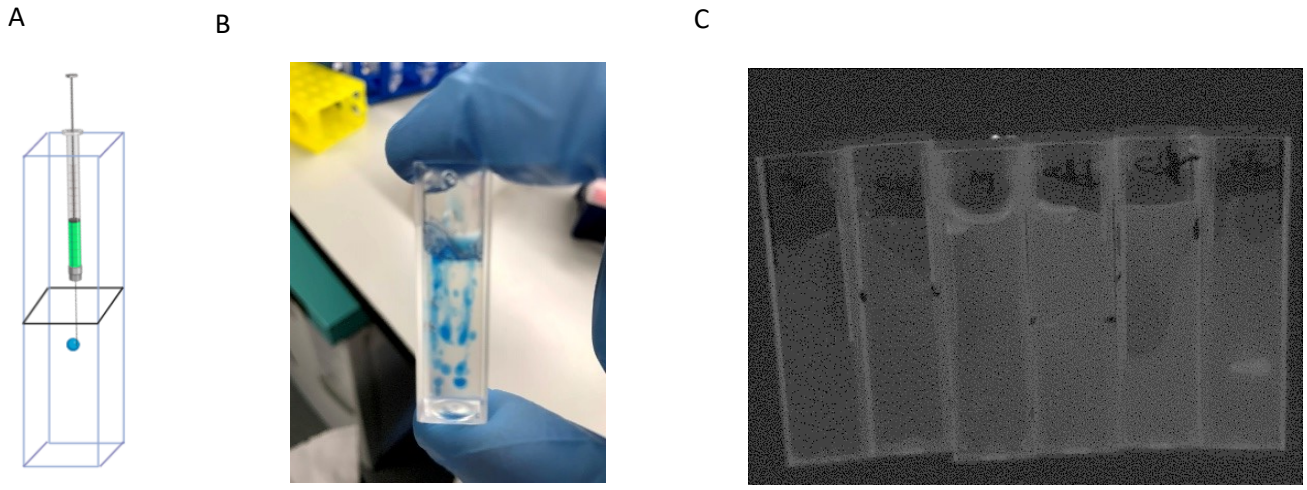


Figure 3.7: *(A) Method for injecting hydrogel into the already existing hydrogel. A Hamilton syringe was used to measure 20 µl of liquid, and then inserted into already existing hydrogel that has been sitting for 5 minutes so that it is not completely set. (B) Multiple injections of agarose containing 10% blue food dye into a 2% agarose gel to test its feasibility. (C) Testing of injecting cells into a cuvette. From left to right: 2 cuvettes of pure agarose hydrogel. A cuvette of agarose with M9-glucose. A cuvette containing cells with no tfLime. A cuvette with cells with no tfLime, with cells injected, in darkness. A cuvette with cells with no tfLime, with cells injected, illuminated with 300 mW/m² green light. All cuvettes were incubated for 5 hours.*

In this section, I investigated possibilities to improve the visualisation of gene expression inside a 3D hydrogel. I attempted killing the cells with UV post-print, which led to also bleaching the fluorophore. For this reason, I performed an experiment where cells were injected in the middle of the hydrogel, and selectively induced with green light, verifying that it was possible to visualise gene expression in the centre of the hydrogel.

3.2.4 Improving the visualisation and printing equipment

While I was able to visualise cells in 3D inside the hydrogel, there were still limitations in the imaging and printing equipment used. On the illumination equipment side, the current illumination setup involved the whole platform being placed in a dark room incubator, with temperature controlled at 37 °C. Ideally, an optogenetic setup would be self-contained, with all the equipment enclosed in a dark box with a 37 °C chamber for the samples, while the lasers would be outside the temperature chamber, to prevent overheating and maintain a constant intensity.

On the imaging side, the gel camera used (BioRad Chemidoc) produced variable image intensities between different repeats, with repeat imaging for the same experiment sometimes varying by almost 2x, raising the need for a more specialised gel imaging equipment. In addition, visualisation became more complicated because of the presence of laser beams and background gene expression. Visualising the gel from outside could be done in one of two directions, either in the direction of the green laser beam, or perpendicular to it. If visualising in the direction of the beam, a voxel would be observed, making it hard to understand the depth at which production would be observed. Similarly, when visualising perpendicular to the beam, the depth and production would be distorted by scattering, masking the exact pattern of production by the background.

3.2.4.1 Improvement of imaging through a gel slicer and a gel scanner

Addressing the imaging point first, I decided that in order to be able to analyse images throughout the volume of the cuvette, it was necessary to observe the gel from a direction that did not interfere with the direction of the beam. This was very hard to do in a non-invasive way, and instead, the most realistic tactic seemed to slice the gel longitudinally to obtain spatial slices across the z axis (Fig. 3.8). In this way, individual slices of hydrogel could be viewed from above, not interfering either with the direction of illumination or with hydrogel. Slices where fluorescence was observed could then be summed in order to get a quantifiable image of the voxels produced in a 3-dimensional reconstruction. These slices would ideally be thinner than the diameter of the laser beam, to enable visualisation through the smallest volume of hydrogel, and summation of fluorescence intensity from many slices to reconstruct the voxels printed.

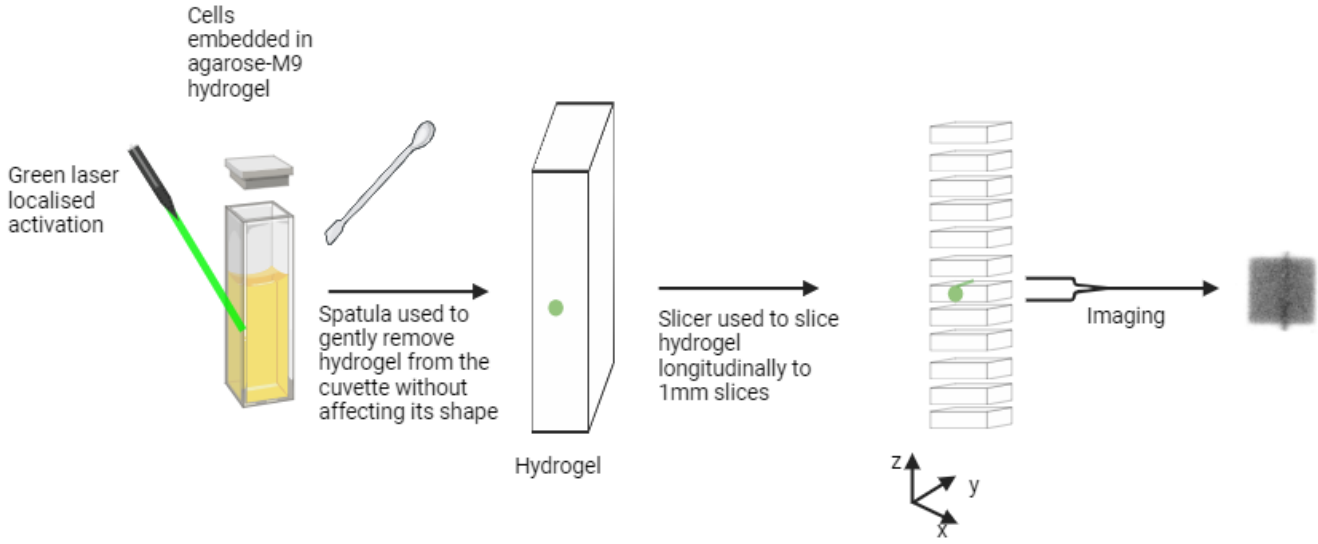


Figure 3.8: *Method for slicing the hydrogel in a longitudinal fashion. Post printing, the hydrogel is cooled down to 4C for at least 1 hour. Then a steel spatula is pressed against the walls of the cuvette to remove the hydrogel without damaging it. Then, the hydrogel, is either imaged whole, or sliced to thin longitudinal slices along the z axis, which are then imaged on a Gel scanner.*

As a first iteration of generating slices, a cryotome (NX70 Cryostat, Epredia, UK) was considered. Briefly, this involved embedding the samples in Tissue TEK OCT medium (Agar Scientific, UK), before using the cryotome at a temperature of -100 °C to generate to slices of 80 µm thickness, which were placed on charged microscope slides (Materials and Methods 7.2.3). In order to practice this technique, using the cryotome was initially attempted with pure agarose hydrogel poured in round containers of 8 mm diameter. This was done because the round containers had a smaller cross-section than the square cuvettes, making them easier to embed in the OCT fluid and slice. However, it was very hard to place the slices on the microscope slides without destroying their structure, as the slices were too thin and the agarose crystallised at low temperatures, leading to folds and cracks (Fig. 3.9).

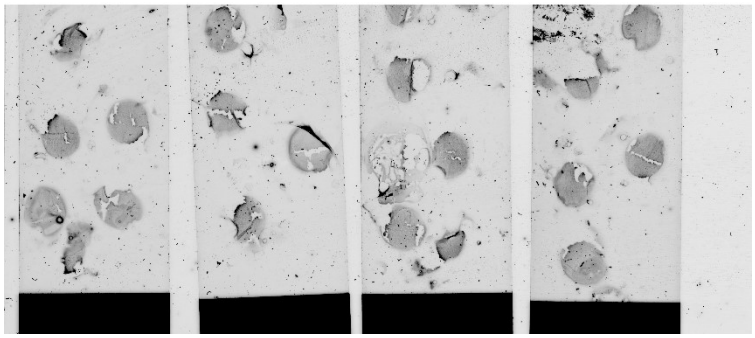


Figure 3.9: *Images of slices obtained using an NX70 cryotome, and round containers for the hydrogels. It was not possible to ensure consistent placing of the slices on the microscope slides. In addition, the process of using the cryotome to slice the samples deforms the slices, making it impossible to maintain the solid structure.*

As a slicing alternative, it was necessary to use a method which would preserve the structure of the slices, perhaps through thicker slices sliced at room temperature. We decided to design and 3D print our own custom gel slicer, with the requirements of being able to slice a hydrogel at room temperature, and produce thicker slices of a consistent thickness of 1 mm as a starting point (Fig. 3.10). The slicer was designed using CAD and 3D printed by Borut Lampret, following setting up the specifications for its functions. The slicer consisted of two separate parts and essentially worked similar to a manual guillotine: the first part was a base with an area where the hydrogel would fit, together with a movable platform to move the sliced hydrogel forward. The base also included a trough that could accept the blade, and another trough that could accept a microscope slide. The second separate part of the slicer was a blade, together with guides to make it fit on a consistent spot on the base. The resulting slicer was able to cut consistent slices to 1 mm +– 0.2 mm thickness, which was thick enough for the slices to maintain their consistency, but also thin enough to allow a 3D reconstruction of the cuvette (Materials and Methods 7.2.3).

In addition to developing the slicer, I also improved imaging by acquiring access to a gel scanner (Amersham Typhoon, UK), which could excite a fluorophore in specific wavelengths, and have standardised gains which could be changed to alter sensitivity and give consistent results.

3.2.4.2 Improvement of illumination through a custom rig

With having a way to image the hydrogel in a more repeatable way, the next step in obtaining consistent quantitative images was to also improve the illumination hardware. In terms of setup, lasers were immobilised in a 3D supported platform, with a network of filters and focusing mechanisms, allowing control of the temperature, and accurate laser intensity over the time of the

print (Materials and Methods 7.2.2). Briefly, it consisted of a movable platform and a system to focus lasers with the required intensity, controlled through a computer programme. Cuvettes could be placed on a platform in a temperature-controlled chamber, while the whole setup was enclosed in a box, to ensure darkness without the requirement for a dark room. The lasers were also changed, using a number of filters and lasers in order to give the ability to give a variety of intensities of red and green light. The green beam used could be approximated with a Gaussian distribution, and the $1/e^2$ diameter of the laser was calculated at 1.1 and 1.12 mm in the y and z directions respectively. In the presence of samples incubated after 3 hours, scattering was also quantified, which made the $1/e^2$ value of the green beam 1.52mm and 1.32 mm at the y and z directions respectively, with the standard distribution curves having wide tails of 1% - 5% intensity to the beam.

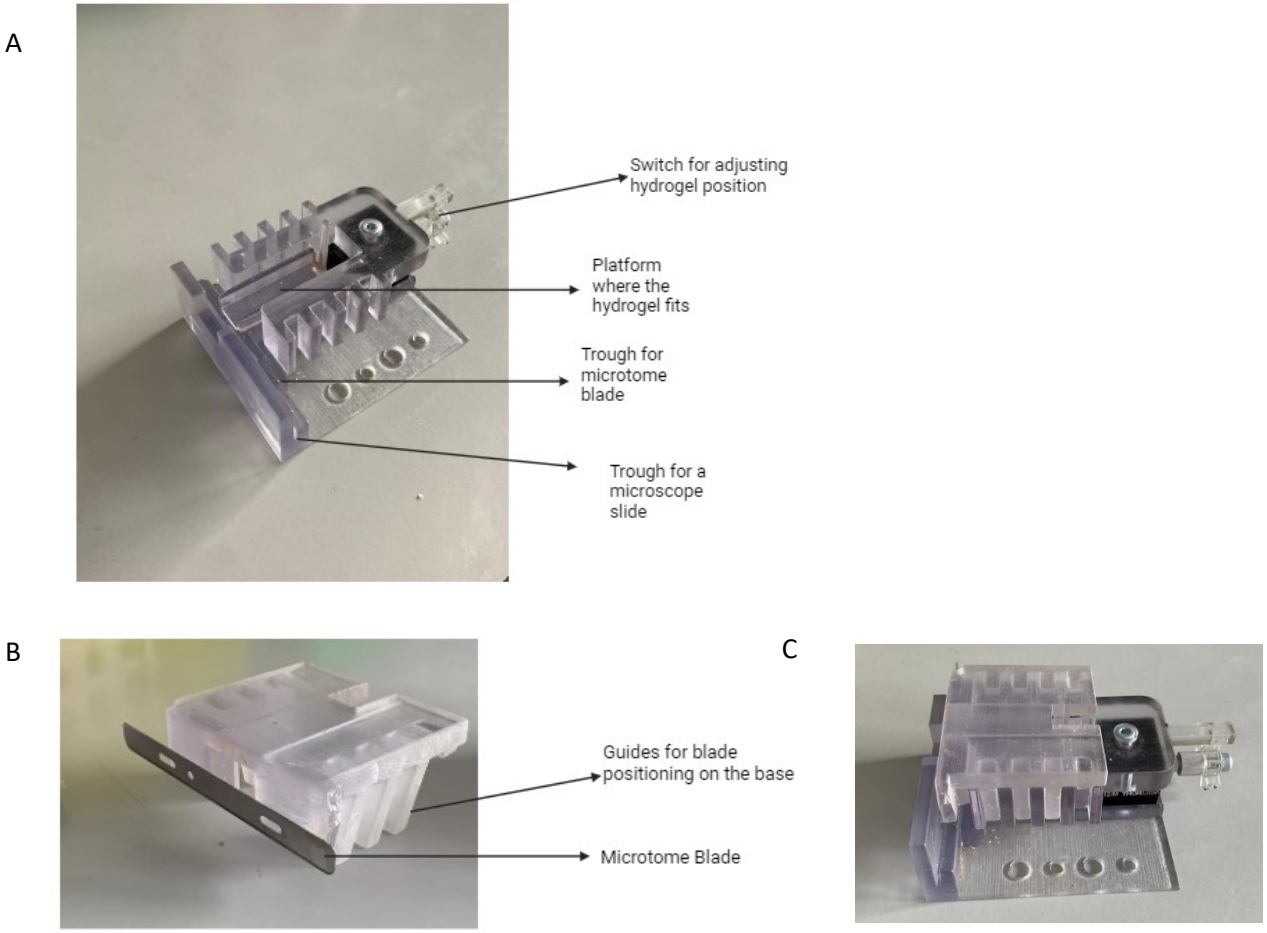


Figure 3.10: *The gel slicer. (A) The base of the slicer, which includes a rolling base for the hydrogel to apply, a switch to move the hydrogel in position in steps of 0.1 mm, and two troughs, one to fit the slicing blade and another to fit the microscope slide on which the slice was deposited. (B) the top part of the slicer, consisting a blade supported by guides to ensure correct and consistent positioning of the blade in relation to the base of the slicer. (C) The assembled slicer, with the blade fitting on top of the base.*

Using the new printing set up, the Typhoon gel scanner and the custom slicer, it was possible to obtain much more accurate prints and images. Fig. 3.11 (A) shows as an example 3 hydrogels imaged in the gel scanner: Media, a sample kept in darkness and a sample illuminated for 3 hours using the new setup by two green lasers, at 300 mW/m^2. Clearly, the depth of the dot could not be distinguished by just looking at the whole cuvette. In (B), the same sample was sliced, indicating the ability to properly image samples using the custom slicer. In this case, the light was enough to go through the whole cuvette in a straight beam (top two slices in the second slide from the right).

Overall in this section, I set about to improve the illumination and visualisation equipment, in order to obtain better quantitative results before attempting to control expression in 3D. We built a better illumination rig with controlled temperature and automated movements of the lasers, a slicer to be able to visualise the hydrogel in 3D, and obtained access to a sensitive gel scanner.

3.2.5 Shotgun experiments for 3D controlled production

3.2.5.1 3D Controlled production: Crossed lasers

Once the printing and imaging procedures were standardised, I decided to start attempting ways to produce a voxel in the centre of the cuvette in a 'shotgun' manner, using only green light, in order to cover as many methods as possible. This was done to allow me to quickly understand the capabilities and limitations of the optogenetic system, illumination and imaging methods in 3D, before fully characterising expression.

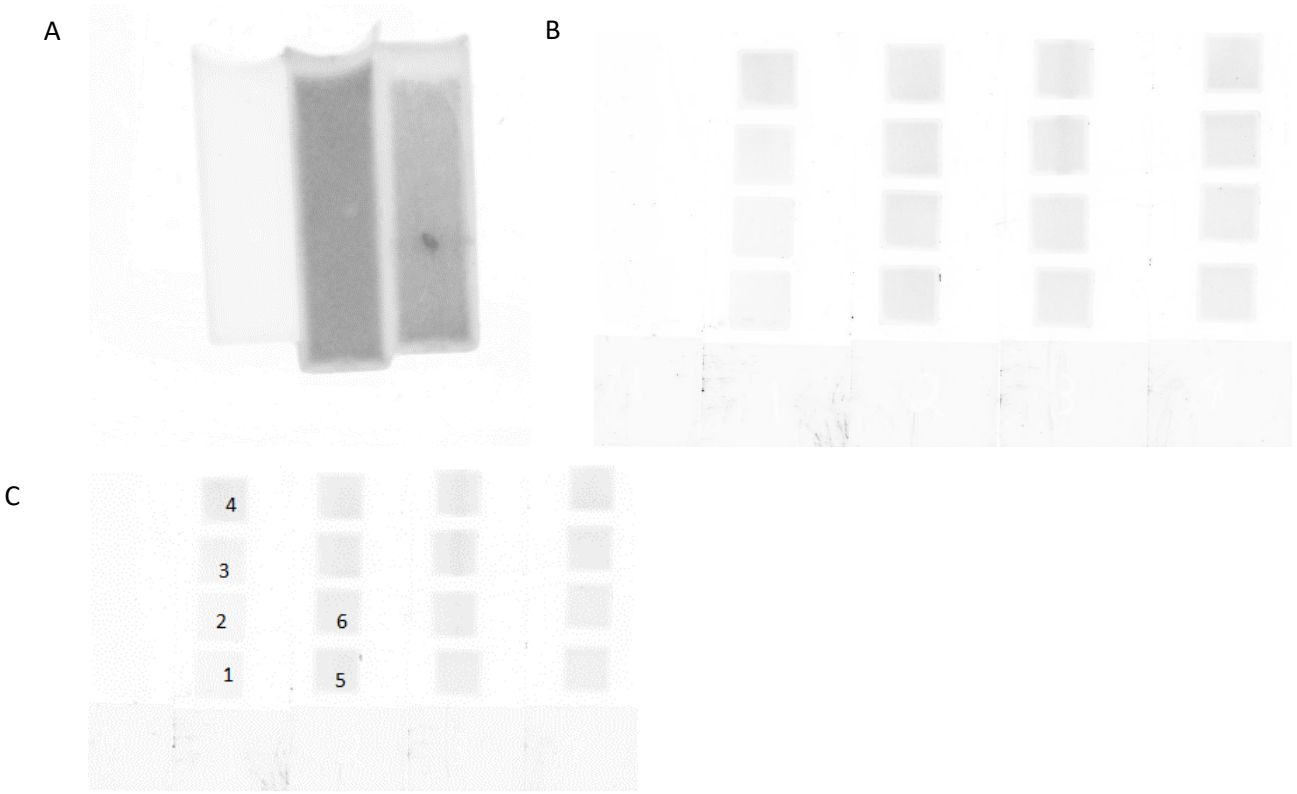


Figure 3.11: *Examples of samples obtained with the new set up and imaging equipment. (A) whole cuvette imaging, indicating how the new equipment generates images with a much better contrast and image quantification possibilities than previous methods. (B) slices, consistent in size and thickness obtained from the gel slicer. (C) The first six slices numbered from top in the cuvette (1) to progressively lower. The left most slide corresponds to slices of the medium, and the other slides correspond to ordered slices from top to bottom of the cuvette. The bottom slice on the left-most slide is the highest point imaged, and the top slice on the same slide is 3 slices below it, therefore ~3 mm lower. The slice immediately below that one is the bottom slice on the second from left slide, and so on.*

To this end, I devised two very different illumination regimes. The methods that I attempted both revolved around ensuring that the centre of the hydrogel would be illuminated with a higher green intensity than the surrounding areas. Because of the scattering of the hydrogel, it would not be possible to physically focus the laser to the centre of the hydrogel with very high precision. Instead, the two methods worked around this by either rotating the hydrogel, or using multiple beams of green light.

These methods were attempted using steady illumination for 3 hours, as this was the time found where the cells would show the least scattering effects, while still having grown from the initial OD700. As per the results in Chapter 2, it was found that cells in the cuvette would reach an OD700

of about 0.05 after 3 hours, which was low enough to allow the light to pass through without significant scattering.

The first method involved green light being supplied to the hydrogel using two orthogonal lasers. If the intensity of each of the beams was low enough, it should not be enough to activate gene expression in the edges of the hydrogel; instead, where the beams meet in the centre, the light energy reaching cells in that position should be enough to activate gene expression (Fig. 3.12).

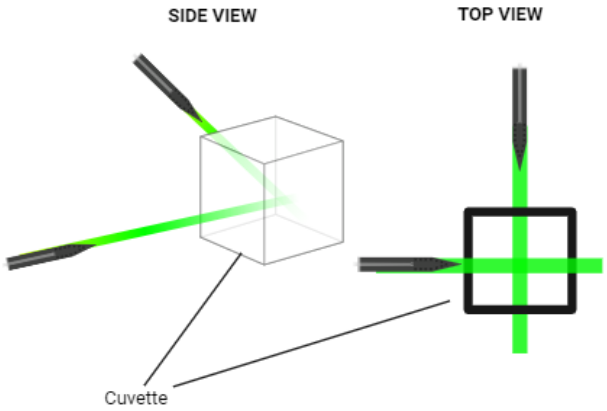


Figure 3.12: *Side and top view of the crossed lasers illumination scheme, from the side view on the left, and a top view on the right. If the intensities of the lasers are low enough, the combination of activation in the middle should lead to a visible voxel in the centre of the cuvette.*

I performed these experiments using a constant intensity of 300 mW/m^2 for each of the lasers, over a continuous illumination time of 3 hours. Results were analysed using both the gel camera and the Typhoon gel scanner, enabling a comparison between the two and showcasing the possibilities of the new imaging method (Fig. 3.13).

First, looking at the whole hydrogel images from both the camera and gel scanner, the importance of looking at gene expression in slices becomes apparent, in order to decipher a 3D image of gene expression. Secondly, the contrast was much more pronounced in looking at gel scanner images vs camera images, as shown by plots of fluorescence intensity across the distance of the surface of the hydrogel. This was also true for images of individual slices (Fig. 3.14).

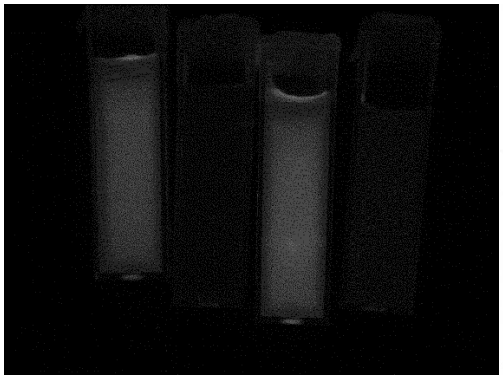
In terms of gene expression and fluorescence intensity, in all images, gene expression along the paths of both laser beams could be seen entering and leaving the hydrogel, indicating that scattering was not enough to deflect the laser beams. However, the fact that fluorescence intensity could be

observed across the full path of the laser beams indicates that the intensity of the beams was already high enough to reach the threshold for gene expression. As a result, saturation in gene expression was already high along the path of each of the laser beams, and therefore their combination did not lead to a single voxel in the centre of the hydrogel.

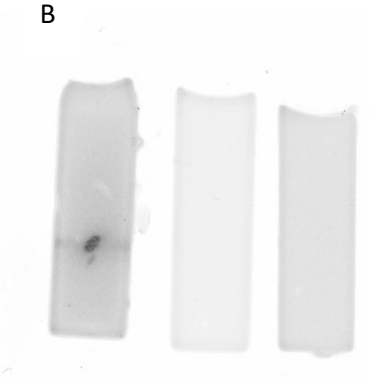
In all gel scanner images, some graininess was observed, indicating that it has something to do with the imaging method. The origin of the graininess in the gel scanner images is unclear. Each pixel in the whole gel images represents an area of 0.001 mm^3 with a depth of 10 mm. At OD700 of 0.005, this volume would represent around 3.2 $x10^5$ cells in the beginning of the experiment, and $1x10^8$ cells in the end. These are sufficiently large numbers to ensure homogeneity in the mixture, so it is more likely that the pattern observed is caused by cells and the hydrogel diffracting incident light in the gel scanner. It is not due to scattering of the incident light during the experiment, however, as this pattern is also observed in locations which had been left in the dark.

In the whole hydrogel images, a 'halo' was seen in the edges of the cuvette, which is sometimes more pronounced than others, and also present in images of individual slices (Fig. 3.14). The origin of this halo effect is also unclear, although it is hypothesised to have something to do with an interplay between the hydrogel, media, cells and tfLime interacting with the edges of the cuvette. This effect was seen on slices not containing cells as well as those containing cells, and it is likely to do with some sort of physical and chemical interaction of a solid hydrogel with the cuvette walls, perhaps enabling some laminar flow on the interface between the walls.

A



B



C

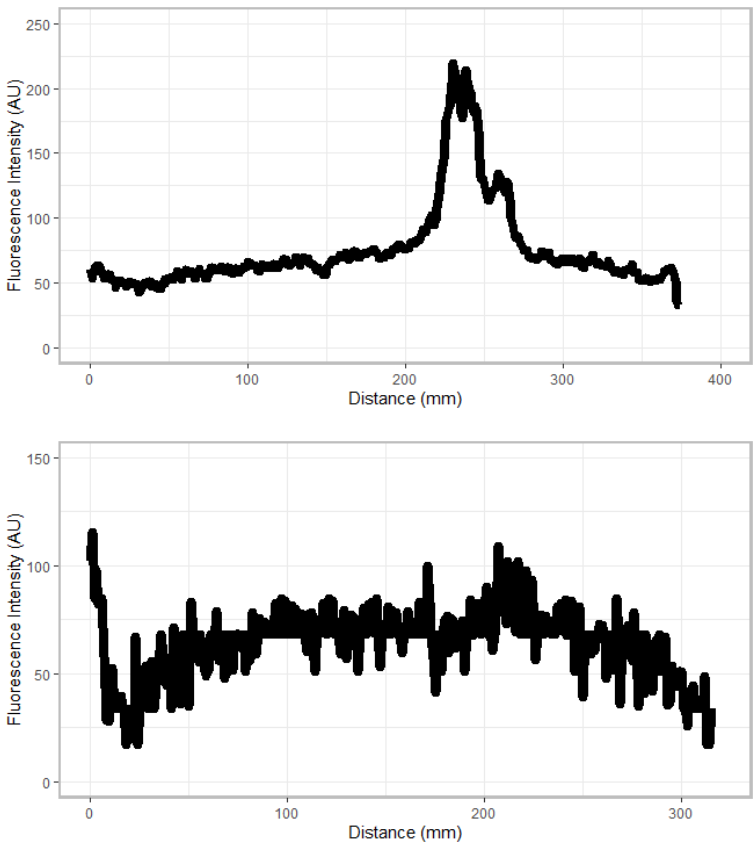


Figure 3.13: *Images of the results of crossed print, both in the camera scanner and gel scanner (A) Gel camera image. From left to right: cuvette left in the dark, cells without dye, cells illuminated, Media. (B) Gel scanner images of a similar print. From left to right: Iluminated cuvette, media and cuvette in darkness (C) Plot profiles for the gel scanner image, followed by plot profile for the camera scanner results, across the length of the hydrogel in images displayed in (A) and (B). Contrast with the camera is barely distinguishable, while the gel scanner gave 200% increase in fluorescence.*

A B

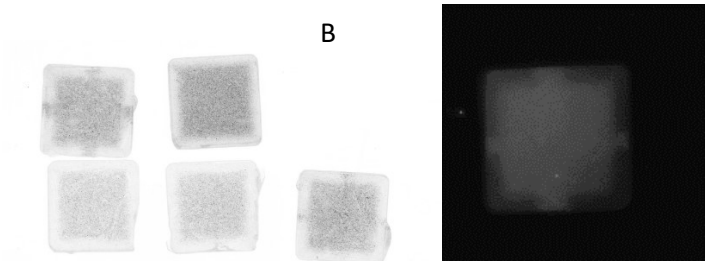


Figure 3.14: *Selected raw images from cuvettes illuminated with crossed laser beams. (A) Imaging of the slices with the gel scanner, showing high contrast in the images. (B) A slice imaged through the gel camera, which was much harder to quantify.*

The origin of the halo effect was briefly investigated using food dye on a 2% pure agarose hydrogel. 1 ml of dye was poured on top of the solid hydrogel and left to diffuse down for 5 hours. The dye appeared to progress about 12 mm into the hydrogel after 5 hours. However, interestingly, when the top part of the hydrogel was sliced to 1mm slices, it appeared that the majority of the dye was diffusing from the edges of the hydrogel, indicating the possibility of flow at the interface between the cuvette walls and the hydrogel (Fig. 3.15).

A B

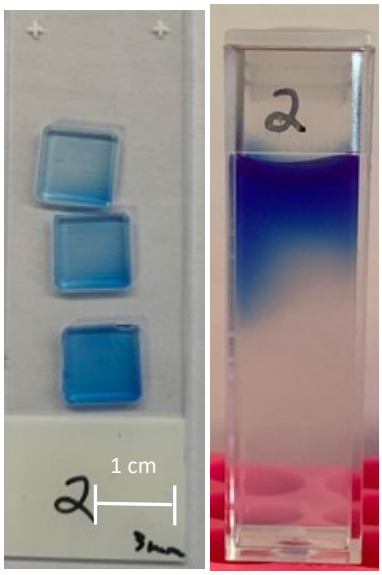


Figure 3.15: *Indication of a possible explanation for the halo effect. 1 ml of food dye was placed on 2% agarose hydrogel and left to diffuse over 5 hours, before slicing the hydrogel and taking photos of the slices. The slices show that the majority of diffusion happens in the sides of the cuvette, possibly due to some surface effects and laminar flow between the edge of the hydrogel and the walls of the cuvette.*

3.2.5.2 3D-controlled production: Rotation

In order to try and dissect the pattern seen when using crossed lasers (Fig. 3.14), a second strategy of illumination was attempted. In this strategy, the hydrogel-containing cuvette would be rotated so that at each point in time, a different position would be illuminated at the edge of the hydrogel. At the same time, the centre of the cuvette would be illuminated continuously. In that way, the radiant exposure of each position at the edge of the cuvette would be reduced, while keeping the same radiant exposure in the middle. If the intensity in the edge would drop below the threshold while the intensity in the middle was above the threshold, this would mean that activation would only be observed in the centre.

This experiment was performed with the same intensity of green light as before (300 mW/m^2), but with a 360° rotation of the sample every 15 minutes. As in a growing population, dilution would have an effect on the ratio of active photoreceptors, it was thought that this would reduce the radiant exposure below the threshold, enough to see effective contrast between the edges of the hydrogel and the centre which would receive continuous illumination.

This experiment was first performed with square cuvettes, and the result was a band of fluorescence on the surface of the cuvette, with no fluorescence in the middle (Fig. 3.16). Therefore, I decided to try this experiment with the cylindrical containers too, as the rotation of the cylindrical containers would allow for more accurate illumination of the centre without diffraction of the light. Still, imaging showed that while a band of activation appeared on the surface of the hydrogel, there was no dot of activation in the middle. This could either be due to scattering of light, or failure to induce enough activation for a visible contrast. Moreover, despite being less pronounced, a small halo effect still appeared on the surface of the hydrogel, indicating that interactions between the components of the hydrogel mix and any surface was possible to give this halo effect.

A

B

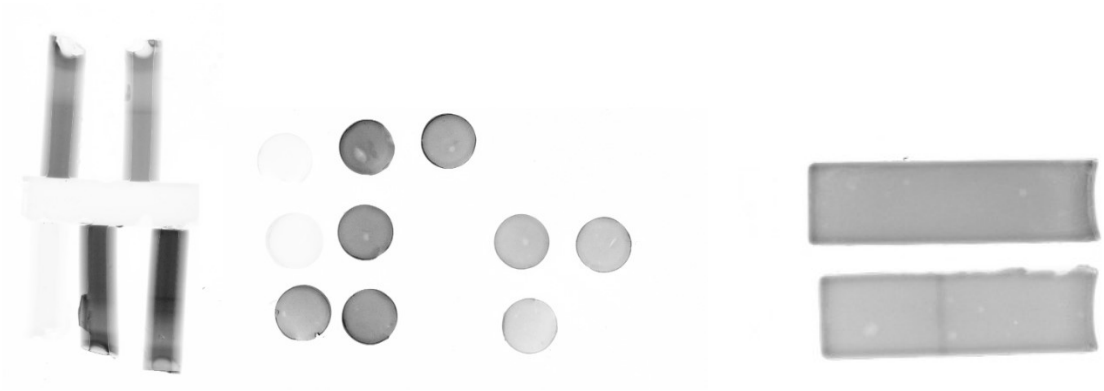


Figure 3.16: *Images of whole hydrogel and slices for the rotation setup (A) printing using a circular container. Whole hydrogel images show a 'band of activation. Looking at individual slices, however, there is no distinguishable activation in the centre of the cuvette. The 5 illuminated slices look darker than the others. (B) Print using a square cuvette. From top to bottom, hydrogel kept in darkness, and hydrogel illuminated with 3-hour illumination and rotation. Only the imaging from the outside of the cuvette is shown as there was no noticeable difference in expression in the middle.*

In this section I used two shotgun approaches to activate gene expression in the centre of the hydrogel, rotation of the hydrogel and illumination with crossed green lasers. In both cases, the entry and exit points of the laser beams were visible, indicating the sensitivity of the system to very low intensities of green light.

3.2.6 Characterisation of a line of gene expression across the hydrogel

The shotgun attempts to activate a voxel in the centre of the hydrogel were not successful, but informed my knowledge in that even low intensities of green light could achieve high activation, while giving information about the halo effect and its possible origins, as well as the graininess of the images observed. To build up on this, I took a more methodical approach in the characterisation of the light intensities that are required to perform 3D bioprinting. This characterisation was done with square cuvettes again, going back to the principle of a single laser in different intensities, but this time with the necessary slicing and imaging equipment in place.

I tried different intensities of light, ranging from 0 to 1.1 W/m^2, in an attempt to cover a large range of intensities. In addition to continuous 3-hour illumination, a second experiment was devised for

this characterisation. Since it was observed that cell growth was limited and the number of cells was low in the beginning of the print (Fig. 2.3), I hypothesised that cells would be unresponsive during this time, and that the bulk of production happened during the latter two hours. Therefore, the second experiment was devised where green light illumination was only applied for the latter two hours of the print. The 'line' attempted was produced in the middle of the hydrogel, 5mm from the bottom, and the hydrogel was sliced to 1 mm slices for purposes of imaging (Fig. 3.17).

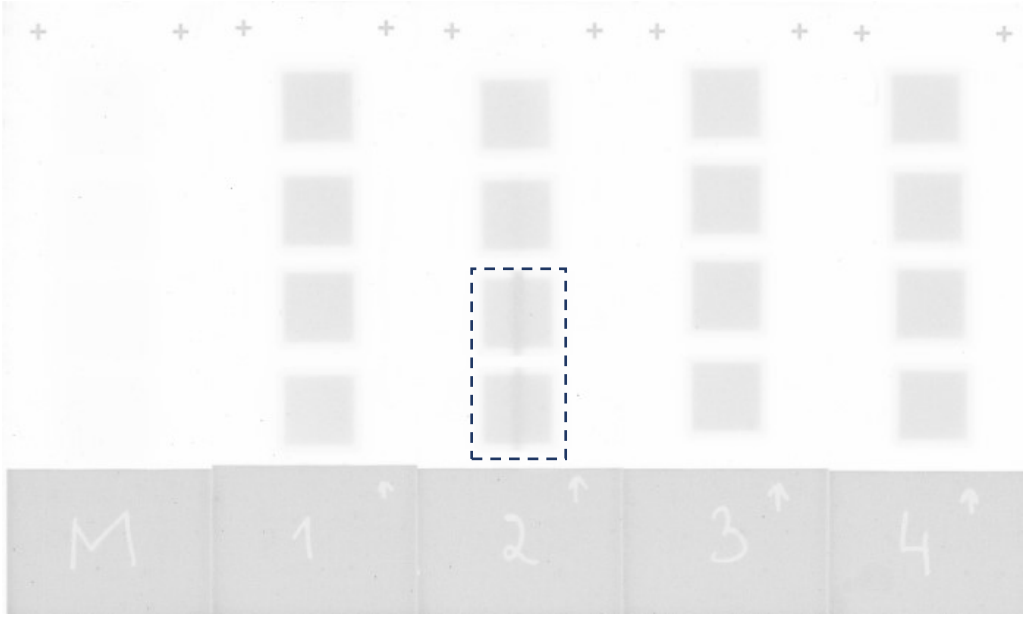


Figure 3.17: *Raw data of printing. Green light intensity = 1.1 W/m². On the left, labelled M, a slide containing 4 slices of a cuvette containing only hydrogel medium with tfLime but no cells. Then labelled 1-4, slides containing slices from the vicinity of the printing area, with the bottom slice in slide 1 representing the highest point, and the top slice in slide 4 representing the lowest point. The slices corresponding to illuminated regions are encased in a dashed-line box. Green light direction was from bottom to top.*

The raw data (Fig. 3.17) indicates the format in which data was obtained in these experiments. Essentially, about 5 microscope slides were cut for each experiment, with 4 slices each. The first one was cut from a control hydrogel containing only the media and tfLime, while the rest were cut to correspond to a rough region of 16 mm around the illuminated area, including areas both above and below it, according to (Fig. 3.12 C). Even in the raw data, a line can be clearly seen on the slices corresponding to the illuminated region. More than one slices show production, as the slicing was not always exactly identical to the position of illumination, and depending on the intensities used, the beam was wider or thinner.

The raw data was analysed individually for each experiment. Briefly, the intensity of each pixel (each pixel corresponding to a 100 μm² square) was recorded in a matrix. The background (medium only) average fluorescence was also recorded, by measuring the average fluorescence intensity in the medium only slices, excluding any halo observed. Background average intensity was subtracted from the slices measured. The fluorescence intensity was then plotted in a heatmap with colours corresponding to each intensity and squares corresponding to each pixel. In addition, fluorescence intensity across the path of the green light beam was plotted (Fig. 3.18).

In the raw data, the direction of the green laser beam came from bottom to top. The analysed slices displayed here, however, were rotated so the beam from left to right, with the line being thickest at the entry point and constantly becoming thinner. The fluorescence intensity values varied between different slices in the same experiment, which received illumination by the same laser, due to the location of physical slicing of the hydrogel, and due to the Gaussian nature of the beam, which meant that likely not one slice contained all the activated cells. For example, one slice might correspond to 75% of the activated area, while another slice only 20%. In addition, the centre of the Gaussian beam was expected to give the highest fluorescence intensity, therefore slices that do not correspond to the centre of the illuminated area will have lower intensity.

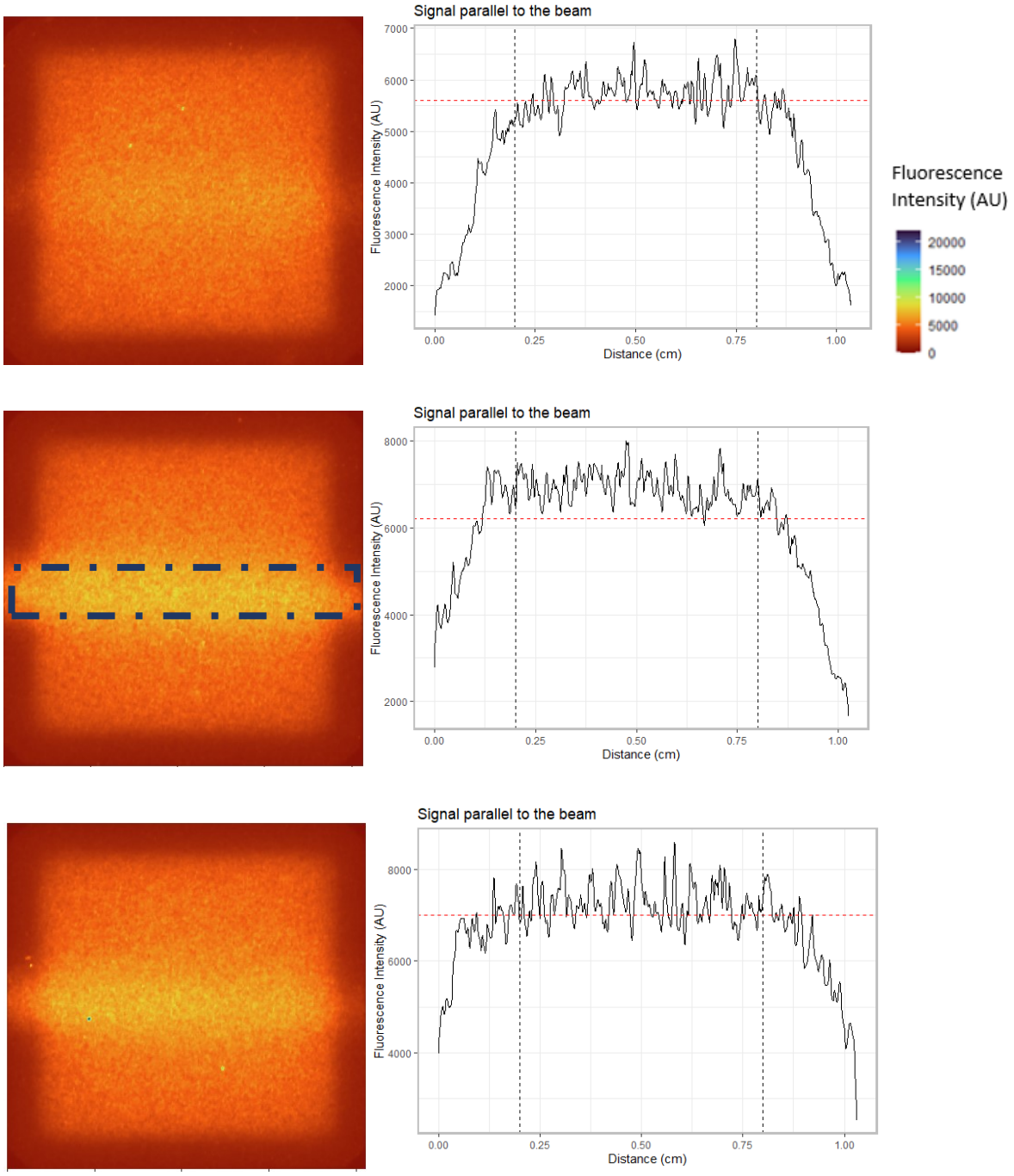


Figure 3.18: *Analysed individual slices and values parallel to the beam. In red dotted line indicates the average fluorescence excluding the halo, while the vertical dotted lines indicate the distances outside of the halo. The area on the slices across which the averages to plot the profiles were taken is indicated in the second slice, as a rectangle across the width of the slice, with a 1 mm thickness.*

The halo effect was very apparent in some slices, contributing to a distance of about 2 mm at the borders where fluorescence intensity rapidly falls. The graininess in the image is also apparent, with fluctuations in the intensities across the beam which can reach up to 15% of the fluorescence

intensity. Excluding the halo, fluorescence intensity across the beam was constant for each individual slice, suggesting the ability of the light to pass through without significant scattering.

In order to obtain a full picture of gene expression in a particular experiment, fluorescence values for all activated slices were then added together to create a sum (Fig. 3.19), over the different green intensities used. The halo effect appeared very defined and prominent, with a consistent width of about 2 mm. In experiments where there was illumination from the beginning of experiment, which are the first row, the contrast of halo and fluorescence intensity appeared stronger than in experiments were there was no illumination for the first hour. Generally, as illumination intensity was increased, the intensity of the resulting line increased too. However, even at the lowest intensities, the laser was strong enough to form a line of increased fluorescence all through the length of the cuvette.

This is explained by the fact that even a low green light intensity should be enough to convert the majority of photoreceptors to the active state, with strong hysteresis and slow reversal. Any dilution of photoreceptors would occur due to cell growth and production of new ground state photoreceptors (Olson et al., 2017). Because of this effect, and the prominence of the line at all points throughout the hydrogel volume, it would be hard to print a dot in the middle through the overlap of multiple beams or rotation of the cuvette, unless the intensity of the beam was so low, that scattering would become a significant limiting factor. In addition, the crossing of beams would make it hard to scale the printing of a dot to printing shapes, as it would lead to overlaps between the beams at different spatial and temporal points, making precise activation of only a desired location impossible.

Because of the nature of the laser, which was applied as a Gaussian beam, the line observed was thicker for higher intensities of light, and surpassed 2 mm for some experiments. To assess the thickness of the activated area in the line, the fluorescence profile perpendicular to the green light beam was calculated, through taking an average across the length of the slice, but over a larger area of obtaining values at each point than in Fig. 3.18, as the width of the rectangle was not limited by the width of the activated region (Fig. 3.20). While intensity and contrast of the line relative to the background was variable, the width of the beam increased from about 1 mm to more than 3.5 mm on the highest green intensity, owing to the Gaussian effects discussed above. Interestingly, values perpendicular to the beam were much more consistent and showed less variation than values across the beam. This is likely because of the larger available points of sampling perpendicular to the beam, while for parallel to the beam samples are limited to the width of the line.

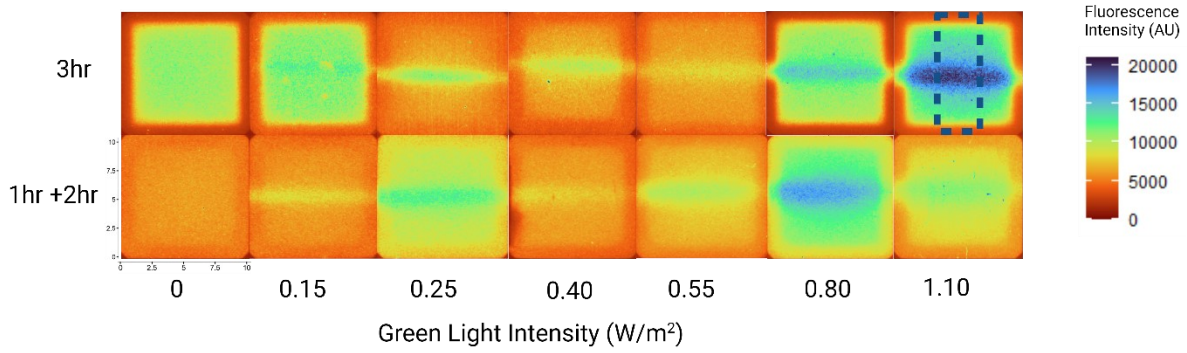


Figure 3.19: *Printing of a line across the cuvette using only green light. Each individual square here is a sum of 2-4 1mm slices. Each for each slice, the background production is subtracted (excluding the halo) and fluorescence is normalised to maximum fluorescence. The area across which averages were taken to plot profiles in Fig. 3.20 is shown in the top right slice, as a rectangle across the length of the slice, with a 4 mm thickness.*

Because the fluorescence intensities were not normalised to actual fluorescence values, it was hard to compare contrast between different experiments, where values differed largely. For this reason, I decided to normalise fluorescence intensity against the highest fluorescence value in each slice (Fig. 3.21). This essentially rescaled all images to a common scale between zero to 1 and allows easy comparison, but was prone to bias from extremely high values, or debris in the imaging. The results indicate that, again, variations in contrast existed between different experiments and intensities used, but all experiments show a distinguishable line, even in the lower intensity.

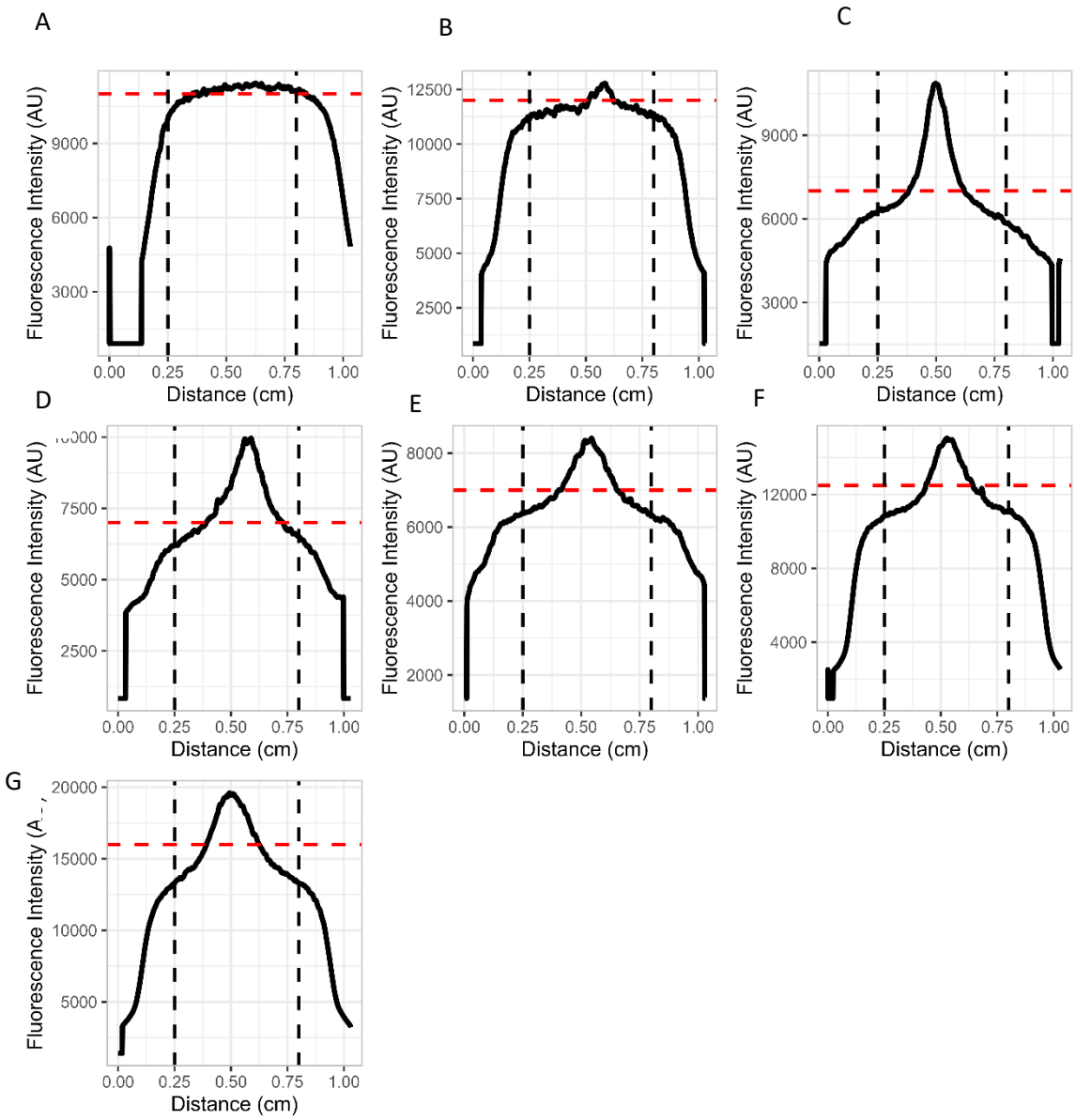


Figure 3.20: *Plot of fluorescence intensity perpendicular to the green Beam.While intensity varies, the width of the beam, for 3 hours continuous illumination. From (A) to (G): Green light at 0, 0.15, 0.25, 0.4, 0.55, 0.8, 1.1 W/m². The vertical lines represent the areas of activation, excluding the halo effect. The red horizontal line corresponds to the mean of the activated area. As light intensity was increased, the width of the peak of the activated area also increased.*

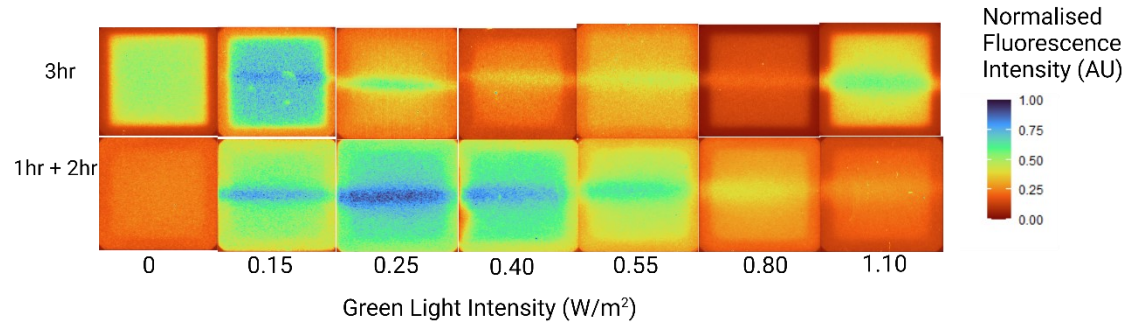


Figure 3.21: *Normalised fluorescence for sums of analysed slices, for different green intensities. Normalisation is performed by dividing each file by the maximum fluorescence value.*

In this section, I took a methodical approach to inducing gene expression in the hydrogel, by illuminating the cuvette with different intensities of green to characterise the formation of a line of gene expression in the hydrogel. I also showed how no illumination in the first hour of incubation, where growth was slower, gave very similar results to illumination for the whole time of incubation.

3.2.7 Combining red and green light to control gene expression in a voxel

The characterisation of printing using only one green laser beam indicated for the first time quantitively how light intensity affected production in a 3D volume. Low intensities could effect activation across the whole hydrogel, and the Gaussian shape of the beam affected the width of the printed volume. These observations, combined with the sensitivity of the system to low light intensities, ruled out activating a single voxel through only using green light. Because of the activation throughout the hydrogel with a single green laser, in order to achieve a voxel, with crossed beams or without, what was necessary from a theoretical perspective was to reduce the activation on the 'tail' of the green laser beam, and be left with a voxel only in the centre.

Due to the choice of CCaSR 3.0 and the ability of red light to inhibit production, it would be possible to apply red light to areas surrounding the voxel where printing is required. Essentially, red light acts to revert active photoreceptors to the inactive state, reducing the rate of gene expression. Building from the results on Chapter 2, it was understood that in order for red light to inhibit gene expression induced by green light under continuous illumination, the red light intensity should be more than 3x higher than that of the green light. In addition, in order to print using red light, it was required to design a beam of red light that would illuminate all areas of a cuvette apart from the centre. This was made by Borut Lampret using a square beam and a beam splitter, which allowed a

light setup as in Fig. 3.22 (Materials & Methods 7.2.2). The red laser was a rectangular beam with a thickness of 2.3 mm in the z axis, and a 2x2.3 mm gap in the middle. Red light intensity was constant in the edges, with 7% of the light intensity in the edges still able to be observed in the centre of the beam, where darkness was desired (7% bleed through).

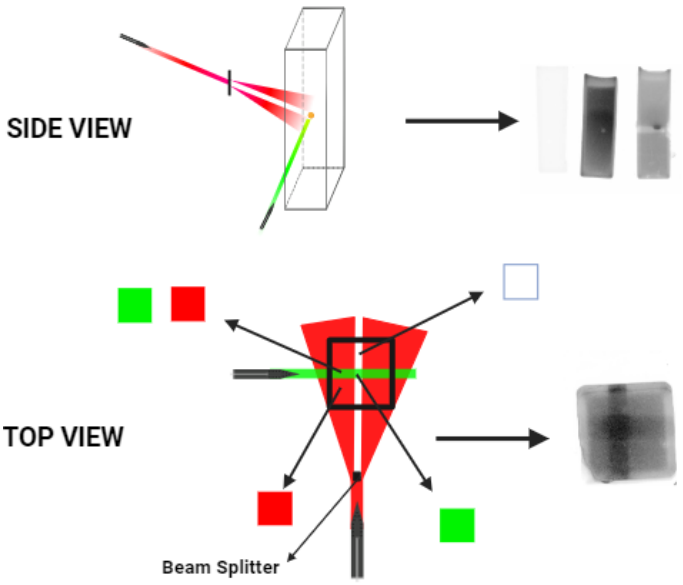


Figure 3.22: *Schematic of the beam in simultaneous red and green illumination, indicating the top and side view of the proposed illumination setup. In the side view, whole cuvette are shown where the rightmost cuvette was activated using 0.8 mW/m² green light, and inactivated with 1.1W/m² red light. The activation point is visible, as well as inactivation from the red light. other cuvettes from left to right are media, and a cuvette incubated in darkness. In the top view, a slice from the same cuvette is shown, indicating the regions where relative activation is expected to be observed, either due to the green light or lack of red light.*

This setup employed perpendicular red and green lights, with the red beam split in order to create a gap of no illumination in its middle. As a result, this protocol generated 4 distinct areas in the illuminated slice. First, there is an area where there is no illumination, as it corresponds to the gap in the red and green beams. In this area expression would be equal to the background expression. Second, there is an area of only red illumination, leading to supressed expression below that of the background. Third, there is an area in the 'tails' of the green beam, where the red and green lasers overlap. Depending on the intensities of the two lasers, the resulting expression can in that area vary from full activation to full repression, but ideally would be similar to background fluorescence.

Finally, in the centre of the slice, there should be an area where there is no red illumination but only green, generating an activated voxel.

A similar characterisation as with the single green light was also performed combining green and red, with all the green intensities used in Fig.3. 19, and two different red light intensities, 1.45 and 2.9 W/m^2 (Fig. 3.23). In these figures, the green laser path was from left to right, while the red laser path was from bottom to top, as in Fig. 3.22. The first observations of this experiment were taken by looking at whole cuvettes, and indicate that even on the outside of the cuvette, red light caused a visible reduction in fluorescence intensity in the region where it was applied. However, in all conditions, in the sliced images a dot could be observed, indicating that while the exact quantifiable values were variable, the results of the print were consistent.

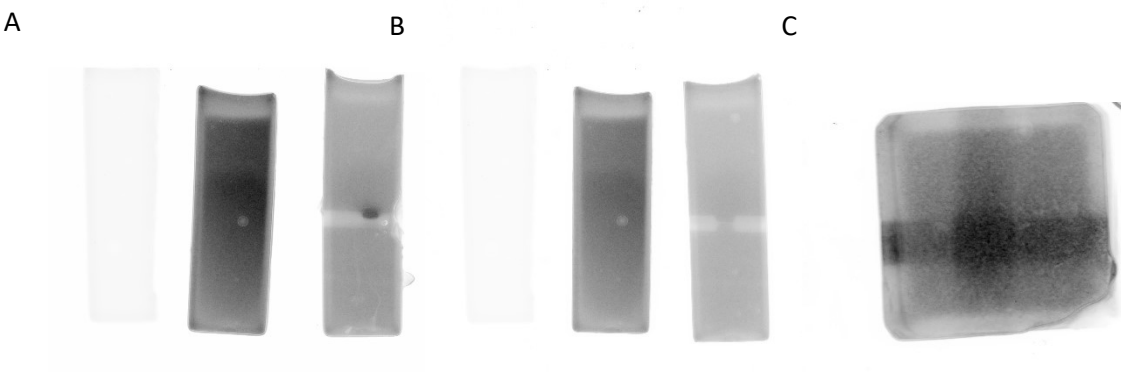


Figure 3.23: *(A-B) Full Hydrogel images of the cuvette with red light printing, imaged from the x and y direction (C) Relevant slice of raw data for printing using both green and red light.*

Following the images with whole hydrogel, the hydrogel was sliced and slices analysed (Fig. 3.24-3.26). For each red light intensity, first the non-normalised raw data is shown, followed by data normalised to a scale of 0-1. Data normalised to values from 0-1 still showed some bias depending on extreme values or debris present in the slices. Therefore, to avoid bias and to obtain the contrast of production compared to the background, 'contrasted' images are shown. These were generated by obtaining the mean of an area in the background of each slice, excluding the halo, and subtracting that mean from the fluorescence intensity in each slice. The values obtained were then divided by the same mean, to give fluorescence intensity in a range of 'fold change' compared to the background.

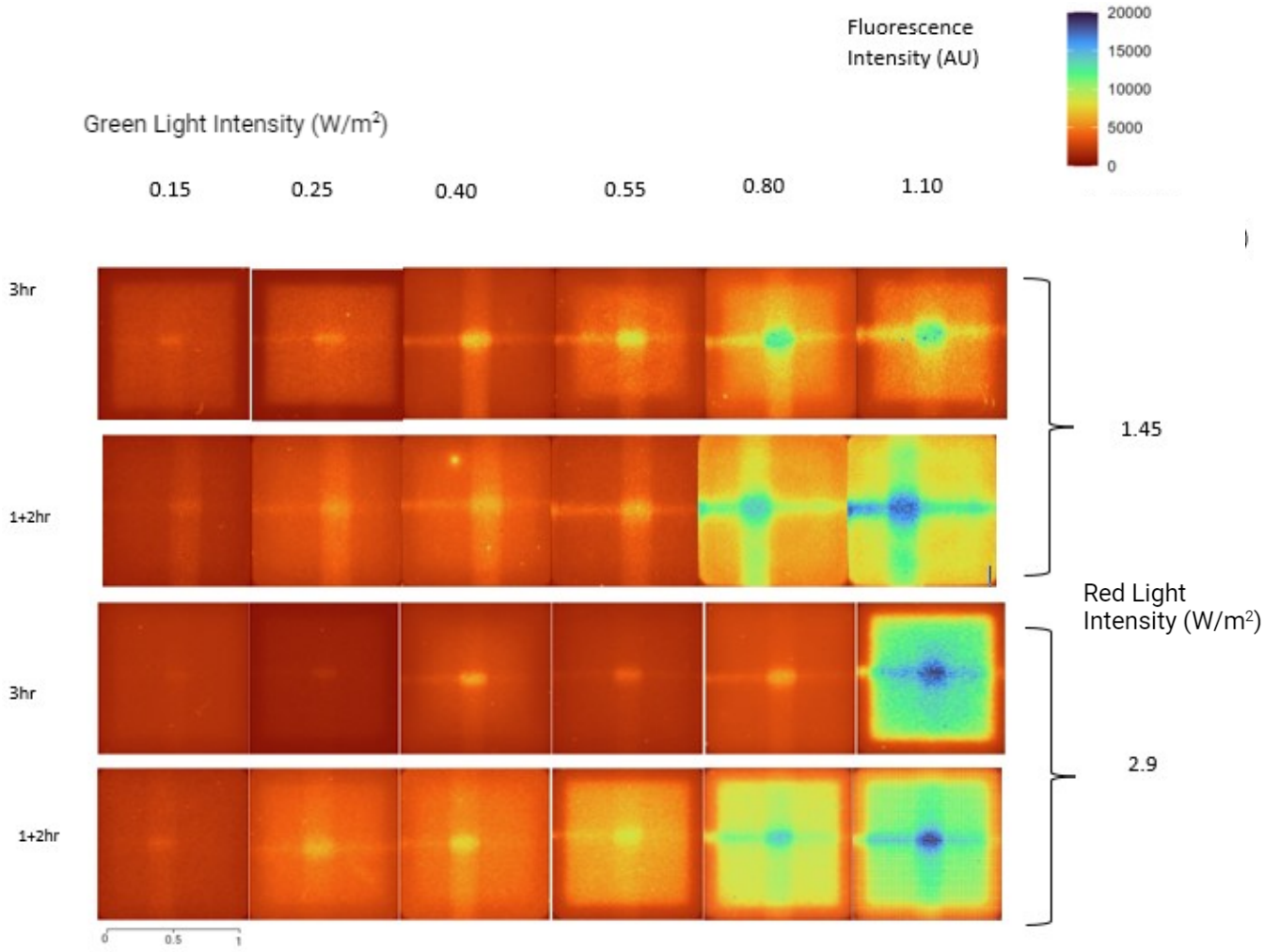


Figure 3.24: *Images of analysed fluorescence for sums of slices. (A) Unnormalised images. The top two rows are for red light at 1.45W/m², 3 hours conitnuous illumination and 1 hour in darkness followed by 2 hours of continuous illumination correspondingly. The next two rows are for 2.9W/m² red light. Green light intensity was increased from left to right. Each slice is 10mm x 10mm.*

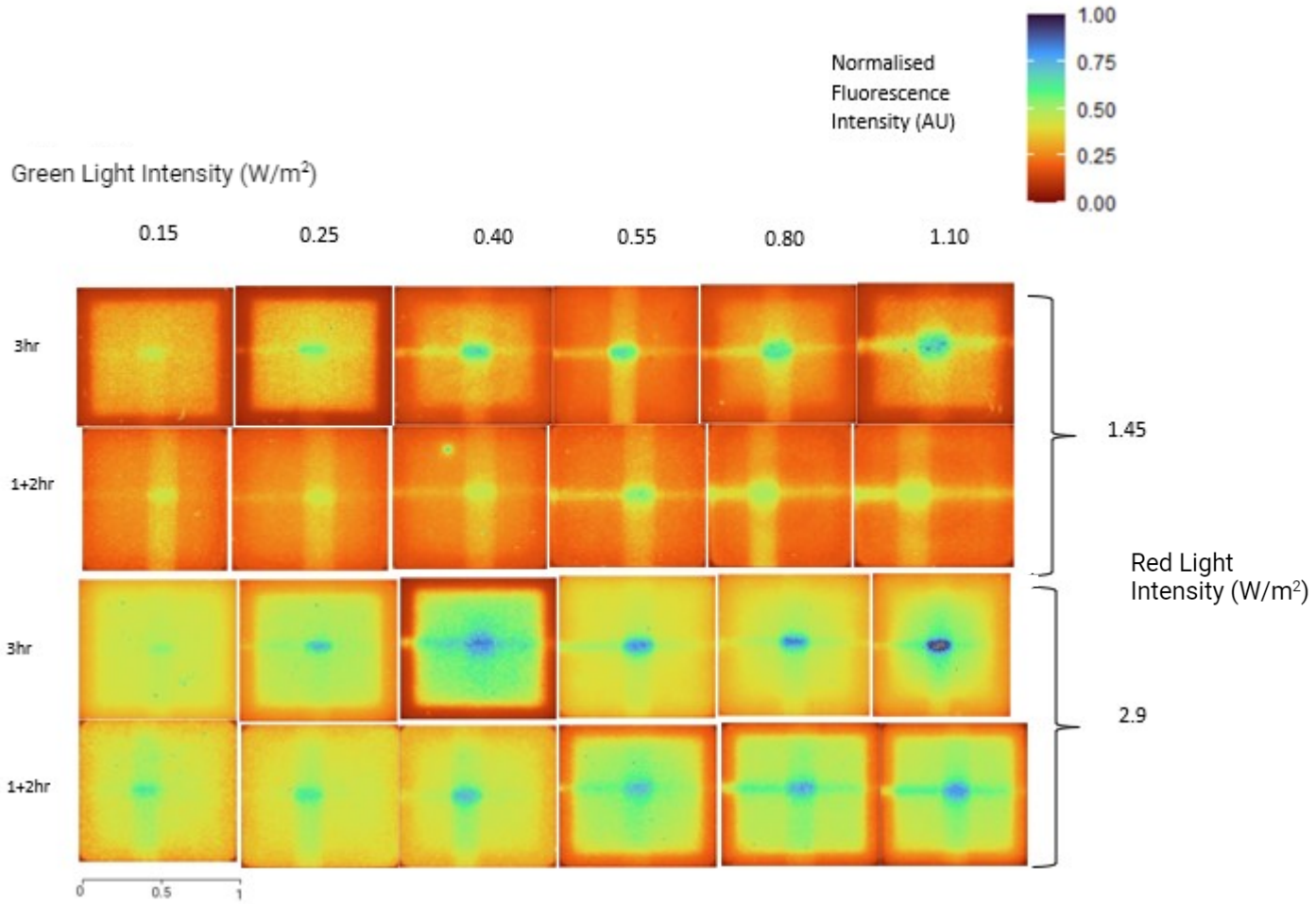


Figure 3.25: *Images of analysed production for the same sums of slices as Fig.3.24. Normalised images from the same slices, normalised against a scale of 0 to 1.*

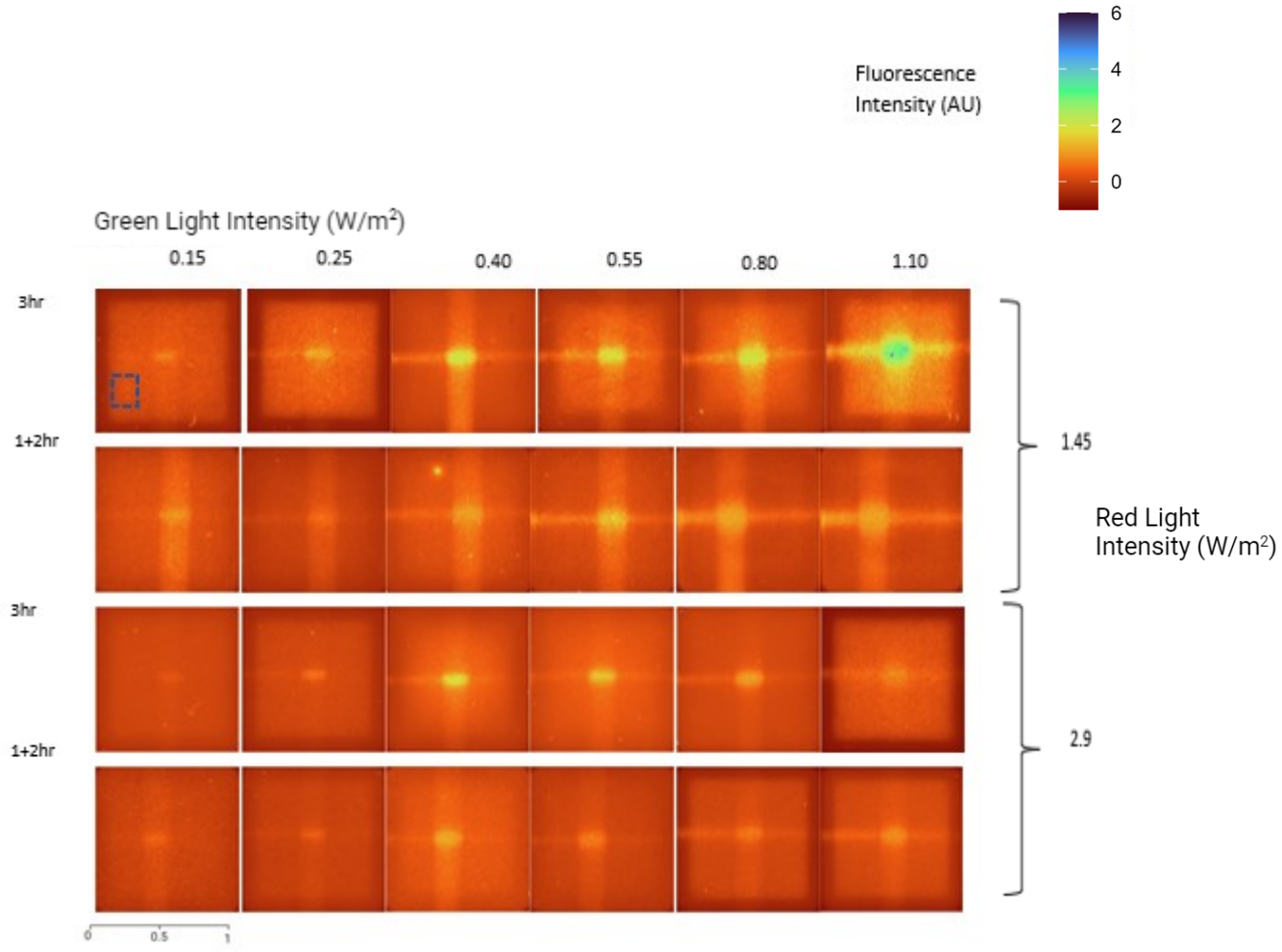


Figure 3.26: *Images of analysed fluorescence for the sums of same slices as Fig.3.24. The same slices, contrasted against the average of an area in the background of a slice (shown in the first slice with a dotted square.*

In the unnormalised data (Fig.3.24), a voxel where gene expression was activated becomes clearly visible in the centre of the slices for both illumination regimes and all combinations of light intensities. At lower green light intensities, the tails of the green light activation are supressed by the red light, while as the green light intensity increases, the thickness and intensity of the tails also increases. For example, for 1.45 W/m² red light, while at 0.15 W/m² green light essentially only a dot can be seen, at 1.1 W/m² a clear line can be seen, which is consistent with the fact that red light needs to be 3-5x the intensity of the green light to fully supress production. Despite differences in background between different experiments, the intensity and size of the activated voxel also generally increased as green light intensity is increased. In the higher red light intensity, there appears to be more overall suppression of the tails of activation on the green light path, but also

some bleed through suppression of production in the central voxel. There appeared to be no significant difference in the effects of continuous 3 hour illumination against 1 hour in the darkness and 2 hours of illumination (t-vaue=-6.57, p= 1.962).

The normalised data shows similar results, where it can clearly be seen how increasing the green light intensity increases the size and contrast of the activated voxel, while increasing the red light intensity acts to restrict the size of the activated voxel and reduce the gene expression in the tails, but had no effect in the intensity of the activated voxel. Red light acted on the tails by deactivating active photoreceptors, thus suppressing gene expression. It also acted in the edges of the activated voxel to suppress gene expression, and prevent the higher intensities of the green beam from causing a wider activated area. Bleed through was around 7%, which was not enough to reduce intensity in the centre of the activated voxel, under any light intensity.

The contrasted data, on the other hand, show similar result as the other two slices, but this time the background was normalised to the same level for all slices, removing differences in background between individual experiments. The area of background average is indicated on the top left slice with a dotted box.

In order to better understand gene expression along the direction of the red and green beams of light, normalised fluorescence intensity was calculated along the path of the green beam (1 x 10 mm), and along the area of no inhibition by red (2 x 10 mm). For each sum of slices, the average fluorescence intensity at each position in a line was calculated, and then fluorescence was normalised by dividing by the maximum fluorescence intensity in all the line, giving a value between 0 and 1. This indicates the level of background gene expression relative to maximum gene expression, as well as the shape of activation across both beams (Fig. 3.27).

For illumination across the path of the green light beam, results are presented for both 3hr continuous illumination and 1hr in darkness followed by 2 hours of illumination for the different intensities of red and green light (Fig. 3.28). As the line goes along the green path, it passes through areas of red illumination, which supress production, followed by the central position where there is only green illumination. The expression was noisy, probably owing to the grainy patterns observed in the images above. In all cases, a peak was observed in the middle, corresponding to the area where green light is not inhibited by red. Some peaks were more pronounced than others, but there is no specific trend of the height of the peak compared to background. This might be because of the

variability observed in the prints, as well as the relationship between red light inhibition and green light activation affecting gen expression in different ways.

For illumination across the path of the absence of red light (Fig.3.29), background fluorescence intensity under darkness was observed in the entry and exit points, whereas in the centre there should be activation due to green light. The results were much smoother compared to the green beam path, owing to the fact that cells in the majority of the volume were not exposed to light, and therefore could show a more consistent background response. As the green light intensity increased, the height of the peak relative to the background also increased. This was more pronounced in the lower red light intensity. I hypothesised that this was because of bleed through of red light at the higher intensity to the illuminated with green area, suppressing activation by the green. This phenomenon would have an oversize effect on when using stronger intensities of red light, therefore suppressing activation by green light.

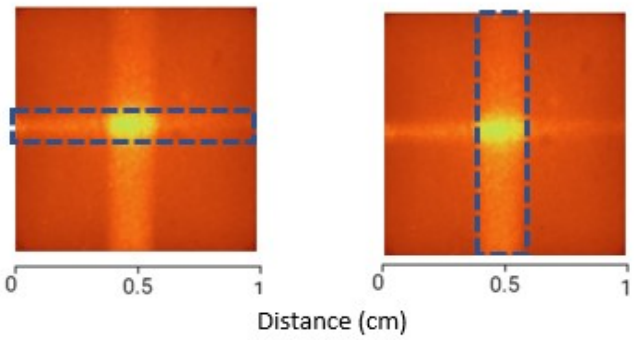


Figure 3.27: *From left to right, examples of the areas used for calculation of the light beam fluorescent values, across the green light path, and the direction of the red light, across the path of no inhibition by red correspondingly.*

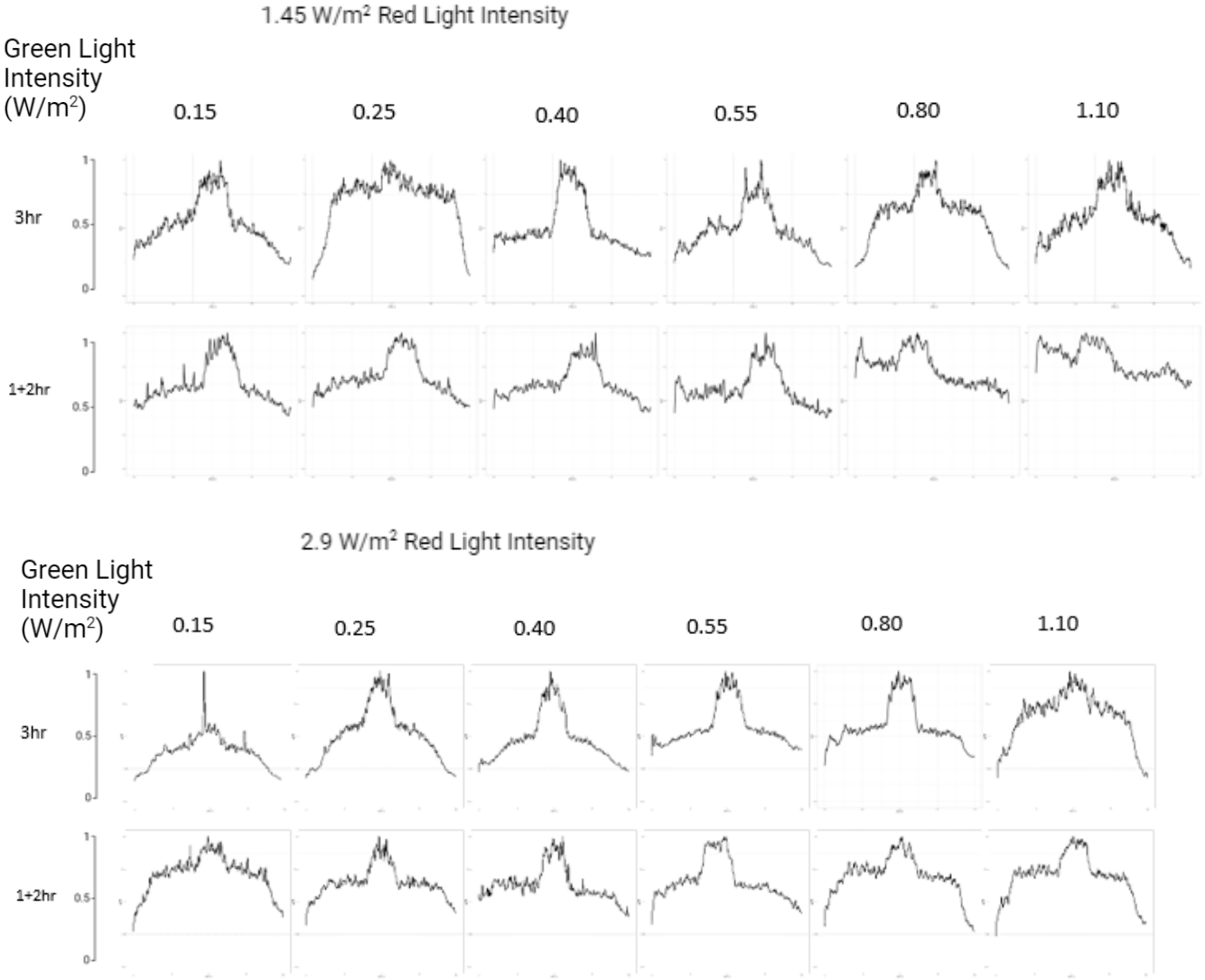


Figure 3.28: *Values across the beam of the green light beam, normalised in values from 0 to 1. First two rows correspond to red light of 1.15W/m² and the second two rows to red light of 2.9W/m².*

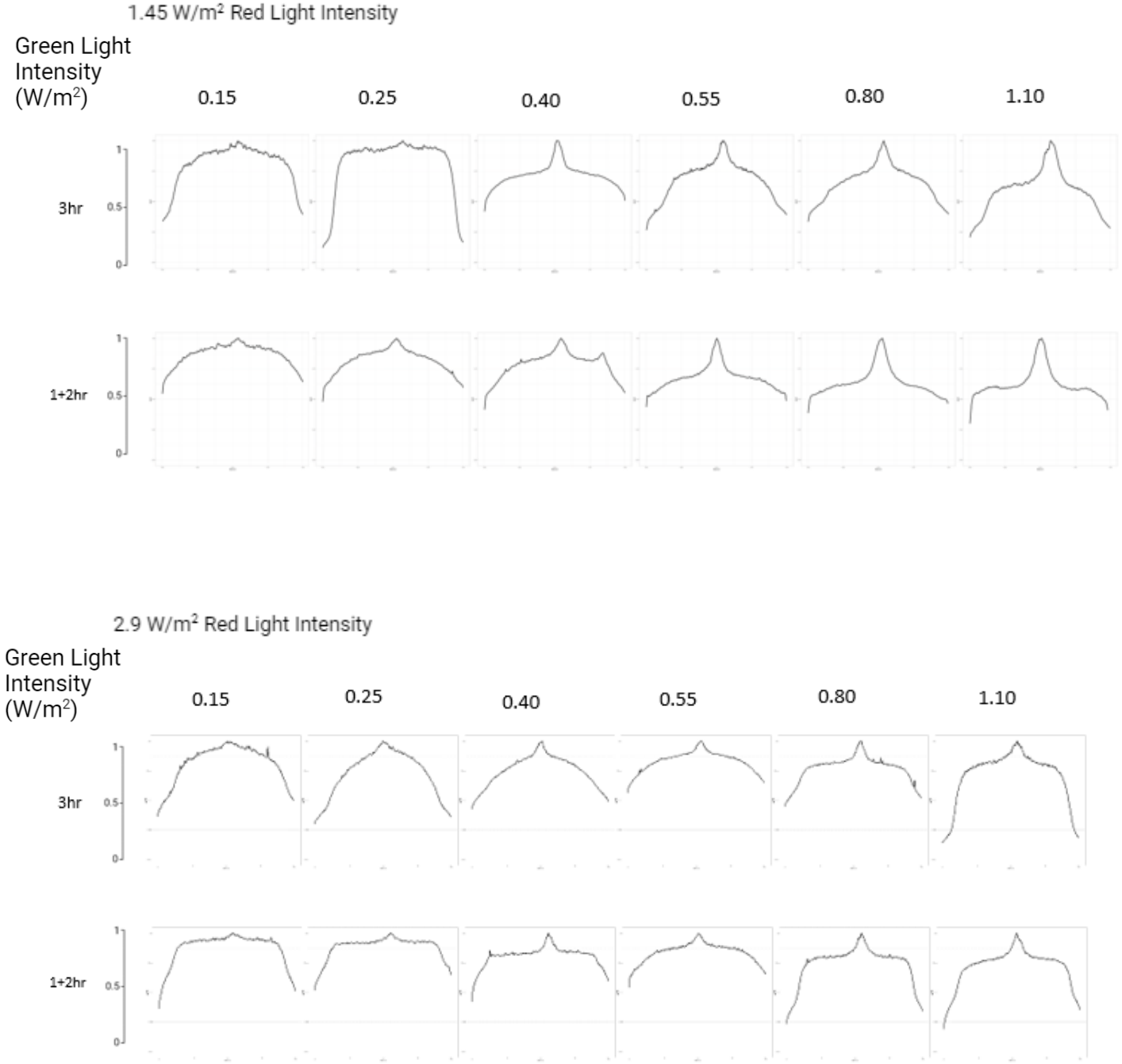


Figure 3.29: *Values across the area of no inhibition by red light, normalised in values from 0 to 1. First two rows correspond to red light of 1.15W/m² and the second two rows to red light of 2.9W/m².*

In this section, I used both red and green light to induce expression in the shape of a dot (voxel) in the centre of the hydrogel. I characterise tdFAST2 in this voxel over different intensities of the lasers, providing a proof of concept for optogenetically-induced 3D expression.

3.3 Conclusions

This chapter uses the knowledge, strains and conditions obtained and optimised in Chapter 2 to attempt control of tdFAST2 expression in 3 dimensions. First, I built an illumination platform based on lasers and the ability to move a cuvette to illuminate different positions. Then, I used this platform to achieve tdFAST2 production by the optogenetically-equipped cells under conditions optimised in Chapter 2, on a Petri dish. With these results in hand, I managed to achieve expression of tdFAST2 on the surface of a cuvette. The limitations in the consistency of the experiments and imaging at this point indicated that a more quantitative way of both optogenetically activating and imaging the results was needed. For this reason, I chose a new imaging machine, built a new optogenetics platform and developed a slicer to image individual positions in the hydrogel.

With this hardware and software established, I tried to achieve 3D expression of tdFAST2 in the centre of the cuvette with two 'shotgun' methods, in order to try and reveal the capabilities of the new system. Both methods were eventually unsuccessful, indicating limitations in the activation of the cells in 3 dimensions, a halo effect observed and the limits of scattering by the cells.

For these reasons, a more systematic approach to 3D production was taken. First, I characterised different intensities of green light on a 3D hydrogel, and built an analysis framework to compare between different experiments. Then, having understood the requirements and possibilities of the green light, I decided to combine green light for activation with red for inactivation around it, creating a voxel of activation only in the centre of the cuvette. I achieved a proof-of-concept optogenetic production in the centre of a cuvette using this technique, and characterised the behaviour of the cells under different red and green lights.

In this chapter the first proof of concept for real 3-dimensional optogenetically induced production is achieved, and a 3-dimensional, detailed characterisation of the system is performed. In the next chapters, I build upon this proof-of-concept by activating two or more voxels in the same area during the print time.

Chapter 4

Optogenetic control of gene expression using discontinuous illumination

4.1 Introduction

In the previous chapters, I investigated the possibility to achieve expression of *tdFAST2* by E.*coli* in a 3-dimensional location under the optogenetic control of CCaSR 3.0, in a 1% agarose-M9 glucose hydrogel matrix. I characterised the system in different continuous illumination conditions. Following this characterisation, I proceeded to induce *tdFAST2* expression in three dimensions, in the shape of a line, as well as a single voxel in the centre of the hydrogel.

In this chapter, I build on this proof-of-concept to move towards the printing of multiple voxels. To achieve this, I first tackle the need for non-continuous illumination. There is a limitation on printing time posed by the system, due to growth and background gene expression, with a ceiling set at 3 hours for tdFAST2. Therefore, in order to combine multiple voxels during this time, in a scalable and versatile way, the illumination equipment needs to move between these voxels during the print. As a result, gene expression needs to be induced without continuous illumination, with each voxel receiving light for a fraction of the duration of the print. I termed this illumination regime discontinuous illumination.

I start by aiming to understand the response of the optogenetic system to discontinuous illumination. I then use discontinuous illumination to achieve tdFAST2 expression in the form of a line in 4 different z-positions ('heights') in the hydrogel, followed by 4 voxels. In order to ensure maximum dynamic range throughout the print, I then modify the discontinuous illumination regime to do multiple passes of a single location, and attempt to print the z-axis voxels and lines using that approach too.

As accurate 3D gene expression in the form of a shape requires control in the z, x, and y-axes, I then moved on to identify 3 arbitrary voxel arrangements in the x/y plane, and 3 methods to achieve each arrangement. I characterise these methods, identifying an optimal method for this arrangement. Finally, with the ability to control voxel position in the x, y, and z-planes, I induce *tdFAST2* expression in a non-trivial shape, that of a double helix. In order to do that, I slice the helix into spatial and temporal segments that could be targeted for printing. I then show how a double helix could be produced using optogenetic activation in 3D, culminating the proof-of-concept in achieving 3D optogenetic control of bacterial production. In this chapter, the laser equipment operation and modelling to identify the necessary intensities of light and illumination durations was performed by Borut Lampret.

Objectives for Chapter 4:

1. Understand how the optogenetic system responds to non-continuous illumination
2. Use non-continuous illumination to activate *tdFAST2* expression in multiple z-position voxels in the centre of the cuvette
3. Optimise non-continuous illumination to account for cell division (periodic illumination)
4. Use optogenetics to activate *tdFAST2* expression in multiple voxels in the same z-position in the centre of the cuvette
5. Use optogenetics to control *tdFAST2* expression in a non-trivial 3D shape, as a proof of concept for optogenetically-enabled 3D bioprinting

4.2 Results and Discussion

4.2.1 Discontinuous illumination can increase contrast

From a theoretical standpoint, continuous illumination uses overlapping red and green light to create a region of activation and suppress gene expression in the entry and exit points of the green beam to shape the voxel. While that is effective in achieving a voxel in the centre of the cuvette, as seen in previous chapters red light needs to be at a much higher intensity than green in order to achieve suppression. At the same time, red bleed through into the green only area also affected gene expression by suppressing maximum gene expression and reducing the width of the activated voxels.

In modelling of the CCaSR system (Olson et al., 2017), gene expression is dependent upon the ratio of active to inactive photoreceptors present in the volume, with green and red light able to activate and deactivate photoreceptors accordingly.

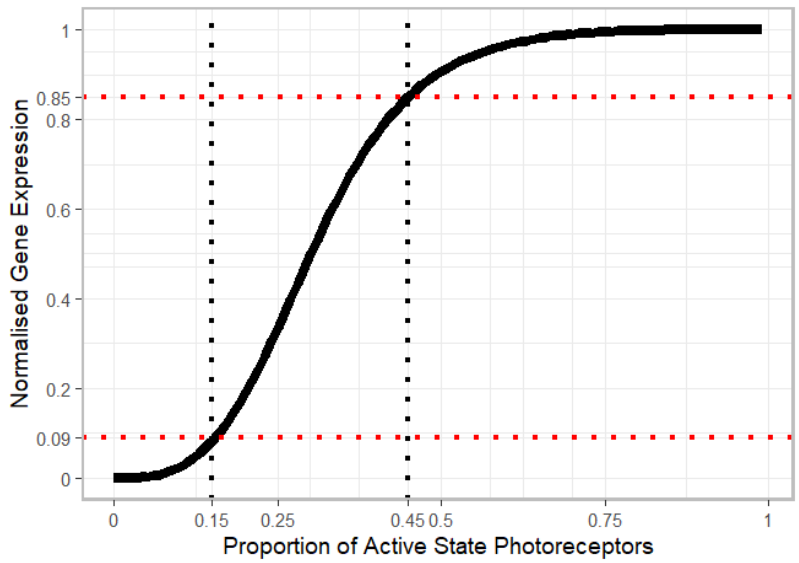


Figure 4.1: *Hill function of the proportion of active state photoreceptors against normalised gene expression. At 30% active photoreceptors gene expression is at 50%, while 45% active photoreceptors are enough to bring gene expression up to 85%, meaning it is not necessary to achieve extremely high proportions of active photoreceptors. Similarly, 15% active photoreceptors only lead to 9% gene expression.*

Conversion of active to inactive photoreceptors and vice versa, is highly dependent on the red and green light intensity correspondingly, according to equations 2.1 and 2.2. Furthermore, as the red light photoconversion rate is smaller than the corresponding green light rate, at the same intensity

of red and green light, activation of photoreceptors would happen at a faster rate than inactivation. In addition, the system displays hysteresis, with very slow, negligible rate of reversal of active state photoreceptors in the darkness (Olson et al., 2017). Therefore, any apparent changes in gene expression over time can be attributed to increased background gene expression through the mere increase in the population of cells, as well as constant production of ground state photoreceptors leading to dilution of active photoreceptors.

The dependence of the output of the system on the ratio of active to inactive photoreceptors, and the extensive modelling work outlined above, enable to 'plan' the illumination and output of the system by setting targets for the proportion of active photoreceptors in the area where expression is desired, as well as where expression is not desired. This can be done by looking at the Hill function for gene expression by CCaSR 3.0, against the ratio of active to ground-state photoreceptors (Fig. 4.1) (after Eqn. 2.3). This graph shows how maximum gene expression is dependent on the proportion of active state photoreceptors, with a maximum asymptote when the ratio is 100%.

In order to roughly identify proportions of active photoreceptors above which gene expression could be termed 'ON' and below which it is 'OFF', the region around the linear part of the Hill function was taken (rightmost and leftmost vertical dotted lines). According to this, for proportions of active state photoreceptors higher than those on the linear part of the Hill function (above 45%) gene expression is above 85%, and the region can be considered activated. Conversely, maintaining the proportion of active photoreceptors under the steep linear part of the curve (under 15%) should give under 9% of expression, essentially representing a deactivated region. For high light intensities, the contrast of gene expression in a voxel depends only on the targeted amount of active photoreceptors in the activated and suppressed region. In order to ensure a high contrast, coupled with high gene expression, a more conservative target proportion of active to inactive photoreceptors was chosen, with 10% in the repressed region, and 63% in the activated region.

Under continuous illumination of a voxel, the ratios between active and inactive photoreceptors is dependent on the ratio of activating and inactivating intensities used. Under discontinuous illumination however, the hysteresis of the system and the sole requirement to reach certain levels of active and inactive photoreceptors make gene expression more dependent on radiant exposure, or energy of a particular wavelength absorbed, rather than just illumination intensity. If a sufficiently high green light intensity is used for a short period of time, it is enough to activate the right proportion of photoreceptors, which would then remain active, and their proportion only be reduced through dilution from cell growth. Similarly, a high enough red light intensity for a short

period of time would work to deactivate photoreceptors in the desired regions increasing the contrast.

The use of discontinuous illumination, with temporally separated red and green illumination is different from overlapped red and green light. In the latter, red light merely suppresses activation, rather than expressly deactivating the photoreceptors. Red light is far more efficient on its own in deactivating photoreceptors (Fig 2.26), allowing discontinuous illumination is thus able to achieve better contrast in theory. Discontinuous illumination is also more efficient than continuous illumination, as it allows the use of lower light intensities of red to achieve the same target levels of active-state photoreceptors. In addition, it allows for easier fine-tuning of the ratios of active-state photoreceptors.

Therefore, knowing the proportions of active photoreceptors to be achieved, the light intensity and time of short illuminations can be calculated. As light intensities are increased, the time to reach the desired activation and deactivation is reduced as less time is required to activate the required proportions of photoreceptors. In this way, red light can be applied more quickly, giving less time for gene expression to occur in undesired areas and therefore reducing background, and leading to higher contrast.

Another advantage of a deactivation procedure is that it allows for essentially 'free time' in activating one voxel during a three-hour print, where no illumination would be used. This free time could be used to print other voxels using the same procedure, essentially allowing for more voxels to be printed to form a shape.

The illumination procedure therefore translates to a protocol where a series of voxels is illuminated with green light to reach activation close to 100% and high proportions of active state photoreceptors. Red light can be used to deactivate photoreceptors in the regions in which they are not desired, leaving behind the activated voxel.

In this section, I have started from the analysis of the system to identify an approximation to the Hill function that allows to choose illumination intensities in order to maximise contrast. Based on these, I identify a regime for discontinuous illumination which can be used to give a higher contrast in the desired voxels, and allow to print multiple voxels at a time.

4.2.2 Discontinuous illumination for a line and a voxel in 3D

In order to assess the power of deactivation in improving dynamic range and allowing for more voxels to be printed, I decided to set up an experiment where four different locations in the height

(z-axis) of the hydrogel were activated in one experiment. Similar to continuous illumination, half the experiments were performed attempting to control expression of *tdFAST2* in a line through the cuvette, and half controlling expression of a voxel (Fig.4.2).

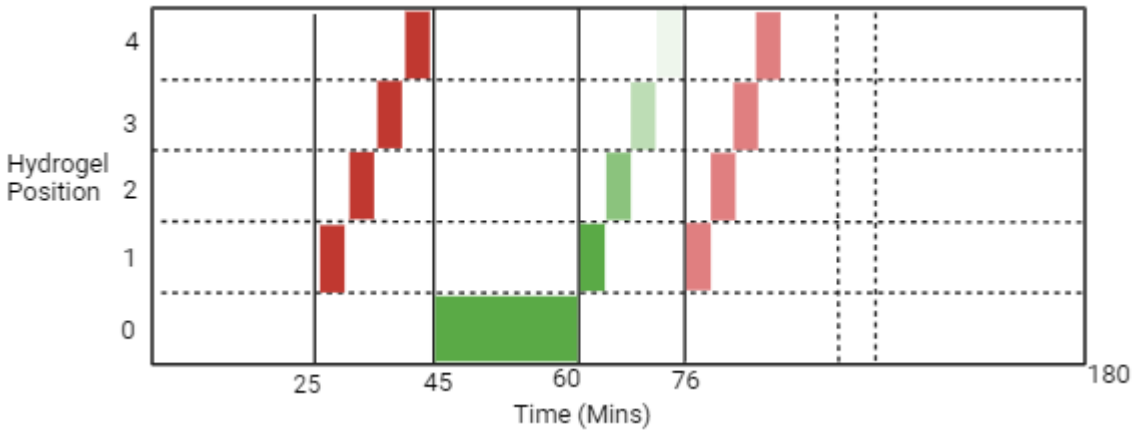


Fig. 4.2: Set up for discontinuous illumination. Each row starting from the bottom represents a z-height in the cuvette, with the bottom one representing warmup for the green laser below the cuvette. The x-axis represents time in minutes. Red and green light was applied sequentially to each position. In experiments aiming for a single activated voxel, red light was applied again after the green beam in the same sequence (shown in pink).

Red light intensity was 32 W/m² for 5 minutes during the first hour of incubation, to achieve initial deactivation of any photoreceptors that could be activated during overnight incubation and preparation of the experiment. This was followed by 4 different green light intensities, at 30, 60, 90 and 120 W/m², each applied for 1 minute sequentially after the first hour of incubation. In the half of the experiments where I attempted to produce a localised voxel, I followed green illumination with red light at 38.4 W/m² for three minutes, which would give a voxel of activation in the centre of the cuvette. This should be sufficient to deactivate the photoreceptors to achieve the maximum possible contrast. Results were analysed and normalised to maximum fluorescence intensity of slices.

In the experiments where only the first of the two instances of red illumination was used, in order to achieve a line, the results show that for all apart from the lowest green illumination, gene expression was virtually the same, indicating a similar degree of activation. Contrast was quite high, indicating that this method was quite successful in achieving similar or better results to continuous illumination (Fig. 4.3 A; Fig. 3.19). In addition, the width of the activated line was thicker than under continuous illumination, indicating high activation through a large proportion of the Gaussian

profile of the laser beam. Interestingly, simulations performed by Borut Lampret (Lampret, 2023) predicted lower expression than that observed (Fig. 4.3 B). The halo predicted by simulations was also stronger, but the halo was in general highly variable between prints and had no correlation with print conditions so was ignored in analysis and treatment of the results.

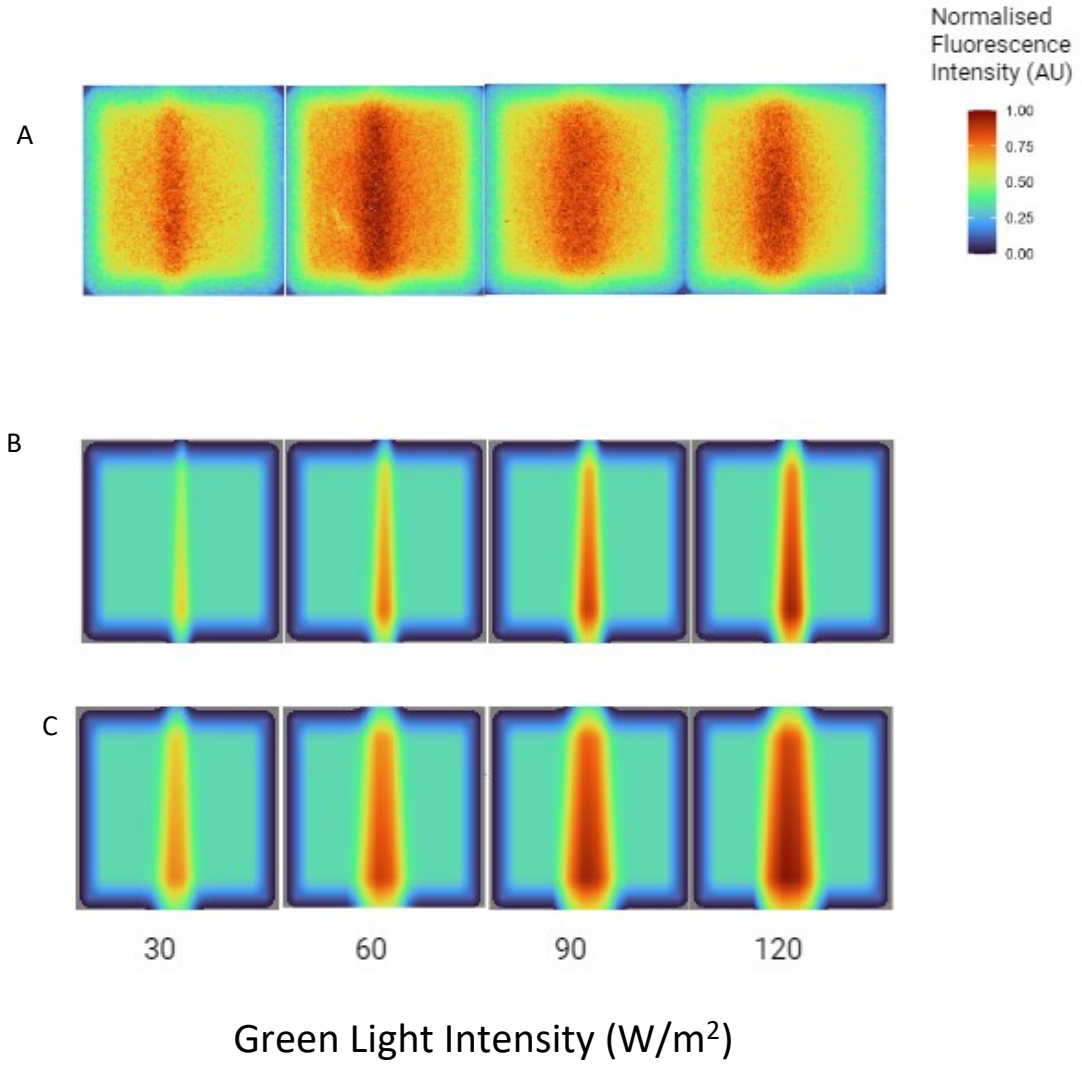


Figure 4.3: *A) A line of tdFAST2 in 4 different heights, produced by 4 different intensities of green light, all lines apart from the first one show similar thickness and intensity, indicating high contrast in gene expression. B) Simulation with the reported green and red light effectiveness. C) Simulations with 5x increased effectiveness of green and red light.*

For the experiment where red light followed the initial green illumination, no fluorescence was observed for any green light intensity in all repeats of the experiment. I hypothesised that this was because red light was more effective than expected. To verify this, I performed an experiment where

green light illumination was the same for all 4 positions, but only two of the positions were illuminated with suppressing red light. Those positions did not show any fluorescence (Fig. 4.4) indicating that the red light was deactivating much stronger than expected.

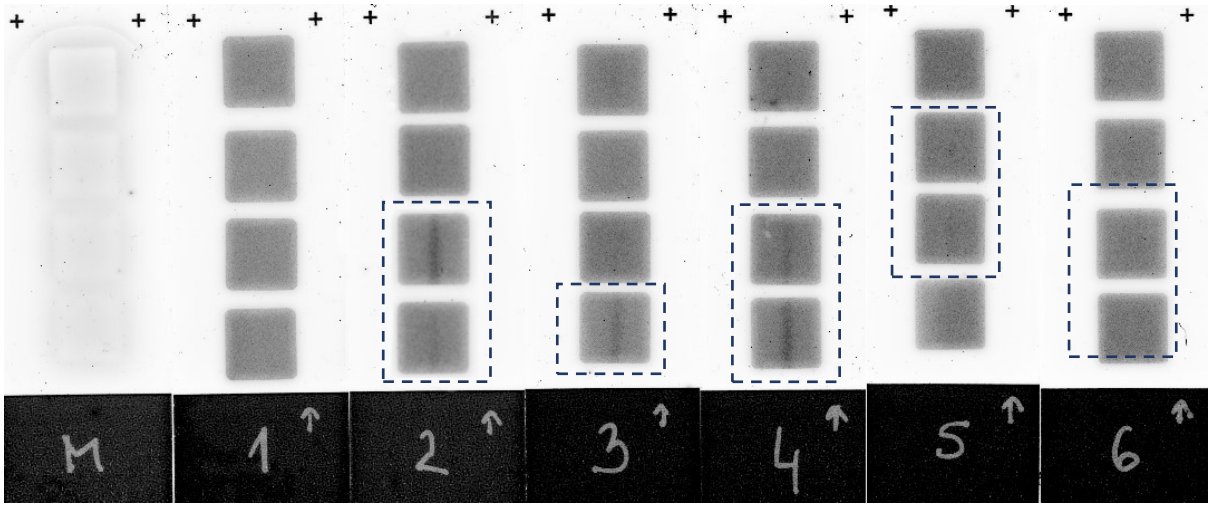


Figure 4.4: *Printing using a hybrid approach of either illumination with red or without. Slices in slides 5 & 6 which were illuminated with red following green illumination show no fluorescence, while slices in 2,3 and 4 show printing of a line, as there was no following red illumination. The slices where expression was expected are put inside the dashed-line box.*

.

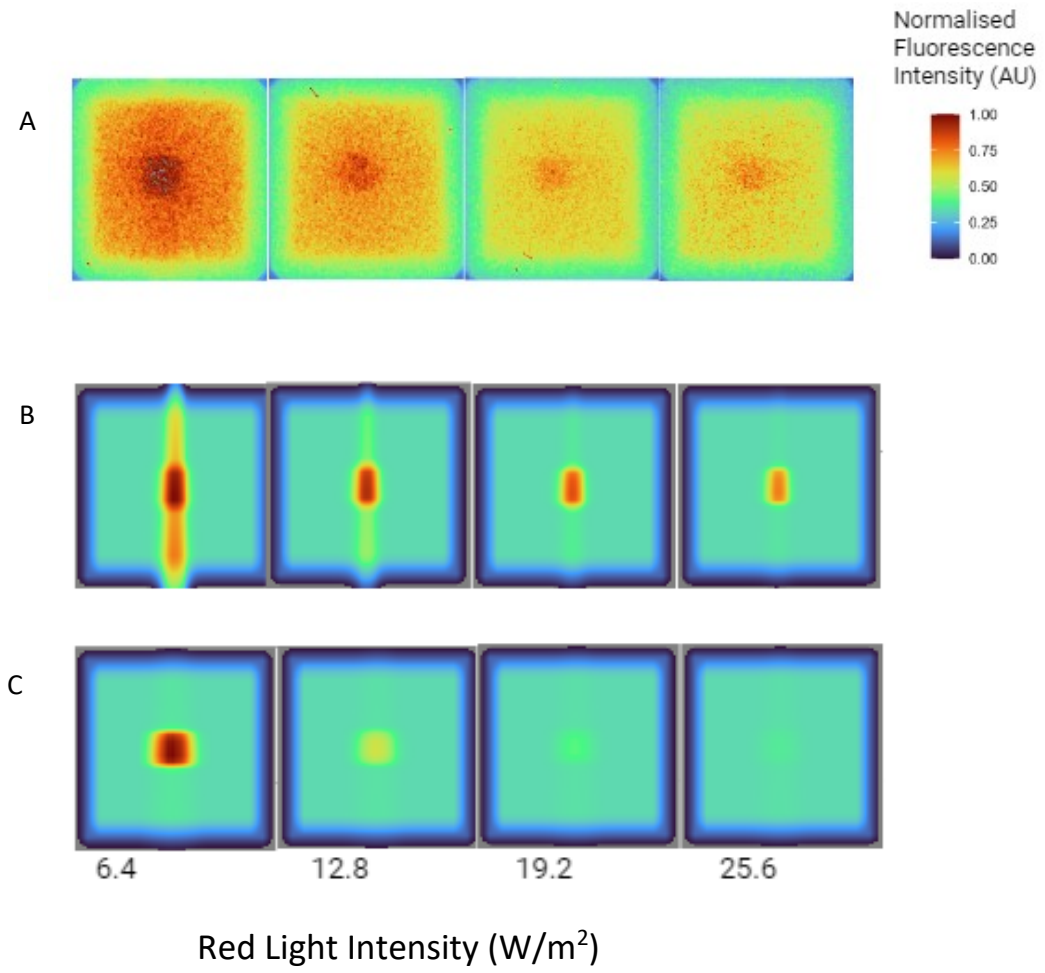


Figure 4.5: *A) Results of discontinuous illumination with different intensities of red light and constant green illumination. (B) Simulation with the reported light effectiveness. (C) simulations with 5x light effectiveness.*

To further assess the effectiveness of red light, I performed an experiment with a constant green light intensity, varying red light intensity over the 4 points. The results (Fig. 4.5 A) indicate gene expression within the activated voxels, showing how discontinuous illumination was able to achieve printing of a localised voxel in a 3D volume. Further, simulations again (Fig. 4.5 B) predicted lower gene expression. This was most apparent under the 6.4 and 12.8 W/m² red light, where in the simulations gene expression in the path of the green beam (in the form of a line) was visible. In the real experiment this gene expression was not visible. The slice illuminated with 12.8 W/m² red light especially demonstrated this, as it showed no traces of expression. This result suggested that the green and red light photoconversion constants, relating to the efficiency of each light to activate or deactivate photoreceptors (Fig. 2.2; Table 2.1) could be higher in this case than previously reported. This could be due to many factors, including the different growth and illumination regimes used, as well as the different reporter.

The two lowest intensities of red light were used to assess the exact discrepancy in the effectiveness of red light. The 6.4 W/m² intensity was 1/6 of the light intensity that was predicted to fully deactivate the tails, and the 12.8 W/m² 1/3 of that intensity. Therefore, the factor by which the effect of light was stronger, was between 3x and 6x. Simulations were thus repeated with 5x increased forward and reverse photoconversion constants, and results were closest to the observed results (Fig. 4.5 C). Interestingly, repeating these simulations for the green light only experiments also corrected for the discrepancies seen in the green-only simulations (Fig. 4.3 C). This effect would not appear in the continuous illumination experiments, as those only depended on the ratios of the light intensities and not radiant exposure, therefore hiding the higher efficiencies of both green and red.

In this section, I showed how discontinuous illumination can be used to achieve gene expression of an arbitrary number of lines and a voxels in different z-positions in the hydrogel. In addition, I identify a discrepancy in the forward and reverse photoconversion rates between the ones reported in literature (Olson et al., 2017), and the apparent one in our system.

4.2.3 Periodic illumination allows to control the photoreceptor ratios throughout incubation

While effective, one limitation of single illumination for each voxel was that gene expression contrast decays over time, mostly due to the dilution of active state photoreceptors by cell division and production of new, ground-state photoreceptors. As a result, a better illumination procedure was devised, periodic illumination. This involved 'top-up' repeat illumination of particular voxels over time, with the aim of maintaining the ratio of active state photoreceptors throughout the print. The same procedure as with the experiments above was repeated to give four lines in different z-positions in the hydrogel, followed by activated voxels in the centre of the cuvette.

To induce gene expression in a line, each location was illuminated with red like section 4.2.2 during the first hour. After that, each z-location was illuminated with green light. This illumination was repeated in periods from 10 to 30 minutes between illuminations until the end of the experiment (3 hrs). In the first 60 minutes, all locations were illuminated with red light at 32 W/m² for 5 minutes, to reduce any gene expression during the preparation of the experiment. Then, all locations were illuminated with 45 W/m² green light for 1 minute. In order to achieve similar gene expression in all periods, green light intensity, for both the initial illumination and 'top-ups' was altered at each position. Illumination intensity was higher for less frequent periods, in order to achieve similar amounts of radiant exposure. In addition, in all experiments, top-up intensities were lower than the

initial one, as they did not aim to activate photoreceptors to a ratio from all being inactive, but rather to maintain the ratio already achieved (Fig. 4.6). The period of illumination showed no significant difference between different periods, as they all showed largely similar fluorescence and contrast (F value 2.492, p = 0.134).

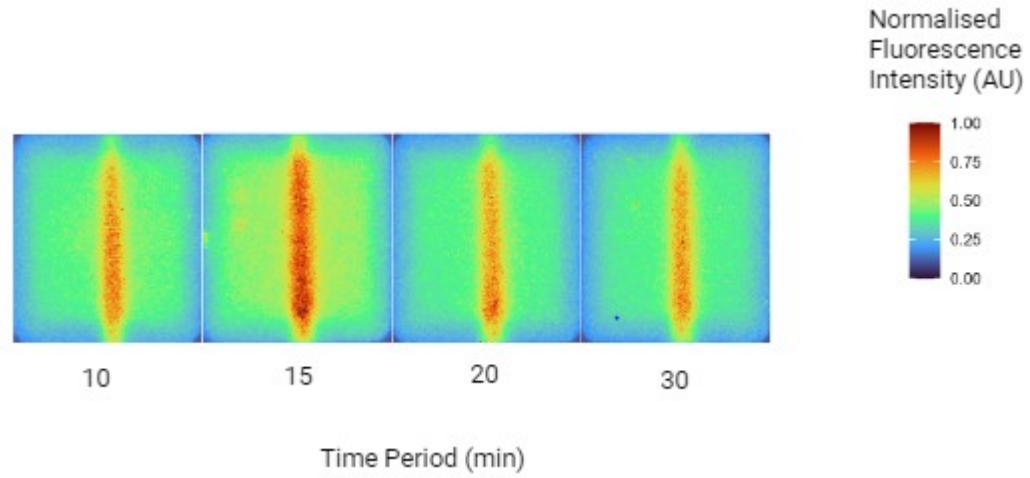


Figure 4.6: *Printing with periodic illumination, with green light illumination repeating at different time periods after 1 hour of darkness. For the four illumination periods 10, 15, 20 and 30 minutes, initial green light was used at 25, 22.5, 21 and 20 W/m² correspondingly for 1 minute as initial illumination after 60 minutes of incubation. Top up illumination intensities were 6.5, 5, 4 and 3 W/m² correspondingly.*

The same experiment was repeated to print a single voxel, as in Section 4.2.2, with red light after green, with intensities chosen without taking into account the new 5x higher photoconversion constants. Similar to the discontinuous illumination experiments, this gave no positive results, indicating again that red light and green light were stronger than expected. A second experiment was then devised in order to investigate the ability to print a voxel. As the period showed no significant effect in gene expression, the period was kept constant at 30 minutes for this experiment. Green light intensity was also kept constant across all voxels, with 45 W/m² initial illumination and 11.5 W/m² top-up illuminations, with illuminations lasting 1 minute each. Like the previous experiments, in the first 60 minutes, all locations were illuminated with red light at 32 W/m² for 5 minutes. Following the first hour, each red light illumination was applied for 2 minutes following the green illumination, and the intensity was the same for the initial and top-up red illuminations. In different voxels, different red intensities were used. Starting from the bottom voxel, red light intensity was 6.4, 12.8, 19.2 and 25.6 W/m² (Fig. 4.7).

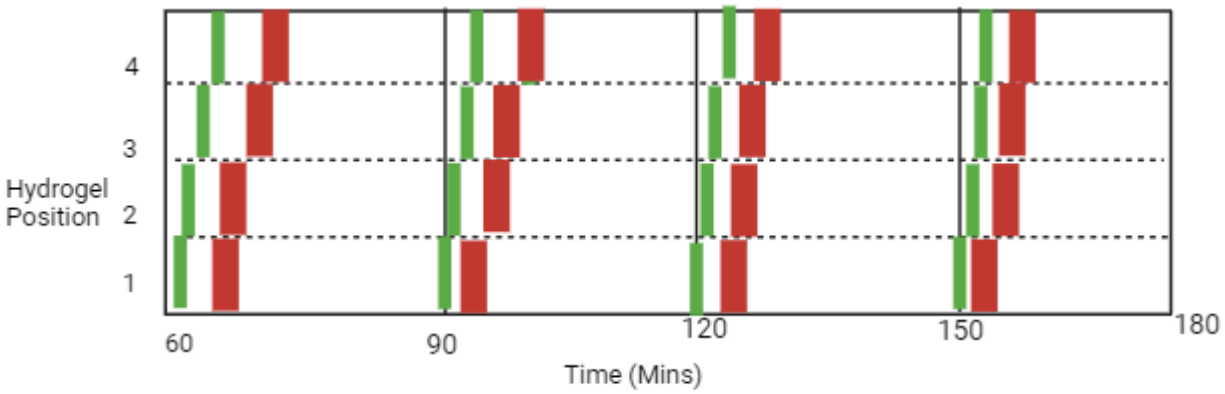


Figure 4.7: *Schematic of periodic illumination in the four voxels at different heights. Each row starting from the bottom represents a z-height in the cuvette, with the bottom one representing warmup for the green laser below the cuvette. The x-axis represents time in minutes. The schematic indicates the order of illumination of each voxel, starting from the bottom to the top.*

Results showed that for all red light intensities there was a clear voxel shaped by the red light, even though contrast was not as great as that observed with discontinuous illumination (Fig. 4.8). Similarly, the lowest two red light intensities in this case showed clear gene expression in the path of the green light, indicating that the top-up green illumination was slightly more efficient in activating photoreceptors than the red in deactivating them. Even though differences between different red light intensities were not as pronounced as in Fig. 4.5, still a decrease in the fluorescence intensity and size of the activated voxel was observed as red light intensity was increased.

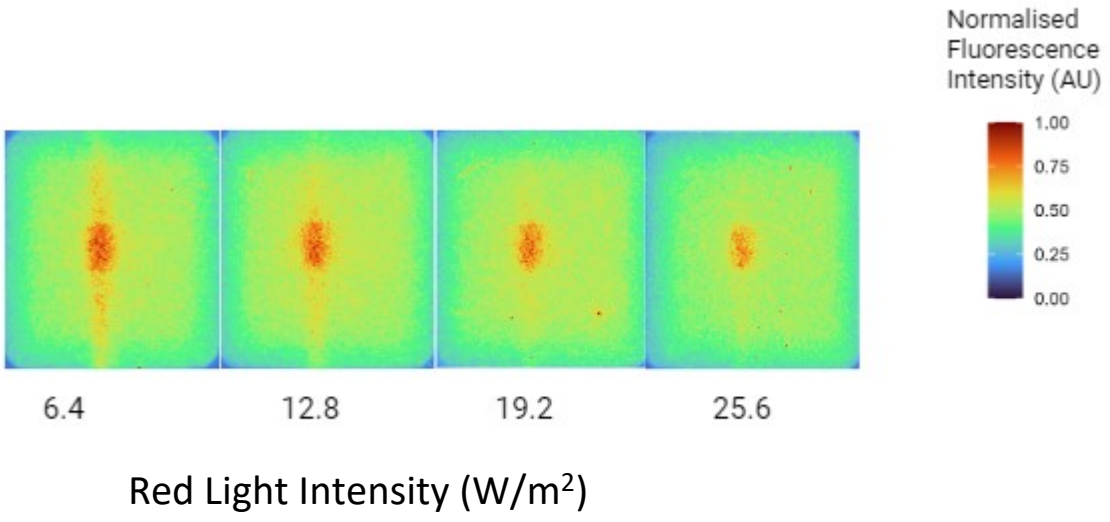


Figure 4.8: *Periodic illumination with different red light intensities.*

In this section, I optimised discontinuous illumination to compensate for growth of the cells, by using top-up, periodic illumination. I show how periodic illumination can be used to print voxels, again verifying the higher photoconversion constants in this case.

4.2.4 Illumination of two voxels

4.2.4.1 Two voxels can be illuminated on the same z-plane

Following successful production of 4 voxels in the z-axis using discontinuous illumination, the next step in 3D production of shapes across a cuvette was to activate expression of 2 voxels in the same height in the cuvette, as this would be necessary in order to achieve 3D printing of complex shapes. Three different arrangements for the voxels were theoretically devised, in relation to the direction of the green light beam: horizontal, vertical and diagonal (Fig. 4.9). In contrast with production at different heights, production at the same height was more complex because the voxels are not independent. In all the arrangements, green light either has to move locations leading to different positions of activation (horizontal), red light has to move locations leading to different positions of deactivation (vertical) or both lights have to move (diagonal). As a result, voxels where off-target gene expression occurs were possible in all conditions, and intensities and times of illumination would need to correct for that, in addition to growth and expression through the print. All voxels in Fig. 4.9 were labelled in order P0-P3 and subsequent figures referring to the illumination protocol (Figs. 4.10, 4.12, 4.14, 4.16, 4.18, 4.20 and Table 4.1) refer to the corresponding voxels as such.

In the horizontal arrangement, unwanted voxels were suspected to be voxels at the bottom, where green light would be strongest with least scattering and attenuation. In the vertical arrangement, a voxel between the two targeted voxels was suspected of having high expression, as it would receive constant green light and red light from the gap between the two voxels. In the diagonal arrangements, the reverse diagonal voxels were suspected of having high production, as they would receive green activation and no red inactivation at complementary timepoints to the intended voxels.

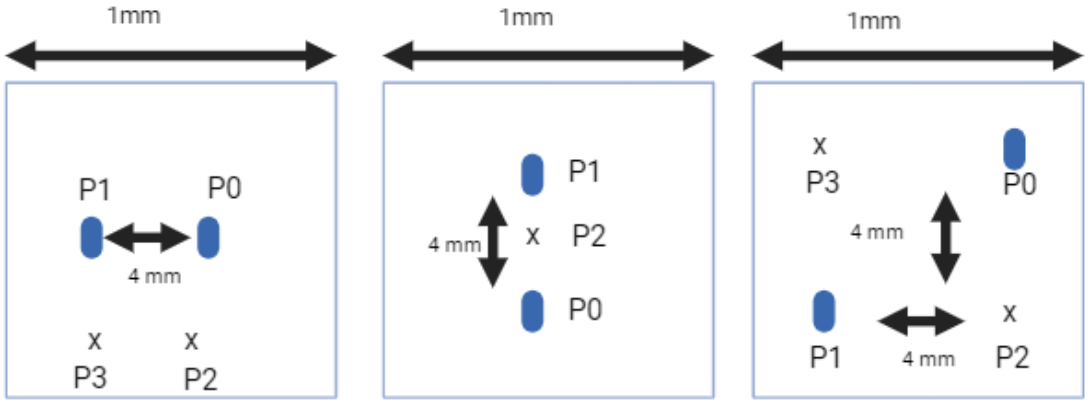


Figure 4.9: *Arrangements of two voxels in the same plane, for purposes of characterisation. All images represent top view of slices. Green light came as a beam from the bottom of each image, and red light came as a split beam from the right-hand side of the images (as in a 90° anticlockwise rotation from Fig. 3.22).*

In order to cover printing possibilities, three different illumination regimes were devised in order to investigate how to minimise interactions between the voxels and achieve the highest possible contrast between each voxel. These are the following:

1. In alternating illumination, the print was split into equally timed intervals. Within each interval, a single voxel was illuminated with a constant intensity of green or red light, before alternating between the voxels for the next interval.
2. Concurrent illumination also separated the printing period to intervals, but made use of deactivation to achieve briefer illumination periods. The aim of concurrent illumination was thus to activate both voxels equally within each interval, while keeping expression in other points to a minimum.
3. Separate illumination was a free approach, that was similar to alternating illumination, but did not require equal intensities or periods of illumination throughout the period of illumination. Instead, it also used activation and deactivation to activate each voxel at the highest possible amount, regardless of the history of illumination or other positions.

Each illumination approach and arrangement was explored, with the intention to identify the best illumination procedure for each arrangement. The intensities and times for each illumination were calculated based on the optogenetic model (Olson et al., 2017). In all instances, in the first 60

minutes, all locations were illuminated with red light at 32 W/m² for 5 minutes, to reduce any gene expression during the preparation of the experiment.

4.2.4.2 Alternating illumination is capable of producing two voxels in different geometries

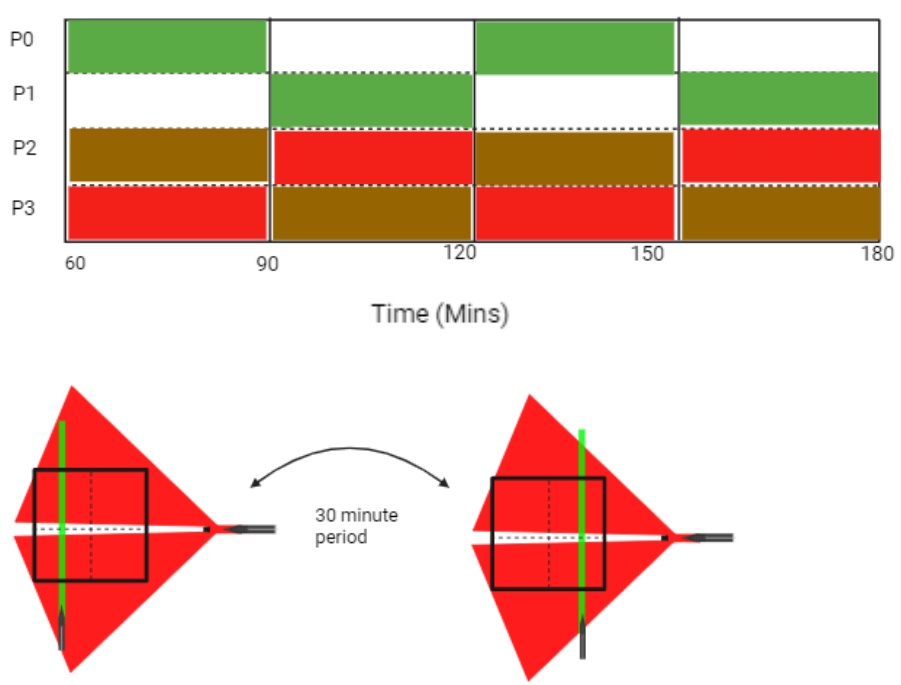
In order to achieve expression in two voxels using alternating illumination I chose a simple procedure, where the green light moved from illuminating the left and right voxels in an equal period of time, while the red light remained stationary, essentially inhibiting throughout (Fig. 4.10).

Voxels in a horizontal arrangement were independent in terms of green light, but coupled through red light bleed through and inhibition. For the process to work, light intensities for both green and red should be high; however, because of red light bleed through leading to inhibition in the desired locations, an optimal intensity for each laser also existed.

In the first hour of each experiment, in all illumination regimes, red light was applied to the cuvette to deactivate any activated photoreceptors from overnight incubation and preparation, as in Fig.4.2, at 32 W/m² for 5 minutes during the first hour of incubation. Following that, green light was applied to each voxel with a period of 30 minutes. Green light intensity was 1.2 W/m² and red light intensity was 9.6 W/m² (Fig. 4.10).

There was clear gene expression in both the desired voxels with a good enough contrast. Gene expression was found to be similar in the two voxels, but a bit wider in p1, which was the second voxel to be illuminated, contrary to expectation (Fig.4.11). This was postulated to be because of red light getting slightly 'weaker' further inside the cuvette, leading to a higher proportion of active state photoreceptors allowed by the red light in p2. There was some limited expression in the unwanted voxels at the bottom of the slice, but the expression in the desired area was much greater to a degree that the required voxels could be clearly distinguished and thresholded.

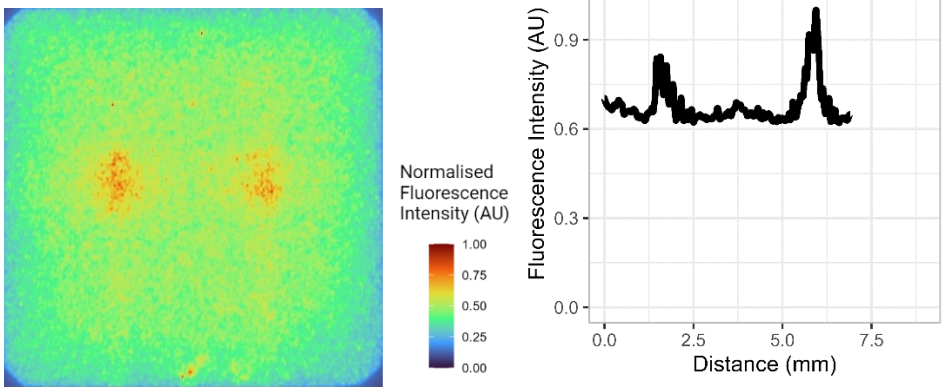
A



B

Figure 4.10: *Indication of the set up for alternating horizontal illumination. A) The illumination seen by each of the voxels over time is outlined, with brown representing both green and red light. p0 and p1 were the voxels where expression was desired, with p2 and p3 voxels where unwanted expression was suspected. B) A top-view schematic of the steps taken during the illumination steps.*

A



B

Figure 4.11: *A) Image of summed and normalised slice. B) Graph of normalised fluorescence values across the x axis (parallel to the red light beam). The halo was excluded in this analysis for ease of demonstration. The distance is from left to right, with the left most peak corresponding to p1.*

In the vertical arrangement of voxels, the situation was exactly the opposite as that of the horizontal arrangement, in that the green light remained constant in a particular position, while the red light

moved between the voxels to define them (Fig. 4.12). When one voxel was only illuminated with green, the other voxel received both green and red light, reaching a steady state, while the background was at constant suppression with red. In cases of very high red intensities, the voxels would therefore reach the same steady state as the background suppressed region, leading to no obvious expression.

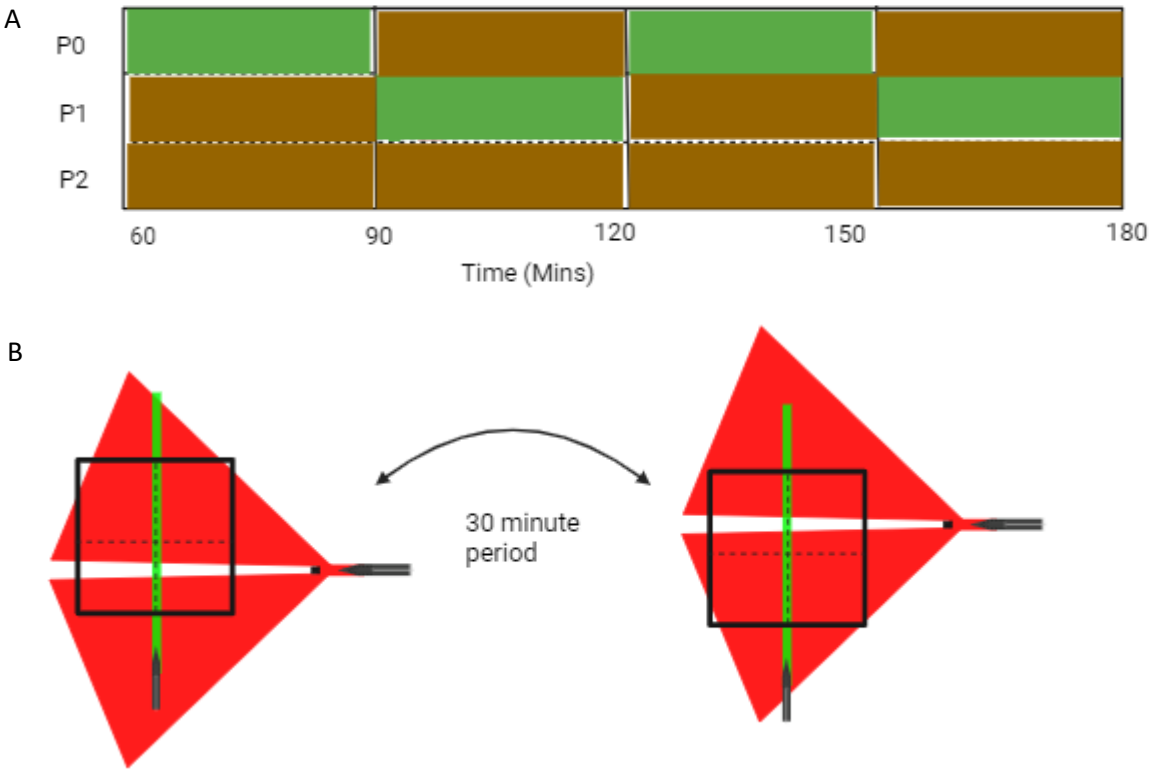


Figure. 4.12: *Indication of the set up for alternating vertical illumination, with the top panel indicating the light received by each voxel, and the bottom panel showing the steps taken during the illumination.*

One way to work around this effect was by reducing red light intensity in efforts to achieve better contrast. Another way was utilising fast green light dynamics, essentially activating each voxel as fast as possible during its illumination to ensure maximum gene expression during the green light illumination, thus reducing the effect of red light deactivation in the voxel of interest, while keeping suppression constant in the background. Therefore, essentially best contrast would be achieved by utilising generally high intensities of both wavelengths of light, with the green : red light intensity ratio higher than other geometries.

A voxel in the centre was predicted to show unwanted gene expression, as it would receive green light without much attenuation that would be seen further in the cuvette, and no red light while the lasers were moving between positions.

Similarly to the horizontal arrangement, red light was used for the first hour followed by illumination at a period for 30 minutes. In this experiment, red light was used at 42.4 W/m², while green light was used at a high 18.6 W/m². The ratio of green to red light intensity in this experiment was double that of the horizontal arrangement, in order to ensure better expression of the desired voxels.

The results show distinct expression in the two desired voxels, as well as a small amount of expression by the voxel in the middle. As expected, p0 showed a higher fluorescence than p1, partly due to less attenuation of the green light, but also due to the fact that p0 was illuminated last, giving it less time to express after activation (Fig. 4.13).

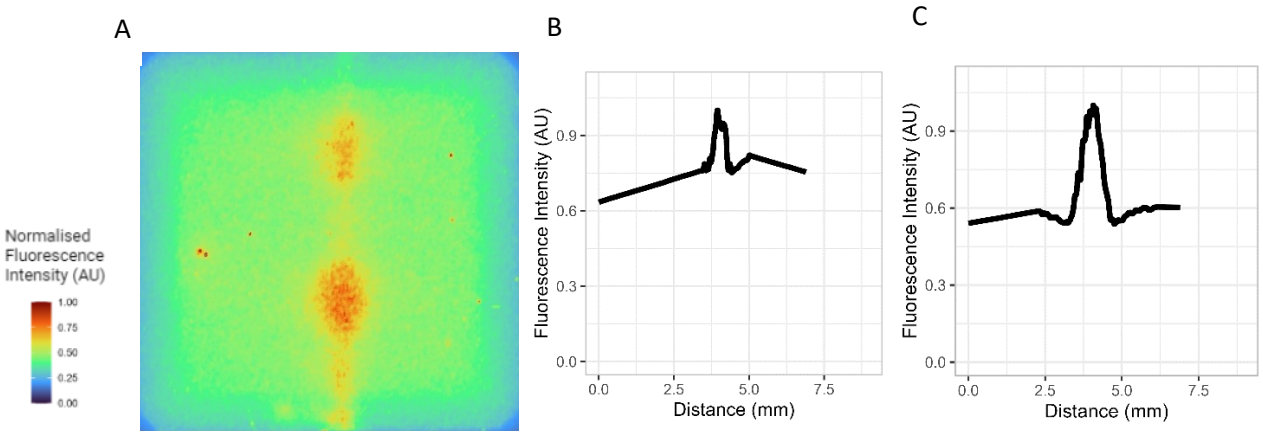


Figure 4.13: *A) Image of summed and normalised slice. B) Graph of normalised fluorescence values across the x axis (parallel to the red light beam) for the top voxel (p1). The halo was excluded in this analysis for ease of demonstration. C) Graph of normalised fluorescence values across the x axis (parallel to the red light beam) for the bottom voxel (p2).*

In alternating diagonal illumination, the two voxels of interest were illuminated either with only green or only red light at all points. However, the other two diagonal points, p0 and p1, were either in darkness or illuminated with green and red light at the same time. Therefore, depending on the magnitude of the red and green light, it is possible for those complementary voxels to achieve higher expression than ones of interest. This would happen if attenuation of light was minimal through scattering, and activation and deactivation rates were comparable, leading to 50% of photoreceptors activated and thus maximum activation.

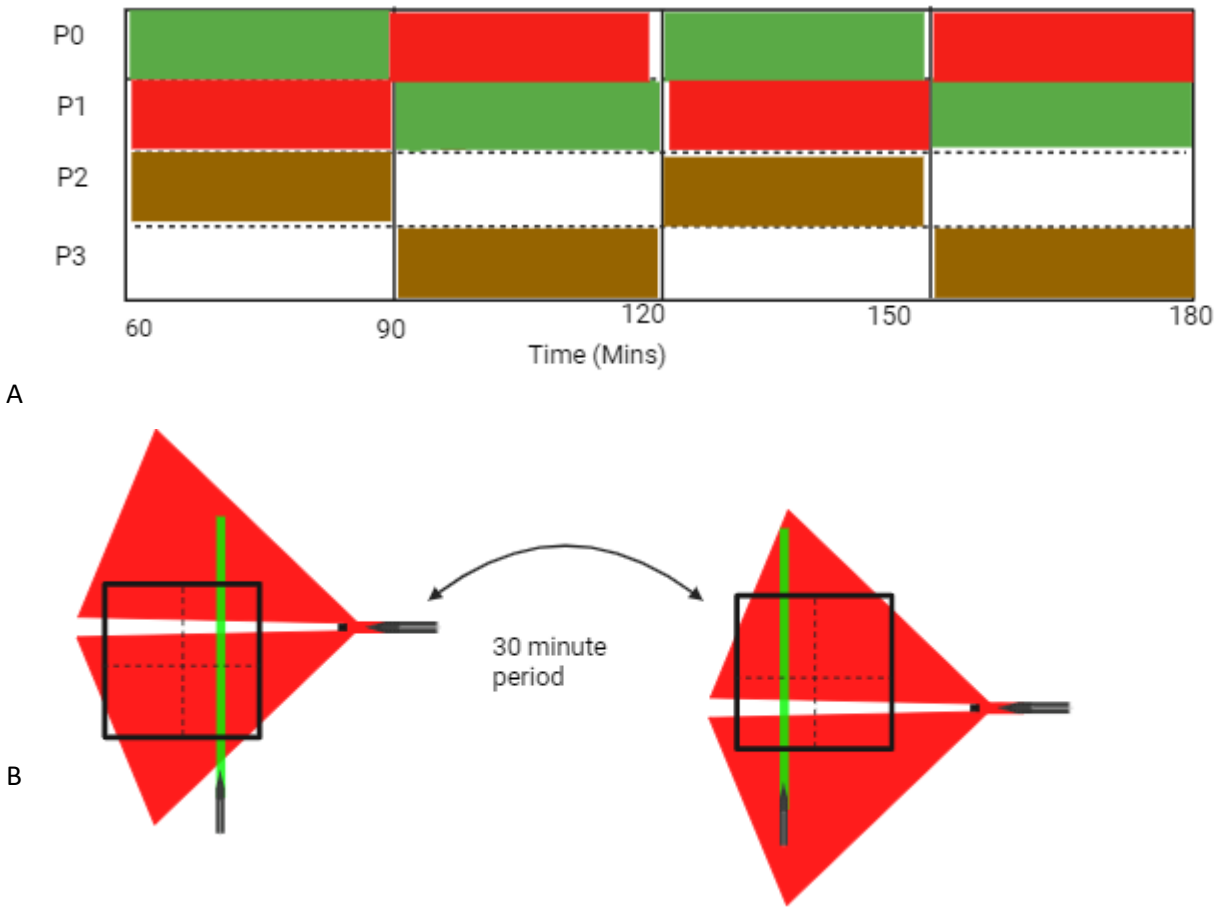


Figure 4.14: *Indication of the set up for alternating diagonal illumination.*

To avoid unwanted gene expression, the rate of activation through green light had to be higher than the rate of deactivation through red light. Again, high intensities of both red and green are required, as well as quick activation using green (Fig. 4.14).

To achieve these results, high green intensity was used at 5.8 W/m², with 8.3 W/m² red light, in this case. Gene expression was very similar between the two desired voxels, with p1 again showing higher intensity than p0. This was because of simultaneous less green light attenuation and more red light attenuation in p1, which also allowed for a wider voxel, despite the fact that it was illuminated last. Similarly, from the unwanted voxels, p2 showed higher fluorescence than p3 as it received more green light due to less attenuation (Fig. 4.15).

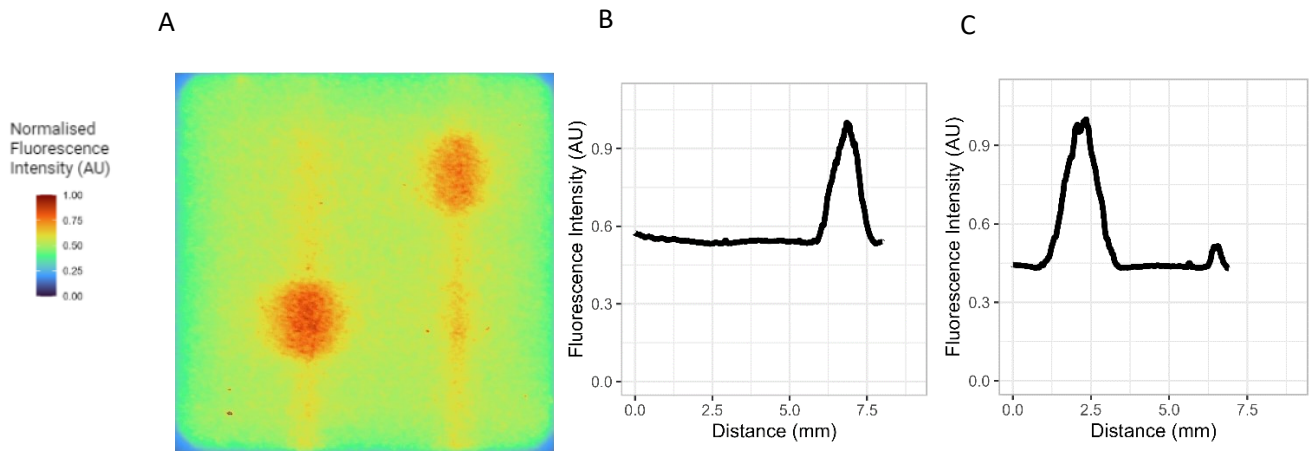


Figure 4.15: *A) Image of summed and normalised slice. B) Graph of normalised fluorescence values across the x axis (parallel to the red light beam) for the top voxel (p0). The halo was excluded in this analysis for ease of demonstration. C) Graph of normalised fluorescence values across the x axis (parallel to the red light beam) for the bottom voxel (p1).*

4.2.4.3 Concurrent Illumination performs best for horizontal voxels

With concurrent illumination, illumination was applied for shorter periods of time, with the aim of activating both voxels equally during each 30-minute period. The horizontal arrangement was again the simplest one, as it involved three simple steps: in the first two steps, each of the voxels was illuminated by green light sequentially, followed by the third step which used red light to deactivate the surroundings and form the voxels. This method therefore involved no coupling between the voxels.

As illumination period was reduced compared to alternating illumination, intensity was increased. Peak green light intensity was used at 96 W/m² and red light at 18.4 W/m². The first voxel was illuminated for 48 seconds every 30 minutes with green, while the second one was illuminated for 96 seconds after that, in order to compensate for the more growth and the red light attenuation (Fig. 4.16). Red light was used for 180 seconds at once.

P1 showed a higher integrated fluorescence than p0 (Fig. 4.16, Fig. 4.9), as well as a wider voxel, both in the direction of the red and green lights. The reason for the high integrated total fluorescence is thought to do with the proportion of active photoreceptors at the end of each green illumination period for p1 compared to p0. The illumination period for p1 was longer, as it was illuminated last, with less time for gene expression from activation until red illumination. However, because of the fast kinetics of photoconversion, this led to a proportion of photoreceptors close to 100%. The distribution of active photoreceptors is not linearly dependent on radiant exposure, as changes in

radiant exposure are more effective at lower active photoreceptor proportions. Therefore, p1 was less susceptible to deactivation leading to higher gene expression (Fig.4.17). In addition, red light attenuation was also thought to play a role. Despite the difference between the two voxels, contrast was very high for both voxels, giving superior results to alternating illumination.

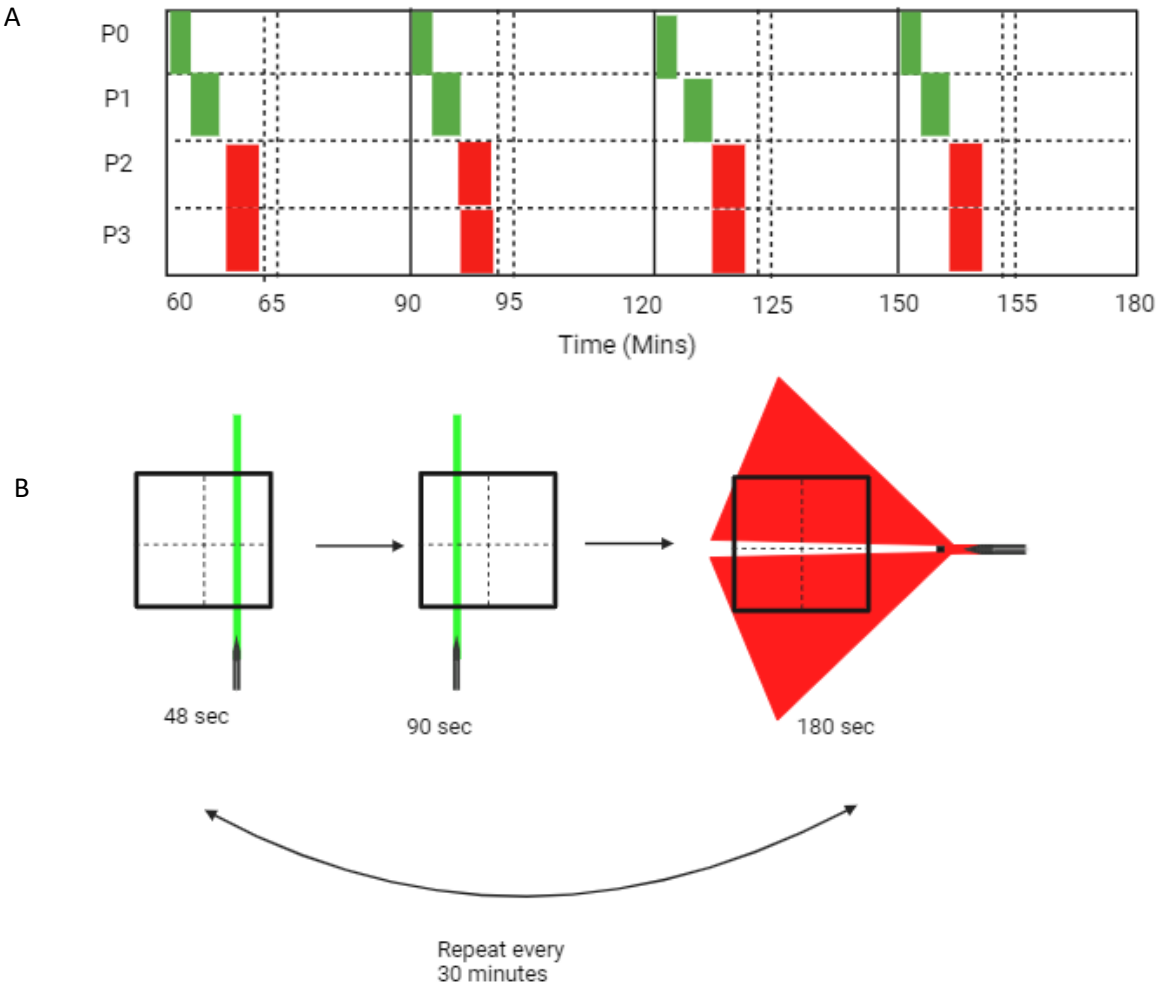


Figure.4.16: *Indication of the set up for concurrent horizontal illumination.*

The approach used for vertical concurrent illumination used the fact that green light does not have to be constantly on in the direction of both voxels. This approach first illuminated one voxel with only green light, with the other voxel therefore receiving both green and red light. In the second step, red light moved to deactivate the large activation in the first voxel, allowing the second voxel to be in the dark, as the green light is turned off, achieving similar proportions of active photoreceptors in both.

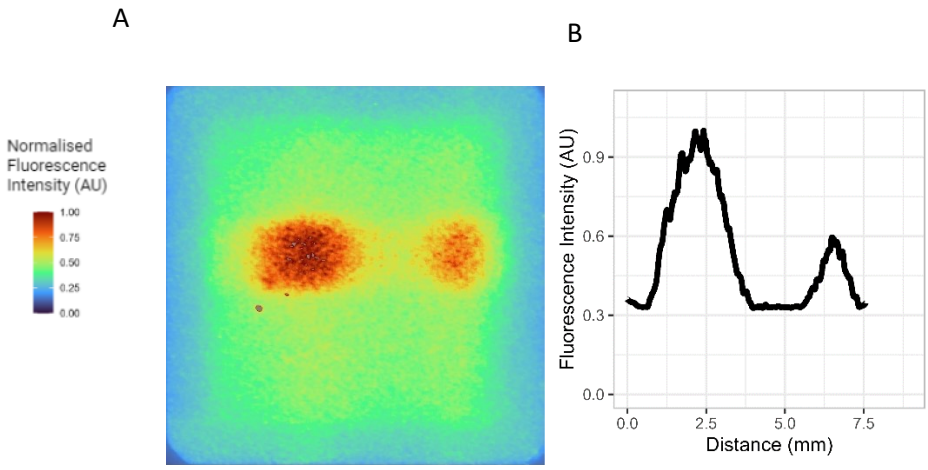
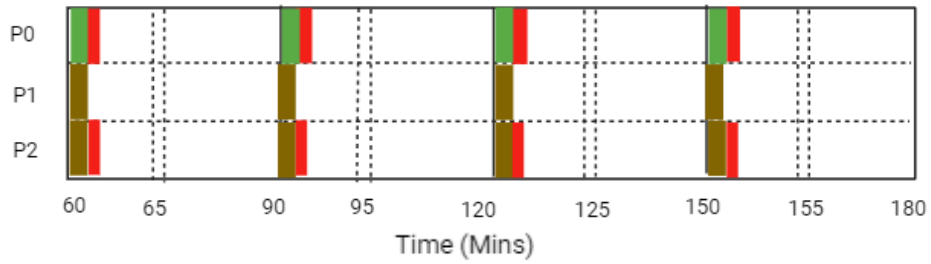


Figure 4.17: *A) Image of summed and normalised slice. B) Graph of normalised fluorescence values across the x axis (parallel to the red light beam). The halo was excluded in this analysis for ease of demonstration. The distance is from left to right, with the left most peak corresponding to p1.*

These two steps were repeated every 30 minutes, with the first step lasting 135 seconds and the second step lasting 33 seconds. The intensities used were 34.8 W/m² for green, and 45 W/m² for red, as these would allow the activation of particular locations to be high, and not be overweighed by the red light inhibition in p1 (Fig.4.18).

Contrast using this approach was lower than with alternating gene expression, indicating that concurrent illumination was not optimal for this geometry. The poorer performance of p1 could be attributed to the deactivation applied in the beginning without any activation. (Fig. 4.19).

A



B

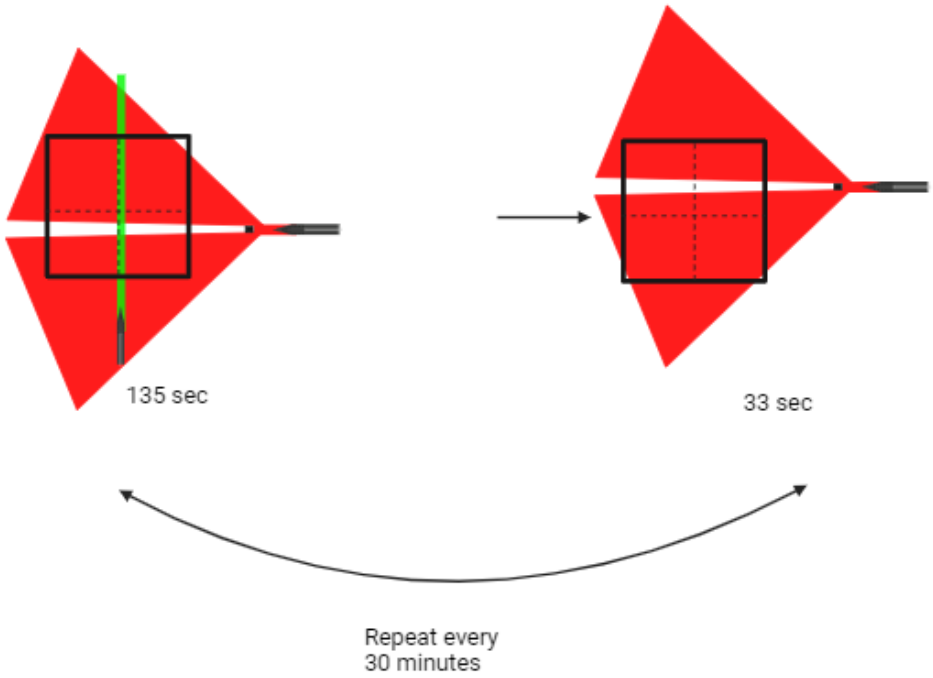


Figure 4.18: *Indication of the set up for concurrent vertical illumination.*

To achieve diagonal voxels using concurrent illumination, a 4-step process was devised. Essentially, for the p0 voxel, there was activation with green to bring the ratio of active photoreceptors to a higher value. As a second step, the voxel was shaped by red light. Then, the second voxel was activated, while the first voxel was under red light, and finally only the first voxel was supressed (Fig. 4.20). This had the effect of bringing both voxels to the same level, with green followed by red illumination in the first one, and green followed by darkness in the second one.

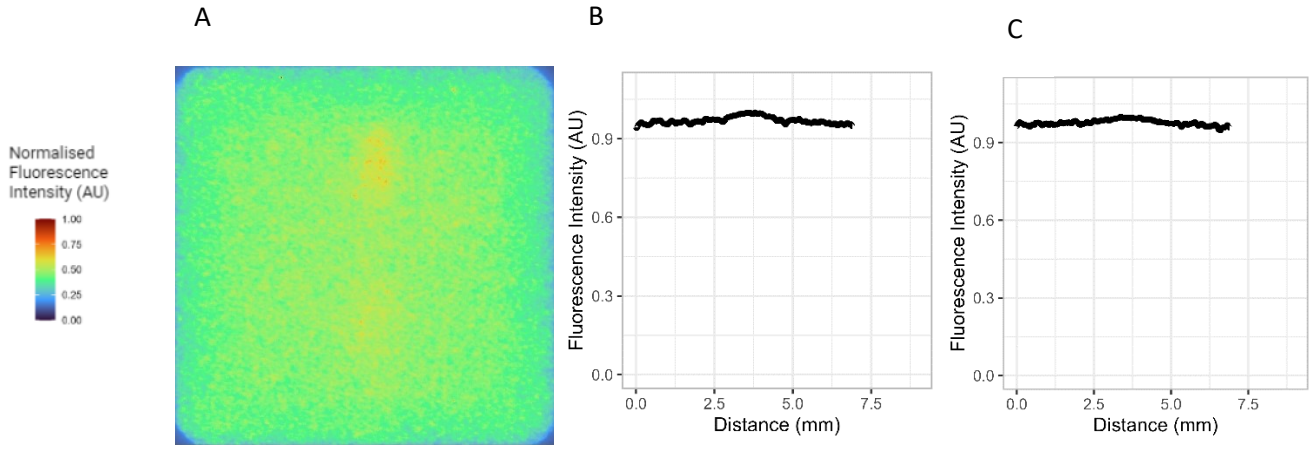
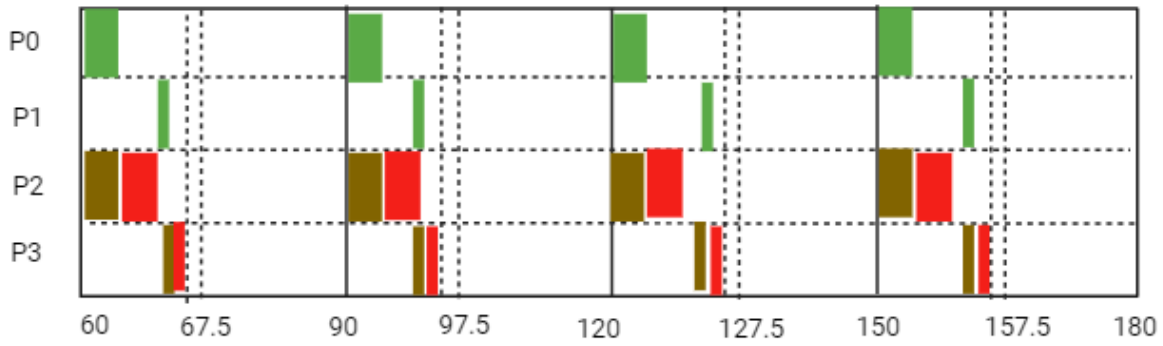


Figure 4.19: *A) Image of summed and normalised slice. B) Graph of normalised fluorescence values across the x axis (parallel to the red light beam) for the top voxel (p1). The halo was excluded in this analysis for ease of demonstration. C) Graph of normalised fluorescence values across the x axis (parallel to the red light beam) for the bottom voxel (p0).*

A



B

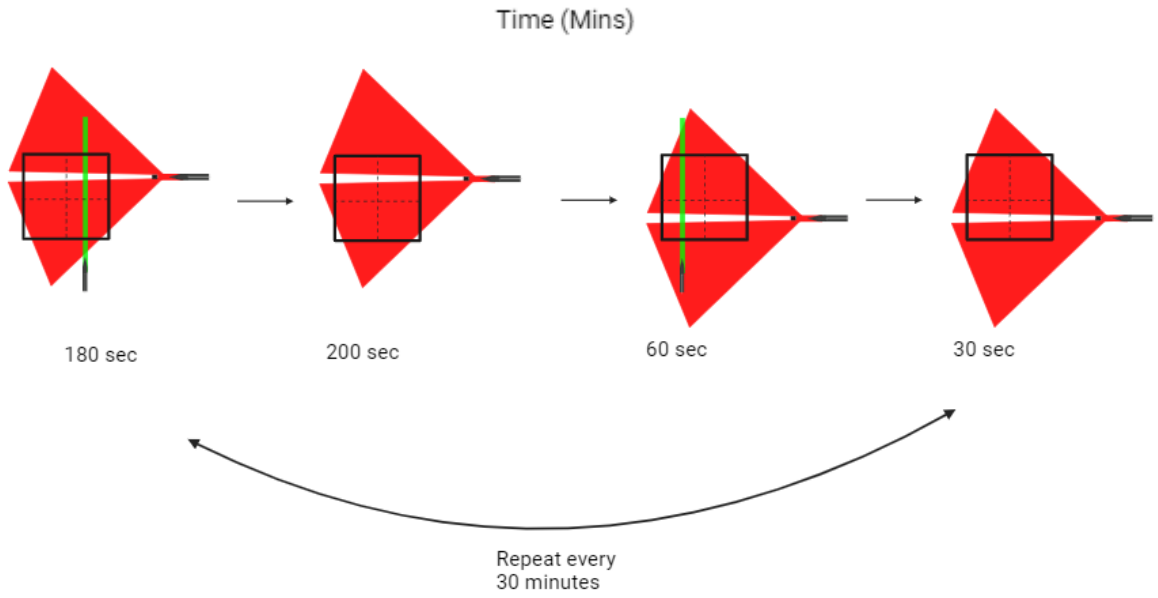


Figure 4.20: *Indication of the set up for concurrent diagonal illumination.*

The illuminations were repeated every 30 minutes from 1 hour onwards. For p0, green light was used at 69.6 W/m² for 180 seconds, followed by red at 14.1 W/m² for 90 seconds. In the bottom voxel, p1: red light was applied at 9.2 W/m² for 200 seconds, followed by green at 23.2 W/m² for 30 seconds.

Differences in the width of the voxels as well as their fluorescence intensities could be attributed to scattering of both green and red light, with the p1 voxel this time being weaker, due to the shorter and later green light illumination (Fig. 4.21). Contrast was again not as good as with alternating illumination, but better than the vertical arrangement, giving very distinguishable voxels.

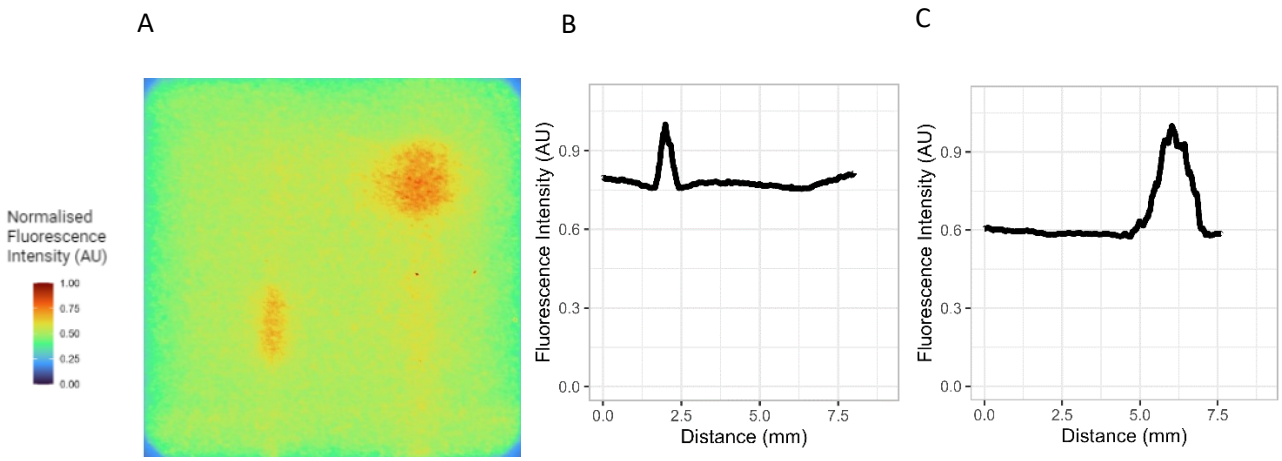


Figure 4.21: *A) Image of summed and normalised slice. B) Graph of normalised fluorescence values across the x axis (parallel to the red light beam) for the top voxel (p0). The halo was excluded in this analysis for ease of demonstration. C) Graph of normalised fluorescence values across the x axis (parallalel to the red light beam) for the bottom voxel (p1).*

4.2.4.4 Separate illumination performs best for diagonal and vertical voxels

Separate illumination only aimed for defining particular voxels adequately through a simplified approach, as a freer version of alternating illumination. For each illumination period, a simple procedure was followed, where green was used to separately specify the first voxel followed by red to shape it. After the first period, the same procedure was repeated for the complementary voxel. For all arrangements of voxels, separate illumination used green light at 69.6 W/m² and red light at 18.4 W/m². These quite high light intensities reflect the brief time of illuminations, and the division of illuminations to fewer periods, as the periods were effectively split between the two voxels. The times of illumination were according to Table 4.1 and Fig. 4.22. Due to the many brief illumination instances, the grids are not shown in order not to overcomplicate the images.

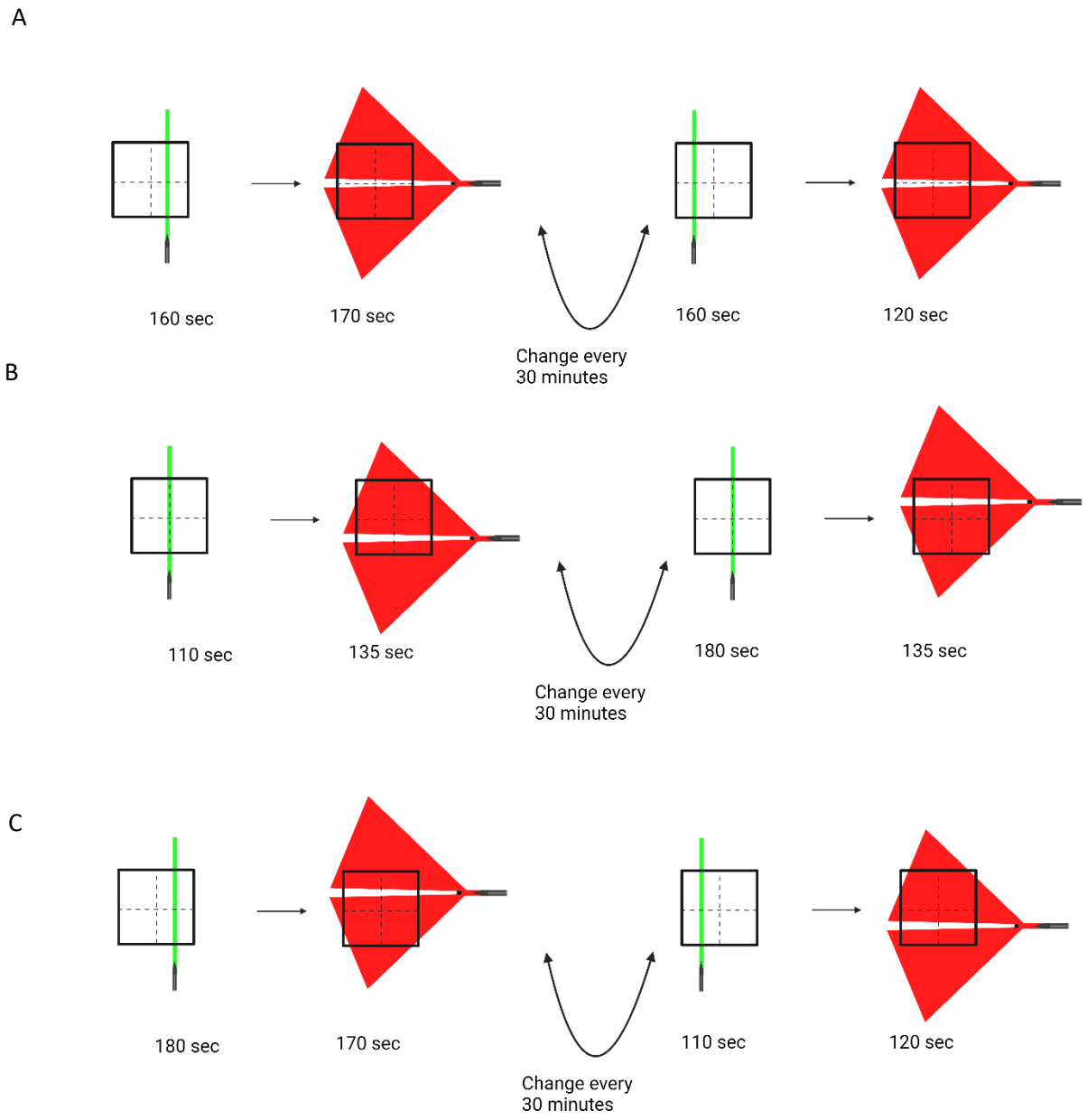


Figure 4.22: *The illumination setups for separate gene expression, for A) Horizontal, B) Vertical and C) Diagonal arrangement of voxels.*

For horizontal illumination, first the first voxel was illuminated with green, followed by deactivation of the unwanted areas to shape the voxel. After 30 minutes, the second voxel was activated, followed by a similar deactivation. (Fig. 4.22). For vertical voxel arrangement, green light was used at the beginning, following by red light shaping p0. Then green light was used again followed by red light to shape p1. Finally for diagonal voxels, a similar approach was used, with red light moving locations every iteration as well as green.

Voxel	P0	P0	P1	P1
Time	**T1**	**T2**	**T1**	**T2**
Horizontal	160	170	160	120
Vertical	110	135	180	135
Diagonal	180	170	110	120

Table 4.1: *The times of illumination for each arrangement with separate illumination. T1-T2 refers to the first and second illumination in temporal order for each voxel.*

Fluorescence intensity in these experiments was unexpectedly high for all conditions. This could be due to lower than expected background gene expression or uncharacterised variation between experiments. Voxels also appeared wider in the vertical and horizontal arrangements, due to the high incident green light intensities used. In all experiments, contrast appeared to be high, with good localisation and comparable sizes and intensities for all voxels (Fig. 4.23-24).

All arrangements of voxels gave high contrast and localisation for the printing of two voxels. Of the three arrangements, separate illumination underperformed slightly only in the horizontal arrangement, where p0 was slightly smaller than p1, similar to what was observed with concurrent illumination. However, in this case the smaller size of p0 could not be attributed to the non-linearity of response of active photoreceptors, as illumination times were similar. Instead, it might be possible that inaccuracies in the green light path and red light attenuation might have played a larger role in this.

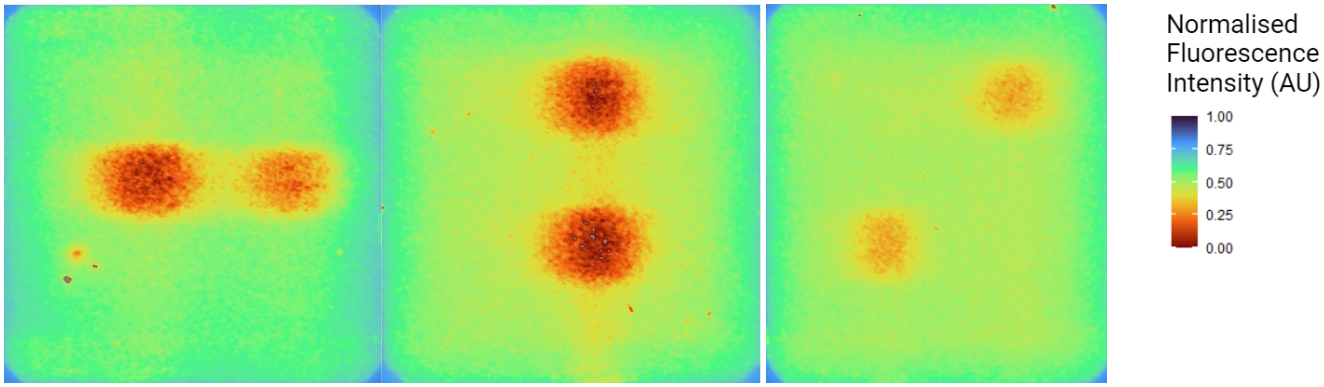


Figure 4.23: *Slices of printing for horizontal, vertical and diagonal arrangements of voxels, with the intensities stated above.*

Overall, separate illumination seemed to be an easy method to achieve gene expression in two separate voxels, that can be scaled up to printing of more voxels, essentially dividing the maximum possible gene expression between the voxels that are printed, reducing the effective contrast. Because of the limitations that scattering poses on the printing time, the main way to increase contrast of multiple voxels is increasing the incident light intensities to reduce printing time. This becomes an issue of light tolerance by the cells. It has already been shown that intensities around 90 W/m^2 for 3 hours kill the cells (see section 3.2.3), so it can be considered that there is also an upper limit in the radiant exposure that can be achieved.

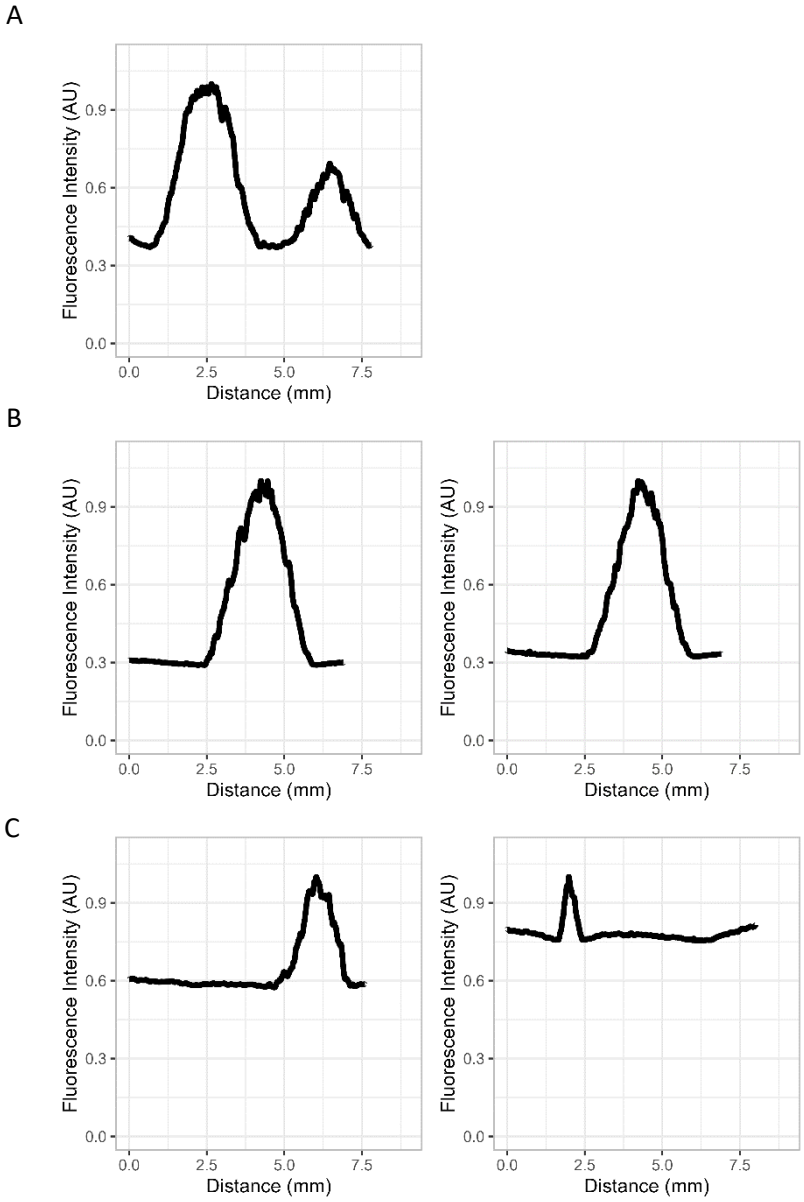


Figure 4.24: *Normalised fluorescence across the x axis for the three geometries with separate illumination. A) Fluorescence for a horizontal arrangement. B) Fluorescence for vertical arrangement. From left to right, the top (p1) and bottom (p0) voxels are presented. C) Fluorescence for a diagonal arrangement of voxel. From left to right, the top (p1) and bottom (p0) voxels are presented.*

Separate illumination was, however, the best candidate for illuminating vertical voxels, as it was based on a deactivation procedure, allowing for a higher range of active photoreceptors to be achieved for each voxel. It outperforms alternating illumination in that it does not need to increase

green light intensity to compensate for green light attenuation, and therefore makes the two voxels independent. In addition, it outperforms concurrent illumination in terms of the achieved contrast.

Separate gene expression was also the best candidate for a diagonal arrangement, with the same advantage over alternating illumination as for vertical voxels. It was simpler than concurrent gene expression, and also offered more consistency as it was less dependent on fluctuations in red and green laser intensity, giving more homogeneous voxels.

Concurrent expression was most suitable for a horizontal arrangement, as it was able to give high gene expression in both voxels. Considerations include the differential red light bleed through at different positions. However, if this is corrected for in the intensities of the green light, any number of horizontal voxels can be illuminated using concurrent gene expression.

Therefore, separate illumination is best for vertical and diagonal arrangements, while concurrent illumination is best in horizontal arrangements. Despite its simplicity, alternating illumination introduces couplings between voxels and does not make use of deactivation procedure to make it sufficiently scalable. In addition, because of the time constraints, the choice of illumination when using multiple voxels depends a lot on the temporal slicing on the voxels through the print time.

In this section, I studied the possibility to illuminate two voxels on the same z-position in the hydrogel, in order to allow control of gene expression of an arbitrary shape in 3D. Three different arbitrary geometric arrangements of voxels were studied, and three different ways to illuminate them. Overall, separate illumination was best for vertical and diagonal voxels, while parallel illumination was best for horizontal voxels.

4.2.5 A combination of illumination methods can print a double helix

Once the illumination procedure for printing voxels in all arrangements in the x, y and z axis was identified, the next step was to identify a way to print a non-trivial 3D shape consisting of voxels that can be connected together as in Fig. 2.3. I decided to print a 3D double helix, because it represents an object that can be made by voxels at multiple arrangements. As it consists of two strands linked at different positions, it is not a shape that can be trivially produced in conventional extrusion-based 3D printing. In addition, it shows another advantage of this 3D printing approach, which is not requiring a solid base to do the printing. It also is a shape that involves illumination in

different positions, and therefore ideal to showcase the capabilities of this optogenetic 3D production approach.

The properties of the helix I attempted to produce included a twist radius of 3 mm, a height of 22 mm, a 2π rad twist rotation and a π rad angle between the two single helices. This double helix was then segmented to 22 points of 1 mm thickness, meaning 22 z-axis points, and two single helices (Fig. 4.25).

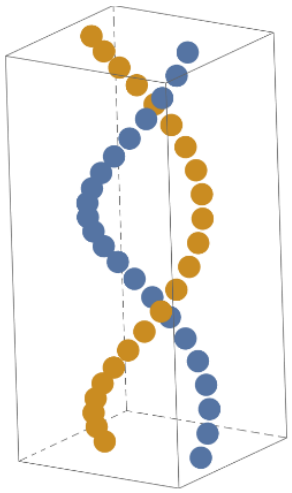


Figure 4.25: *Schematic of the double helix parameters aimed. Double helix with the 22 z-slices aimed. The x-slices are also denoted with two different colours.*

In order to achieve a 3D shape using this approach, it was necessary to split the gene expression by the cells to both temporal and spatial 'slices', or instructions to activate individual voxels. Z-slices, each corresponding to a particular height in the helix, were chosen by identifying the number of points required to produce the helix, and involved slices that are independent on the x-axis, enabling activation in an arbitrary order.

In addition to z-slices, slices in the x/y plane were also devised. The nature of the double helix allowed an easy division into x-slices, with each slice corresponding into one of the two helices. Based on the illumination procedures considered in Section 4.4, x-slices could be devised so that each slice would correspond to voxels in a roughly horizontal arrangement, allowing for deviations in order to increase print fidelity. Sets of slices were arranged in parallel or diagonal arrangement between them. This would allow for concurrent illumination within each x-slice, and parallel illumination between x-slices.

Following this, the helix was further divided to temporal slices, or the order by which slices were illuminated. This posed an issue, due to the temporally changing nature of the culture. This nature stems from the fact that starting OD700 should be as low as possible to reduce scattering, and bacterial responses have been characterised and assessed in exponential state. With this limitation in mind, slices illuminated later during the print would be affected by the higher OD700, leading to different aberrations due to light scattering or more background expression, while slices printed earlier on would also be affected by dilution of photoreceptors due to cell growth. Therefore, temporal slicing could occur either with repeating illumination of the same x-slice in a second timepoint during the print, or by changing the duration of illumination for each slice. The two-pass method is superior for bioprinting compared to single passes at different times, because it is more resistant to variations in growth, and also reduces any bias for the x-slices illuminated last, if the total illumination for each x-slice is shorter than a temporal slice. Therefore, a multi-pass temporal slicing was used, alternating between x-slices and allowing each voxel to be illuminated twice.

With this design in mind, the three-hour print consisted of a first hour of dark incubation, followed by segmentation of the next two hours to eight 15-minute temporal slices, which alternated between the two x-slices. As each x-slice consisted of 22 z-slices, each z and x-slice was illuminated for 40 seconds, including activation and deactivation, with the aim of achieving the maximum possible activation. For this reason, light intensities were set high. Finally, the light intensities were identified to achieve high activation, and target ratio of active photoreceptors in the background areas at 0.1. This was achieved by a red light intensity of 27.6 W/m², and peak green light at 75 W/m². The intensities were adjusted to correct for light attenuation according to Fig. 4.26 .

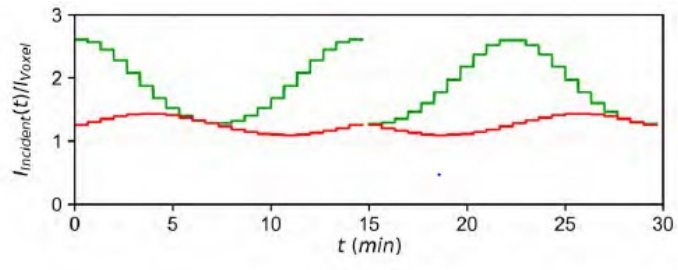


Figure 4.26: *Incident intensities used during the print of a double helix normalized to the respective intensity required at all voxels. Colours correspond to the colour of incident light (adapted from Borut Lampret's thesis).*

Since the thickness of the red beam was 2.3 mm, higher than the thickness of a z-slice, the position of red and green was adjusted to allow for printing and deactivation of multiple slices through the print. The green beam was placed at the top of the red beam's profile, creating essentially two 1 mm regions. This geometry was used to apply the deactivation procedure in less time, as the overlap of green and red could happen at the same time in two different voxels starting from the bottom and moving up, as the second voxel is activated by a green beam on the top of the red beam, the first voxel was deactivated using the red light only.

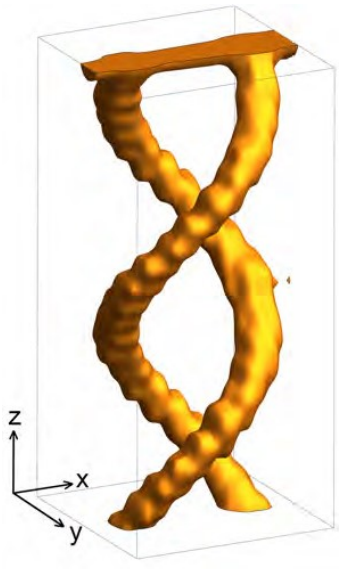


Figure 4.27: *Simulation of the double helix printed under the parameters chosen.*

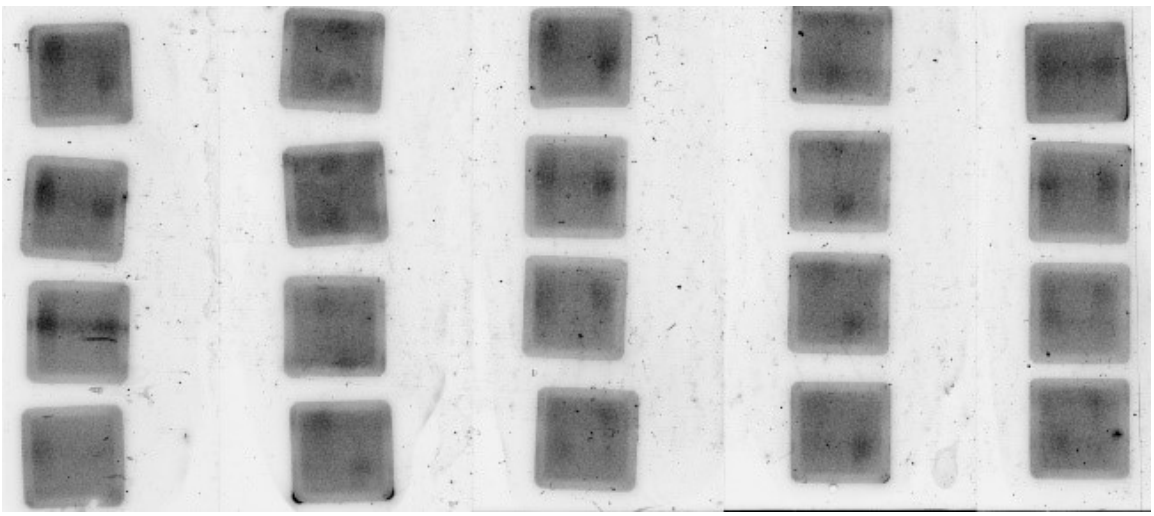


Figure 4.28: *Raw data for the double helix print. In height, the bottom left slice represents the highest position, with the top right slice the lowest.*

A simulation of the double helix, calculated by Borut Lampret with these parameters and by thresholding all slices where fluorescence intensity was above 25% of maximum, indicates the ability to print a clearly defines double helix (Fig. 4.26). The two voxels at the top of the helix were not exposed to red deactivation, leading to a line connecting them. This was also repeated in the voxels at the beginning of the helix, as well as the middle, representing connecting points in the double helix. The actual print of the helix also gave individual voxels suggesting that the 3D printing of the double helix worked with high contrast (Fig. 4.27). 20 physical hydrogel slices were taken, as each was slightly thicker than 1 mm. in the raw data, the individual voxels as well as lines connecting them can be clearly distinguished.

In order to reconstruct the helix, slices of interest were extracted and a threshold for fluorescence intensity set, which varied between different slices by +- 6%. A binary colour was assigned to values above and below the threshold (Fig 4.28 A-B), and slices were then stacked with a 1 mm spacing. This gave a 3D object which resembled the targeted double helix (Fig. 4.28 C). Different structural variations of the helix, such as wider pieces can be attributed to scattering, mainly of green light, as well as misalignment of the z-slices with physical slicing, which can give wider voxels. The helix that was illuminated as the second x-slice is narrower than the first, due to less time for gene expression. In addition, in places where the x-distance between two voxels was greatest, the red light would be more greatly offset, resulting in the red light gap covering the intended voxels, making the actual voxel narrower.

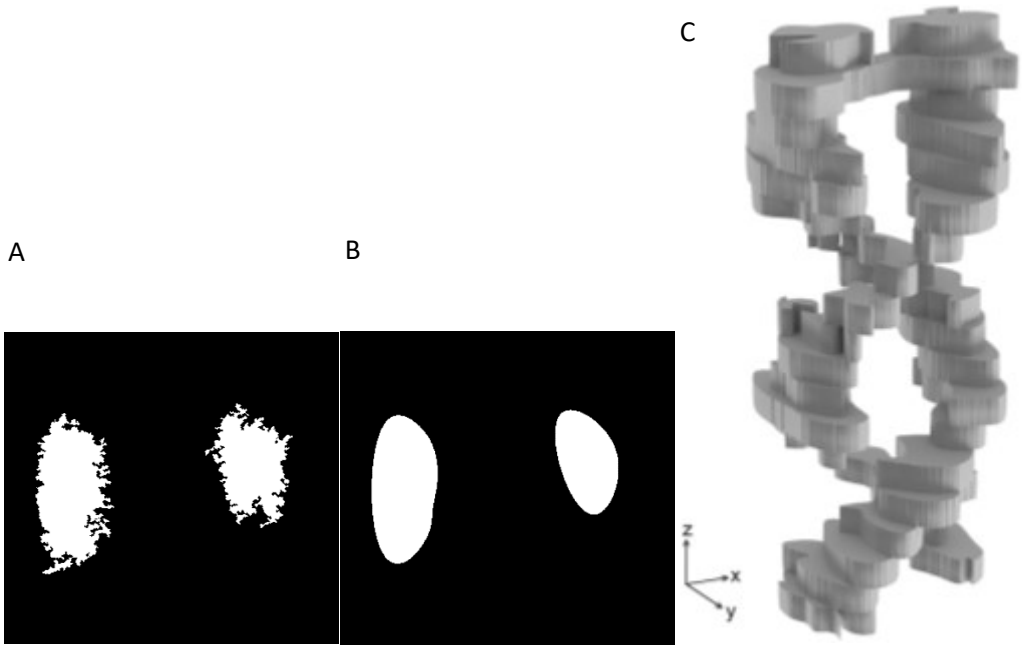


Figure 4.29: *Figures example of two voxels on the same level after thresholding (A) and smoothing (B). (C) Results of the double helix print after thresholding and smoothing.*

Overall, in this section I used the knowledge on discontinuous illumination of multiple voxels in different arrangements, to print a non-trivial shape, such as the double helix inside the hydrogel. Using tdFAST2. For this, it was necessary to split the print into temporal and spatial slices, and organise the printing on each voxel to maximise contrast.

4.3 Conclusions

In this chapter, the ability to print a single voxel in the centre of the print volume is taken and transformed into the ability to optogenetically activate gene expression in a 3D shape.

As a first step, I started with the premise that for multiple voxels to be printed, each individual voxel must be shaped by illuminating it for less time than the time of printing. Thus, the ability to activate a voxel in the 3D volume without the need for continuous illumination was understood, both in theory and by performing a characterisation of the effects of non-continuous illumination. The effectiveness of the system was identified as a balance between the ratio of the proportions of active state photoreceptors in the desired voxel and in the surrounding areas. Due to the extreme hysteresis demonstrated, where active photoreceptors remain active unless deactivated, the ability to temporally separate green and red illuminations was used as a method to achieve greater contrast. The process of discontinuous illumination thus made activation of the system depend not solely on light intensity, but on overall light energy absorbed at a particular wavelength.

Discontinuous illumination was used to produce a line of activation in four different z-locations in the volume. Attempts to print a dot with green illumination followed by red deactivation in the same procedure failed, and the hypothesis that both the red and green effectiveness was greater than reported was assessed with simulations, and trying different intensities of each wavelength. The results suggested that both wavelengths were 5x stronger in effect in our case than reported.

One limitation of the discontinuous illumination approach was that, while the photoreceptors remain active for long time, because of cell division and growth, background expression increases over time, while active photoreceptors get diluted by nascent ground-state photoreceptors. Therefore, a variation of discontinuous illumination with frequent top-ups of the photoreceptor ratios was devised and characterised, which was termed periodic illumination. This illumination was again characterised for a line and single voxel in the volume, showing how good contrast could be achieved in multiple voxels at once using non-continuous illumination.

The next step after establishing periodic illumination, was to be able to achieve control of multiple voxels during the print time, not only on the z-axis but also on the x/y plane. As a thought experiment, two voxels were considered, which could be in 3 rough geometries: horizontal, vertical and diagonal. For each of these geometries, three different ways to achieve voxel activation were

tested in practice. It was found that for the vertical and diagonal approach, a method where each voxel was illuminated separately and independently gave the best results, while for the horizontal approach a free form illumination using deactivation was best. Some aberrations and effects due to red and green light scattering were also identified.

With these approaches clarified, I decided to print a double helix, as it was a non-trivial shape that could showcase the abilities of the optogenetic system. In order to do that, a plan was devised on the size of the helix, deciding to print two interlocking helices of 22 voxels each. The double helix was sliced in localised and temporal slices, allowing for the production of a double helix. When adequately thresholded and analysed, the produced material accurately corresponds to a double helix, showcasing the possibility to optogenetically control gene expression in a 3D setting using microorganisms.

Chapter 5

Optogenetic control of biomaterial and enzyme production in 3D

5.1 Introduction

In the previous chapters, I started from the basis of an *E. coli*-based optogenetic system, which I characterised, and showed its ability to activate expression of a reporter molecule, tdFAST2, in bacteria embedded in a 3D hydrogel matrix. I showed how expression of *tdFAST2* can be induced to produce multiple voxels in arbitrary positions in a 3D volume. I then controlled *tdFAST2* expression in multiple voxels to achieve reporter molecule production in non-trivial shapes, such as that of a 3D helix.

This was an advancement in the field of optogenetic control of bacterial production. It showed an instance of bacterial-driven optogenetic activation in 3 dimensions, as opposed to traditional optogenetic results in 2-dimensional Petri dishes. In addition to an optogenetic breakthrough, this result was foreseen as a new avenue in improving 3D printing of biomaterials. Light-driven applications have been used in conventional 3D printing for years, and confer advantages to 3D printing, such as the ability to produce non-trivial shapes, acute angles, the ability to achieve smooth transitions and the ability to print composites (Kelly et al., 2019; Bernal Nunez et al., 2022). Using an optogenetic approach such as the one developed in the previous chapters to 3D print different biomaterials can thus have a similar effect in 3D Bioprinting, enabling a suite of

applications, such as biodegradable and responsive materials for sensors, structures and medical applications (Gilbert & Ellis, 2018).

In order to move the technology used in the previous chapters from optogenetics to 3D Bioprinting, several issues would have to be faced. Firstly, each material cloned under optogenetic control would affect growth and gene expression by the cells, and therefore different printing durations or illumination intensities might be necessary for each material. Secondly, printing a fluorescent molecule is different from printing an enzyme, or an enzymatic cascade leading to a detectable product. For a fluorescent molecule, the only step standing between protein translation and detection is protein folding, and in the case of tdFAST2, binding to a dye. In the case of enzymes with a detectable product, the kinetics of the enzymes would also have to be considered, as they would probably give a temporal delay to detection of the product, and depending on the kinetics, also an amplification of the product in background and under induction. These would affect both the illumination and incubation time as well as the dynamic range.

Thirdly, there are several limitations with printing a solid product using optogenetics. In order to print a solid-state product, expression has to be adequately high to give connected products, either coupled with secretion, cell surface expression or cell bursting. In addition, non-transparent products have optical effects. In the worst case, a solid product will prevent light from passing through the hydrogel after a certain level of production, therefore reducing the ability to print, and having to alter the printing strategy to achieve production in the desired locations. In the best case, solid products would lead to more scattering of light, reducing contrast and affecting the ability to localise voxels. In any case, printing of a solid material in a 3D supporting hydrogel would also require an ability to remove the hydrogel, by means of heating or dilution, without affecting the product.

In this chapter, with all these considerations in mind, I built upon the proof-of-concept with a fluorescent reporter, to attempt production of two proof of concept biomaterials using this approach. First, I attempt to print poly(hydroxybutyrate) (PHB), a soft bioplastic that can be produced by *E.coli.* I characterised gene expression by the cells in a 96-well plate and a flow cytometer, and then attempted to print in 3-dimensions until a scattering and contrast limitation was reached. As a second 'product' of this optogenetic approach, I aimed to show the versatility of the approach by using 3D bioprinting to create a gradient hardness hydrogel through a gradient of the enzyme agarase. These two materials show both the versatility and abilities of the approach to produce different materials, and highlight potential steps for improvement of the technology.

Objectives:

- Assemble a PHB production pathway under optogenetic control
- Characterise optogenetic control of PHB production by *E. coli*
- Control PHB production in particular 3D locations using optogenetics
- Control production of 3D shapes using PHB
- Control fluorescent reporter production in the whole cuvette in the form of a gradient
- Control whole cuvette production of PHB in the form of a gradient
- Express agarase under optogenetic control
- Control the properties of a hydrogel in the whole cuvette using optogenetics

5.2 Results and Discussion

5.2.1 Combinatorial Assembly of a PHB pathway in *E. coli*

As a first approach for the production of biomaterials I decided to print PHB. PHB is a soft polymer, with a low melting point that is natively produced by *Cupriavidus necator*. PHB has been widely used in synthetic biology, as different researchers have analysed the enzymes involved to optimise production in *C. necator*, and cloned genes encoding for PHB production to other organisms, including *E. coli* (Rahman et al., 2013; Cavalheiro et al., 2009).

Traditionally, PHB is produced from the downstream metabolism of acetyl CoA, through the PhaCAB operon in *C. necator*. This includes 3 genes: *phaA*, encoding a 3-ketothiolase, which catalyses the conversion of 2 molecules of acetyl-CoA to acetoacetyl-CoA; *phaB*, encoding an NADPH-dependent acetoacetyl-CoA reductase, which produces 3-hydroxybutyl-CoA from acetoacetyl coA; *phaC*, encoding poly(hydroxyalkanoate) synthase, which catalyses the polymerisation of 3-hydroxybutyl-CoA into PHB (Wang & Yu, 2007; Turco et al., 2021; Introduction 1.2.2.2).

In addition, three other genes have been identified as playing an important role in the production of PHB in *E. coli*: *atoB* encodes for a naturally evolved analog of *phaA*, which could potentially give optimised codon usage in transferring the pathway to *E. coli*. In addition, *gapN* and *gapC* have been identified as genes encoding for proteins which increase availability of NAD(P)H in *E. coli*, increasing the efficiency of phaB. *gapC* encodes for glyceraldehyde-3-phosphate dehydrogenase, which converts glyceraldehyde-3-phosphate (G3P) to 1,3-bisphosphoglycerate. *GapN* encodes an enzyme, which converts glycerate 3 phosphate into 3-phosphoglycerate, releasing NADPH (Introduction 1.2.2.2).

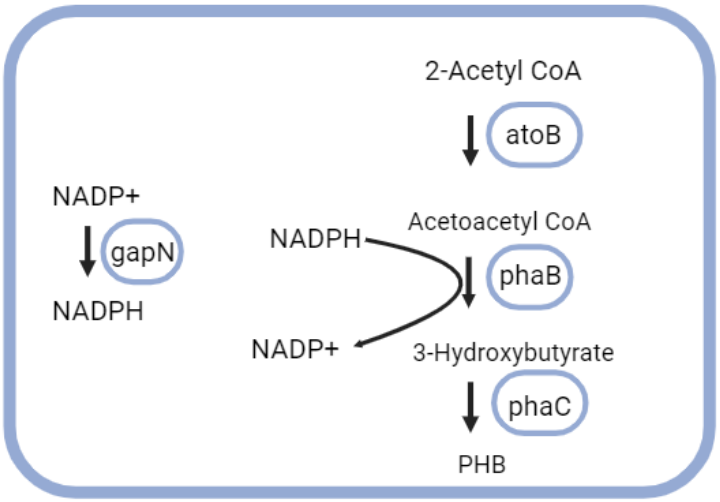
These genes were combined to a genetic library by George Taylor and Martin Todd, with the aim of performing a combinatorial screen to identify the combination of genes that showed the highest production of PHB when cloned together. The six genes were mixed with an equimolar mixture of RBSs that have been shown to allow for a range of expression levels, under the control of the rhamnose-inducible PrhaBAD promoter, which showed low leakiness and a high dynamic range (Hjelm et al., 2015; Taylor et al., 2019). T1 was used a strong transcriptional terminator (Zampini et al.,2016).

Following design and combinatorial assembly of the pathway using Start-Stop assembly (Taylor et al., 2019), clones were sorted according to fluorescence intensity using a FACS machine (Materials and Methods 7.3.3.9). The ten highest producing clones were further assessed using microscopy and flow cytometry, and the top producing clone was identified and sequenced.

PHB production was quantified indirectly by means of fluorescence intensity. In order to image PHB, staining with a dye is still necessary, as it enables fluorescent detection. Nile Red is a dye that non-specifically stains PHB, as well as lipids through hydrophobic interactions (Juengert et al., 2018), has a fluorescent excitation maximum at 544 nm and emission at 634 nm and is membrane permeable. In order to verify PHB production, the highest-producing rhamnose-inducible PHB clone (termed CPHB3) was stained with Nile Red and imaged alongside DH10B cells stained with Nile Red, indicating that the difference could even be visible with naked eye (Fig. 5.1).

The top producing clone contained as expected, *phaB* and *phaC* from the *C. necator phaCAB* operon. *Atob* was the gene at the beginning of the pathway, as it had optimised codon usage in *E.coli*, while *gapN* was used as the source of NADPH (Fig. 5.1).

A



B

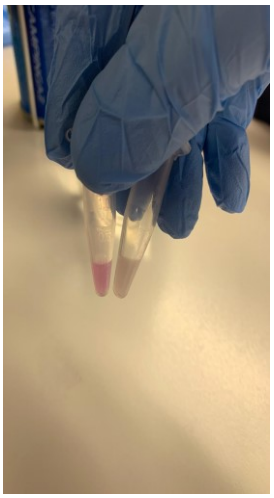


Figure 5.1: *A) Schematic of PHB production in E. coli. B) Stained samples of the PHB-producing clone (left) and wild type DH10B cells, stained with Nile Red.*

Following combinatorial assembly, PHB production by different clones assembled was assessed by means of flow cytometry. The top producing clone was sequenced, and the RBSs and genes identified in the order they were used. The order of the genes in the operon was *PhaC, atoB, PhaB, gapN*. The RBSs used for each of the genes were RBS 33, RBS 44, RBS 58 and RBS 13 in order (Taylor et al., 2019) (Figs. 5.1 & 5.2).

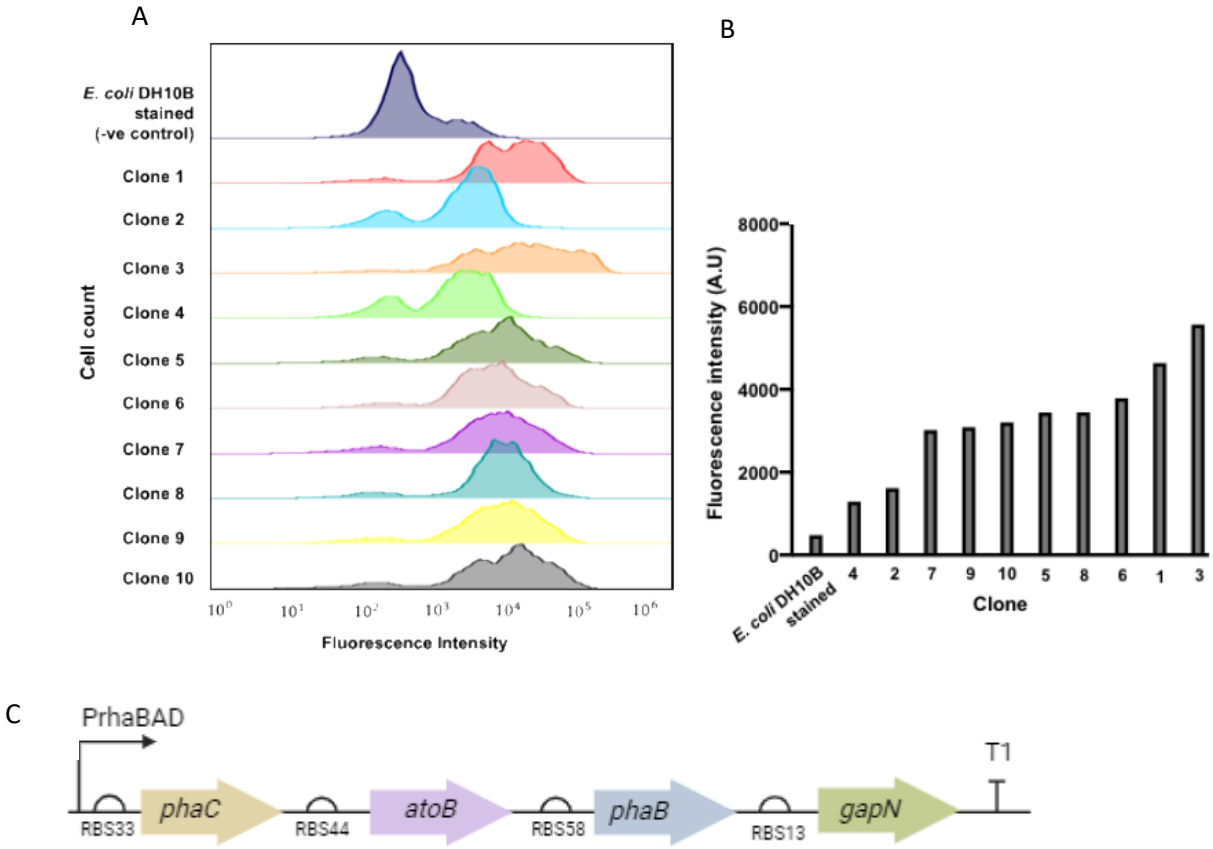


Figure 5.2: *Assessment of PHB-production under rhamnose induction. A) Schematic of flow cytometry with different PHB-producing clones. B) Geometric mean of fluorescence intensity for the different clones. These two images were modified from Martin Todd's Masters Thesis (Todd, 2019). C) Sequence schematic for PHB production under PrhaBAD control (CPHB3).*

Overall, the dynamic range observed in PHB production with rhamnose induction, compared to control cells was promising as to the detectability of PHB. In addition, microscopy indicated that cells with high PHB production would swell and burst with PHB. This was promising, as it allowed for a potential for PHB production by different cells to be exported from the cells in a 3D context, potentially forming a 3-dimensional material.

In this section a module encoding PHB production under rhamnose control in *E. coli* was built and assessed, indicating a high dynamic range.

5.2.2 PHB production under optogenetic control in liquid media

Having established the dynamic range and production of PHB under rhamnose control, the next step was to establish PHB production under optogenetic control. In order to achieve this, I cloned the PHB-producing operon from CPHB3, including the genes and RBSs found during the screening of the combinatorial assembly results, into the pSR58.6 plasmid, and using this operon to replace

sfGFP under control of the PcpG2-172 promoter (Fig. 5.3). The resulting plasmid, together with the CCaSR 3.0 helper plasmid NO286.3 were then transformed into *E. coli* TOP10, to give a strain encoding PHB production under CCaSR 3.0 control (strain termed BP18) (Fig. 5.3).

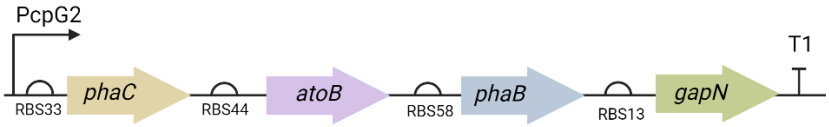


Figure 5.3: *Schematic of the order of genes in PHB production under CCaSR 3.0 control (BP18).*

I then proceeded to characterise growth and gene expression of PHB by BP18 cells. I used a similar method to the initial characterisation of CCaSR 3.0. I first investigated growth and gene expression in darkness in liquid, before testing the response of the cells to light in liquid and solid media over 5 hours.

BP18 in darkness had generally slower dynamics than CCaSR 3.0. At first glance, both the OD700 and fluorescence intensity curves showed a similar shape as the standard bacterial growth and production curve, with an initial lag phase, exponential region and then levelling off at the end for stationary phase (Fig. 5.4). For OD700, exponential phase for BP18 started after about 100 minutes and ended after around 500 minutes. This was shorter and a bit delayed compared to CCaSR3.0, where exponential phase started slightly earlier, at 60 minutes, and lasted until 500 minutes (Figs 2.3 & 2.6). CCaSR had OD700 of around 0.05 after 200 minutes of incubation, whereas BP18 was at about 0.025. In addition, after 6 hours, BP18 OD700 plateaued around 0.3 AU, whereas CCaSR plateaued around 0.4 AU.

The beginning of exponential increase in fluorescence intensity for BP18 was around 200 minutes, while for CCaSR 3.0 and BP16 it was around 100 minutes. The increase in fluorescence intensity was much slower in BP18 than both other strains (Fig. 5.4, 2.8 & 2.16). Of course, the scale and wavelengths used were different, as CCaSR 3.0 used a fluorophore and BP16 used a dye with a excitation/emission spectrum similar to GFP, while BP18 uses a dye with an excitation/emission spectrum closer to that of mCherry, making it impossible to compare maximum fluorescence between the two. However, dynamics can be compared, for example by comparing the fold difference between maximum fluorescence under green light and minimum fluorescence under red light. For CCaSR 2.0 and 3.0, for example (Fig. 2.3), the half maximal fluorescence intensity was reached around 300-350 minutes, while for BP18 half maximal fluorescence was reached at 450 minutes, indicating a 30% delay in reaching half-maximum. After 180 minutes, which was the 3D

printing time, the fluorescence reached by the CcaSR strains was about 25% of maximum fluorescence. For BP18, at 180 minutes only 8% of maximum fluorescence was reached. Instead, 25% of maximum fluorescence was reached at 330 minutes.

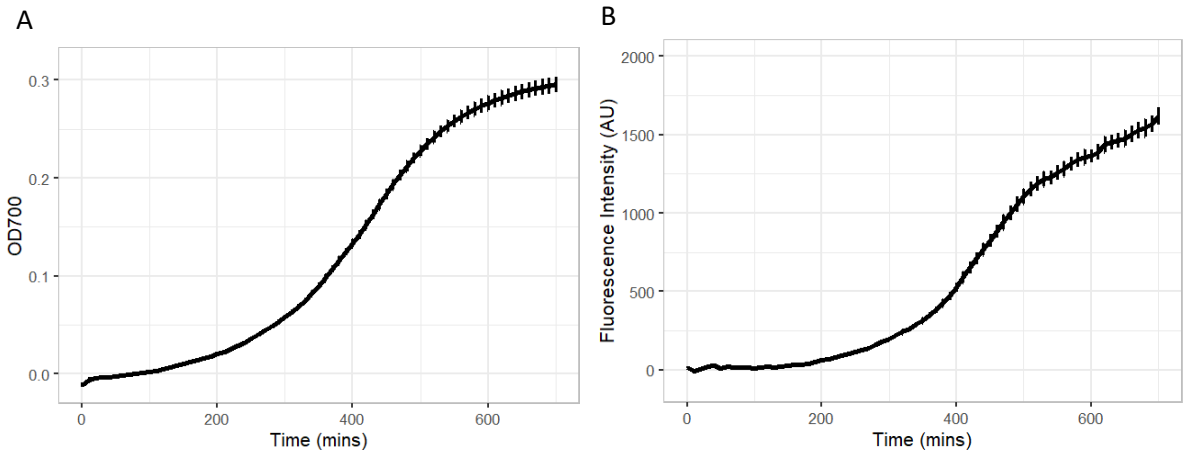


Figure 5.4: *OD700 (A) and fluorescence intensity (B) for BP18 in a liquid M9-glucose media (n= 4, error bars represent standard error).*

These results indicated that there was significant burden imposed on the system, both on growth and gene expression. On the growth front, burden imposed by transcribing and translating 4 large enzymes would be much larger than that of one small protein, taking away resources from cell division towards transcription and translation (Ceroni et al., 2018). In addition, it is possible that PHB is also toxic to the cells (Bokrova et al., 2019). The delay in fluorescence can partly be attributed to burden and toxicity as well. However, some of the delay might also come from the fact that enzymes, as opposed to fluorescence proteins were produced. Therefore, in BP18 there were steps between translation of the enzymes and production of the product, which would not be present for sfGFP or tdFAST2.

In order to further investigate the dynamics of the enzymes, the kinetics of the enzymes involved in PHB production were investigated by looking into the kinetic parameters for each of the enzymes involved in the pathway. Interestingly, the lowest k_{cat}/K_m was shown by Phab, essentially limiting the supply of 3-hydroxybutyl CoA to phaC. (Table 5.1). It is also possible that by transferring these enzymes to *E. coli,* both their expression numbers and kinetic properties might be altered in the new context. Of course, expression level of these enzymes would also affect flux through the pathway.

Enzyme	K_{cat} (s-1)	K_m(mm)	K_{cat}/k_m (s-1 mm-1)
phaB	0.5	0.005	10
phaC	44	0.19	231.6
atoB	6.5	0.47	13.8
gapN	17.7	1.7	10.4

Table 5.1: *The parameters for each of the enzymes involved in PHB production. Parameters are from (Belova et al., 1997; Normi et al., 2005; Filinger et al., 2000)*

BP18 was also tested in liquid through use of the light plate, to see its response to different red and green light intensities. OD700 showed an exponential increase over time, consistent with bacterial dynamics, but no difference in growth was observed between different illumination intensities. This might be because even small amounts of expression of PHB were already burdensome and toxic enough that higher expression did not have a significant effect (Fig. 5.5). All curves, under no green light and with green light showed a very similar trend, reaching OD700 of around 0.11 after 5 hours.

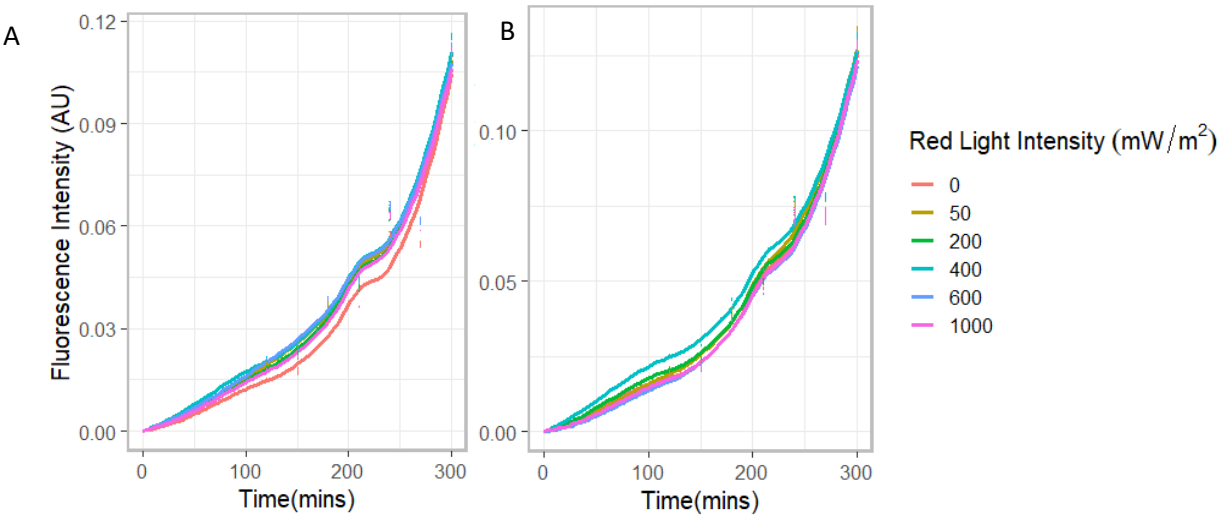


Figure 5.5: *OD700 over time with different red light intensities by BP18 in liquid media. A) Red light intensities were applied with no green light. B) Red light was applied in a background of 1 W/m² green light illumination (n = 3, error bars represent standard error).*

Regardless of differences in OD700, fluorescence intensity varied between different light intensities and wavelengths. Similar to what was observed in CCaSR 3.0 and BP16, fluorescence intensity generally increased with green light intensity and decreased with red light intensity. Like the GFP

and tdFAST2 versions, in BP18 red light was less efficient than green, only managing to significantly reduce fluorescence for green intensities below 200 mW/m². For 200 mW/m² green light, red light above 600 mW/m² showed some suppression, suggesting again a difference of about 5x required for red light to suppress green light effectively (Fig. 5.6 A-D).

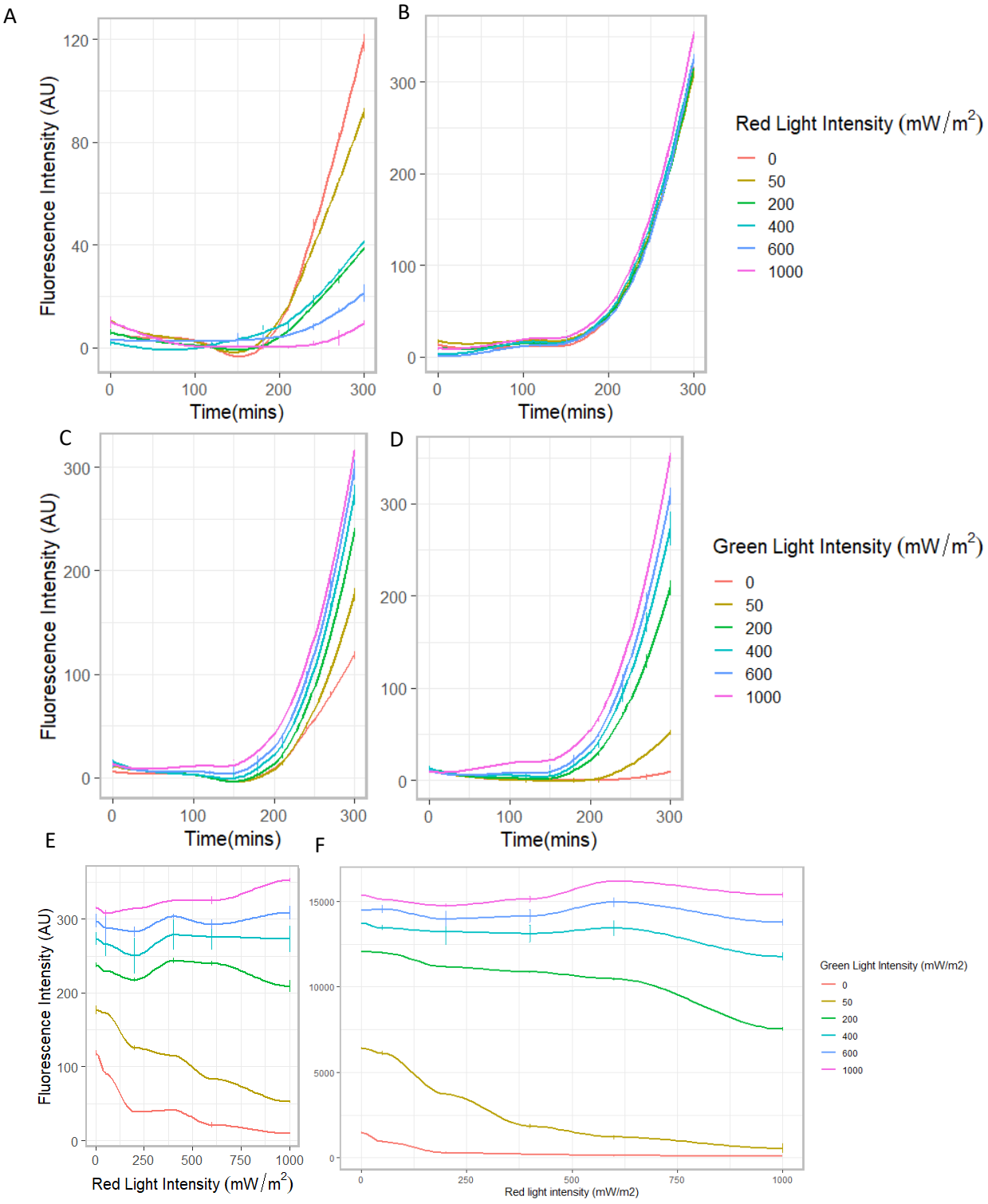


Figure 5.6: *Fluorescence intensity over time with different light intensities, by BP18 in liquid media. A) Different red light intensities in no green light. B) Different red light intensities with 1 W/m²*

green light. C) Different green light intensities with no red light. D) Different green light intensities with 1 W/m² red light. E) Red and green light intensities at 300 minutes for BP18. F) Red and green light intensities at 300 minutes for BP16 (n = 3, error bars represent standard error).

The range of activation for BP18, was compared by calculating the fold difference between cells illuminated with 1 W/m² green and no red light, compared with cells 1 W/m² red and 0.2 W/m² green light. This range was about half that of CCaSR3.0 and BP16 (Fig. 5.6 E-F). This was also consistent when comparing other intensities, such as over time change in fluorescence in BP18 for no red, red at 1000 mW/m², no green and green at 1000 mW/m². The shape and pattern of graphs was very similar to Fig. 2.8. However, the differences in the maxima reached between different graphs, as well as within each graph showed that the range was lower, and red light was even less efficient at reducing fluorescence.

The lower range can be explained again by the enzymatic form of production against production of a fluorogen. Due to the amplification of enzymatic cascades, depending on the level of saturation and activation of individual enzymes, the background can be higher and dynamic range generally reduced. This partly applies to the lower efficiency of red light, as the half-life of the enzymes would reduce dynamic range specifically on inhibition. In addition, as the mixture is generally red in colour due to the addition of Nile Red, red light is reflected more than green, and therefore less red light is perceived by cells.

By studying fluorescence divided by OD700 (Fig. 5.7), the same observations can be made with regards to the dynamic range. In addition, fluorescence/OD700 appeared to peak slightly before 300 minutes as the cells started growing faster from 270-300 minutes. This is consistent with a delay in catalysis by the enzymes, as they are produced at a higher rate by more cells, but some time is required until this is seen in production of the end product.

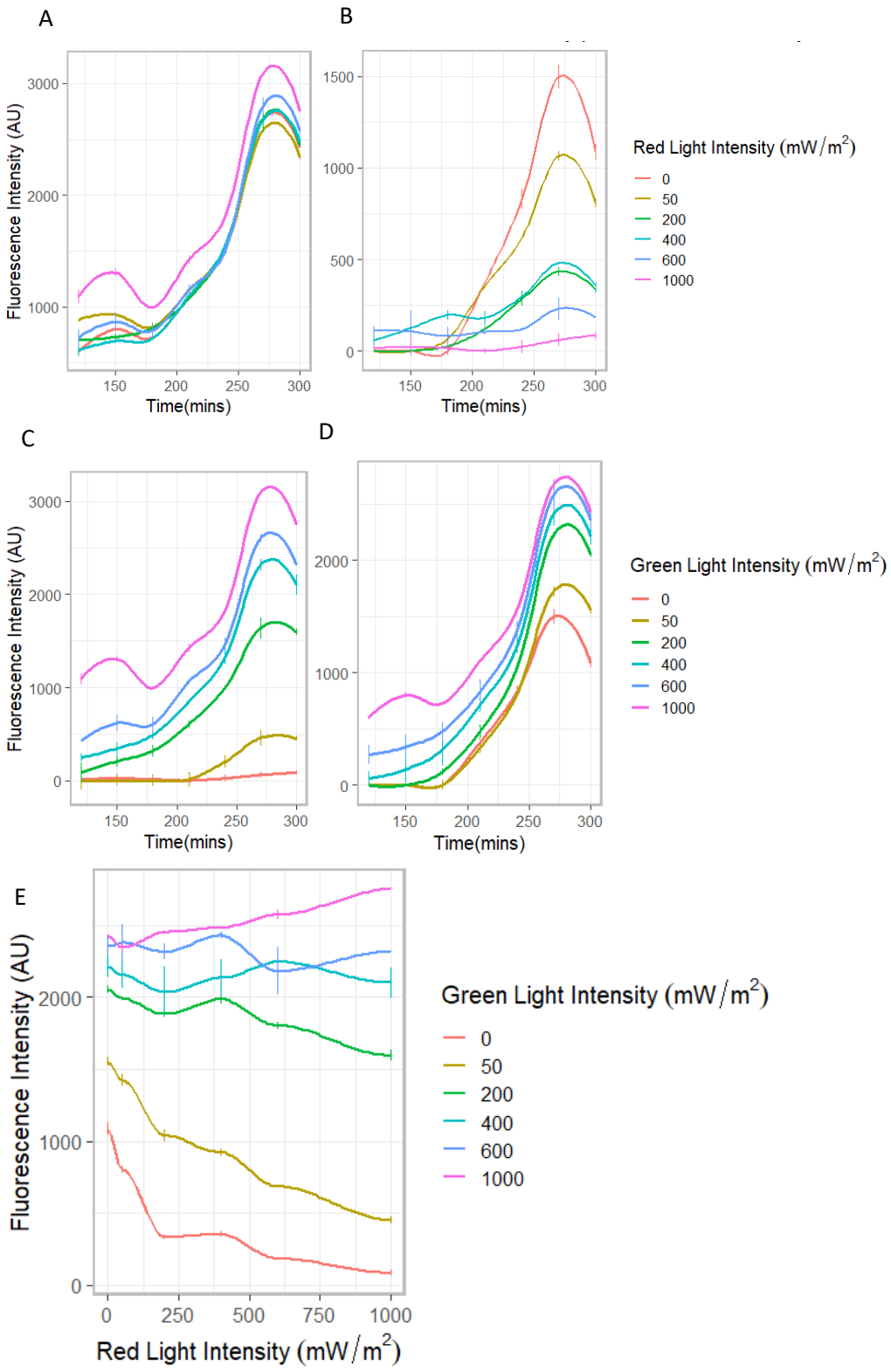


Figure 5.7: *Fluorescence intensity/OD700 by BP18 in liquid media. Different red light intensities with 1 W/m² green B) Different red light intensities in no green. C) Different green light intensities with 1 W/m² red. D) Different green light intensities with no red. E) Red and green light intensities at 300 minutes for BP18 (n = 3, error bars represent standard error).*

Fluorescence intensity change rate over time (Fig. 5.8) was assayed after the first two hours of incubation, during the early exponential part of cell growth. Fluorescence intensity increased linearly over time, indicating an increase in production of PHB following the initial lag phase. Increasing red light intensity had little effect on the rate of fluorescence intensity change for higher green light intensities, only starting to have an effect at red light above 500 mW/m^2. For the no green and the lowest green light intensity used however, increasing the red light intensity visibly slowed down fluorescence intensity increase.

Interestingly, in darkness as well as in the presence of lower green light intensities, fluorescence intensity change rate levelled off over time, and this levelling off became more apparent with increasing red light intensity. This is likely because of dilution of active photoreceptors with growth, which were not replenished as fast with lower green light intensities.

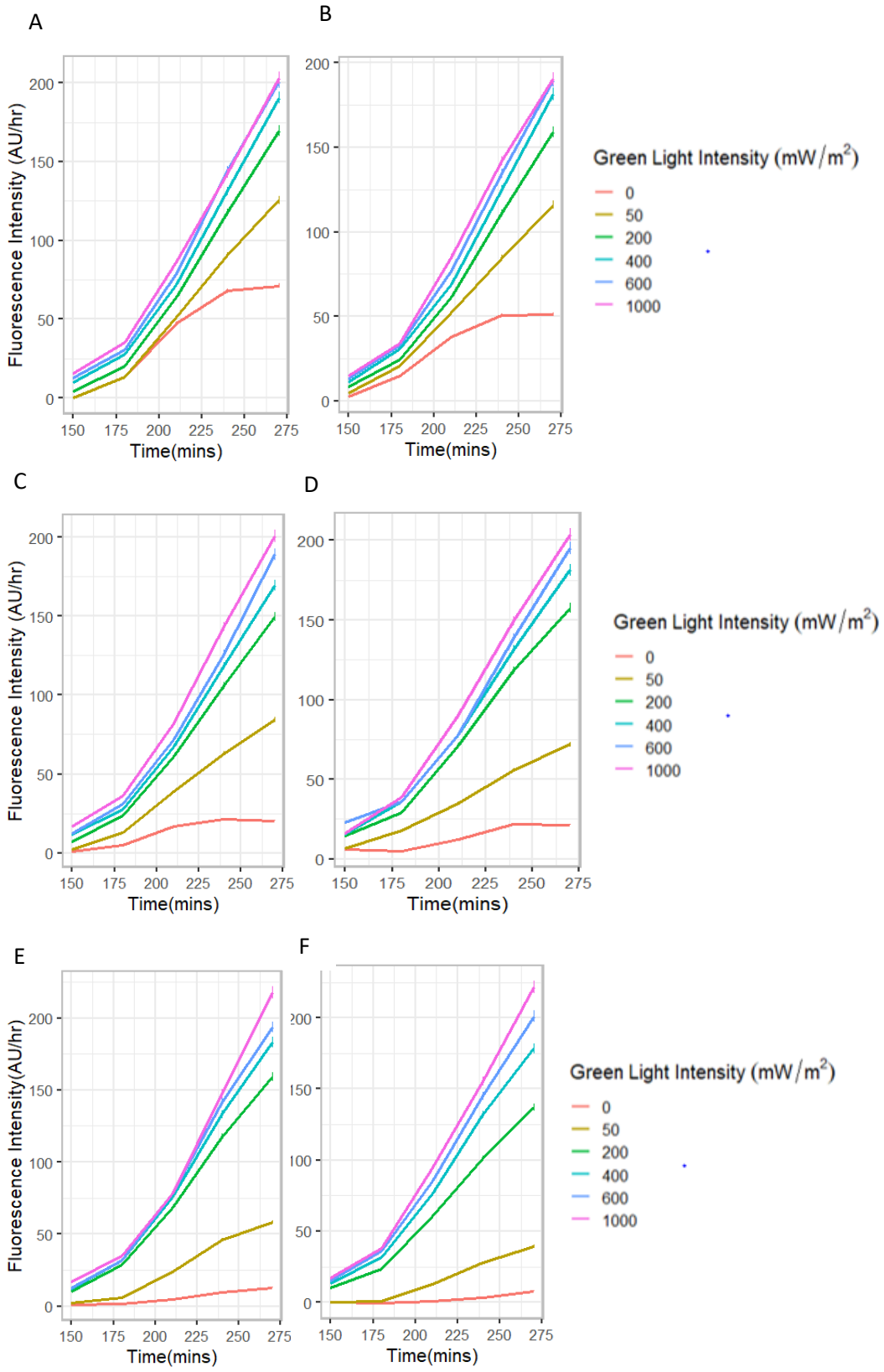


Figure 5.8: *Fluorescence intensity change rate over time. Results are shown for all green light intensity, while each panel from left to right and top to bottom corresponds to an intensity of red light intensity. Intensities of red light used were: 0, 50, 200, 400, 600 and 1000 mW/m² (n = 3, error bars represent standard error).*

To further assess PHB production under different intensities of light, BP18 cells were incubated for 5 hours under darkness, red light at 1 W/m² and green light at 1 W/m², followed by quantification by flow cytometry (Fig. 5.9). All samples showed a large population of non-activated cells, potentially corresponding to dye not binding to the already-made PHB. When gated for that population, the cells exhibited the expected behaviour, with cells under green showing higher fluorescence intensity than those in dark and red. Interestingly, the range between red, green and dark fluorescence production under the flow was much lower than that observed under BP16 (Fig. 2.8).

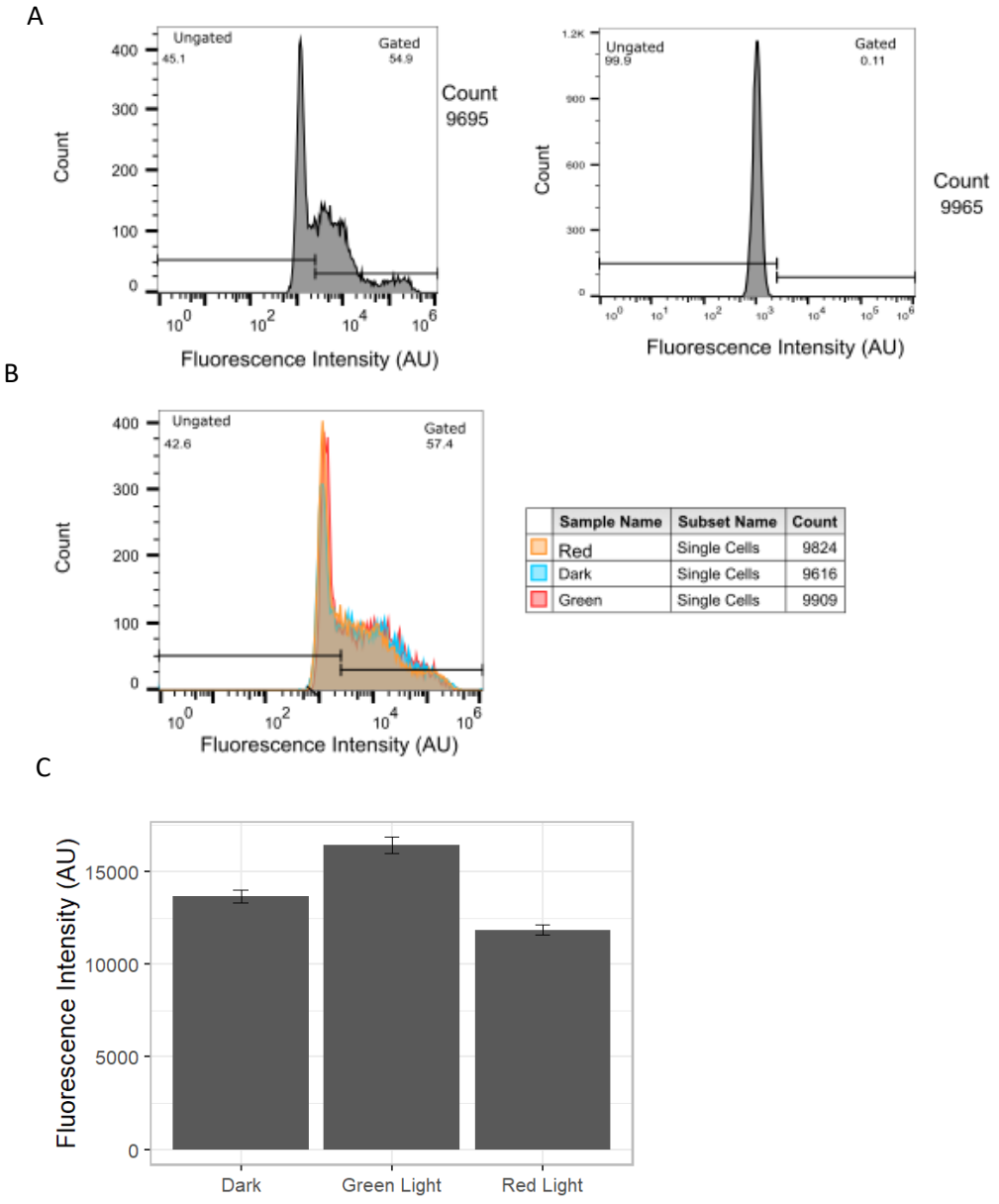


Figure 5.9: *Flow cytometry of BP18. A) Control of BP18 cells with Nile Red, and BP18 without a dye, from left to right, showing the position of gating. B) Overlay of the 3 conditions, with the gate shown and percentage of cells on either side of the gate. C) Bar plot of positive populations. (n = 3, error bars represent standard error).*

In this section, the PHB production module was cloned under CCaSR 3.0 control and characterised under liquid media, indicating a dynamic range slightly smaller than tdFAST2 under different illumination regimes.

5.2.3 PHB production under optogenetic control in solid media

Having established the slower growth and PHB production in liquid media, it was possible to move on and test production and growth in solid media. As a first iteration, I performed the experiment in the same 1% agarose hydrogel that was used in the proof of concept print with tdFAST2, with M9-glucose (Fig. 5.10). As expected, growth was slightly slower than in the liquid, reaching about 80% of the OD700 reached after 500 minutes in liquid. Fluorescence intensity was lower too, plateauing at 80% of maximum fluorescence in liquid. Both OD700 and fluorescence intensity also plateaued earlier than in the liquid, starting to enter stationary phase around 500 minutes, while in liquid culture stationary phase started after 600 minutes.

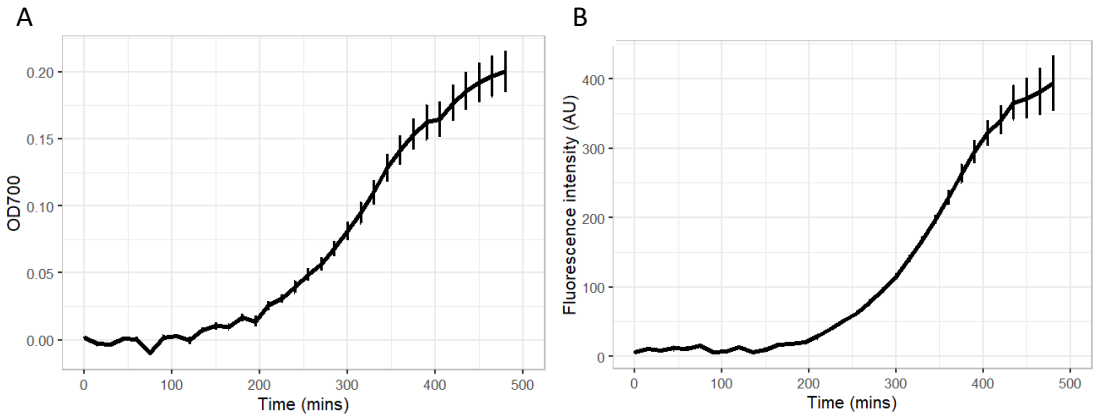
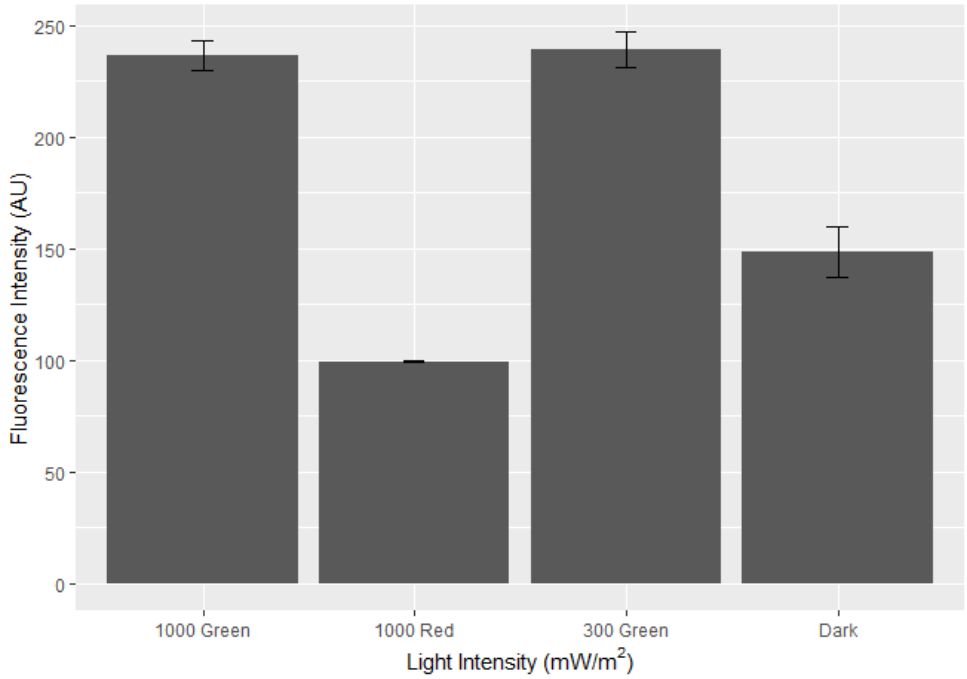


Figure 5.10: *OD 700 and fluorescence intensity over time in 1% agarose M9/glucose hydrogel (n = 3, error bars represent standard error).*

Similar with CCaSR 3.0, and because of the different wavelengths used for fluorescence detection, I wanted to compare between different growth media in agarose, in order to check whether LB was still masking fluorescence, or if the richer media like LB would allow for higher gene expression to compensate for it. For this reason, I prepared media containing 1% agarose and either M9-glucose or LB, and bacteria incubated in these media for 360 minutes under different light intensities, and results assayed. The experiment performed in LB did not show higher fluorescence overall (Fig. 5.11). Bacteria grown in M9 showed consistently higher fluorescence by 40 AU (20-40%), indicating some masking of fluorescence by using LB. Therefore, M9 was kept as the growth media of choice for this experiment.

A



B

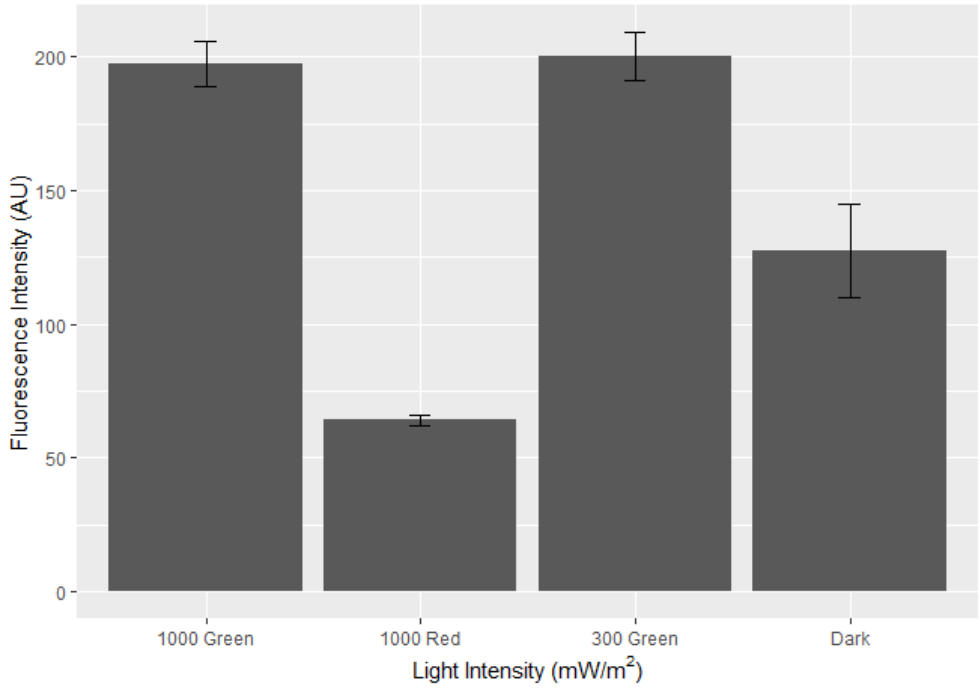


Figure 5.11: *Fluorescence intensity after 360 minutes, for 1% agarose media containing either LB (A) or M9/glucose (B) (n = 3, error bars represent standard error).*

Having established the media and background production of PHB, I then went on to characterise response and production by BP18 to a variety of light intensities, in the M9-agarose hydrogel (Fig. 5.12-13).

Overall, growth was very similar to that observed in liquid, and did not vary again between different illuminations. It was hypothesised that the initial burden observed was already toxic enough to the cells, that all other effects did not have a significant effect (Fig. 5.12).

Fluorescence intensity in hydrogel over time was not much lower than in liquid media, indicating that PHB production was not significantly affected by the change in media and absence of oxygen (Fig. 5.13). Red light, however, seemed to be less effective under no green light, compared to the experiment in liquid media. For example, under no green light, 200 mW/m^2 red light was enough to reduce fluorescence intensity to effective minimum in liquid, while it was 50% higher than minimum in the hydrogel (Fig. 5.13 A). This might be because of the lower transparency of the hydrogel, which is exacerbated by the presence of Nile Red. However, looking at red light under different intensities of green (Fig. 5.13 D) as well as the chart of the combination of wavelengths at 300 minutes (Fig. 5.13 E), it appears that a high red light intensity is slightly more effective at suppressing red green light related gene expression. The effect of red light was calculated by comparing fluorescence intensity in the samples illuminated with maximum red and green, against samples illuminated with maximum red and either no green or green at 60 mW/m^2. This range was about 60% higher than that of liquid media, indicating more effective suppression by the red light. In addition, higher green intensities seemed to have a closer fluorescence intensity profile, showing a saturation of production at low intensities of green light.

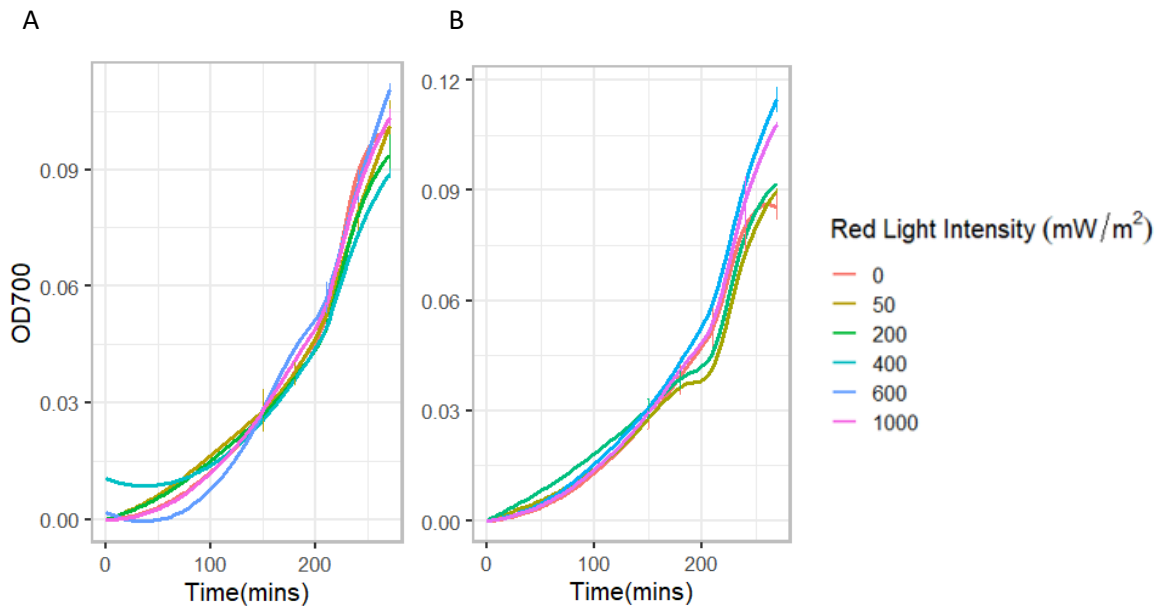


Figure 5.12: *OD700 over time under different light intensities in a 1% agarose-M9/glucose hydrogel. A) Red light intensities were applied with no green light. B) Red light was applied in a background of 1 W/m² green light illumination (n = 3, error bars represent standard error).*

There results were encouraging regarding the effectiveness of the red light in supressing green light, but also worrying about the ease of saturation of the system by low intensities of green. Ultimately, what these results meant was that the effect of red light in supressing both the tails of production when activating a voxel, as well as the voxel itself through scattering, were quite significant and should be taken into account. In addition, the contrast compared to BP16 in hydrogel was around 25% lower than that of BP16 in hydrogel, making the print yet harder.

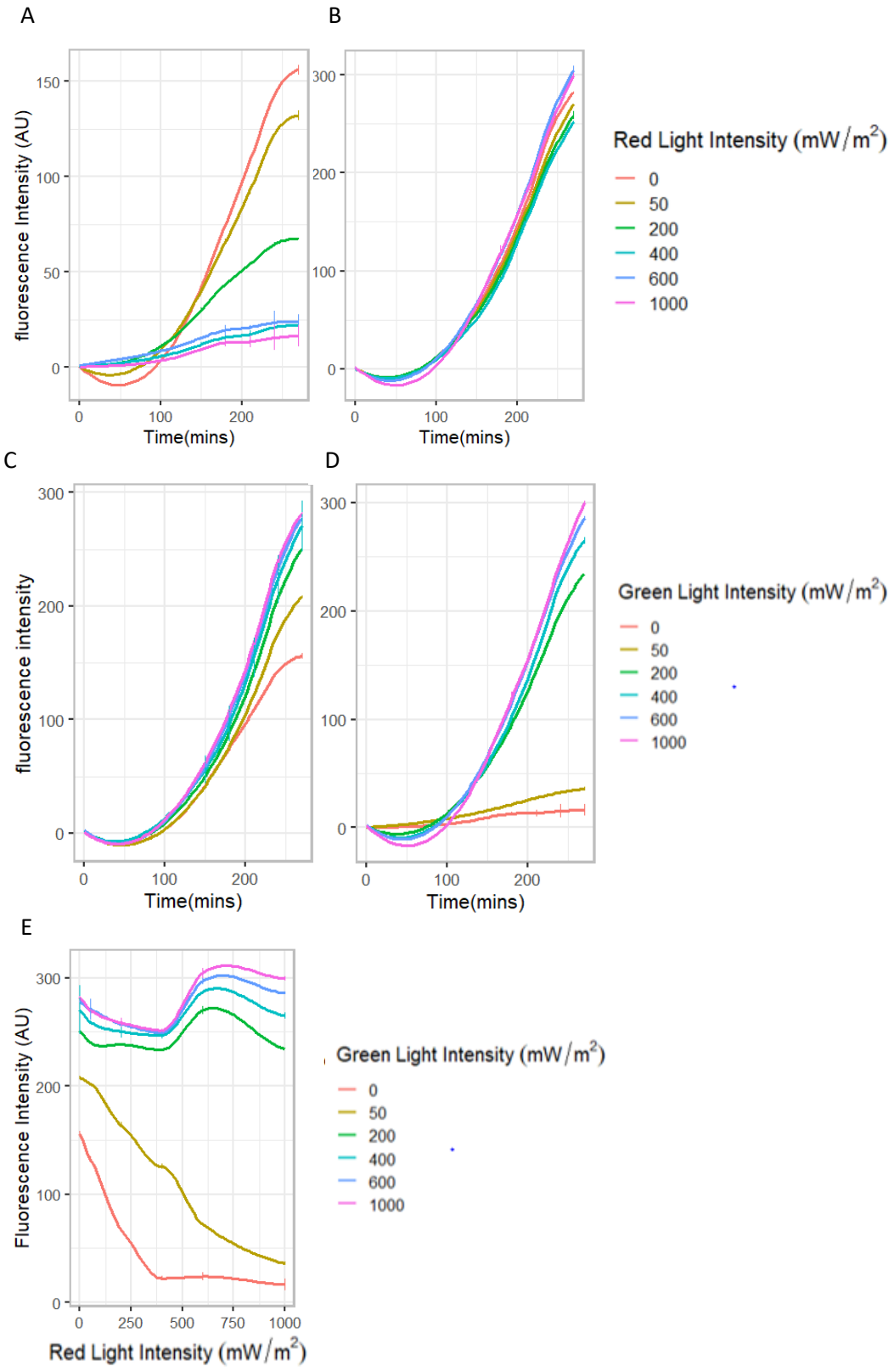


Figure 5.13: *Fluorescence intensity under different light intensities in a 1% agarose-M9/glucose hydrogel. A) Different red light intensities in no green. B) Different red light intensities with 1 W/m² green. C) Different green light intensities with no red. D) Different green light intensities with 1 W/m² red. E) Red and green light intensities at 300 minutes for BP18 (n = 3, error bars represent standard error).*

In this section, PHB production was assessed under different illumination intensities in solid media, to again indicating slower growth and production of PHB, compared to tdFAST2 expression.

5.2.4 Optogenetic control of PHB production within a cuvette with continuous illumination

Despite the limitations of the slower growth and production, as well as the lower contrast, I set about attempting to quantify production of PHB in 3 dimensions. Because of these limitations, however, the printing procedure was slightly altered. Because of the slower growth and production, it was postulated that a longer time would be needed for cells to reach necessary contrast and production, and the slower growth would mean the presence of fewer cells which would not interfere as much with light. For this reason, initial prints attempted characterisation of printing a line under continuous illumination for a range of times, from 5 to 7 hours (Fig. 5.14).

In order to fully assess the capabilities of printing the line, it was first attempted with a high green light intensity of 1.45 W/m^2, to see which incubation times gave the most consistent results (Fig. 5.15). The slides were analysed in the same way as Chapters 3 and 4, with normalising to the maximum production.

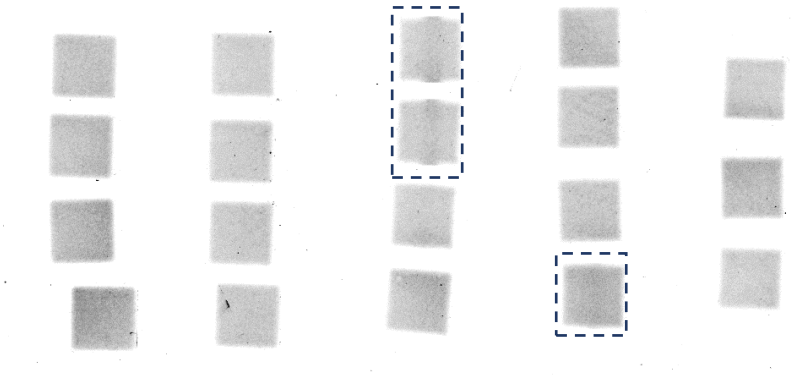


Figure 5.14: *Darkened and contrasted data of PHB printing of line. In the top two slices in the third column, and bottom slice in the fourth column (in dashed rectangles), the line of gene expression can be faintly seen.*

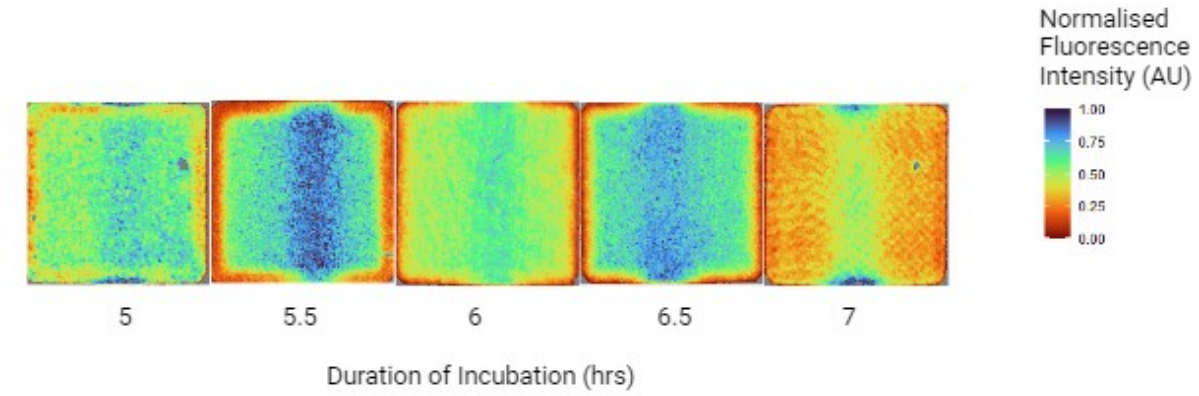


Figure 5.15: *Analysed data of PHB line with different times of incubation. Light intensity was 1.4 W/m² green.*

A clear line was produced by all periods of illumination, with perhaps 5.5 hours giving the clearest line, and slightly fading for longer incubations. Similarly to BP16, a halo was observed in most prints. The width of the printed line was about 2.5 mm, much larger than the width of the laser, partly due to the high green intensity used, and partly due to light scattering due to growth of the cells.

The profiles of the prints, parallel and perpendicular to the direction of the green line were also plotted (Fig. 5.16). The most significant observation of these plots was again, the width of the activated beam in the perpendicular plots, as well as, comparing them to plots of BP16 (Chapter 3), the lower contrast of the printed line to the background (Fig.3.18-3.21. The plots parallel to the beam were qualitatively very similar in shape to those for BP16, with some variability but overall constant intensity throughout the line, except for the halo areas.

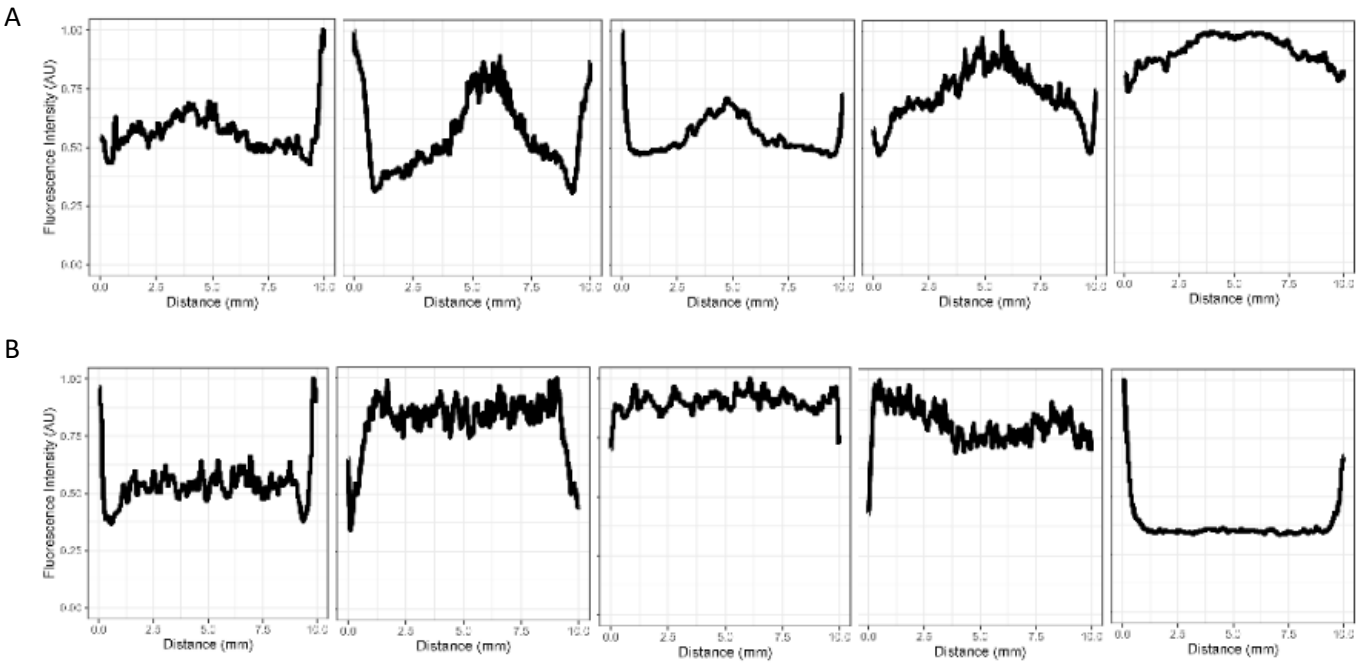


Figure 5.16: *Plots parallel and perpendicular to the line. A) Plots of light intensity perpendicular to the green beam. B) Plots parallel to the direction of the green beam. From left to right, duration of incubation is increased as in (Fig. 5.15).*

The same printing was performed for 5 hours with LB media, in order to assess again whether LB would be a candidate for 3D printing of PHB (Fig. 5.17). However, the contrast with LB was diminished, as M9 at 5 hours gave superior results.

Because of the clear line in most prints using M9, I decided to continue the print using the lowest of the incubation periods. This was done because for prints producing a voxel or multiple voxels, scattering would start to play a more important role, and localisation was important. In addition, to improve localisation I attempted to reduce the width of the line by using a lower green light intensity, at 0.8 W/m² (Fig. 5.18).

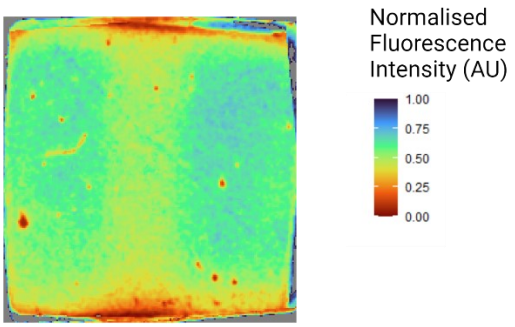
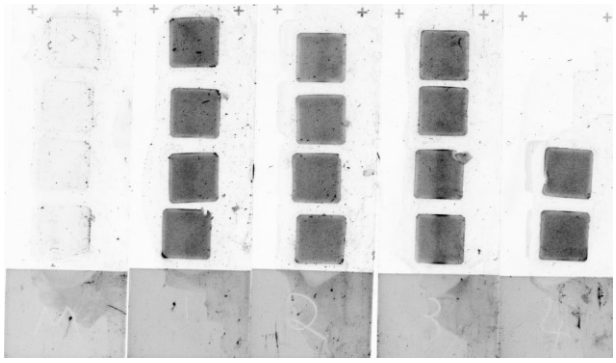


Figure 5.17: *Slice of PHB print in LB media using 1.4 W/m² green light for 5 hours.*

Using 0.8 W/m² green, the line and contrast was still very clear, with much better localisation, of a width of the line at about 1.7 mm, suggesting an improvement in localisation without sacrificing peak intensity and production.

A



B

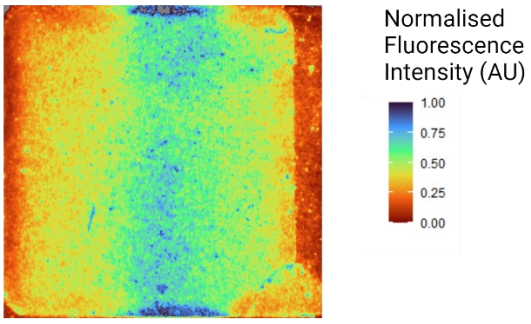


Figure 5.18: *Printing for 5 hours with a lower intensity. A) Raw data of the print for 5 hours using 0.8W/m² green. B) Analysed slice of the same print.*

Having achieved a print of a line using constant illumination, the next step was to use constant illumination to achieve a voxel of PHB in the centre of the cuvette. For these experiments, the 5-hour illumination was used, as it gave clear results with 1.4 W/m² as well as with 0.8 W/m² green light intensity. In addition, a 30-minute illumination with red light was performed for the first half

hour of the experiment, with 1.45 W/m² red light, in order to deactivate any already active photoreceptors from the preparation of the experiment. All experiments, apart from the first one indicated, were performed with 1 W/m² green light, while the red light intensity was varied, in order to identify a combination that would work with the highest contrast.

The voxels appear much less clearly defined than when printing with tdFAST2 (Fig. 5.19, Fig. 3.20). At lower red light intensities, the dot is clear, as it was much wider than the green light beam, but its intensity was similar to the beam and the tails are very visible. At the same time, the beam in the direction of the red light beam is not visible in any condition. In addition, at higher red light intensities, the activated voxel seemed to disappear together with the tails of the beam. It is likely that these effects were seen because of higher scattering in the 5-hour incubation, in combination with the lower contrast of PHB printing, including the earlier saturation with red and smaller red light effect.

The lower contrast of PHB printing is consistent with the observations of the voxel prints using the lower red light intensities. There, red light was not capable of totally eliminating production by the peak intensity of the green beam, but was able to supress the edges of the green beam where intensity was lower, making the beam narrower and therefore the voxel appear wider, even if it was not substantially more activated than the peak of the green beam. As red light intensity increased, it became enough to suppress the tails, but scattering also became too great, so that the voxel area also received a significant amount of red light to suppress production and therefore contrast was lost.

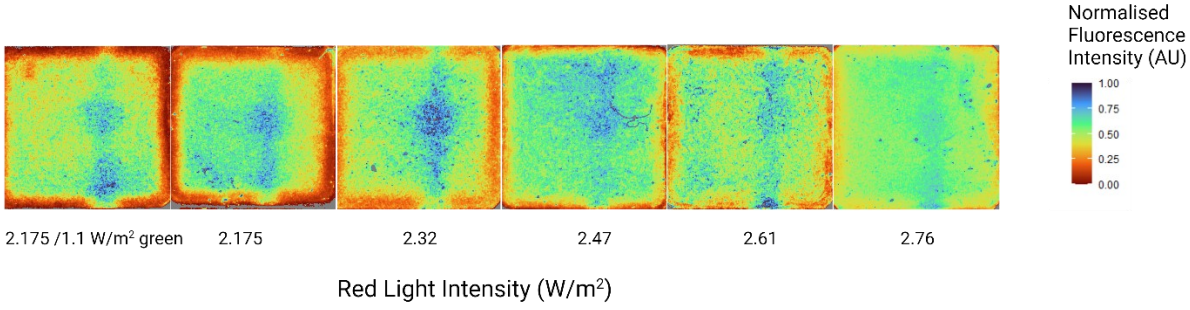


Figure 5.19: *Image of voxels with different intensities of red. Green light was 1.1 W/m² in all cases.*

The profile plots of the beams parallel to the green and red light also show the difference between the efficiency of green light activation and the inefficiency of red light suppression clearly (Fig. 5.19). Values parallel to the direction of the green light essentially show the intensity of the beam, and only in the middle red light of 2.32 W/m² is there a distinguishing peak in the activated voxel.

This is consistent with the smaller effects of red suppression in Nile Red. In contrast, in the plots across the beam of the red light, the voxel is more clearly distinguished, as it was shaped by the presence of green light rather than the absence of red. Still, the highest contrast was found at 2.32 W/m² red light.

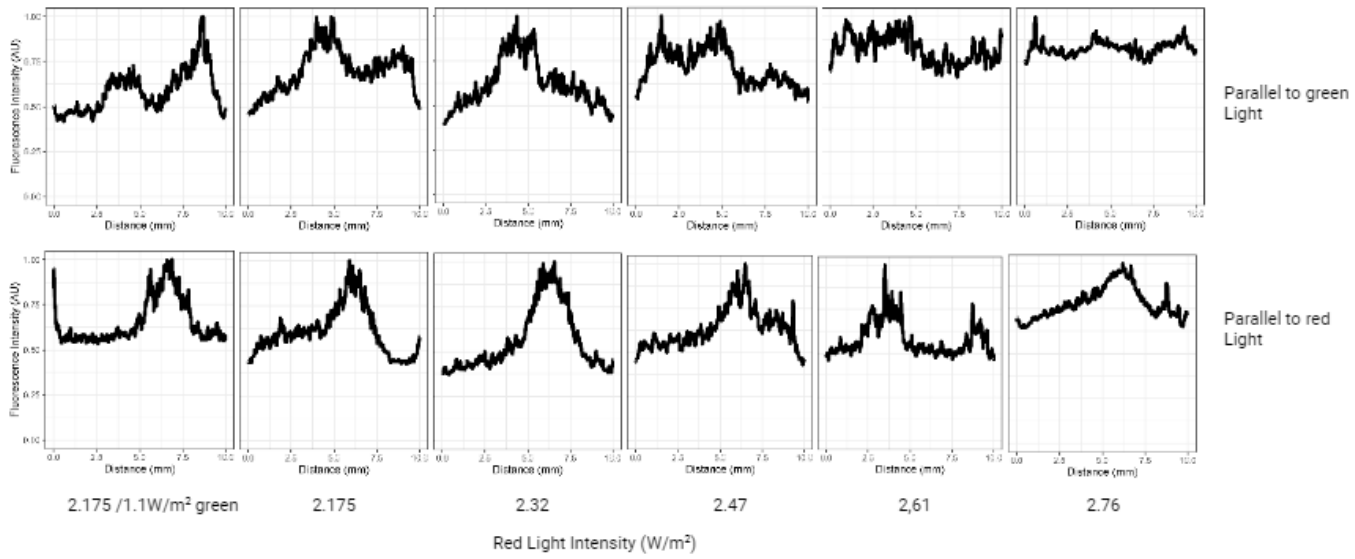


Figure 5.20: *Image with the analysed lines for slices observed in Fig. 5.19.*

In this section, PHB production was controlled in three dimensions under continuous illumination, giving a line and a voxel of PHB production. Again, despite the contrast visibility PHB gave a lower contrast than tdFAST2.

5.2.5 Optogenetic control of PHB production within a cuvette with discontinuous illumination

In order to improve upon production of PHB in 3 dimensions, as well as move to producing more than one voxel, the next step was to attempt the production of PHB under discontinuous illumination. Again, a similar procedure as in Chapter 4 was followed, whereby green light was used to activate, followed by deactivating red light, in order to produce 4 voxels in different positions in the z axis of the cuvette. Images were analysed by subtracting background fluorescence and normalising to average fluorescence of background in the slice.

As a first step, a 5-hour illumination was used with 45 W/m² green light intensity, supplied every 30 minutes for 1 minute, followed by red light for 2 minutes. The red light intensity was varied from 6.4 W/m² to 25.6 W/m², in steps of 6.4 W/m², in order to give a range of activation. The illumination was done in such a way that the top voxel received the highest red light, with voxels every 5 mm

receiving less and less red light. While some activation was observed in the form of a small voxel with green light tails around it, for the two lower red light intensities used, the contrast was very low and the prints were not considered a success (Fig. 5.21). Interestingly, almost all intensities of red showed similar results.

In efforts to increase the contrast, I reduced the incubation period, in order to slightly reduce scattering. Incubation was only reduced by half an hour, giving 4.5 hours of incubation, while light intensities remained the same. However, while the tails of the green light remained the same, the contrast was not improved, suggesting 5 hours was a more likely incubation time.

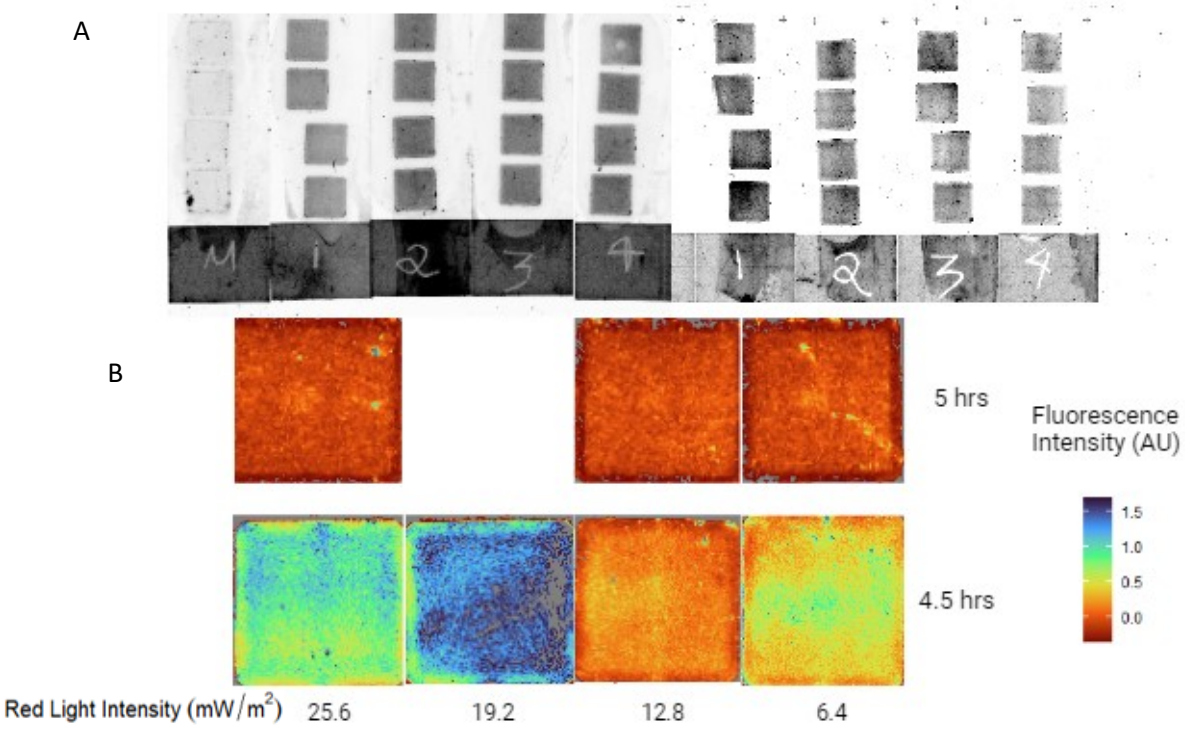


Figure 5.21: *Initial PHB discontinuous illumination voxel experiments. A) Raw, contrasted data of the 5-hour print(left) and the 4.5-hour print (right). B) Analysed slices. Green light was kept constant at 45 W/m². The second slice at the 5-hour incubation is not shown as there was no distinguishable production.*

The next step was to keep the same gradient with lower red light intensities, from 1.6 W/m² to 6.4 W/m² in steps of 1.6 W/m², and use it with a gradient of increasing green light intensities from 45 to 67.5 W/m² in steps of 7.5 W/m², in an attempt to make a more pronounced voxel of production (Fig. 5.21). there was variability in the results of the experiment, with some repeats showing lines, and others showing activation of the voxel. The activated voxels were more pronounced at the weaker green light, while the weakest green light was not able to show any activation at all.

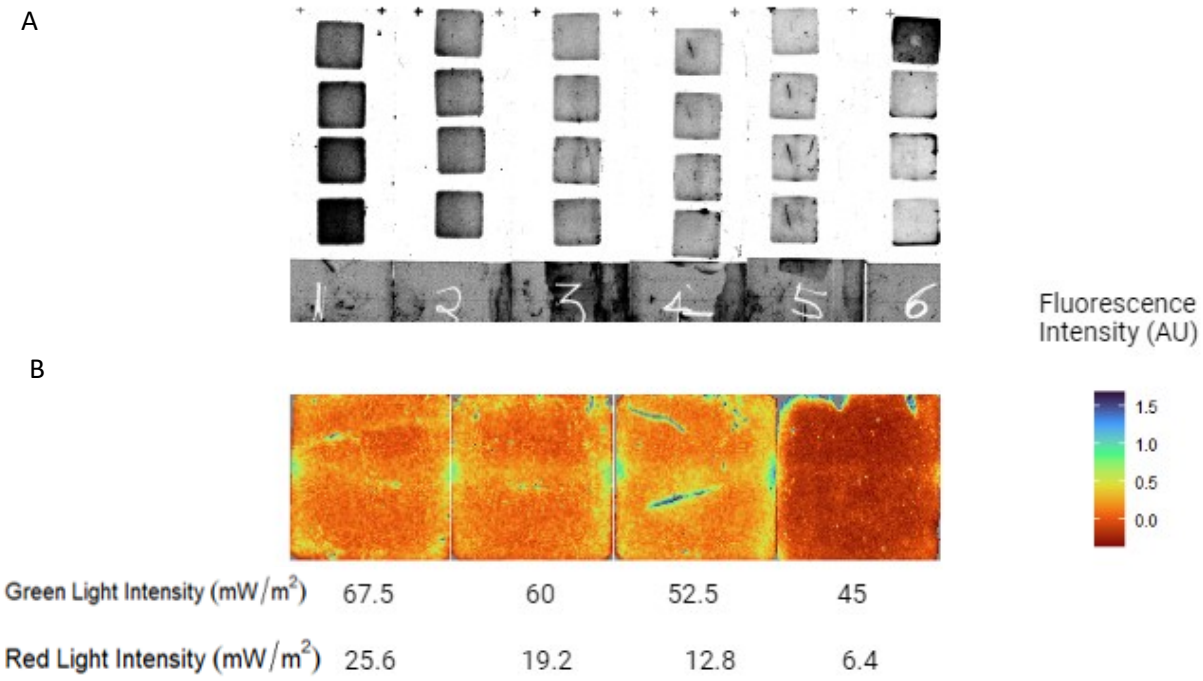


Figure 5.22: *5-hour incubation with gradient green and red light. A) Contrasted image. B) Analysed slices.*

Finally, green was used at 60 W/m² while red was used in a gradient of 6.4, 8, 9.6, 9.6 W/m², in an effort to both activate the central voxels more and also supress the corners, while trying to account for any scattering through the higher green intensity (Fig. 5.23). This print gave the highest contrast of all, specially at higher reds. While the tails of production were still visible, the voxel of activation was clear as in Fig. 5.19, through the higher width of the voxel. However, still the presence of the tails and very low contrast of activation would make it very hard to translate the parameters of this experiment to producing two voxels in the same z-level.

This final successful print was repeated with a lower temperature, in an attempt to be closer to the optimum for *C. necator* which is around 30 °C. A compromise temperature of 34 °C was attempted, but this gave no improvement in the contrast or the clarity of the voxel printed (data not shown).

The reasons for the failure in achieving localisation of a well-contrasted voxel using discontinuous illumination are various. They include the lower contrast of the system for PHB, the red dye used for imaging, and the toxicity of PHB production. In addition, the longer printing time and contrast also contributed to the failure. Ultimately, by achieving production of a single voxel, even at low contrast, I showed the limitations of the system, which would have to be addressed before increasing contrast and attempting production of multiple voxels.

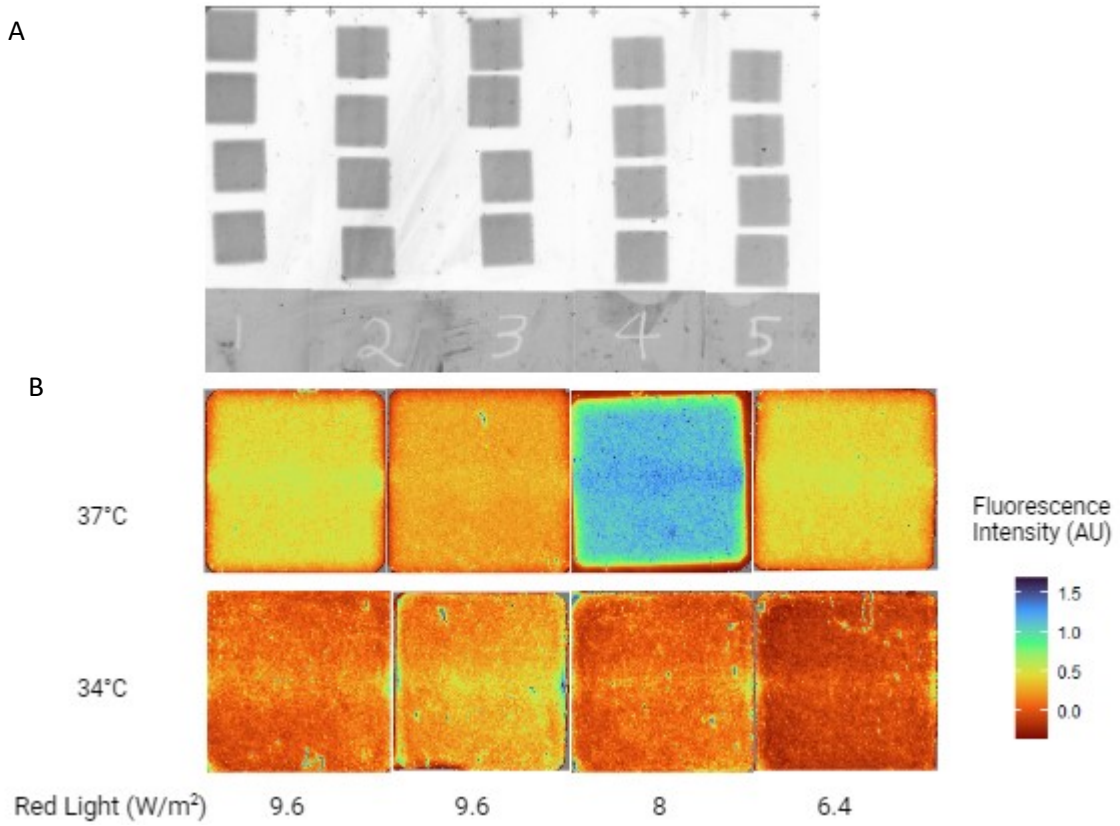


Figure 5.23: *5-hour incubation with gradient green and red light at 2 different temperatures. A)raw data for the 37 °C incubation. B) Slices from incubation at 37 °C and 34 °C.*

As a last step in investigating optogenetic production of PHB, I wanted to test whether PHB was produced in a high enough density to form a solid biomaterial that could be freestanding, with PHB produced from adjacent cells interconnected. For this reason, I looked at samples under the microscope to assess the extent of PHB production and interconnectivity. I used PHB samples incubated under red light, darkness and green light for 5 hours, and observed them either in brightfield or red fluorescence channels, to look at Nile Red (Fig. 5.24).

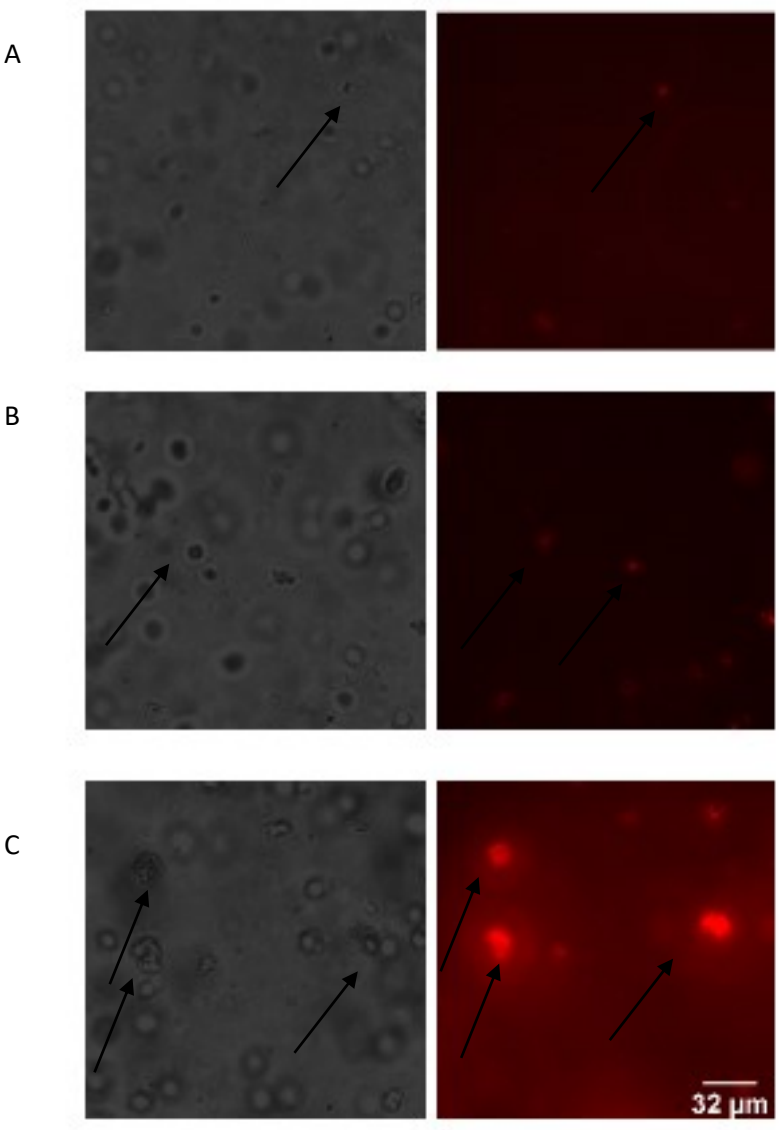


Figure 5.24: *Microscopy of PHB producing cells, in brightfield (LEFT) and RFP channel (right). From top to bottom: BP16 in red light at 1 W/m², darkness and green light at 1 W/m² incubation. All samples were incubated for 5 hours.*

PHB could be seen in all cases, forming white inclusion bodies inside the cells, which seemed to deform the cells. This is likely to also have had an effect both in the scattering observed, and slow growth of the cells due to toxicity. In addition, as activation was increased from red to darkness and then to green light, the size and frequency of these deformed cells increased. At no point, however, was the PHB able to extend past a single cell and connect cells together, indicating the PHB printed could not act as a bona fide biomaterial. This was therefore another limitation to be considered when trying to print PHB.

In this section, I used discontinuous illumination to produce a voxel of PHB. Such a voxel was achieved, but the contrast was too low to be taken to the production of a whole shape.

5.2.6 Ability to control production in the whole hydrogel

Producing materials in the centre of the cuvette and accurately localising materials in a particular location to produce 3D shapes is a major advantage of the current 3D bioprinting approach developed here. Another advantage of the ability to apply optogenetics to spatial control of bioproduction is its versatility, giving the ability to produce the desired effects in multiple shapes and directions. In addition, producing inside a hydrogel has limitations of extracting the necessary material from the hydrogel, but optogenetics can also be used to functionalise a whole 3D print volume.

One such envisioned idea was to apply optogenetics to the printing of gradients in a 3D volume. Optogenetics can, by varying light intensity, be used to activate different amounts of production in a continuous manner. In addition, filters exist with continuously varying neutral density (ND), which allow a gradient of light to reach the locations desired.

Gradient material optogenetics have been applied in 2 dimensions, as well as in pseudo 3-dimensions, to help cure the surface of materials at a shallow depth (Wang et al., 2020). As an addition to this approach, our envisioned approach would use the CCaSR 3.0 system to produce a gradient of activated materials throughout the whole volume of a cuvette instead, again moving optogenetic control to 3 dimensions in this discipline.

In terms of materials that could be printed with this approach, tdFAST2 was used to achieve proof of concept. As seen in Fig. 2.20, different incubation times can affect tdFAST2 expression in the whole cuvette. In addition, red light can affect localised expression, again both on the surface and the inside of the cuvette.

In order to achieve a gradient, a method for the illumination of the whole cuvette had to be devised. What was needed was essentially a uniform or almost uniform source of light throughout the length of the cuvette, with the ability to change the intensities and wavelengths of incident light in particular locations. For this reason, I decided to use the 96-well light plate, which contained LED lights at a distance of 2.04 mm between adjacent LEDs, making them almost continuous. As the diameter of each LED well, the smallest unit of intensity control in the light plate, was around 6.96 mm. However, I needed to make the gradient more uniform and continuous. For this reason, I used

a gradient ND filter (ThorLabs), with ND gradient between 0.04 and 4.0 over 50 mm allowing intensities to range from the original intended one to one with 10^4-fold suppression (Fig. 5.25).

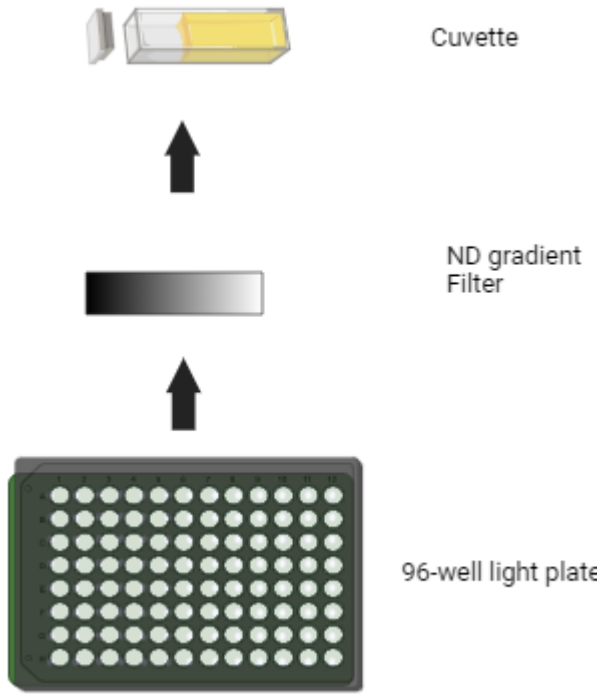


Figure 5.25: *The light plate set up for a gradient experiment, with the gradient ND filter and cuvette on top.*

In printing in a gradient manner, achieving contrast is not brought about by the contrast between red and green lights, or activation and inactivation. Rather, as a first choice I wanted to achieve a gradient with continuous illumination, and the changes in expression brought about by different rates of activation over the incubation time.

To achieve this, the main source of contrast would come from the gradient filter itself, as it can reduce light intensity by 4 orders of magnitude in a continuously variable way, while the control of the light plate only allowed light intensity variation up to 255-fold. However, the postulated higher efficiency of green light in addition, would make it very easy for gene expression to be seen throughout the cuvette even with the gradient filter.

In this section, I designed a regime for controlling gene expression in the whole of the hydrogel, for the control of gradient gene expression throughout the hydrogel.

5.2.7 Production of tdFAST2 in a gradient in the whole cuvette

As a first step, I used BP16 to control production of tdFAST2 in the whole cuvette in a gradient. In order to be able to see a gradient, I performed the experiments with a uniform low green light intensity of 120 mW/m² on the light plate. In this way, the unsuppressed region of the light plate, in the most transparent part of the gradient filter would be illuminated with intensities of ~110 mW/m² for 3 hours, reaching high levels of activation. On the other hand, the most suppressed region would receive green light at 12 mW/m², essentially perceived as if it were in darkness. The fluorescence intensity of the whole cuvette was then measured directly in the gel scanner. The intensity and gradient were measured by taking a mean of an area across the centre of the cuvette, along the long part. Cells were inhibited for by exposure to red light at 2 W/m² for 10 minutes, to suppress any background expression. It was hypothesised, that since this experiment was not as dependent on absolute localisation, it could tolerate more scattering, provided that cells are still in early exponential phase and able to respond to higher green light intensities through higher gene expression. For this reason, the experiment was repeated for an incubation of 3 hours and 45 minutes, which gave overall higher fluorescence than the other experiments (Fig. 5.26).

The fluorescence data was analysed by plotting the area along the length of the cuvette, excluding any halo present, and plotting the profile across the length of the cuvette. Analysis was performed by subtracting average fluorescence from hydrogel containing only media and no cells, and normalising to the maximum fluorescence value.

Interestingly, in all the prints, the gradient was linear through the length of the cuvette. The decrease in fluorescence intensity was about 3000 AU per cm. The linearity of the gradient was the case as the logarithmic change in light intensity contrasts with the exponential part of the Hill function, resulting in linear dynamics in cell response. Controls of medium showed very low fluorescence, with cells kept in darkness for the incubation period also showing uniform but lower fluorescence. In contrast, cells kept in full illumination without an ND filter for the duration of the experiment showed higher and uniform fluorescence.

In some of the raw images a halo can be seen, which varied in degree of contrast and width. These halos were ignored from the analysis, as they were not part of the print. In addition, in most hydrogels an increase in intensity was observed on the surface at either end of the cuvette. For the surface at the top of the cuvette, this was attributed to contact with oxygen, which would help cells grow and produce faster. For the bottom of the cuvette, the reason for the higher intensity can be

attributed to similar reasons as that of the halo, that is contact with the surface, laminar flow and any oxygen diffusion through the barrier with the surface.

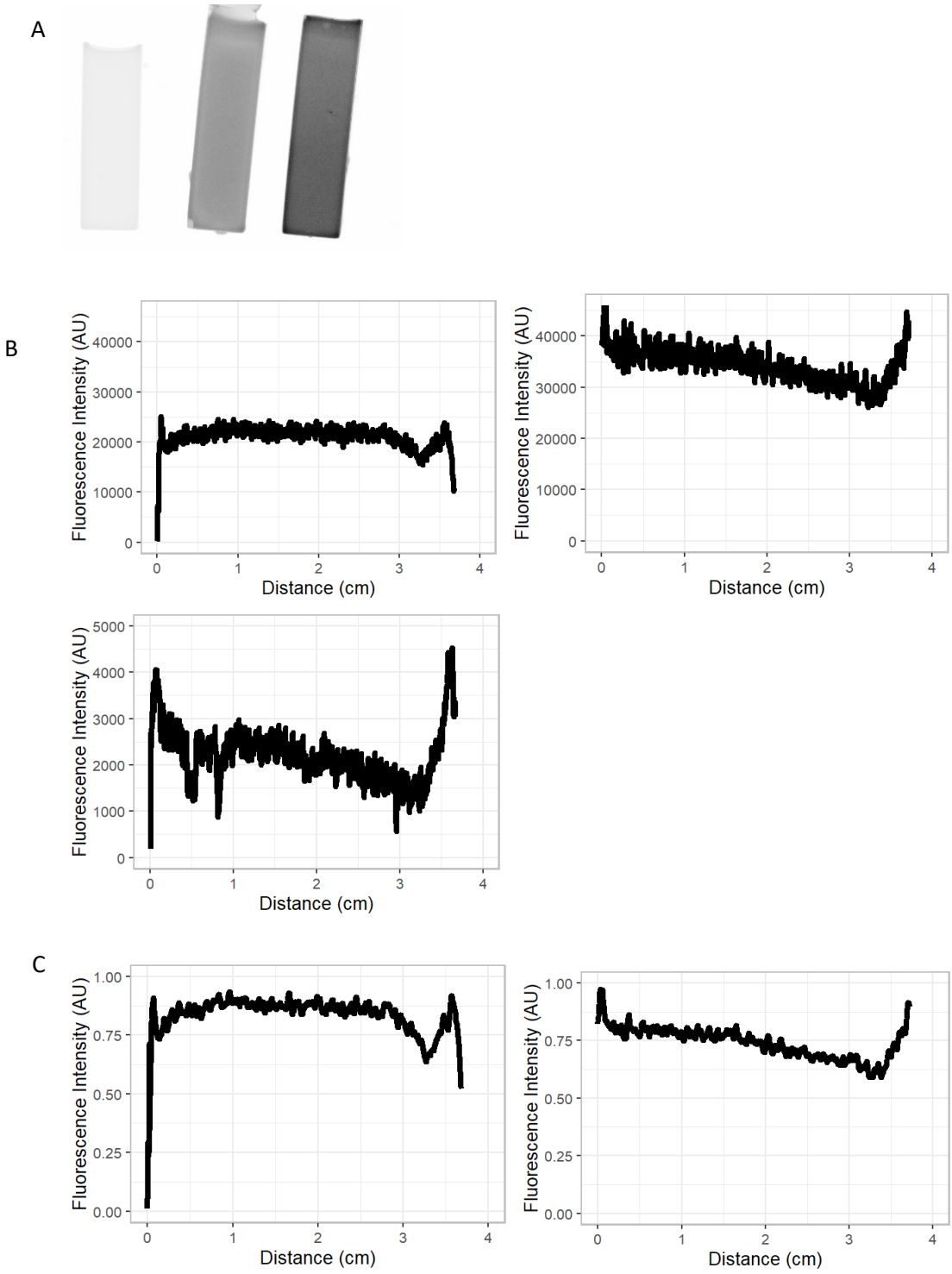


Figure 5.26: *A) images of tdFAST2 gradient. From left to right, media, hydrogel in the dark for 3 hours, gradient hydrogel. B) Raw data for the hydrogel in the dark, tdFAST2 gradient for 3.75 hours, and tdFAST2 for 3 hours. C) Normalised data for the 3.75 hour dark and gradient print hydrogels.*

Through the performance and quantification of these experiments, an interesting effect was observed relating to visualisation of fluorescence. More specifically, the temperature of the hydrogel at the time of imaging played a large role in the fluorescence observed, with higher fluorescence intensity observed for colder hydrogels. This was explainable to a degree, as lower temperatures are generally associated with higher fluorescence intensity, through less quenching of fluorophores, as well as stronger bonds within the fluorescent protein (Ogawa et al., 1995). In this case, higher fluorescence could also be associated with more stable binding between tdFAST2 and tfLime at lower temperatures.

To demonstrate this, I designed an experiment where samples either containing media or media with cells were incubated for 3 hours, with green light or in the dark, and then quenched at 4 °C to stop production. Following this, samples were treated differentially by either warming the samples up to 37 °C, leaving them at room temperature (25 °C), leaving them at 0 °C or cooling down to -20 °C before imaging. Samples at 37 °C showed the least fluorescence, followed by samples kept at room temperature, while samples at 0 °C and -20 °C showed similar fluorescent intensities (Fig. 5.27).

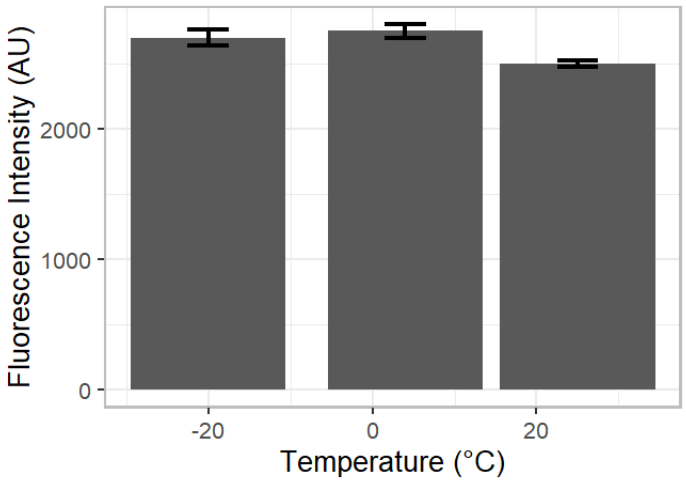


Figure 5.27: *The effect of temperature on fluorescence. Fluorescence intensity for samples incubated for the same time, but imaged at -20, 0 and 25 °C (n=3 error bars represent standard error) (t-test= 0.784) .*

Overall, in this section, I used BP16 to achieve *tdFAST2* expression in a gradient through the length of the hydrogel, through modifying the illumination method. This showed the versatility of the illumination method in proof of concept.

5.2.8 Optogenetic production of PHB in a whole cuvette

Following the simplicity of the approach and ease of obtaining results in printing a gradient with tdFAST2, the next step was to use gradient printing in order to print a biomaterial. For this reason, I decided to work towards producing a gradient of PHB across the length of the cuvette. As BP18 grew slower than BP16, the incubation was performed for a longer time than the tdFAST2 incubations, this time at 5 hours.

The first experiments aimed to establish the response of BP18 to whole cuvette illumination, and ability to control the whole volume, cuvettes containing BP18 were either kept in the dark or illuminated with 100 mW/m² green light for 5 hours (Fig. 5.28). The difference in fluorescence was large, indicating promising results for printing a PHB gradient.

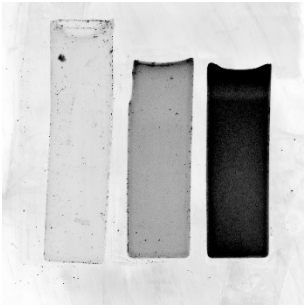


Figure 5.28: *Production of PHB in a whole hydrogel. From left to right, a media sample, PHB left in the dark, and PHB incubated with green light for 5 hours.*

In order to achieve the desired contrast, I started by using the same exact set up as with tdFAST2, but for a 5-hour illumination. As seen before with PHB, the contrast observed was too little and there was no efficient production (data not shown). It is likely that the intensity used was not adequate to achieve visible results. In addition, the surface of the cuvette in the PHB experiments showed extremely high fluorescence. This can be attributed to the position of PHB in the metabolic pathway, downstream of glycolysis, which would make it dependent on oxygen. Moreover, there was very little difference in fluorescence intensity between PHB cuvettes in the dark vs illuminated conditions, indicating that activation was very little. This again points to the lower activation and dynamic range seen by the optogenetic system in the activation of PHB.

In order to improve gradient PHB production, I decide to slightly increase green light intensity to 170 mW/m², in order to see some activation in the non-suppressed areas. This approach yielded a

PHB gradient (Fig. 5.29). The gradient of PHB production was not as steep as that of tdFAST2, owing to lower dynamic range.

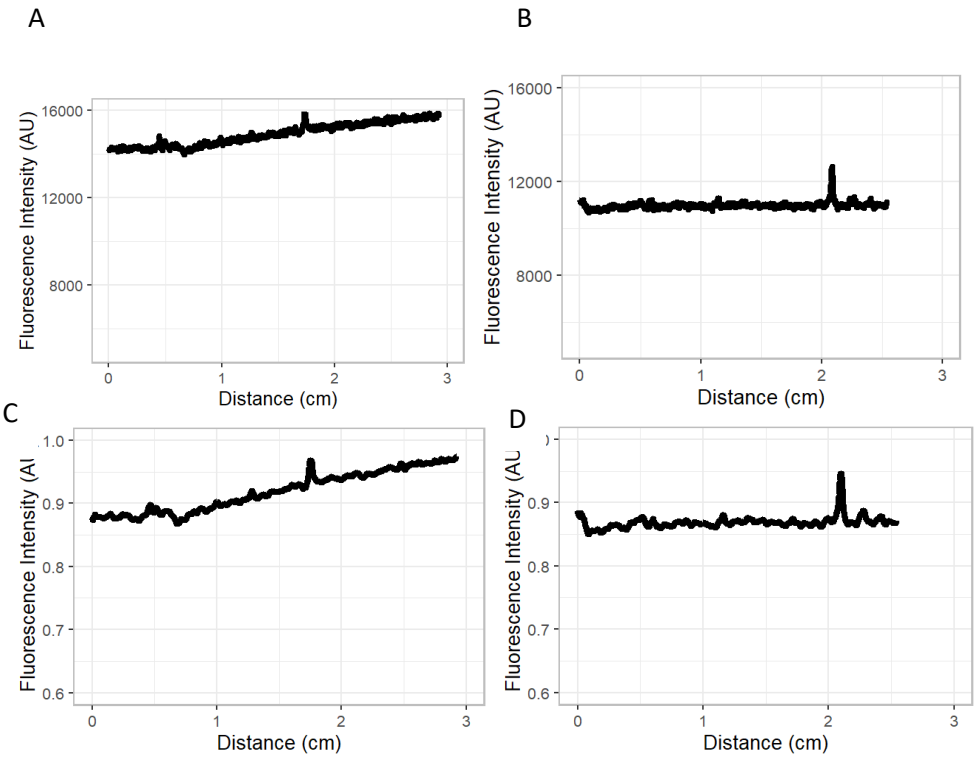


Figure 5.29: *Production of a gradient of PHB in the whole cuvette. A-B) unnormalized and C-D) normalised data. A & C are gradient, B & D are just agarose hydrogel incubated in darkness for 5 hours.*

5.2.9 Agarase gradient production

One limitation of trying to print materials inside, or through an agarose hydrogel, is the fact that in order for these materials to become useful, significant post-processing would be necessary in order to extract the material. This can be performed by removing the hydrogel, through means of heat or other physical means, and a material would be left in shape only if produced in adequate density by the cells. As seen by microscopy on PHB (Fig. 5.24), this was not the case for the materials and timeframes used in the proof of concept.

For this reason, I decided to attempt printing using a 'material' that would modify the properties of the hydrogel itself, reducing or even eliminating the need for post processing. A biomineralization pathway was first considered as a candidate for a material that could be printed as a gradient. Patterned mineralisation has been researched before, both two dimensions, as well as in gradient

form in near-3D. However, it is not optimal for 3D optogenetics, as locations of gene expression would quickly become opaque and scatter light preventing accurate production.

Instead, because of the low-gelling agarose base of the hydrogel, I decided to produce beta-agarase as a gradient. Beta agarase is natively found in agarolytic bacteria such as *Agarivorans albus*, and digests agarose to give neoagarooligosaccharides (Fig. 5.30). It has a turnover number of 41, and low K_m of 0.024, meaning that it is highly efficient and processive enzyme. If incubated for a long time, agarase is able to therefore liquefy agarose, while at intermediate activity levels over shorter incubations, it is able to make agarose hydrogels softer. The aim of production of agarase therefore was production of a variable hardness hydrogel seeded with *E. coli* cells.

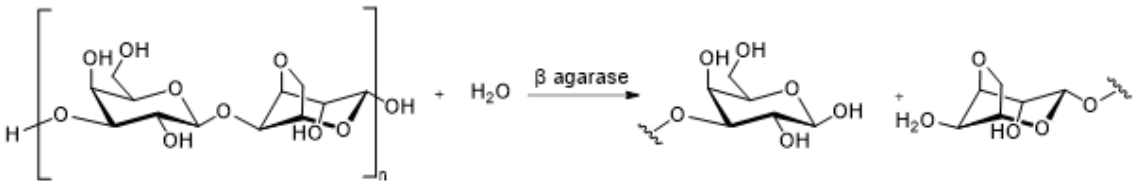


Figure 5.30: *The digestive reaction of beta-agarase.*

As a first step in agarase production, I wanted to prepare the visualisation of agarase inside the hydrogel. Due to the non-fluorescent nature of this material, I needed to identify a visual or indirect way to quantify its activity. For this reason, I purchased commercial beta-agarase (ThermoFisher, UK), and applied 2 µl on the surface of a 2% agarose-only cuvette. The cuvette was then incubated at room temperature overnight. The next day, the diffusion and activity of the agarase could clearly be seen as a clear, 5 mm thick band on the surface of the cuvette, while the hydrogel at that location felt much softer than the rest of the hydrogel to the touch (Fig. 5.31).

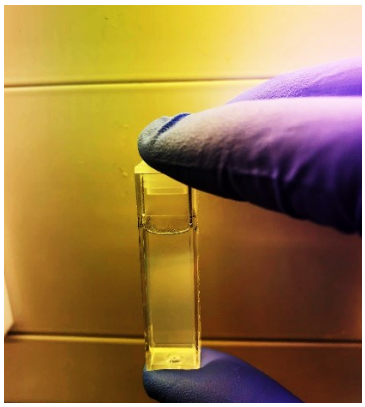
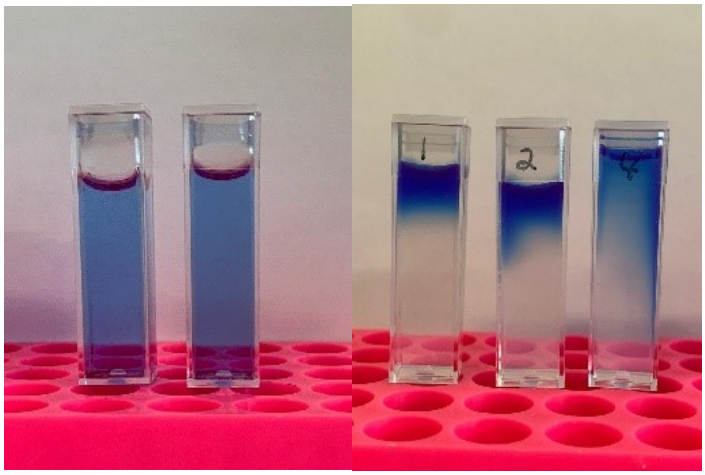


Figure 5.31: *Agarase diffusing down a gel indicating visualisation.*

While encouraging in terms of the ability of agarase to digest the hydrogel, this result meant that high activity would be needed to see clear results. In addition, quantification through absorbance measurements could be made harder by the presence of cells and M9 in the hydrogel. For this reason, I decided to test out another optical approach for agarose hardness. To do this, I made use of food dye, and the fact that a lower agarose hardness through higher agarase activity is analogous to a lower concentration hydrogel, with larger pores allowing easier diffusion.

I therefore diffused blue food dye (Tesco, UK) down cuvettes containing agarose hydrogels of various concentrations (1%, 2%, 4%), as well as water as a control. At first, I placed 20 µl of dye onto the surface of the hydrogel, and imaged its diffusion after 7 hours (Fig. 5.32). The progress of the dye after the required time was 5, 7 and 20 mm respectively for each agarose concentration. Interestingly, at first glance the dye appeared to diffuse easier in higher concentration agarose.

A B



C D

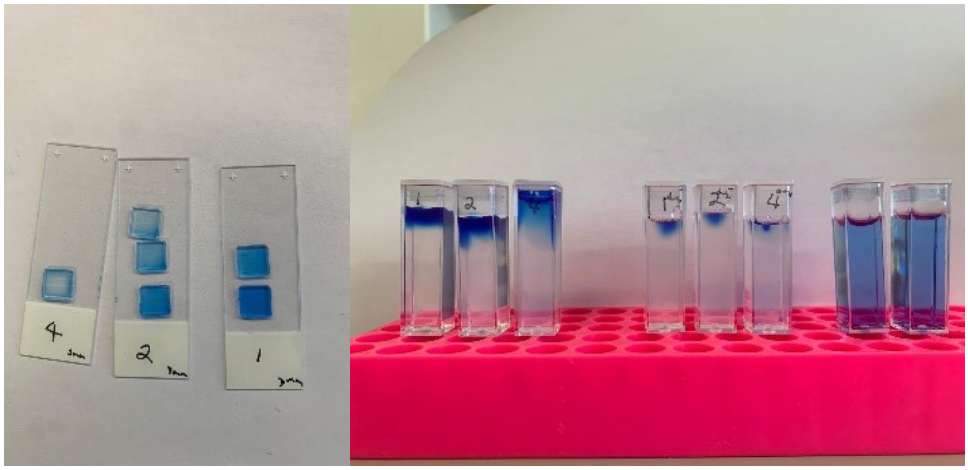


Figure 5.32: *Using a dye to assess diffusion down the cuvette to visualise agarose concentration. A) Water controls with the food dye after 7 hours. B) Experiments with agarose at 1%, 2% and 4% respectively, with food dye dissolved from the top, after 7 hours of incubation. C) Slices from the top for the agarose samples in (B. D) All samples, in groups of three from left to right: Samples with dye dissolved through the whole hydrogel, samples with dye dissolving from a small hole in the top, water controls.*

However, I observed that the majority of diffusion observed appeared to be through the corners or edges of the cuvette. For this reason, after 7 hours I sliced all hydrogels to slices. While at 4% agarose the diffusion appeared to be faster, the centre of the cuvette at the surface had very little dye, and virtually most of the diffusion was happening through the interface between the walls and the edges of the cuvette, through capillary action. On the contrary, 1% agarose showed the least diffusion when viewed from the outside, but the centre of the hydrogel was fully blue, indicating

good diffusion to the hydrogel, and less capillary flow. The lower capillary flow can be explained also through the lower hardness of the cuvette, which created less of a hard boundary between hydrogel and cuvette walls.

To remove any capillary flow bias, I repeated the experiment by carving a small (2 mm diameter) hole on the top surface of each hydrogel, and adding 1 μl of dye there, followed by 3 hours of incubation. At the end of the 3 hours, the results were imaged, and indeed the diffusion was proportional to the concentration of the agarose hydrogel as expected, with dye dissolving less in higher agarose concentration. However, this result was still not perfectly quantitative, and diffusion was too slow to reach the whole volume of the cuvette (data not shown).

In order to visualise the hydrogel, I had to use an indirect mechanical method. I decided to infer agarase activity by proxy of hydrogel hardness, through measuring a hydrogel's Young's modulus with an Instron. Young's modulus was calculated by calculating the stress of pressing the samples, (force/area of sample) divided by the strain (change in length/original length), for the linear part of the compression of the samples (Materials and Methods 7.3.3.10).

Cloned constructs were verified both in terms of sequence, but also by plating and observing visually the digestion of LB agar, thereby assessing agarase activity as well. As seen, agarase under the optogenetic control was able to create, a visible in two dimensions, 'halo' of digestion, were agar was softer than the surrounding areas.

These results, observed in darkness, meant that there was also significant background production and activity of agarase, and therefore prints for a gradient would have to be kept brief, and under low illumination to prevent additional activation of the suppressed areas. In addition, red illumination at the beginning would be necessary to supress any stray production from activation during hydrogel preparation.

In order to quantify these, as well as obtain a timeframe for growth and production by the agarase optogenetic constructs, a 96-well plate background growth experiment was performed, this time in LB media, as fluorescence was not being measured. Strains expressing agarase under optogenetic control (strain termed BP19) were found to grow much slower than all other strains. However, production was clear as the hydrogel was much softer (Fig. 5.33). In addition, the flat Petri dish was also kept incubated for a day to see when digestion becomes visible (Fig. 5.34).

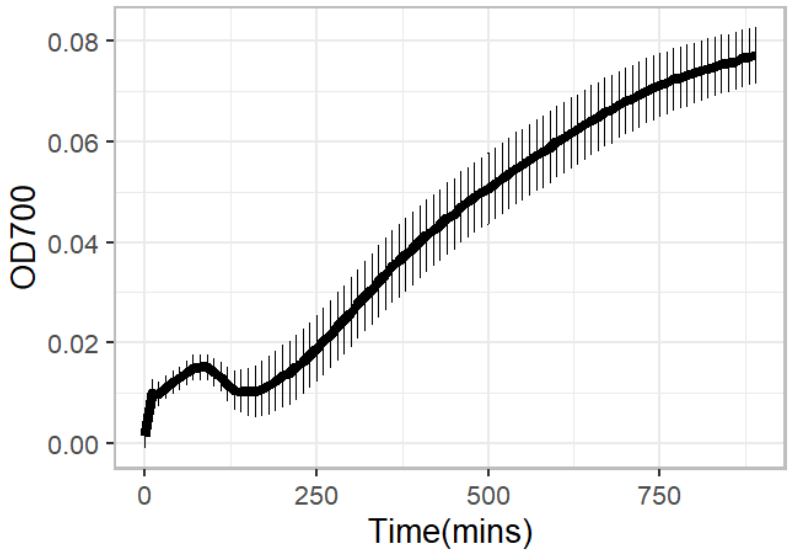


Figure 5.33: *OD700 for agarase-producing cells over time (n = 3, error bars represent standard error).*

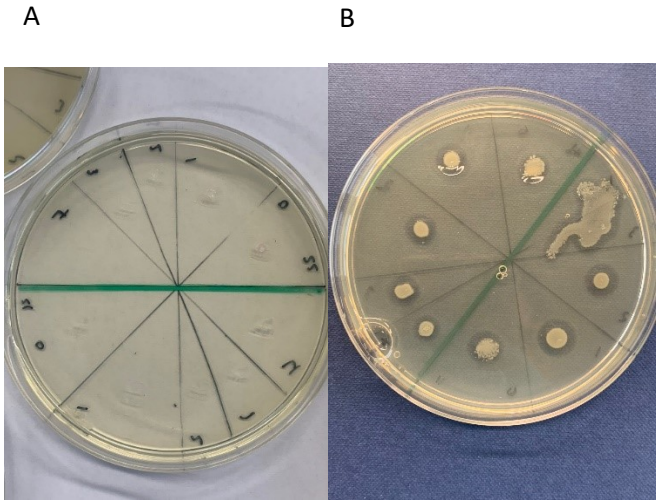


Figure 5.34: *Images of imaging of agarase expressing cells in a 2D plate (A) at the beginning of incubation and (B) after a 10-hour incubation. Different spots are replicates, with the top right spot having run off.*

Following this characterisation, I attempted to control production of agarase in the whole hydrogel. I used a similar light intensity as that used for the PHB, (170 mW/m^2), and kept the incubation at 3 hours. I then tested the whole hydrogel in an Instron (Fig. 5.35). The Young's modulus of hydrogels incubated in green light was 10% lower than those incubated in darkness indicating the effectiveness of the optogenetic approach. In addition, all agarase hydrogels were softer (lower Young's modulus) than media hydrogels, highlighting the action of the agarase. Interestingly, the

presence of wild-type cells themselves also made the hydrogel softer, probably through interfering with cross linkages in the agarose.

I then proceeded to print the hydrogel in a gradient form, through the use of the filter. In order to visualise the gradient, the hydrogel was sliced into three 1 cm^3-sized cubes, through the use of an adaptor for the 3D printed slicer. Each cube represented a position in the cuvette, which should progressively get softer as the agarase activity increased. This was exactly what was observed, with a constant decrease in Young's modulus. The softest part had a similar Young's modulus to that of the fully illuminated cuvette, as expected, while the hardest part similar to a cuvette incubated in the dark (Fig. 5.36).

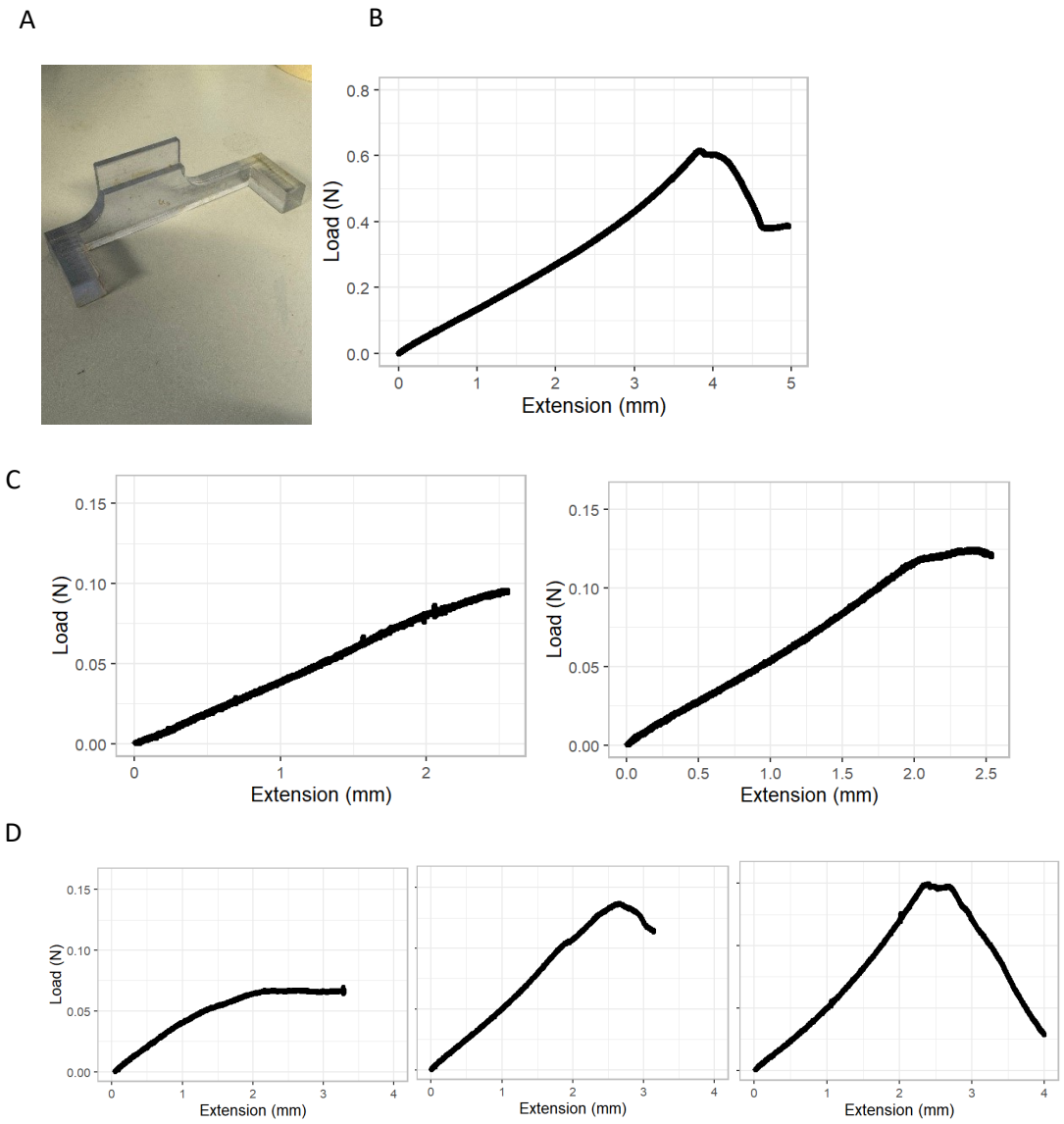


Figure 5.35: *Raw data from gel hardness measurements. A) the adaptor used to slice 10 mm slices for instron tests. B) Medium toughness measurement C)Load against extenstion. From left to right, hydrogel samples incubated in 170 mW/m² for 5 hours, or in darkness. D) The gradient print, starting from the part of the cuvette that received the most light, to the part that received the least.*

In this section I studied how to create a gradient hardness hydrogel. I started from investigating visual methods to assess hardness, followed by testing the effect of commercial agarase on digesting agarose. I then cloned agarase under optogenetic control, and produced a gradient hardness hydrogel.

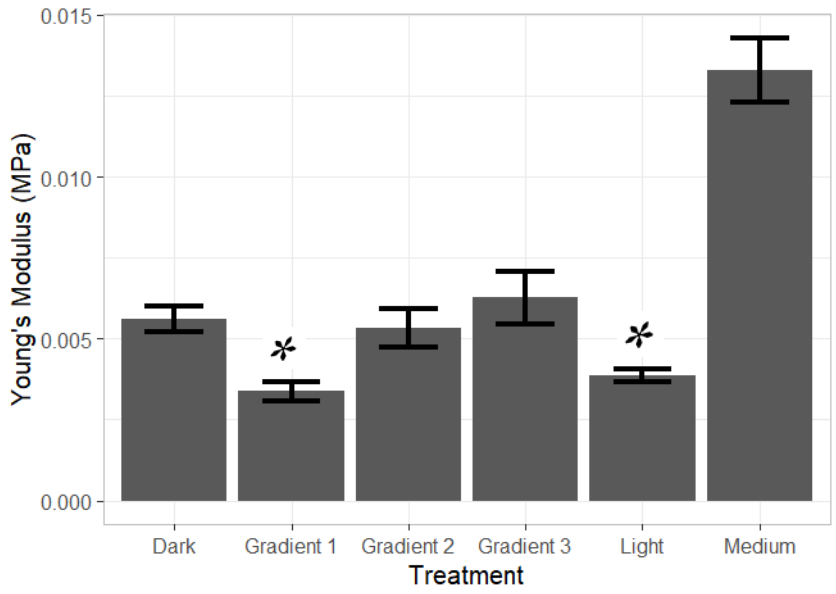


Figure 5.36: *Young's modulus for hydrogels incubated under different conditions (n = 4, error bars = standard error). Gradient 1-3 are different 1x1 cm points along the length of the hydrogel that was exposed to gradient illumination, with Gradient 1 receiving the most light and Gradient 3 the least.*

5.3 Conclusions

This chapter described the application of the proof-of-concept 3D optogenetic control technology developed in the previous chapters, by using the technology to attempt the 3D printing of bona fide biomaterials.

I first attempted to 3D print a bioplastic, PHB. We started by developing a metabolic pathway for producing PHB in *E. coli,* followed by cloning the pathway under CCaSR 3.0 optogenetic control. I characterised the performance of the optogenetic PHB-producing strain in liquid and gel, ensuring that the growth media and incubation times and illumination intensities used were appropriate.

Following characterisation, I produced a line and a localised voxel of PHB in the centre of the hydrogel using continuous illumination. I attempted to produce a voxel in the centre of the cuvette using discontinuous illumination too, but the contrast was much too low to enable printing. In addition, microscopy showed that PHB production was too localised to produce a bona fide biomaterial.

As a next application of the bioprinting technology, I stepped away from localised hydrogel production and towards controlling the properties of the whole hydrogel, through production of gradient biomaterials in the 3D space. Production of a gradient in the whole cuvette is much easier than production of a localised voxel conceptually, as it involved only overlaying the cuvette on a gradually changing light intensity gradient. In this case, I used the light plate and a variable ND filter.

I started with a proof-of-concept production of tdFAST2, which indicated how a very low intensity of continuous green light was enough to achieve a gradient. I applied the same principle to print PHB in a gradient, showing how the principle could be applied to different materials. Finally, I attempted the goal of the whole hydrogel functionalisation experiments which was to functionalise the whole cuvette by printing a gradient of agarase, creating a gradient hardness hydrogel. Following cloning and characterising the growth of the agarase construct, I managed to print a gradient hardness hydrogel, quantified through Young's modulus measurements.

Chapter 6

Conclusions and Future Work

6.1 Conclusions

The work presented in this thesis resulted in the development of a novel 3D bioprinting method to activate gene expression, in an arbitrary 3D geometry, by *E.coli* embedded in a hydrogel matrix. Precise 3D control to achieve non-trivial shapes was shown using a proof of concept protein-fluorogenic dye conjugate, and to a certain degree using a bioplastic, PHB. Optogenetic control across the whole matrix volume was shown in the form of a gradient, with the protein-dye conjugate, PHB and a digestive enzyme modifying the properties of the whole matrix, agarase.

The presented method manages to achieve 3D printing by dispensing with the need for printable support, through having the build volume filled with a support hydrogel. It also dispenses with the need to use toxic photoinitiator compounds, through the use of optogenetics. The CCaSR 3.0 optogenetic system was used to make cells responsive to light, and a localised distribution of illumination is used to achieve production of either voxels in the centre of the build volume, in any order and in a non-continuous manner; or whole-volume gradients.

I started building this technology using a bottom-up approach. In Chapter 2, I started from first principles, setting up the requirements of the parameters of the biological system, such as the need for the support matrix to allow cell growth and light penetration, and low autofluorescence for the growth media. I then set about to characterise each one of these parameters to identify the optimal optogenetic system and conditions for this application. I chose *E.coli* cells for their ease of husbandry and genetic manipulation, and chose the CCaSR 3.0 two-component optogenetic system, for its high dynamic range, low background and ability to activate and deactivate the cells. I identified a 1% agarose hydrogel as the best option for a support matrix, as it allowed for cell growth

without interfering with light. I identified M9 as the media with the least autofluorescence, allowing detection of a fluorescent product, and I identified tdFAST2 as a molecule that would allow fluorescent detection in anaerobic conditions. Bringing all these components together, I characterised growth of the cells and their responses to green and red light, in order to set intensities for continuous illumination to observe maximal response as well as the required incubation time to balance gene expression with minimal light scattering. Other than the choice and characterisation of the biological system, conclusions from this chapter include the high sensitivity of the CCaSR 3.0 *E.coli* cells to light, as well as the ability to grow and produce adequately inside and agarose hydrogel.

In Chapter 3, I built upon Chapter 2 by testing the whole system in 3D, with the aim of achieving production of a single dot (voxel) in the centre of the hydrogel. Initial tests for optogenetic activation in a Petri dish and a cuvette yielded low contrast and difficulty in characterisation. Therefore, I went through several iterations of changing the illumination, incubation and visualisation systems, before settling on the ones that gave accurate quantifiable gene expression, together with a way to visualise it. I then tested the capabilities of this equipment and the ability to visualise production to test some shotgun attempts at producing a voxel in the centre of the hydrogel. Finally, I performed a systematic characterisation of the system, using different intensities of green light first to observe gene expression in the shape of a line, followed by the combination of green with suppressive red light, to achieve gene expression in a single voxel in the centre of the cuvette. Again, in this chapter the very high sensitivity of the system to both green and red light was noted, with very low intensities capable of achieving an effect. In addition, the degree to which light scattering from the hydrogel and cell growth affected gene expression and imaging was also observed, especially for the printing of a voxel through the combination of green and red lights.

In Chapter 4, I again built upon the results from Chapter 3. In order to move on from producing a single voxel to 3D printing shapes, it is necessary for light to be able to move between different locations during the print. Because of the limitations presented to the system by the continuous growth and gene expression of cells, this meant that discontinuous illumination was necessary. I started from a theoretical viewpoint, understanding how red light could be used to deactivate photoreceptors in a much more efficient way than suppression of production, because of the negligible rate of dark photoconversion and hysteresis observed in the system. I use these tenets to design parameters to produce lines across the hydrogel and voxels in 4 different z-positions in the hydrogel, indicating the capabilities of this approach. Simulation of printing in this way also

uncovered that both the red and green light photoconversion constants appeared in our case to be higher than the ones reported (Olson et al., 2017) by a factor of 5. New simulations agreed with this number, indicating that the system in this case was even more sensitive to changes in green and red light.

Moving from periodic illumination and with the aim of printing as many voxels as possible, we devised a new method for illumination based on discontinuous illumination and illuminating the sample for a short period of time with a high intensity of light. This was based upon the concept of the system responding to the total light energy, regardless of the period of illumination. This was true, with the exception of dilution of photoreceptors through cell division, which is why we included 'top up' illuminations in the discontinuous illumination approach. Again, we characterised production of lines and voxels in the z-axis of the hydrogel, with simulations agreeing about the higher photoconversion constants. We also printed pairs of single voxels in the same z-position, in a diagonal, horizontal and vertical arrangement. Different ways to produce these voxels were attempted. Separate illumination, where each voxel was activated as much as possible over time, showed the best performance for a diagonal and vertical arrangement of voxels. On the other hand, concurrent illumination, where the print was split into time frames, and both voxels were aimed to be activated to the same degree at each time frame, gave the best results for a horizontal arrangement of voxels.

These results, and ability to print multiple voxels allowed us to move on to producing a non-trivial shape, that of a double helix, through the combination of, in total, 44 pixels in 3 hours of incubation. To achieve this, the build volume was sliced to temporal and spatial segments, allowing the clear production of a 3 dimensional object.

In Chapter 5, having achieve proof of concept 3D bioprinting of non-trivial shapes, I moved on to apply this technology to the printing of different materials. I first tackled PHB, a bioplastic that has been widely studied in synthetic biology. We first identified a pathway for the production of PHB in *E. coli,* and I transformed this pathway under CCaSR 3.0 control. I characterised growth of the cells harbouring the pathway and PHB production in response to different wavelengths and intensities of light, noticing the toxic effect of PHB production on cell growth. In addition, I noticed the lower contrast of PHB, characterised by reduced response to red suppression and early saturation under green light.

Following 2-dimensional characterisation, I printed PHB in a 3D hydrogel, first using constant illumination, producing a line and a voxel in the centre of the hydrogel, noticing how the lower dynamic range and higher scattering due to the longer incubation time led to less observable production. This was also verified when moving to discontinuous illumination to print 4 voxels in different z-positions in the hydrogel, which resulted in too little contrast to allow the print of proper 3-dimensional objects with PHB. Microscopy also verified that the concentration and placement of PHB in the print volume was not enough to give a solid material.

In addition to printing specific voxels in the centre of the cuvette, I wanted to showcase the versatility of optogenetics for 3D control, by controlling gene expression through the whole build volume. For this reason, I designed a method to print a gradient of a material through the whole cuvette. I first showcased this method with the ability to print tdFAST2 and PHB, before using it to alter the properties if the whole hydrogel, by using beta-agarase to create a gradient hardness hydrogel.

Overall, this bottom-up approach has given substantial insight into the use of optogenetics for positional control of 3D gene expression. Knowledge of light distribution, scattering and the changes in the temporal response of cells to illumination were all factors found to influence the results, while also, the nature of the molecule expressed and method of detection were found to have a huge impact on the print. Limitations thus include scattering of light, persistence of activation in photoreceptors, the geometry of light used as well as the temporal change of cell response due to growth and gene expression.

The current state of the art includes extrusion based printing (Lehner et al., 2017), while recent approaches able to print gradients through biomineralization, but without accurate 3D spatial control (Wang et al., 2020). Therefore, this approach contributes to the state-of-the-art as it is the establishment of the first method to control gene expression by immobilised bacteria in true three dimensions, with accurate placement of specific voxels in the 3D matrix. It is the first method to be able to produce specific shapes in 3D through connecting these voxels. It has also shown how these methods can be used to print different materials, and be modified to functionalise the containing hydrogel, for the first time.

6.2 Future work

Future work for this project can be split into addressing current limitations, and extending the project further, with current limitations needing to be prioritised before any extension.

Current limitations of this method include, first and foremost, the issue of scattering affecting both the resolution and contrast of the print. Any methods to improve this system should start from reducing scattering. To this end, different hydrogels can be considered, with the requirements that they still provide solid support and allow cells inside them to respond to optogenetics. In addition, a major source of scattering is cell division. Ways to limit cell division without affecting expression can be considered, such as for example the use of Q-cells (Thomson et al., 2017). This would also solve dilution of photoreceptors, allowing single illuminations to be used for activation in the duration of the print, allowing for longer prints. Of course, since modelling and characterisation has been done in exponential growth, it would have to be modified in this case.

A second limitation is the solidity of the material produced. Especially in low cell concentrations and brief incubation times, it would be very hard to form proper solid materials at the correct concentration. In order to rectify this, it might be possible to consider longer printing times, perhaps with Q-cells. Synthetic cells, resposnsive to optogenetic inputs, might also be helpful in this regard (Booth et al., 2017). In addition, biochemical methods might also allow for increase in the substantiality of materials printed. For example, any bioaggregation or biofilm formation modules, possibly under optogenetic control, could allow cells to come closer, forming more substantial materials. In addition, linkage proteins such as SpyTag-SpyCatcher pairs might also allow this. At any rate, cell surface display or secretion of materials would also help in this regard (Gilbert & Ellis, 2019; Sankaran et al., 2018). In this case, better secreting strains like *Pseudomonas spp.* might be better suited.

A problem with printing more substantial materials, however, would come with the possibility of these materials scattering light, or even masking regions to be printed. For this reason, it is necessary to work on optimising the delivery of light in terms of illumination structure and illumination protocol for each activation and shape, in both temporal and spatial slices. For example, it might be possible to focus the green light, or to overlap the directions of red and green light, to improve any localisation effects.

Another limitation of the system is that of its dynamic range, which can be increased through biochemical means. For example, the digitaliser module used in Ch. 2 yielded no improvement in contrast, but it is possible that either tweaking that system, or using a different molecular toggle switch could allow CCaSR 3.0 contrast to be increased. This can also be achieved by tweaking the CCaSR system itself to further optimise dynamic range.

In terms of extensions to the system, the most obvious one is that of increasing the build volume. This can be achieved by ensuring a more transparent hydrogel, as well as an activating beam that can be focused to give specific activation. In addition, printing different materials for different applications is also possible using this system. For example, biomineralization modules, or specialised biosensors should be possible. Applications of such 3D systems can be many, from medical uses to sensing and responding and built environment applications. A key component to building upon this platform is also that of combining multiple wavelengths, such as the RGB systems recently developed (Fernandez-Rodriguez et al., 2017), or combining optogenetics with different approaches such as chemical stimuli or electrobiology. These would allow the system to print multiple materials and composites, possibly allowing even logic gates to be implemented in 3 dimensions. Of course, all these applications are dependent upon improving the dynamic range and accuracy of the system, which remains the largest limitation at the moment.

Chapter 7

Materials and Methods

7.1 Materials

7.1.1 *E. coli* strains

TOP10 *E. coli* (OneShot, Thermo Fisher Scientific) (F- mcrA (mrr-hsdRMS-mcrBC) 80lacZ M15 lacX74 recA1 ara 139 (ara-leu)7697 galU galK rpsL (StrR) endA1 nupG) was used for cloning purposes. Chemical competent cells were prepared following the protocols below.

7.1.2 Plasmids used in this work

Plasmids used in this work include:

- pNO286-3 (Plasmid #107746, Addgene; spectinomycin resistance)
- pSR58.6 (Plasmid #63176, Addgene, chloramphenicol resistance), pSR58.6 was modified to create subsequent plasmids
- BP16: Modified pSR58.6 where the *sfGFP* gene was replaced by the *tdFast2* gene (acquired from Twinkle Factory Biosciences) using start-stop assembly, according to protocols below. Chloramphenicol resistance.
- pCB3: Plasmid created by the Start-Stop combinatorial assembly of 4 genes producing PHB. Kanamycin resistance.
- BP19: modified pSR58.6, where the *sfGFP* gene is replaced by the PHB -producing ORF from pC3. Chloramphenicol resistance.
- pA1: modified pSR58.6, where the *sfGFP* gene is replaced by the agarase gene from *Agarivorans albus* Chloramphenicol resistance.
- pS238D●M: De Lorenzo Lab (Calles et al., 2019, kanamycin resistance)

These strains were used to give the following resulting strains:

Strain	Description	Reference
CCaSR 2.0	sfGFP under optogenetic control	Scmidl et al., 2014
CCaSR 3.0	sfGFP under optogenetic control	Ong & Tabor, 2018
BP16	TdFAST2 under CCaSR 3.0 control	This study
Digitalizer (DM238)	sfGFP toggle switch, inducible with methyl benzoate	Calles et al., 2019
Digitalizer (BPD1)	TdFAST2 toggle switch, under CCaSR 3.0 control	This study
CPHB3	PHB under PrhaBAD control	This study
BP18	PHB under CCaSR 3.0 control	This study
BP19	Beta-agarase under CCaSR 3.0 control	This study

Table 7.1: *Strains used in this study.*

7.1.3 Antibiotics

Antibiotics were dissolved in the appropriate solvent as described in Table 5.1 to prepare antibiotic stocks. Antibiotic stocks were filter sterilised using 0.22 µm filters. Tetracycline was stored in black Eppendorf tubes to prevent light degradation. All stocks were stored in a -20◦C freezer.

Antibiotic	Solvent	Stock Concentration	Working Concentration
Ampicillin	DdH2O	100mg/ml	100 µg/ml
Kanamycin	DdH2O	50mg/ml	50 µg/ml
Spectinomycin	DdH2O	60mg/ml	60 µg/ml
Streptomycin	DdH2O	100mg/ml	100 µg/ml
Chloramphenicol	100% EtOH	34mg/ml	34 µg/ml
Tetracycline	70% EtOH 30% ddH2O	10 mg/ml	10 µg/ml

Table 7.2: *Antibiotics used in this study.*

7.1.4 Inducers and dyes

Dyes were prepared by dissolving in the appropriate solvent as described in the Table 5.2 below. Dyes were filter sterilised with a 0.22 µm filter and stored in the -20◦C freezer. Food dye wherever mentioned was Tesco blue food colouring, 60 mL.

Chemical	Solvent	Working Concentration	Source
tfLime	DMSO	2.5uM	Twinkle Biosciences
Nile Red	ddH2O	15ug/ml	Sigma Aldrich
3-Methyl Benzoic acid (Methyl Benzoate)*	ddH2O	0.5-2mM	Sigma-Aldrich
L-Rhamnose	DdH2O	0.2-0.6mg/ml	Sigma-Aldrich

Table 7.3: *Inducers and dyes used in this study.*

*Preparation of 3- Methyl Benzoic acid involved adding NaOH (2M) dropwise, to reach a pH of 7-7.5.

7.1.5 Media and Buffers

7.1.5.1 M9 Medium

Rich 2x glucose M9 media (referred to as M9 media) used in our hydrogel experiments consisted of M9 minimal salts (5X) supplemented with 0.4% casaminoacids (MP Biomedicals), 0.5 mg/ml thiamine hydrochloride, 4 mM $MgSO_4$, 0.2 mM $CaCl_2$, 1.6% glucose, and the appropriate antibiotic(s). This media was then mixed with 2% agarose as described in 5.1.5.3 to give 1% agarose-1x M9-Glucose media.

Components were wrapped in aluminium foil and solution was filtered using the Nalgene vacuum filtration system. M9 Salts (5X), casamino acids, $MgSO_4$ and $Cacl_2$ stock solutions were sterilised by autoclaving and stored at room temperature. Thiamine hydrochloride was sterilised using a 0.22 µm filter and stored at room temperature in a wrapped in aluminium foil to shield it from light. Glucose solution was filter sterilised on stored at 4◦C.

Volume	Component (concentration)
78ml	ddH_2O*
80ml	M9 Salts (5x) (56.4g/L)
10ml	Thiamine Hydrochloride (10mg/ml)
16ml	Glucose (10%) (10g/100ml)
8ml	Casamino Acids (10%) (10g/100ml)
8ml	MgSO4 (0.1M)
400µl	$CaCl_2$ (0.1M)

Table 7.4: *Protocol to make 200 mL of rich 2x M9* 1.6% glucose supplemented with Casaminoacids*

*To make 1x rich M9 media with Glucose for the liquid experiments, 278mL ddH2O was used instead of 78mL, to have the same amount of all the ingredients in a total volume of 400mL.

7.1.5.2 Terrific Broth (TB)

TB was prepared by mixing 47.6 g of Terrific Broth (Modified) (ThermoFisher Scientific, UK) in 900 ml of ddH_2O and 8ml of 100% glycerol (G 5150). Sufficient ddH_2O was added to bring the volume to 1 L. The resulting mixture was sterilised by autoclaving.

7.1.5.3 Solid Hydrogel Agarose medium

To prepare solid hydrogel medium for the 3D printing and light plate experiments, 2% low gelling point agarose hydrogel was prepared by mixing 2g of low gelling agarose (Sigma Aldrich, UK) in 100ml of ddH2O in a conical flask, followed by autoclaving to sterilise it. This mixture was heated to 65°C in a microwave to liquefy it, and kept in a waterbath at 41°C. It was then mixed inside a falcon tube, using a stripette, in a 1:1 volume ratio with 2x M9 media (described in 6.1.5.1) inoculated at the relevant concentrations with the specific bacterial culture, dyes and antibiotic. The culture was then poured inside a polystyrene cuvette (BetterEquipped, UK) and put in a fridge at 4°C for at least 15 minutes to solidify. Alternatively, for plate reader experiments, the Falcon tube containing the liquid culture was poured inside a sterile empty Petri dish, kept in a water bath at 40°C, and a multipipette (Gilson) was used to pipette into a 96-well plate. In the case of different nutrient media used (such as LB and TB), media were again prepared to double the normal concentration and mixed in the same way as M9 to give a 1x hydrogel. For Petri dish solid state illumination experiments, the same procedure was followed, but 10 ml of the hydrogel media was poured into the Petri dish before putting in the fridge to cool down.

7.1.5.4 Pluronic- F127 medium

Pluronic-F127 medium was prepared in a 20% concentration by mixing 20 g of Pluronic-F127 powder (Sigma-Aldrich, UK) in 100 ml of ddH_2O, followed by shaking and incubating in a fridge at 4 °C for at least 3 hours to ensure dissolving of the mixture. The resulting solution was then autoclave sterilised and stored at 4 °C. Preparation of Pluronic-F127 media occurred by simply mixing Pluronic-F127 with M9 media in the falcon tube, as 6.1.5.3, without any of the heating steps.

7.1.5.5 Sodium Alginate medium

Sodium alginate (Sigma-Aldrich) was dissolved in 1% D-mannitol (Sigma-Aldrich) to give a concentration of 1.5%. This was then filter sterilised using 0.22 µm filters. For gelation, 2.7 ml of the above sodium alginate solution were mixed with 60 µl of 1.2M CaSO4*2H2O (Sigma Aldrich), and diluted with 240µl of ddH2O. Again, preparation of sodium alginate gel occurred by mixing with M9 media as in 6.1.5.3.

7.1.5.6 SOB Medium

SOB medium used for the preparation of competent cells was made by mixing a SOB (Mg-) solution and a Magnesium Mix solution. The SOB (Mg-) solution (20g/L tryptone from casein, 5g/L yeast extract, 0.6g/L NaCl, 0.2g/L KCl) was mixed and autoclave sterilised. The Magnesium mix solution (0.5M $MgCl_2$, 0.5M MgSO4) was mixed and autoclave sterilised. When SOB was needed for competent cell preparation, 1 L of SOB (Mg-) was mixed with 20 mL of Magnesium Mix under sterile conditions to obtain SOB.

7.1.5.7 SOC Medium

SOC medium used for recovery of transformed *E. coli* cells, was made by mixing 1 L of sterile SOB (6.1.5.6) with 20 ml of 20% filter sterilised glucose solution.

7.1.5.8 TSS buffer

To prepare 50 ml of TSS buffer, 5 g of PEG 3350, 1.5 ml of 1 M MgCl2 (or 0.30 g of MgCl2*6H20) were mixed, and LB media were added to up to 47.5 ml. The buffer was filter sterilised with a 0.22 µm filter. 2.5 ml of DMSO was then added and the buffer was stored in the fridge at 4◦C.

7.1.5.9 PBS buffer

1 L of 10X PBS buffer was prepared by dissolving PBS tablets (Sigma Aldrich, UK)) according to the manufacturer instructions. The buffer was autoclaved and stored at room temperature.

7.2 Equipment

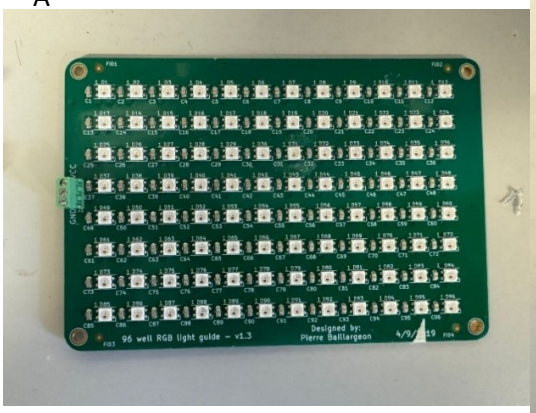
7.2.1 96-well Light Plate

The light plate was made by combining a 96 and 384 well RGB light panel power board with a 96-well RGB LED microplate light panels (Both by Maplebear Electronics, USA, available at tindie.com). These parts were wired together, with the light plate connected to the powerboard, and the powerboard connected to the light plate as well as an Arduino UNO microcontroller, according to (Baillargeon et al., 2019). The specific wiring involved connecting vCC ports together, GND ports together, as well as the data port on the light plate to the power board (Fig.6.1).

The printed circuit board had LEDs corresponding to red (630 nm), green (510 nm) and blue light (460 nm), which could be controlled to give intensities from 0 (darkness) to 2550 mW/m², in steps of 10 mW/m², verified using a light meter (PM16-120 and PM16-121, Thorlabs). Differences in light intensity between wells were +- 0.5%. The light-plate was used inside a temperature-controlled incubator that was itself covered with cardboard and aluminium foil to ensure darkness.

In terms of ensuring uniform illumination on each well, a µClear flat bottom black 96-well plate (Greiner, UK) was fitted on top of the light panel, so that each well on the plate was on top of a group of LEDs (a group consisted of 3 LEDs, one red, one blue and one green). A Kimberly-Clarke Professional Kimwipe (Thermo Fisher, UK) was secured on top of the plate to ensure the light was uniformly scattered for each well (Fig.2.5). This allowed, for each light experiment, a new 96-well plate to fit on top of this set-up to allow independent illumination of each well. The illumination of each individual well was controlled with a custom Arduino code. A sample code is available on https://github.com/pierrebaillargeon/Microplate-Assistive-Pipetting-Light-Emitter/blob/master/Arduino/RGB%20light%20panel%20test/LightPanelExample/LightPanelExample.ino.

A



B



C

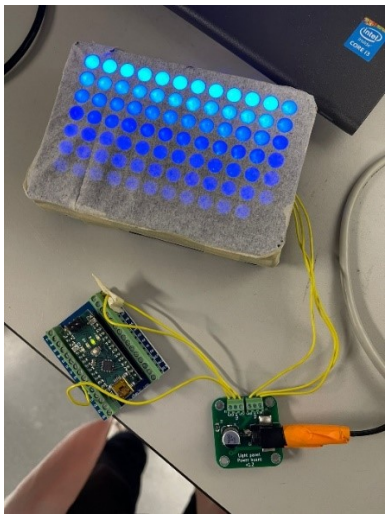


Figure 7.1: *Assembly of the light plate. A) The Arduino Uno used in making the 96-well light plate B) The 96-well light panel used in the plate. C) The assembled plate light to different intensities of blue light, showing the connections of the electronic components of the light plate, consisting of the 96-well LED panel, the light panel power board and the Arduino UNO. The wiring involved connecting the power board to the LED panel (5V to VCC, GND to GND, Data to central socket) and also wiring the power board to the Arduino (5V to Vim, GND to GND, data to socket).*

7.2.2 Mechanical Apparatus

The mechanical apparatus for Bioprinting was prepared by Borut Lampret (Borut Lampret, 2023). The initial mechanical apparatus consisted of a support structure with aluminium profiles, and a manual translation system. This was fitted with two individual collimated lasers (ThorLabs, UK). The lasers obtained were green lasers at 515 nm, with a maximum power of 0.9 mW and a beam diameter of 3.5mm (93.5 W/m2 maximum intensity). These lasers were fitted with Neutral Density

(ND) Filters (ThorLabs, UK) with ND ranging from 1.0 to 2.0, therefore allowing for intensities as low as 935 mW/m^2.

The mechanical apparatus used from Ch.3.5.1 was better characterised and is described in more detail below (Fig. 7.2). The same platform was modified for the rotation experiments by changing the cuvette holder to a cylindrical one that could rotate with a motor (FL42STH47-1206A) (Fig.6.2B).

It consisted of a support structure made from aluminium profiles, and a translation system. The translation system itself consisted of an incubation chamber and three orthogonal translation stages, one for each plane (X, Y and Z). Each translation stage consisted of:

• Plastic support structures, designed in Fusion 360 (Autodesk) and 3D printed with Poly(lactic acid) (PLA) using a fused deposition modeling (FDM) 3D printer (LulzBot TAZ 6, Fargo Additive Manufacturing Equipment 3D)

• A ball nut and a ball threaded screw (AluFlex)

• Tapped 8 mm steel guide rods (Misumi)

• A nema 17 stepper motor (FL42STH47-1206A)

The outer part of the incubation chamber was composed of a plastic platform, mounted onto the Z-translation stage, and covered by a transparent acrylic box. The inside part of the incubation chamber consisted of a custom cuvette receptacle printed by a polyjet 3D printer (Objet500, Stratasys), an NTC thermistor (MF52D-103f-3950), a fan (FH4010SH), and a heater cartridge (from a LulzBot TAZ 6 hotend). This was inserted into an aluminium heat sink.

The optical apparatus consisted of two laser optical systems, green at 515 nm and red at 650 nm. It also consists of the optical power measurement equipment. The systems were mounted to the main support with black panels (Foamex, KJN Automation).

The green 515 nm light was generated by a 50 mW green diode laser, with an optical power stabilising at 43.5+-0.5 mW (OFL299, OdicForce). The laser beam was coupled to a single mode fibre optic cable (P1-405B-FC-1, Thorlabs). The beam emitted by the fibre optic cable was transported and focused by a series of lenses and a mirror to the build volume. The beam diameter was 1mm at the centre of the build volume. Correcting the position of the last lens and adjusting the beam diameter shifted the focus position, resulting in a converging beam. Therefore, the diameter of the beam was 1.15 mm at the entry point of the build volume and 1.05 +– 0.05 mm at the exit. A mirror

(BB1-E02, Thorlabs) was used to deliver the beam to the build volume at a 90° angle relative to initial optical path, and align the beam with the X translation stage.

The red 650 nm light was generated by a 200 mW red diode laser (OFL384-V2, OdicForce, UK). The beam had a flat-top shaped intensity profile, which was collimated by an adjustable built-in collimating lens to 4 mm in diameter. The measured optical power output of the laser is 170 +- 2 mW. The laser was mounted on a custom designed and FDM 3D printed adapter that fit into another mounting adapter (AD16F, Thorlabs) that screwed into a lens mount.

The red and the green lasers' optical power output was controlled by TTL modulation, and intensities were measured by two optical power meters (PM16-120 and PM16-121, Thorlabs). In both optical systems the beams were split using a beam splitter, before entering the incubation chamber. The intensity profiles of the green and red light beams were measured using a CMOS camera (MER-500-14U3M-L, Daheng Imaging).

The apparatus was controlled by a microcontroller (ELEGOO MEGA 2560 R3, Elegoo) with a custom Arduino programme, which involved executing G-code commands and maintaining the chamber temperature. The microcontroller controlled the stepper motors, the lasers' TTL modulation, and temperature inside the incubation chamber. The microcontroller was controlled by a desktop computer, which also controlled the power supply for the lasers(DP832A, Rigol) .

The main G-code commands used were G0, G1 and G4:

- G0 - linear movement with lasers off
- G1 - linear movement with at least one active laser
- G4 – No movement with or without active lasers

Each of these commands was supplemented by additional parameters, including movement and light intensities. The main parameters used were:

- M17, M18 - turn the motors on or off.
- M141 - set the maximum and minimum temperature within the incubation chamber.
- M230 - wait until the maximum set temperature is reached.
- G28 - move to the home position.
- M2 - end of program.

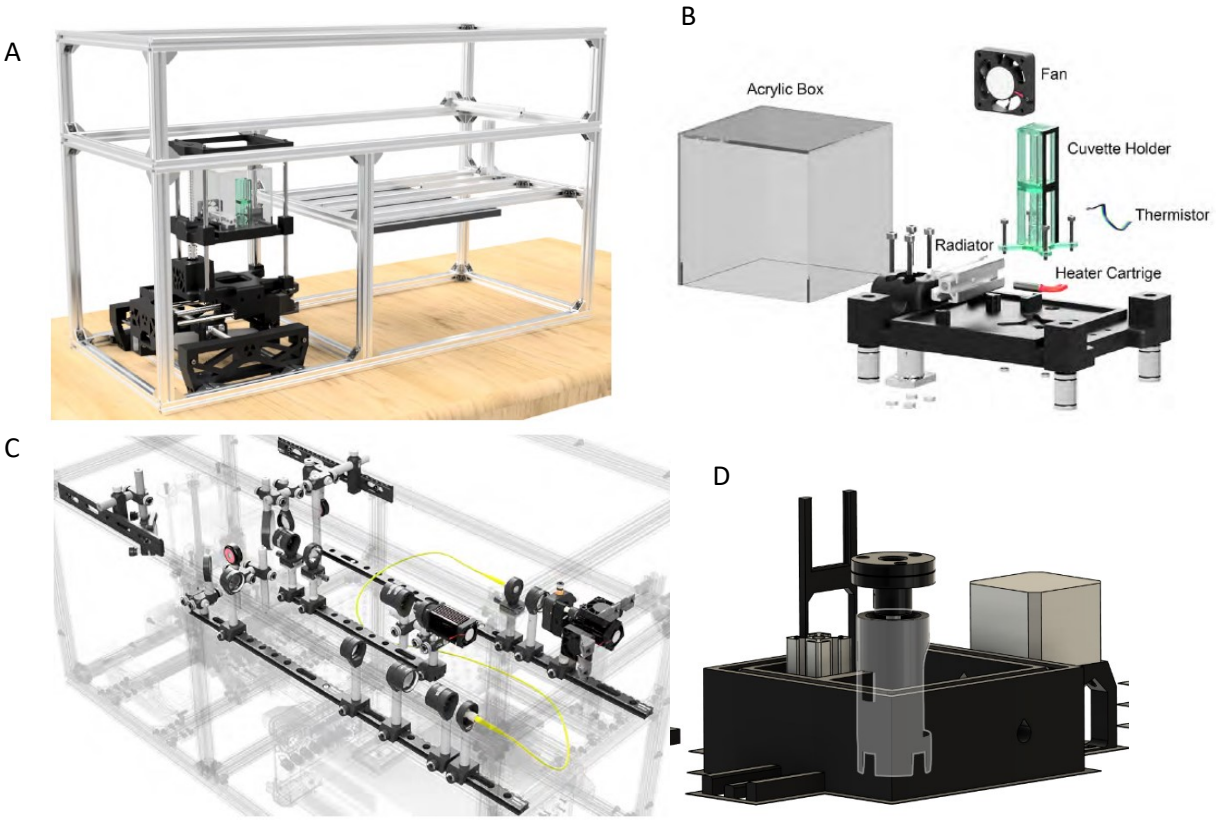


Figure 7.2: *A) Render of the bioprinting illumination platform. B) Exploded view of the incubation chamber. C) View of the optical setup. D) Adaptation of the incubation chamber for rotation experiments. Figure adapted from Borut Lampret's thesis (Lampret, 2023)*

7.2.3 Hydrogel Slicer

In order to visualise slices of the hydrogel for the 3D printing, a custom slicing rig, capable of slicing 1mm thick slices was designed in Fusion 360 and 3D printed in a polyjet 3D printer (Fig.3.10). Additional components of the slicing rig include a microtome blade (MX35 Ultra,Epredia) glued to the front of the slicer and a translation stage (DT12/M, Thorlabs). A wheel with numbered spoked was attached to the micrometer knob, to enable small movements of 50μm. For the agarase gradient measurements, an adaptor to the rig was also printed in the same way.

7.3 Methods

7.3.1 Molecular Biology Methods

7.3.1.1 Culturing Cells

E. coli strains were grown and selected in Lysogeny Broth (LB) medium at 37 °C. In the presence of plasmids with antibiotic selection cassettes, the LB medium was supplemented with the appropriate antibiotics at the working concentrations mentioned in Table 7.2. For solid culture (in Petri dishes, not solid-state experiments), Petri dishes were prepared using LB-agar (Sigma- Aldrich) according to the manufacturer's instructions, with around 10ml of LB-agar per Petri dish and the antibiotics at the necessary concentrations. Cells were then streaked onto dried Petri dishes, and incubated over night at a 37 °C incubator. For liquid cultures, single colonies were picked and grown overnight in 5 ml of LB inside a 15 ml tube, in a 37 °C shaking incubator.

7.3.1.2 Competent cells preparation and transformation

TOP10 strains were prepared using the TSS competent cells method (Chung et al., 1989). A single colony was inoculated in 5 ml of LB in a 15 ml culture tube and grown to saturation over night in a shaking incubator at 37 ◦C. The next day, 1ml of the saturated culture was used to inoculate 100ml of LB in a 500ml conical flask. Cells were grown at 37 °C in a shaking incubator until OD700 0.5-0.7, and then transferred to an ice bath for 10 minutes. Following this, all steps were performed at 4 °C. the culture was split to two 50ml falcon tubes, which were centrifuged for 10 minutes at 300rpm. The supernatant was discarded, and cells resuspended in 5mL of SOC buffer before being aliquoted to batches of 200 µl in 0.2ml PCR tubes sitting on dry ice. Aliquots were stored at -80 °C. OD700 was measured as it has less interference with red light, both in inactivating the cells and reading the output.

To transform DNA, aliquots were thawed for 10 minutes on ice, and 100 pg – 1ng of DNA (~1 µl) added to the tube. Following addition of the DNA, cells were kept on ice for 30 minutes, heatshocked at exactly 42C for 30 seconds and then placed back on ice for 5 minutes. The transformed cells were mixed with 800µL LB media in a 1.5mL Eppendorf Tube and the culture was incubated for 1 hour at a 37C shaking incubator. Following this, 200µL of the culture was plated on selective LB agar plates supplemented with the corresponding antibiotic.

Before using the cells for transformation experiments, transformation efficiency (TE) of the aliquoted cells was measured by transforming 100 pg of pUC19 in 50 µl of cells. Cells were outgrown in 250 µl of LB, 10 µl was diluted to 1 ml of fresh LB and30 µl plated on ampicillin selective LB agar plate. TE was calculated using the following formula: TE =colonies/µg/Dilution = colonies/0.001/((10/300)*(30/1000)).

7.3.2 General DNA Manipulation

All the genetic parts built during this study were constructed using the cloning techniques described in the section below. They were either generated using one or a combination of the described techniques. Oligonucleotides were designed using Benchling and ordered from Integrated DNA Technologies (IDT, UK). When larger parts were not readily available in the lab, they were ordered as gBlocks from IDT.

All enzymes were obtained for NEB unless otherwise stated. Q5 High-Fidelity Mastermix (NEB, UK) was used for DNA amplification under the manufacturer's protocol. Colony PCR was done using the GoTaq Green Mastermix Mix (Promega, UK) using the manufacturer protocol. Qiagen kits were used for the following techniques: gel extraction, PCR cleanup and plasmid miniprep. DNA concentrations were measured using the NanoDrop 1000 Spectrophotometer (NBS Biologicals).

7.3.2.1 PCR

PCR reactions were performed in accordance with the NEB standard Q5 High-Fidelity 2X Mastermix (NEB) protocol (https://www.neb.com/en-gb/protocols/2012/12/07/protocol-for-q5-high-fidelity-2x-master-mix-m0492). Following a PCR reaction, 1 µl of DpnI (NEB) was directly added to the 25 µl PCR reaction for a 1-hour digestion at 37 °C. The reaction was then purified by gel electrophoresis (in 1% TAE, with NEB 1kb PlusDNA Ladder and NEB Quick-Load Purple loading dye, and DNA was extracted from the gel according to the Qiagen kit protocol.

7.3.2.2 START/STOP Assembly

START/STOP assembly was used to modify the pSR58.6 plasmid to encode *tdFAST* instead of *sfGFP*, and to build the PHB expression cassette. We used the protocol developed by Taylor and colleagues (Taylor et al., 2019). New promoters, RBSs and terminator parts were cloned into the level 0 backbone using PCR described above. START/STOP assembly was used specifically for plasmids pCB3 and BP16, while the rest were cloned using Gibson Assembly.

7.3.2.3 Gibson Assembly

Gibson assembly was used to modify the pSR58.6 plasmid to produce respectively, PHB, Agarase, and the Agarase FAST fusion. NEBuilder Hifi Assembly Mix (NEB) was used for Gibson assembly reactions following the manufacturer's protocol:

(https://www.neb.com/engb/protocols/2014/11/26/nebuilder-hifi-dna-assembly-reaction-protocol).

7.3.3 Assays, data collection and analysis

7.3.3.1 3D Bioprinting experiments

Printing samples were prepared by taking single colonies from Petri Dishes, and growing them overnight according to 6.3.3.1. The 15ml tube containing the culture was wrapped in aluminium foil to ensure dark conditions. Then, the liquid part of the hydrogel was prepared first, by mixing together the 2xM9-glucose media to a total volume half of that required for that of the experiment, with dye and antibiotics at double the required concentration, and cells to an OD700 of 0.01. Then, this liquid culture was mixed with molten 2% agarose hydrogel, as in 6.1.5.3, to create a hydrogel with the M9, dye and antibiotics at 1x concentration, cells at OD700 of 0.005 and 1% agarose. The samples were then kept in the fridge to solidify before being used in experiments. Each cuvette sample was prepared to 4ml total volume, while the 96-wel plate gel samples were prepared so that each well would receive 200µl of sample.

For cuvette experiments, after preparation, cuvettes were kept in the fridge at 4 °C for up to 2 days before use. Before each experiment, the lasers were turned on and left to warm up for 5-10 minutes, where their intensities were measured to be verified to be within the required range. The laser output was regulated by using neutral density filters to ensure output between 22-100%. Once the laser powers were verified, the rest of the system was turned on. The hydrogel filled cuvettes were removed from the fridge in darkness and placed in the incubation position, while the control cuvettes were placed in the bottom of the chamber. The G-code was run, consisting of an initial incubation to bring the chamber to 37 °C (about 7 minutes). In cases of experiments requiring an initial dark incubation, experiments were run in overlap, with the cuvettes for subsequent experiments placed in the dark in the incubation chamber for an initial hour, in order to stagger experiments and allow more experiments to be performed in a day. At the end of the experiment, the cuvettes were removed in the dark, placed in an ice bath for 2 minutes to quench any reactions and growth, wrapped in aluminium foil and stored in the 4 °C fridge for up to two days before imaging.

7.3.3.2 Hydrogel Slicing

In the cryotome experiment, an NX70 cryotome was used for slicing. The hydrogel samples were first removed from the cuvette or container, either by softly breaking the cylindrical, glass containers, or by using a steel spatula through the interface between the hydrogel and the cuvette walls, for cube cuvettes. The sample was then cut using a scalpel in to two equal size samples. Each sample was embedded in Tissue TEK OCT medium (Agar Scientific, UK), inside a plastic container. The sample was then placed on a metal cryo-bar, and inserted into the cryotome for cooling to -100 °C. The cryobar with the solidified sample was then placed on the platform and sliced using a blade (MX35 Ultra, Epredia) to 80µm thick slices. A microscope slide (SuperFrost Plus, Epredia) was used to catch the slices.

In the custom slicing experiments, the custom slicer was used. The slicing process works by placing an adhesive microscope slide on the base of the rig (SuperFrost Plus, Epredia). The guide of the rig is then connected to the base via a translation stage, which allows a movement of 0.35mm per revolution. Therefore, inserting the hydrogel on the base of the slicing rig, touching the microscope slide. Then, by lowering the slicer and subsequently replacing the hydrogel rouching the microscope slide, subsequent 1mm slices could be created. The length of the hydrogel was measured every 16 slices to determine average slice thickness, which was 0.92± 0.02 mm across 30 slices.

7.3.3.3 Hydrogel Image acquisition

In order to image the hydrogel following printing, a number of methods were used. In the earlier experiments, a gel camera (BioRad Chemidoc) was used to image the whole cuvette. Using a steel spatula, the hydrogel was removed from the cuvette, by pushing the spatula to the bottom of the cuvette and then slowly removing it, so as not to damage the hydrogel. In subsequent visualisations, the Amersham Typhoon was used for visualising, using the following settings depending on what was visualised. For all visualisations, a resolution of 10µm per pixel was used. The gain for all experiments was set at 500 V.

Each fluorescence image of an individual experiment consisted of four control sample slices on one microscope slide and at least 16 hydrogel culture slices on at least four microscope slides (4 slices per slide). First, a thin transparent plastic film (Breathe-Easy, Diversified Biotech) was placed on the gel imager platform, to prevent scratching of the glass, and prevent any interference patterns from air gaps between the glass surfaces. The slides were then placed on this film. In order to further reduce internal reflection due to the sharp edges of the slices, molten 2% low-gelling agarose was used to cover the slices on the microscope slides, in order to supress these reflections. This was

created by heating a low-gelling agarose to 60C inside a Falcon tube, and then slowly pipetting 1ml aliquots to cover the slices on the microscope slides. This was followed by letting the agarose on the slides solidify.

7.3.3.4 Hydrogel Image analysis

Fluorescence images were analysed using a custom Python programme and FIJI/ImageJ. The analysis took as input the raw 16-bit grayscale data image generated by the gel scanner. Slices from the input image were generated by creating a binary image and determining the contours of each slice, with given threshold values, identified from peaks in the histogram of pixel values, followed by manual inspection. A histogram had three peaks, corresponding to: the area within hydrogel culture slices not affected by the halo effect, the whole hydrogel culture slices, and the control slices.

After isolating the slices, slices of interest were manually selected, extracted from the programme and aligned. The images were then automatically aligned and overlapped with manual inspection, and pixel values summed.

The pixels were then analysed, excluding the presence of a halo, to give the following outputs:

• Average fluorescence value of control sample slices, corresponding to media, but covering all ambient light from the film, microscope slide and hydrogel

• Average fluorescence value of hydrogel culture slices where no printing was performed

• Average fluorescence values of columns parallel to the green beam path, on the green beam path

Average fluorescence values of columns parallel to the red beam path, in the place of the voxel.

• An image of fluorescence values of the printed image, for both individual printed slices and the summed image.

Normalisation of the images was done by as described in the relevant results chapters. Briefly, for normalisation either maximum fluorescence in the slice was used to divide the fluorescence of all pixels. Alternatively, an average fluorescence of the area was calculated, subtracted from each pixel, and then used to divide the pixel values.

7.3.3.5 Plate-reader timecourse assays

Non-optogenetic time-course assays were performed in clear flat-bottom 96-well plates (Costar), while light-sensitive assays were performed with µClear flat bottom black 96-well plates (Greiner).

For all experiments, there were three biological replicates in the same Spark (Tecan) microplate reader. For each condition, at least 3 technical replicates were also included.

Briefly, for plate reader experiments the subsequent protocol was followed: Cells transformed with the constructs of interest and control plasmids not harbouring the genes of interest were grown overnight with 5 mL of 1x M9-glucose supplemented with the appropriate antibiotics, in a 37 °C shaking incubator. The next day, OD700 of each sample was measured in a spectrophometer (WPA Biowave II).

For liquid media plate reader experiments, each sample was diluted to OD700 0.005 in fresh 1x M9 - glucose supplemented with the appropriate antibiotics and dye where necessary (volume was adjusted depending on the experiment).

For solid-media plate reader experiments, each sample was diluted to OD700 0.01 in fresh 2x M9 - glucose supplemented with the 2x concentration of appropriate antibiotics and dyes where necessary (volume was adjusted depending on the experiment). This mixture was then mixed with an equal volume of 2% Low gelling agarose, to give a final 1% agarose-1xM9 mixture with OD700 0.005 and 1x concentration of dye and antibiotics.

In both cases, 200 µL of each sample was then transferred into each well sterile 96-well plate and covered with a Breath-Easy membrane (Sigma-Aldrich). In solid-state experiments, wells were put in a fridge at 4 °C for 15 minutes to solidify the hydrogel. In liquid experiments where anaerobic conditions were required, 50µl of paraffin oil (Sigma-Aldrich) were added to ensure anaerobic respiration.

The plate was placed into a microplate reader and incubated at 37 ◦C for the duration of the experiment (Tecan Spark: Double orbital shaking, 1.5 mm amplitude, Manual gain=65, z-position= 30000). All fluorescence measurements were read from the bottom of the plate. Measurements of OD700 and fluorescence were taken every 15 minutes, unless stated otherwise. For optogenetic experiments, the 96-well plate was incubated on the optogenetic apparatus. It was removed from the optogenetic apparatus in darkness, and quickly placed on the plate reader every 30 minutes, unless described otherwise, to take fluorescence and OD measurements/ Following measurements, the 96-well plates were replaced on the optogenetic apparatus. The whole removal process took less than 80 seconds. In all plate reader experiments, cells were grown for 3 -20 hours according to the experiment.

Protein/Aptamer	Excitation (nm)(bandwidth)	Emission (nm)(bandwidth)
sfGFP	485 (20)	535 (25)
TdFAST -Lime	485(20)	535(25
PHB- Nile Red	560(20)	645(40)

Table 7.5: *Emission and excitation wavelengths used for each fluorescent protein and dye on the Tecan Spark plate-reader.*

7.3.3.6 Food Dye Experiments

Food dye experiments were performed by using Tesco blue food colouring. In injection experiments, 20 µl of dye was injected using a Hamilton Syringe Model 1705 (Hamilton, UK). For dye diffusion experiments, dye was simply pipetted onto the solidified hydrogel as explained in the specific chapters.

7.3.3.7 Bleaching experiments

The tfLime bleaching experiments were performed by using liquid media with cells as in preparing a normal culture, but bleaching was performed by exposure to UV from a UVP transilluminator at 302 nm for 10 minutes.

7.3.3.8 Plate reader analysis

In all plate reader experiments, Fluorescence intensity and OD data were exported into an Excel Spreadsheet and analysed using a custom R script. OD raw data were first blanked, by subtracting, at each time point, the mean of M9 media well replicates over time. Fluorescence intensity was also blanked by subtracting fluorescence intensity of non-fluorescent cells incubated in the plate reader as controls. from non-fluorescence cells was also subtracted from Fluorescence raw data. Following this, data were split by condition and plotted using the R 'ggplot2' package (Wickham, 2016). Timecourse data, except for growth rate and rate of fluorescence production were smoothed using the R 'loess' method (smoothing parameter: 0.3). Growth rate and fluorescence production rate were calculated as described here:

$$Growth\ Rate = \frac{\ln(OD_{t3}) - \ln(OD_{t1})}{t3 - t1} \qquad \text{(Equation 7.1)}$$

$$Fluorescence\ Rate = \frac{\ln(F_{t3}) - \ln(F_{t1})}{t3 - t1} \qquad \text{(Equation 7.2)}$$

Where t1 corresponds to 0 min after induction, t2 to 15 min after induction and t3 = 30 min after induction. Rates were calculated directly from the mean of 3 biological replicates.

7.3.3.9 Flow cytometry measurements

Flow cytometry was used to measure gene expression by counting the number of fluorescent cells and non fluorescent cells. Flow samples were taken by pipetting 1 µl of cell culture into a 96-well palte (Costar) with each well filled with 200 µl PBS. Cell fluorescence was measured in the Attune NxT (Thermo Scientific) flow cytometer using the following parameters: FSC 660 V, SSC 500 V, 420 V, blue laser BL1 (488 nm ex./530(30) nm em.) 450 V, yellow laser YL2 (561 nm ex./620(15) nm em.)560 V. The following threshold were used: AND FSC 0.5x1000, AND SSC 4x1000. 5 mixing cycles were used between each sample. 10,000 cells were collected for each sample and data were analysed using FlowJo and plotted with R. In FlowJo, I first gated *E. coli* cells from dust and cell debris by plotting SSC-A vs FSC-A. Then I gated the *E. coli* population to find the singlets population by plotting FSC-H vs FSC-A. Finally, the red and non-red singlets populations were determined by plotting BL1-H vs YL2-H. Three biological replicates were performed, and the mean and standard error were calculated.

7.3.3.10 Material Hardness assays

The material (agarose hydrogel) hardness assays were performed using a mechanical toughness instron 5543 (Instron, UK), under compression mode, with a 10N Load cell. The load cell movement was controlled for a movement of 0.4mm/minute, with measurements obtained every 0.05 seconds. Each sample was tested in 3 biological replicates, and standard error was calculated. Experiments were run until 10 minutes were passed, the hydrogel was compressed by 50%, or there was a drop in force required to achieve compression.

In calculating Young's Modulus, the Youngs modulus formula was used, over the initial, linear part of the compression experiments:

$$E = \frac{F/A}{\Delta L/L} \qquad \text{(Equation 7.3)}$$

Where E is the Young's modulus in MPa, F is the force in Newtons, A is the surface area of the hydrogel in m^2, ΔL is the change in thickness of the hydrogel in metres, and L is the original thickness of the hydrogel in metres.

In the whole hydrogel toughness measurements, the whole hydrogel was assayed, with hydrogels with dimensions: 40x10x10 mm. For gradient experiments, the hydrogel slicer was used with an adaptor, to create cubes of 10x10x10 mm, at different positions in the cuvette, which were assayed individually. Each hydrogel gave at least 3 such cubes.

7.3.3.11 Plate digestion assay

The plate digestion assay was performed by taking an overnight growth of the BP18 strain, as in 5.2.1.1, and 5 µl of turbid culture were added on each spot in an LB agar plate complemented with the right antibiotics. The plate was then incubated for the indicated amount of time in 37C.

7.3.3.12 Microscopy Assays

Microscope images were taken using a Nikon Eclipe Ti microscope (Nikon, USA). The lens used was the 20x lens, while images were obtained in brightfield and RFP channels (Excitation XXX), under a gain of YYYY. Images were analysed with FIJI/ImageJ.

7.3.3.13 Hydrogel absorbance assays

For hydrogel absorbance assays, hydrogels were prepared using (5.1.5.3 - 5.1.5.5) and mixed inside a cuvette with M9. The hydrogels were then measured with a WPA Biowave II spectrophotometer.

Bibliography

1. 1. Remington, S.J., 2011. Green fluorescent protein: a perspective. *Protein Science*, *20*(9), pp.1509-1519.
2. Plamont, M.A., Billon-Denis, E., Maurin, S., Gauron, C., Pimenta, F.M., Specht, C.G., Shi, J., Quérard, J., Pan, B., Rossignol, J. and Moncoq, K., 2016. Small fluorescence-activating and absorption-shifting tag for tunable protein imaging in vivo. *Proceedings of the national academy of sciences*, *113*(3), pp.497-502.
3. Tebo, A.G., Pimenta, F.M., Zhang, Y. and Gautier, A., 2018. Improved chemical-genetic fluorescent markers for live cell microscopy. *Biochemistry*, *57*(39), pp.5648-5653.
4. Müller, M., Becher, J., Schnabelrauch, M. and Zenobi-Wong, M., 2015. Nanostructured Pluronic hydrogels as bioinks for 3D bioprinting. *Biofabrication*, *7*(3), p.035006.
5. Song, S.J., Choi, J., Park, Y.D., Hong, S., Lee, J.J., Ahn, C.B., Choi, H. and Sun, K., 2011. Sodium alginate hydrogel-based bioprinting using a novel multinozzle bioprinting system. *Artificial organs*, *35*(11), pp.1132-1136.
6. MacWilliams, M.P. and Liao, M.K., 2006. Luria broth (LB) and Luria agar (LA) media and their uses protocol. *ASM MicrobeLibrary. American Society for Microbiology*, *2006*.
7. Paliy, O. and Gunasekera, T.S., 2007. Growth of E. coli BL21 in minimal media with different gluconeogenic carbon sources and salt contents. *Applied microbiology and biotechnology*, *73*, pp.1169-1172.
8. Krause, M., Ukkonen, K., Haataja, T., Ruottinen, M., Glumoff, T., Neubauer, A., Neubauer, P. and Vasala, A., 2010. A novel fed-batch based cultivation method provides high cell-density and improves yield of soluble recombinant proteins in shaken cultures. *Microbial cell factories*, *9*, pp.1-11.
9. Rahman, A., Linton, E., Hatch, A.D., Sims, R.C. and Miller, C.D., 2013. Secretion of polyhydroxybutyrate in Escherichia coli using a synthetic biological engineering approach. *Journal of biological engineering*, *7*(1), pp.1-9.
10. Gardner, T.S., Cantor, C.R. and Collins, J.J., 2000. Construction of a genetic toggle switch in Escherichia coli. *Nature*, *403*(6767), pp.339-342.

11. Wang, J. and Yu, H.Q., 2007. Biosynthesis of polyhydroxybutyrate (PHB) and extracellular polymeric substances (EPS) by Ralstonia eutropha ATCC 17699 in batch cultures. *Applied microbiology and biotechnology*, *75*, pp.871-878.
12. Calles, B., Goñi-Moreno, Á. and de Lorenzo, V., 2019. Digitalizing heterologous gene expression in Gram-negative bacteria with a portable ON/OFF module. *Molecular systems biology*, *15*(12), p.e8777.
13. Cavalheiro, J.M., de Almeida, M.C.M., Grandfils, C. and Da Fonseca, M.M.R., 2009. Poly (3-hydroxybutyrate) production by Cupriavidus necator using waste glycerol. *Process biochemistry*, *44*(5), pp.509-515.
14. Kim, D.K., Kim, S.J. and Kang, D.H., 2017. Bactericidal effect of 266 to 279 nm wavelength UVC-LEDs for inactivation of Gram positive and Gram negative foodborne pathogenic bacteria and yeasts. *Food research international*, *97*, pp.280-287.
15. Rosas-Val, P., Adhami, M., Brotons-Canto, A., Gamazo, C., Irache, J.M. and Larrañeta, E., 2023. 3D printing of microencapsulated Lactobacillus rhamnosus for oral delivery. *International Journal of Pharmaceutics*, *641*, p.123058.
16. Hirsch, M., Lucherini, L., Zhao, R., Saracho, A.C. and Amstad, E., 2023. 3D printing of living structural biocomposites. *Materials Today*, *62*, pp.21-32.
17. Zub, K., Hoeppener, S. and Schubert, U.S., 2022. Inkjet printing and 3D printing strategies for biosensing, analytical, and diagnostic applications. *Advanced Materials*, *34*(31), p.2105015.
18. Booth, M.J., Restrepo Schild, V., Box, S.J. and Bayley, H., 2017. Light-patterning of synthetic tissues with single droplet resolution. *Scientific reports*, *7*(1), p.9315.
19. Wilson Jr, W.C. and Boland, T., 2003. Cell and organ printing 1: protein and cell printers. *The Anatomical Record Part A: discoveries in molecular, cellular, and evolutionary biology*, *272*(2), pp.491-496.
20. Axpe, E. and Oyen, M.L., 2016. Applications of alginate-based bioinks in 3D bioprinting. *International journal of molecular sciences*, *17*(12), p.1976.
21. Lehner, B.A., Schmieden, D.T. and Meyer, A.S., 2017. A straightforward approach for 3D bacterial printing. *ACS synthetic biology*, *6*(7), pp.1124-1130.
22. Dou, C., Perez, V., Qu, J., Tsin, A., Xu, B. and Li, J., 2021. A state-of-the-art review of laser-assisted bioprinting and its future research trends. *ChemBioEng Reviews*, *8*(5), pp.517-534.

23. Douillet, C., Nicodeme, M., Hermant, L., Bergeron, V., Guillemot, F., Fricain, J.C., Oliveira, H. and Garcia, M., 2022. From local to global matrix organization by fibroblasts: a 4D laser-assisted bioprinting approach. *Biofabrication*, *14*(2), p.025006.
24. Ostrovidov, S., Salehi, S., Costantini, M., Suthiwanich, K., Ebrahimi, M., Sadeghian, R.B., Fujie, T., Shi, X., Cannata, S., Gargioli, C. and Tamayol, A., 2019. 3D bioprinting in skeletal muscle tissue engineering. *Small*, *15*(24), p.1805530.
25. Michael, S., Sorg, H., Peck, C.T., Koch, L., Deiwick, A., Chichkov, B., Vogt, P.M. and Reimers, K., 2013. Tissue engineered skin substitutes created by laser-assisted bioprinting form skin-like structures in the dorsal skin fold chamber in mice. *PloS one*, *8*(3), p.e57741.
26. Shaukat, U., Sölle, B., Rossegger, E., Rana, S. and Schlögl, S., 2022. Vat photopolymerization 3D-printing of dynamic thiol-acrylate photopolymers using bio-derived building blocks. *Polymers*, *14*(24), p.5377.
27. Zheng, Z., Eglin, D., Alini, M., Richards, G.R., Qin, L. and Lai, Y., 2021. Visible light-induced 3D bioprinting technologies and corresponding bioink materials for tissue engineering: a review. *Engineering*, *7*(7), pp.966-978.
28. Zhang, F., Zhu, L., Li, Z., Wang, S., Shi, J., Tang, W., Li, N. and Yang, J., 2021. The recent development of vat photopolymerization: A review. *Additive Manufacturing*, *48*, p.102423.
29. Kelly, B.E., Bhattacharya, I., Heidari, H., Shusteff, M., Spadaccini, C.M. and Taylor, H.K., 2019. Volumetric additive manufacturing via tomographic reconstruction. *Science*, *363*(6431), pp.1075-1079.
30. Hirose, Y., Shimada, T., Narikawa, R., Katayama, M. and Ikeuchi, M., 2008. Cyanobacteriochrome CcaS is the green light receptor that induces the expression of phycobilisome linker protein. *Proceedings of the National Academy of Sciences*, *105*(28), pp.9528-9533.
31. Todd, M., 2019. A high-throughput synthetic biology approach to optimise the production of the biopolymer, Poly-3-hydroxybutyrate.
32. Lampret, B., 2023. Selective Gene Expression in Hydrogel Suspended Escherichia coli through Optogenetics by Spatiotemporally Controlled Light for the Purposes of Additive Manufacturing.
33. Bernal, P.N., Bouwmeester, M., Madrid-Wolff, J., Falandt, M., Florczak, S., Rodriguez, N.G., Li, Y., Größbacher, G., Samsom, R.A., van Wolferen, M. and van der Laan, L.J., 2022. Volumetric bioprinting of organoids and optically tuned hydrogels to build liver-like metabolic biofactories. *Advanced Materials*, *34*(15), p.2110054.

34. Hirose, Y., Shimada, T., Narikawa, R., Katayama, M. and Ikeuchi, M., 2008. Cyanobacteriochrome CcaS is the green light receptor that induces the expression of phycobilisome linker protein. *Proceedings of the National Academy of Sciences*, *105*(28), pp.9528-9533.
35. Baumschlager, A. and Khammash, M., 2021. Synthetic biological approaches for Optogenetics and tools for transcriptional Light-control in bacteria. *Advanced Biology*, *5*(5), p.2000256.
36. Darwin, C., 1859. On the origins of species by means of natural selection. *London: Murray*, *247*, p.1859.
37. Boyden, E.S., Zhang, F., Bamberg, E., Nagel, G. and Deisseroth, K., 2005. Millisecond-timescale, genetically targeted optical control of neural activity. *Nature neuroscience*, *8*(9), pp.1263-1268.
38. Molday, R.S. and Moritz, O.L., 2015. Photoreceptors at a glance. *Journal of cell science*, *128*(22), pp.4039-4045.
39. Legris, M., Ince, Y.Ç. and Fankhauser, C., 2019. Molecular mechanisms underlying phytochrome-controlled morphogenesis in plants. *Nature communications*, *10*(1), p.5219.
40. Smith, H., 2000. Phytochromes and light signal perception by plants—an emerging synthesis. *Nature*, *407*(6804), pp.585-591.
41. Fushimi, K. and Narikawa, R., 2019. Cyanobacteriochromes: photoreceptors covering the entire UV-to-visible spectrum. *Current opinion in structural biology*, *57*, pp.39-46.
42. Deisseroth, K., 2011. Optogenetics. *Nature methods*, *8*(1), pp.26-29.
43. Tandar, S.T., Senoo, S., Toya, Y. and Shimizu, H., 2019. Optogenetic switch for controlling the central metabolic flux of Escherichia coli. *Metabolic engineering*, *55*, pp.68-75.
44. Wang, S. and Urban, M.W., 2020. Self-healing polymers. *Nature Reviews Materials*, *5*(8), pp.562-583.
45. Wang, L.J., Chang, Y.C., Sun, R. and Li, L., 2017. A multichannel smartphone optical biosensor for high-throughput point-of-care diagnostics. *Biosensors and Bioelectronics*, *87*, pp.686-692.
46. Levskaya, A., Chevalier, A.A., Tabor, J.J., Simpson, Z.B., Lavery, L.A., Levy, M., Davidson, E.A., Scouras, A., Ellington, A.D., Marcotte, E.M. and Voigt, C.A., 2005. Engineering Escherichia coli to see light. *Nature*, *438*(7067), pp.441-442.
47. Gilbert, C. and Ellis, T., 2018. Biological engineered living materials: growing functional materials with genetically programmable properties. *ACS synthetic biology*, *8*(1), pp.1-15.

48. Gilbert, C., Tang, T.C., Ott, W., Dorr, B.A., Shaw, W.M., Sun, G.L., Lu, T.K. and Ellis, T., 2021. Living materials with programmable functionalities grown from engineered microbial co-cultures. *Nature materials*, *20*(5), pp.691-700.
49. Reshetnikov, V.V., Smolskaya, S.V., Feoktistova, S.G. and Verkhusha, V.V., 2022. Optogenetic approaches in biotechnology and biomaterials. *Trends in Biotechnology*.
50. Benner, S.A. and Sismour, A.M., 2005. Synthetic biology. *Nature reviews genetics*, *6*(7), pp.533-543.
51. Cohen, S.N., Chang, A.C., Boyer, H.W. and Helling, R.B., 1973. Construction of biologically functional bacterial plasmids in vitro. *Proceedings of the National Academy of Sciences*, *70*(11), pp.3240-3244.
52. Gibson, D.G., Young, L., Chuang, R.Y., Venter, J.C., Hutchison III, C.A. and Smith, H.O., 2009. Enzymatic assembly of DNA molecules up to several hundred kilobases. *Nature methods*, *6*(5), pp.343-345.
53. Engler, C., Kandzia, R. and Marillonnet, S., 2008. A one pot, one step, precision cloning method with high throughput capability. *PloS one*, *3*(11), p.e3647.
54. Liu, S., Zhang, M., Ren, Y., Jin, G., Tao, Y., Lyu, L., Zhao, Z.K. and Yang, X., 2021. Engineering Rhodosporidium toruloides for limonene production. *Biotechnology for Biofuels*, *14*(1), pp.1-11.
55. Baeshen, N.A., Baeshen, M.N., Sheikh, A., Bora, R.S., Ahmed, M.M.M., Ramadan, H.A., Saini, K.S. and Redwan, E.M., 2014. Cell factories for insulin production. *Microbial cell factories*, *13*(1), pp.1-9.
56. Liu, L., Li, J., Gai, Y., Tian, Z., Wang, Y., Wang, T., Liu, P., Yuan, Q., Ma, H., Lee, S.Y. and Zhang, D., 2023. Protein engineering and iterative multimodule optimization for vitamin B6 production in Escherichia coli. *Nature Communications*, *14*(1), p.5304.
57. Skatrud, P.L., 1992. Genetic engineering of ß-lactam antibiotic biosynthetic pathways in filamentous fungi. *Trends in biotechnology*, *10*, pp.324-329.
58. Hedges, S.B., 2002. The origin and evolution of model organisms. *Nature Reviews Genetics*, *3*(11), pp.838-849.
59. Blount, Z.D., 2015. The unexhausted potential of E. coli. *Elife*, *4*, p.e05826.
60. Liu, A.P., Appel, E.A., Ashby, P.D., Baker, B.M., Franco, E., Gu, L., Haynes, K., Joshi, N.S., Kloxin, A.M., Kouwer, P.H. and Mittal, J., 2022. The living interface between synthetic biology and biomaterial design. *Nature materials*, *21*(4), pp.390-397.
61. Chen, A.Y., Zhong, C. and Lu, T.K., 2015. Engineering living functional materials. *ACS synthetic biology*, *4*(1), pp.8-11.

62. Wei, W., Petrone, L., Tan, Y., Cai, H., Israelachvili, J.N., Miserez, A. and Waite, J.H., 2016. An underwater surface-drying peptide inspired by a mussel adhesive protein. *Advanced functional materials*, *26*(20), pp.3496-3507.
63. Wan, H., Leung, N., Algharaibeh, S., Sui, T., Liu, Q., Peng, H.X. and Su, B., 2020. Cost-effective fabrication of bio-inspired nacre-like composite materials with high strength and toughness. *Composites Part B: Engineering*, *202*, p.108414.
64. Foong, C.P., Higuchi-Takeuchi, M., Malay, A.D., Oktaviani, N.A., Thagun, C. and Numata, K., 2020. A marine photosynthetic microbial cell factory as a platform for spider silk production. *Communications biology*, *3*(1), p.357.
65. Ma, L., Pang, A.P., Luo, Y., Lu, X. and Lin, F., 2020. Beneficial factors for biomineralization by ureolytic bacterium Sporosarcina pasteurii. *Microbial cell factories*, *19*(1), pp.1-12.
66. Blamires, S.J., Spicer, P.T. and Flanagan, P.J., 2020. Spider silk biomimetics programs to inform the development of new wearable technologies. *Frontiers in Materials*, *7*, p.29.
67. Luengo, J.M., Garcıá, B., Sandoval, A., Naharro, G. and Olivera, E.R., 2003. Bioplastics from microorganisms. *Current opinion in microbiology*, *6*(3), pp.251-260.
68. Zinn, M., Witholt, B. and Egli, T., 2001. Occurrence, synthesis and medical application of bacterial polyhydroxyalkanoate. *Advanced drug delivery reviews*, *53*(1), pp.5-21.
69. Madison, L.L. and Huisman, G.W., 1999. Metabolic engineering of poly (3-hydroxyalkanoates): from DNA to plastic. *Microbiology and molecular biology reviews*, *63*(1), pp.21-53.
70. Barnard, G.N. and Sanders, J.K., 1989. The poly-β-hydroxybutyrate granule in vivo: a new insight based on NMR spectroscopy of whole cells. *Journal of biological chemistry*, *264*(6), pp.3286-3291.
71. Anderson, A.J. and Dawes, E., 1990. Occurrence, metabolism, metabolic role, and industrial uses of bacterial polyhydroxyalkanoates. *Microbiological reviews*, *54*(4), pp.450-472.
72. Choi, J. and Lee, S.Y., 1999. Factors affecting the economics of polyhydroxyalkanoate production by bacterial fermentation. *Applied Microbiology and Biotechnology*, *51*, pp.13-21.
73. Steinbüchel, A. and Füchtenbusch, B., 1998. Bacterial and other biological systems for polyester production. *Trends in biotechnology*, *16*(10), pp.419-427.
74. Di Lorenzo, M.L. and Silvestre, C., 1999. Non-isothermal crystallization of polymers. *Progress in Polymer Science*, *24*(6), pp.917-950.
75. Lemoigne, M., 1926. Products of dehydration and of polymerization of β-hydroxybutyric acid. *Bull Soc Chem Biol*, *8*, pp.770-782.

76. Eggink, G., Huijberts, G.N. and de Waard, P., 1994. Biosynthesis of Poly (3-Hydroxyalkanoates) by Pseudomonas Putida. In *Frontiers of Polymers and Advanced Materials* (pp. 607-612). Boston, MA: Springer US.
77. Juodeikiene, G., Vidmantiene, D., Basinskiene, L., Cernauskas, D., Bartkiene, E. and Cizeikiene, D., 2015. Green metrics for sustainability of biobased lactic acid from starchy biomass vs chemical synthesis. *Catalysis Today*, *239*, pp.11-16.
78. Huisman, G.W., Wonink, E., Meima, R., Kazemier, B., Terpstra, P. and Witholt, B., 1991. Metabolism of poly (3-hydroxyalkanoates)(PHAs) by Pseudomonas oleovorans. Identification and sequences of genes and function of the encoded proteins in the synthesis and degradation of PHA. *Journal of Biological Chemistry*, *266*(4), pp.2191-2198.
79. Sudesh, K., Abe, H. and Doi, Y., 2000. Synthesis, structure and properties of polyhydroxyalkanoates: biological polyesters. *Progress in polymer science*, *25*(10), pp.1503-1555.
80. Wang, J. and Yu, H.Q., 2007. Biosynthesis of polyhydroxybutyrate (PHB) and extracellular polymeric substances (EPS) by Ralstonia eutropha ATCC 17699 in batch cultures. *Applied microbiology and biotechnology*, *75*, pp.871-878.
81. Oeding, V. and Schlegel, H.G., 1973. β-Ketothiolase from Hydrogenomonas eutropha H16 and its significance in the regulation of poly-β-hydroxybutyrate metabolism. *Biochemical Journal*, *134*(1), pp.239-248.
82. Turco, E., Savova, A., Gere, F., Ferrari, L., Romanov, J., Schuschnig, M. and Martens, S., 2021. Reconstitution defines the roles of p62, NBR1 and TAX1BP1 in ubiquitin condensate formation and autophagy initiation. *Nature communications*, *12*(1), p.5212.
83. Banerjee, S. and Mitra, D., 2020. Structural basis of design and engineering for advanced plant optogenetics. *Trends in plant science*, *25*(1), pp.35-65.
84. Hjelm, A., Karyolaimos, A., Zhang, Z., Rujas, E., Vikstrom, D., Slotboom, D.J. and de Gier, J.W., 2017. Tailoring Escherichia coli for the l-Rhamnose PBAD promoter-based production of membrane and secretory proteins. *ACS Synthetic Biology*, *6*(6), pp.985-994.
85. Brautigam, C.A., Smith, B.S., Ma, Z., Palnitkar, M., Tomchick, D.R., Machius, M. and Deisenhofer, J., 2004. Structure of the photolyase-like domain of cryptochrome 1 from Arabidopsis thaliana. *Proceedings of the National Academy of Sciences*, *101*(33), pp.12142-12147.
86. Ogawa, H., Inouye, S., Tsuji, F.I., Yasuda, K. and Umesono, K., 1995. Localization, trafficking, and temperature-dependence of the Aequorea green fluorescent protein in cultured vertebrate cells. *Proceedings of the National Academy of Sciences*, *92*(25), pp.11899-11903.

87. Chung, C.T., Niemela, S.L. and Miller, R.H., 1989. One-step preparation of competent Escherichia coli: transformation and storage of bacterial cells in the same solution. *Proceedings of the National Academy of Sciences*, *86*(7), pp.2172-2175.
88. Sankaran, S., Deshmukh, K., Ahamed, M.B. and Pasha, S.K., 2018. Recent advances in electromagnetic interference shielding properties of metal and carbon filler reinforced flexible polymer composites: A review. *Composites Part A: Applied Science and Manufacturing*, *114*, pp.49-71.
89. Thomson, N.M., Shirai, T., Chiapello, M., Kondo, A., Mukherjee, K.J., Sivaniah, E., Numata, K. and Summers, D.K., 2018. Efficient 3-Hydroxybutyrate Production by Quiescent Escherichia coli Microbial Cell Factories is Facilitated by Indole-Induced Proteomic and Metabolomic Changes. *Biotechnology Journal*, *13*(5), p.1700571.
90. Normi, Y.M., Hiraishi, T., Taguchi, S., Sudesh, K., Najimudin, N. and Doi, Y., 2005. Site-directed saturation mutagenesis at residue F420 and recombination with another beneficial mutation of Ralstonia eutropha polyhydroxyalkanoate synthase. *Biotechnology letters*, *27*, pp.705-712.
91. Evelson, P., Susemihl, C., Villarreal, I., Llesuy, S., Rodríguez, R., Peredo, H., Lemberg, A., Perazzo, J. and Filinger, E., 2005. Hepatic morphological changes and oxidative stress in chronic streptozotocin-diabetic rats. *Annals of hepatology*, *4*(2), pp.115-120.
92. Belova, L.L., Sokolov, A.P., Sidorov, I.A. and Trotsenko, Y.A., 1997. Purification and characterization of NADPH-dependent acetoacetyl-CoA reductase from Methylobacterium extorquens. *FEMS microbiology letters*, *156*(2), pp.275-279.
93. Bokrova, J., Marova, I., Matouskova, P. and Pavelkova, R., 2019. Fabrication of novel PHB-liposome nanoparticles and study of their toxicity in vitro. *Journal of Nanoparticle Research*, *21*, pp.1-12.
94. Ceroni, F., Boo, A., Furini, S., Gorochowski, T.E., Borkowski, O., Ladak, Y.N., Awan, A.R., Gilbert, C., Stan, G.B. and Ellis, T., 2018. Burden-driven feedback control of gene expression. *Nature methods*, *15*(5), pp.387-393.
95. Taylor, G.M., Mordaka, P.M. and Heap, J.T., 2019. Start-Stop Assembly: a functionally scarless DNA assembly system optimized for metabolic engineering. *Nucleic acids research*, *47*(3), pp.e17-e17.
96. Zampini, M., Mur, L.A., Rees Stevens, P., Pachebat, J.A., Newbold, C.J., Hayes, F. and Kingston-Smith, A., 2016. Terminator Operon Reporter: combining a transcription termination switch with reporter technology for improved gene synthesis and synthetic biology applications. *Scientific Reports*, *6*(1), p.26572.

97. Juengert, J.R., Bresan, S. and Jendrossek, D., 2018. Determination of polyhydroxybutyrate (PHB) content in Ralstonia eutropha using gas chromatography and Nile red staining. *Bio-protocol*, *8*(5), pp.e2748-e2748.

98. Oesterhelt, D. and Stoeckenius, W., 1973. Functions of a new photoreceptor membrane. *Proceedings of the National Academy of Sciences*, *70*(10), pp.2853-2857.

99. Zemelman, B.V., Lee, G.A., Ng, M. and Miesenböck, G., 2002. Selective photostimulation of genetically chARGed neurons. *Neuron*, *33*(1), pp.15-22.

100. Nagel, G., Ollig, D., Fuhrmann, M., Kateriya, S., Musti, A.M., Bamberg, E. and Hegemann, P., 2002. Channelrhodopsin-1: a light-gated proton channel in green algae. *Science*, *296*(5577), pp.2395-2398.

101. Shimizu-Sato, S., Huq, E., Tepperman, J.M. and Quail, P.H., 2002. A light-switchable gene promoter system. *Nature biotechnology*, *20*(10), pp.1041-1044.

102. Krishnamurthy, V.V., Khamo, J.S., Mei, W., Turgeon, A.J., Ashraf, H.M., Mondal, P., Patel, D.B., Risner, N., Cho, E.E., Yang, J. and Zhang, K., 2016. Reversible optogenetic control of kinase activity during differentiation and embryonic development. *Development*, *143*(21), pp.4085-4094.

103. Nihongaki, Y., Kawano, F., Nakajima, T. and Sato, M., 2015. Photoactivatable CRISPR-Cas9 for optogenetic genome editing. *Nature biotechnology*, *33*(7), pp.755-760.

104. Glantz, S.T., Carpenter, E.J., Melkonian, M., Gardner, K.H., Boyden, E.S., Wong, G.K.S. and Chow, B.Y., 2016. Functional and topological diversity of LOV domain photoreceptors. *Proceedings of the National Academy of Sciences*, *113*(11), pp.E1442-E1451.

105. Koyanagi, M. and Terakita, A., 2014. Diversity of animal opsin-based pigments and their optogenetic potential. *Biochimica et Biophysica Acta (BBA)-Bioenergetics*, *1837*(5), pp.710-716.

106. Ikeuchi, M. and Ishizuka, T., 2008. Cyanobacteriochromes: a new superfamily of tetrapyrrole-binding photoreceptors in cyanobacteria. *Photochemical & Photobiological Sciences*, *7*(10), pp.1159-1167.

107. Ziegler, T. and Möglich, A., 2015. Photoreceptor engineering. *Frontiers in molecular biosciences*, *2*, p.30.

108. Kenney, L.J. and Anand, G.S., 2020. EnvZ/OmpR two-component signaling: an archetype system that can function noncanonically. *EcoSal Plus*, *9*(1), pp.10-1128.

109. Losi, A., Polverini, E., Quest, B. and Gärtner, W., 2002. First evidence for phototropin-related blue-light receptors in prokaryotes. *Biophysical journal*, *82*(5), pp.2627-2634.

110. Fernandez-Rodriguez, J., Moser, F., Song, M. and Voigt, C.A., 2017. Engineering RGB color vision into Escherichia coli. *Nature chemical biology*, *13*(7), pp.706-708.

111. Amoutzias, G.D., Robertson, D.L., Van de Peer, Y. and Oliver, S.G., 2008. Choose your partners: dimerization in eukaryotic transcription factors. *Trends in biochemical sciences*, *33*(5), pp.220-229.

112. Tabor, J.J., Levskaya, A. and Voigt, C.A., 2011. Multichromatic control of gene expression in Escherichia coli. *Journal of molecular biology*, *405*(2), pp.315-324.

113. Olson, E.J., Hartsough, L.A., Landry, B.P., Shroff, R. and Tabor, J.J., 2014. Characterizing bacterial gene circuit dynamics with optically programmed gene expression signals. *Nature methods*, *11*(4), pp.449-455.

114. Hirose, Y., Shimada, T., Narikawa, R., Katayama, M. and Ikeuchi, M., 2008. Cyanobacteriochrome CcaS is the green light receptor that induces the expression of phycobilisome linker protein. *Proceedings of the National Academy of Sciences*, *105*(28), pp.9528-9533.

115. Ong, N.T. and Tabor, J.J., 2018. A miniaturized Escherichia coli green light sensor with high dynamic range. *ChemBioChem*, *19*(12), pp.1255-1258.

116. Huang, Y., Xia, A., Yang, G. and Jin, F., 2018. Bioprinting living biofilms through optogenetic manipulation. *ACS synthetic biology*, *7*(5), pp.1195-1200.

117. Sun, W., Shi, S., Chen, J., Zhao, W., Chen, T., Li, G., Zhang, K., Yu, B., Liu, D., Chen, Y. and Ying, H., 2022. Blue Light Signaling Regulates Escherichia coli W1688 Biofilm Formation and l-Threonine Production. *Microbiology Spectrum*, *10*(5), pp.e02460-22.

118. Moser, F., Tham, E., González, L.M., Lu, T.K. and Voigt, C.A., 2019. Light-controlled, high-resolution patterning of living engineered bacteria onto textiles, ceramics, and plastic. *Advanced Functional Materials*, *29*(30), p.1901788.

119. Adlung, N. and Scheller, S., 2023. Application of the Fluorescence-Activating and Absorption-Shifting Tag (FAST) for Flow Cytometry in Methanogenic Archaea. *Applied and Environmental Microbiology*, *89*(4), pp.e01786-22.

120. Romano, E., Baumschlager, A., Akmeric, E.B., Palanisamy, N., Houmani, M., Schmidt, G., Öztürk, M.A., Ernst, L., Khammash, M. and Di Ventura, B., 2021. Engineering AraC to make it responsive to light instead of arabinose. *Nature chemical biology*, *17*(7), pp.817-827.

121. Wang, X., Chen, X. and Yang, Y., 2012. Spatiotemporal control of gene expression by a light-switchable transgene system. *Nature methods*, *9*(3), pp.266-269.

122. Baumschlager, A., Aoki, S.K. and Khammash, M., 2017. Dynamic blue light-inducible T7 RNA polymerases (Opto-T7RNAPs) for precise spatiotemporal gene expression control. *ACS synthetic biology*, *6*(11), pp.2157-2167.

Appendix

Table of Sequences used

Name	Sequence	Source
sfGFP	atgcgtaaaggcgaagagctgttcactggtgtcgtccctattctggtggaactggatggtgatgtcaa cggtcataagttttccgtgcgtggcgagggtgaaggtgacgcaactaatggtaaactgacgctgaag ttcatctgtactactggtaaactgccggtaccttggccgactctggtaacgacgctgacttatggtgt tcagtgctttgctcgttatccggaccatatgaagcagcatgacttcttcaagtccgccatgccggaag gctatgtgcaggaacgcacgatttcctttaaggatgacggcacgtacaaaacgcgtgcggaagtga aatttgaaggcgataccctggtaaaccgcattgagctgaaaggcattgactttaaagaagacggcaa tatcctgggccataagctggaatacaattttaacagccacaatgtttacatcaccgccgataaacaa aaaaatggcattaaagcgaattttaaaattcgccacaacgtggaggatggcagcgtgcagctggctg atcactaccagcaaaacactccaatcggtgatggtcctgttctgctgccagacaatcactatctgag cacgcaaagcgttctgtctaaagatccgaacgagaaacgcgatcatatggttctgctggagttcgta accgcagcgggcatcacgcatggtatggatgaactgtacaaa	Ceroni et al., 2018
TdFAST2	ATGGAACATGTTGCATTTGGTAGCGAAGATATTGAAAATACCCT GGCCAAAATGGATGATGGTCAGCTGGATGGTCTGGCATTTGGT GCAATTCAGCTGGACGGTGATGGTAATATTCTGCAGTATAATGC AGCCGAAGGTGATATTACCGGTCGTGATCCGAAACAGGTTATTG GCAAAAACTTCTTCAAAGATGTTGCACCGGGTACAGATAGTCCG GAATTTTATGGTAAATTCAAAGAAGGTGTTGCCAGCGGTAATCT GAATACCATGTTTGAGTGGATGATTCCGACCAGCCGTGGTCCGA CCAAAGTTAAAATCCATATGAAAAAAGCACTGAGCGGTGATAGCT ATTGGGTTTTTGTTAAACGTGTTGGTGGTGGTAGCGGTGGTGG TGAACATGTGGCCTTTGGCTCAGAAGATATCGAGAACACCTTAG CAAAAATGGACGACGGCCAGTTAGATGGCCTGGCCTTCGGAGC CATTCAATTAGATGGTGATGGCAACATCCTGCAATACAATGCCG CAGAAGGCGATATCACAGGACGCGATCCTAAACAAGTGATTGGT AAGAACTTTTTCAAGGACGTTGCCCCTGGCACCGATTCACCTGA ATTCTATGGCAAGTTTAAAGAGGGCGTTGCATCAGGCAATCTGA ACACAATGTTCGAATGGATGATCCCTACCTCTCGCGGTCCGACA AAGGTGAAGATTCACATGAAAAAGGCCCTGTCAGGTGATTCATA TTGGGTGTTCGTGAAACGCGTT	Adlung et al., 2023
Digitaliser	ttaattaaacgttcgtaatcaagccacttccttttgcattgacgcagggtgtcggaaggcaactcgc cgaacgcgctcctatagttttcagcgaagcgtcccaaatgtaagaagccgtagtctagggctatctc agttatactacgcacattggcactgggatcgttcaagcaggcgcggatgctttcgagcttgcggttg cggatgtagttcttcggcgtggtgccggcgtgcttctcgaacaaattgtagagcgagcgtggactca tcatcgccagctccgctaaccgctcaaggctgatattccgtttgagattctcctcaatgaattgaacg actcgctcgaaagacgggttacctttgctgaaaatttcacggctgacattgctgcccagcatttcgag cagcttggaagcgatgatccccgcatagtgctcttggacccgaggcatcgactttgtatgttccgctt cgtcacaaactaacccgagtagattgataaagccatcgagttgctggagattgtgtcgcgcggcgaa acggataccctccctcggcttgtgccaattgttgtcactgcacgcccgatcaaggaccactgagggc aatttaacgataaatttctcgcaatcttctgaataggtcaggtcggcttggtcatccggattgagcag caatagttcgcccggcgcaaaatagtgctcctggccatggccacgccacaggcaatggcctttgag	Calles et al., 2019

tattatttgcagatgataacaggtctctaatccaggcgagattaccctcacgctaccgccgtagctga
ttcgacacagatcgaggcatccgaagattctgtggtgcagcctgcctgccgggcgcccgcccttgg
gcaggcgaatagagtgcgtaccgacatactggttaacataatcggagactgcatagggctcggcgt
ggacgaagatctgacttttctcgttcaataagcaaaaatccatagttcacggttctcttattttaatgt
gggctgcttggtgtgatgtagaaaggcgccaagtcgatgaaaatgcatctcgacgtgatgcgtatac
gggttacccccattgccacgttgcgccatccttttgcaatcagtgaccactttccaagcaaaaata
acgccaagcagaacgaagacgttctttttaagaagcgagaacaccagaagttcgtgctgtcggggc
atggggcgacgaattggcggataaaggggatctgctggatattacggccttttaaagaccgtaaag
aaaaataagcacaagttttatccggcctttattcacattcttgcccgcctgatgaatgctcatccgta
attacgtatggcaatgaaagacggtgagctggtgatatgggatagtgttcacccttgttacaccgttt
tccatgagcaaactgaaacgttttcatcgctctggagtgaataccacgacgatttccggcagtttcta
cacatatattcgcaagatgtggcgtgttacggtgaaaacctggcctatttccctaaagggtttattga
gaatatgtttttcgtctcagccaatccctgggtgagtttcaccagttttgatttaaacgtggccaatat
ggacaacttcttcgcccccgttttcaccatgcatgggaattagcttgatctgaccaacgaccggtag
cggagctatccaacggcggtataccaggaaaacacacagcaggtacatcagaacagtaccatgact
gaagaacaaatagttttttcctgatccataaagcagaacggcctgctccatgacaaatctggctccc
caactaatgccccatgcagccagcataaccagcataaagtgcagtgtccggtttgatagggataagt
ccagccttgcaagaagcggatacaggagtgcaaaaaatggctatctctagtaaggcctacccctta
ggctttatgcaacagaaacaataataatggagtcatgaccatgcctaggaggaaaaaacatatggtg
aaaccagtaacgttatacgatgtcgcagagtatgccggtgtctcttatcagaccgtttcccgcgtggt
gaaccaggccagccacgtttctgcgaaaacgcgggaaaaagtggaagcggcgatggcggagctga
attacattcccaaccgcgtggcacaacaactggcgggcaaacagtcgttgctgattggcgttgccac
ctccagtctggccctgcacgcgccgtcgcaaattgtcgcggcgattaaatctcgcgccgatcaactg
ggtgccagcgtggtggtgtcgatggtagaacgaagcggcgtcgaagcctgtaaagcggcggtgcac
aatcttctcgcgcaacgcgtcagtgggctgatcattaactatccgctggatgaccaggatgccattg
ctgtggaagctgcctgcactaatgttccggcgttatttcttgatgtctctgaccagacacccatcaac
agtattatttttctcccatgaagacggtacgcgactgggcgtggagcatctggtcgcattgggtcacc
agcaaatcgcgctgttagcgggcccattaagttctgtctcggcgcgtctgcgtctggctggctggca
taaatatctcactcgcaatcaaattcagccgatagcggaacgggaaggcgactggagtgccatgtc
cggttttcaacaaaccatgcaaatgctgaatgagggcatcgttcccactgcgatgctggttgccaac
gatcagatggcgctgggcgcaatgcgcgccattaccgagtccgggctgcgcgttggtgcggatatc
tcggtagtgggatacgacgataccgaagacagctcatgttatatcccgccgttaaccaccatcaaac
aggattttcgcctgctggggcaaaccagcgtggaccgcttgctgcaactctctcagggccaggcggt
gaagggcaatcagctgttgcccgtctcactggtgaaaagaaaaaccaccctggcgcccaatacgca
aaccgcctctccccgcgcgttggccgattcattaatgcagctggcacgacaggtttcccgactggaa
agcgggcagcatcatcaccaccatcattaggatggtggtgatgataatggctagccgtaaaggtgaa
gaactgttcaccggtgttgttccgatcctggttgaactggatggtgatgttaacggccacaaattctc
tgttcgtggtgaaggtgaaggtgatgcaaccaacggtaaactgaccctgaaattcatctgcactacc
ggtaaactgccggttccatggccgactctggtgactaccctgacctatggtgttcagtgtttttctcgt
tacccggatcacatgaagcagcatgatttcttcaaatctgcaatgccggaaggttatgtacaggagc
gcaccatttctttcaaagacgatggcacctacaaaacccgtgcagaggttaaatttgaaggtgatac
tctggtgaaccgtattgaactgaaaggcattgatttcaaagaggacggcaacatcctgggccacaaa
ctggaatataacttcaactcccataacgtttacatcaccgcagacaaacagaagaacggtatcaaag
ctaacttcaaaattcgccataacgttgaagacggtagcgtacagctggcggaccactaccagcaga
acactccgatcggtgatggtccggttctgctgccggataaccactacctgtccacccagtctaaact
gtccaaagacccgaacgaaaagcgcgaccacatggtgctgctggagttcgttactgccgcaggtat
cacgcacggcatggatgaactctacaaataagaattcgagctcggtacccggggatcctctagagt
cgacctgcaggcatgcaagcttgcggccgcgtcgtgactgggaaaaccctggcgcaaagcccgcc
gaaaggcgggcttttctgttataaacgcagaaaggcccacccgaaggtgagccagtgtgactctagt
agagagcgttcaccgacaaaaacagataaaacgaaaggcccagtctttcgactgagcctttcgtttt

	atttgatgcctggctcgagctcgagaaaaaaagcccggacgactgttcgggcttgtctttttatatgt tggaaaatcagtggcaatgcaatggcccaacagaaaatggtgaaaccagtaacgttatactgaatct aagtatcaatgtgagcgctcacaagtcaacactctttttgataaaactagt	
PHB	atggcgaccggcaaaggcgcggcagcttccacgcaggaaggcaagtcccaaccattcaaggtcac gccggggccattcgatccagccacatggctggaatggtcccgccagtggcagggcactgaaggca acggccacgcggccgcgtccggcattccgggcctggatgcgctggcaggcgtcaagatcgcgccg gcgcagctgggtgatatccagcagcgctacatgaaggacttctcagcgctgtggcaggccatggcc gagggcaaggccgaggccaccggtccgctgcacgaccggcgcttcgccggcgacgcatggcgca ccaacctcccatatcgcttcgctgccgcgttctacctgctcaatgcgcgcgccttgaccgagctggc cgatgccgtcgaggccgatgccaagacccgccagcgcatccgcttcgcgatctcgcaatgggtcga tgcgatgtcgcccgccaacttccttgccaccaatcccgaggcgcagcgcctgctgatcgagtcggg cggcgaatcgctgcgtgccggcgtgcgcaacatgatggaAGATCTgacacgcggcaagatctc gcagaccgacgagagcgcgtttgaggtcggccgcaatgtcgcggtgaccgaaggcgccgtggtgtt cgagaacgagtacttccagctgttgcagtacaagccgctgaccgacaaggtgcacgcgcgcccgct gctgatggtgccgccgtgcatcaacaagtactacatcctggacctgcagccggagagctcgctggt gcgccatgtggtggagcagggacatacggtgtttctggtgtcgtggcgcaatccggacgccagcat ggccggcagcacctgggacgactacatcgagcacgcggccatccgcgccatcgaagtcgcgcgcg acatcagcggccaggacaagatcaacgtgctcggcttctgcgtgggcggcaccattgtctcgaccg cgctggcggtgctggccgcgcgcggcgagcacccggccgccagcgtcacgctgctgaccacgctg ctggactttgccgacacgggcatcctcgacgtctttgtcgacgagggccatgtgcagttgcgcgagg ccacgctgggcggcggcgccggcgcgccgtgcgcgctgctgcgcggccttgagctggccaatacc ttctcgttcttgcgcccgaacgacctggtgtggaactacgtggtcgacaactacctgaagggcaaca cgccggtgccgttcgacctgctgttctggaacggcgacgccaccaacctgccggggccgtggtact gctggtacctgcgccacacctacctgcagaacgagctcaaggtaccgggcaagctgaccgtgtgcg gcgtgccggtggacctggccagcatcgacgtgccgacctatatctacggctcgcgcgaagatcata tcgtgccgtggaccgcggcctatgcctcgaccgcgctgctggcgaacaagctgcgcttcgtgctgg gtgcgtcgggccatatcgccggtgtgatcaacccgccggccaagaacaagcgcagccactggact aacgatgcgctgccggagtcgccgcagcaatggctggccggcgccatcgagcatcacggcagctg gtggccggactggaccgcatggctggccgggcaggccggcgcgaaacgcgccgcgcccgccaac tatggcaatgcgcgctatcgcgcaatcgaacccgcgcctgggcgatacgtcaaagccaaggcatA TCGGATTGGATCCAAAGGAGGTTATACCGatgaaaaattgtgtcatcgtcag tgcggtacgtactgctatcggtagttttaacggttcactcgcttccaccagcgccatcgacctggggg cgacagtaattaaagccgccattgaacgtgcaaaaatcgattcacaacacgttgatgaagtgattat gggtaacgtgttacaagccgggctggggcaaaatccggcgcgtcaggcactgttaaaaagcgggct ggcagaaacggtgtgcggattcacggtcaataaagtatgtggttcgggtcttaaaagtgtggcgctt gccgcccaggccattcaggcaggtcaggcgcagagcattgtggcgggggggtatggaaaatatgagt ttagccccctacttactcgatgcaaaagcacgctctggttatcgtcttggagacggacaggtttatga cgtaatcctgcgcgatggcctgatgtgcgccacccatggttatcatatggggattaccgccgaaaac gtggctaaagagtacggaattacccgtgaaatgcaggatgaactggcgctacattcacagcgtaaa gcggcagccgcaattgagtccggtgcttttacagccgaaatcgtcccggtaaatgttgtcactcgaa agaaaaccttcgtgttcagtcaagacgaattcccgaaagcgaattcaacggctgaagcgttaggtgc attgcgcccggccttcgataaagcaggaacagtcaccgctgggaacgcgtctggtattaacgacgg tgctgccgctctggtgattatggaagaatctgcggcgctggcagcaggccttacccccctggctcgc attaaaagttatgccagcggtggcgtgccccccgcattgatgggtatggggccagtacctgccacgc aaaaagcgttacaactggcggggctgcaactggcggatattgatctcattgaggctaatgaagcatt tgctgcacagttccttgccgttgggaaaaacctgggctttgattctgagaaagtgaatgtcaacggc ggggccatcgcgctcgggcatcctatcggtgccagtggtgctcgtattctggtcacactattacatgc catgcaggcacgcgataaaacgctggggctggcaacactgtgcattggcggcggtcagggaattgc gatggtgattgaacggttgaattaaAAAAAAAAAAAAAAAAAAAAAAAAAAAAAA AAAAAAAAAAAAAAAAAAgtGtctccgggctatatcgccaccgacatggtcaaggcgat	This study

	ccgccaggacgtgctcgacaagatcgtcgcgacgatcccggtcaagcgcctgggcctgccggaag agatcgcctcgatctgcgcctggttgtcgtcggaggagtccggtttctcgaccggcgccgacttctc gctcaacggcggcctgcatatgggctCTACGTTTTTTAGAAAAAGGAGGTATG CGAGatgtttgaaaatatatcatcaaatggagtttataaaaatctatttgatggaaaatgggttgaa agtaagacaaataaaaccatagaaacgcattctccttatgatggaagtttaattggaaaagttcagg ccttatcaaaagaggaagttgatgagatttttaaaagttcaagaacagctcagaaaaaatggggtga aactccaataaatgagcgtgctagaatcatgcgtaaagcagctgatatactagatgataacgcagaa tatatagcaaaaattctttcaaatgagatagcaaaagatttaaaatcttctctttcagaagtaaaaag aacagctgattttataagatttacagctaatgaaggtactcatatggaaggagaagctattaactcag ataatttttcctggttctaaaaaagataaactttctctagttgaaagagttcctttaggaatagttttagc tatatctccttttaattatcctgtaaatctttctgggtctaaggttgctccagcacttatagctggaaat agtgttgttttaaaaccttctacaactggtgctataagcgcacttcatcttgcagaaatttttaatgca gctggtctgccagcaggtgttttaaacactgtaacaggaaaagggtctgaaataggcgattatttaat tacccatgaagaagtaaactttattaactttacgggaagctctgctgtaggtaagcatatttcaaaaa tagctggaatgatacctatggttcttgagcttggtggtaaagatgctgctatagttctcgaagatgcc aatcttgaaacaacagctaaaagcatagtatctggagcatatggatactccggccaaaggtgtactg ctgtaaaaagagttcttgtaatggataaagtagctgatgaattagttgaacttgttacaaaaaaagtt aaagaattaaaggtaggtaatccttttgatgatgttacaataaccccacttatagacaacaaggcag cagattatgttcaaactctcattgacgacgctatcgaaaagggtgcaactcttatcgttggaaataag cgtaaagaaaatttaatgtatcctactttatttgataatgtaactgctgatatgcgtattgcttgggaa gaaccatttggaccagttttacctattattcgtgtaaaaagcatggatgaagcaatagaattagcaaa tagatctgaatatggccttcaatctgcagtatttactgaaaatatgcatgatgccttttatattgccaat aaattagatgttggaactgttcaagtaaataataagcctgaaagaggcccagatcacttcccattcct tggaacaaagtcatcaggtatgggcactcaaggaattcgatacagtatagaggcaatgacaaggca taaatcaatagttttaaacctataatgatgataataatctagacca	
Agarase	ATGAAAGGTTTTACGAAACATTCTATTCTGATGGCTTGCAGCATT GGTCTGGCTATTAACGCTACGGCGGCGGACTGGGACAACATTC CGATCCCGGCCGAACTGGATGCAGGCCAGTCTTGGGAACTGCA GCAAAACTACAGTGACTCCTTCAACTACAGTGGCAAAAACTCCAC CTTCACGGGTAAATGGAAAGATTCATACTTCCATTCGTGGACCG GTCCGGGTCTGACGCACTGGAGCTCTGATGAATCTTGGGTGGG CGACGGTAACCTGATTATCTCAGCCTCGCGTCGCCAGGGCACC AATAAAGTGAACGCAGGTGTTATCACCAGTAAAACGAAAGTGAAA TATCCGATCTTCCTGGAAGCCAGCATTAAAGTTTCTAATCTGGAA CTGAGTTCCAACTTTTGGCTGCTGAGCGAAAATGATCAGCGTGA AATCGACGTTCTGGAAGTCTATGGCGGTGCCCGCCAAGATTGG TACGCAAAAAATATGAGCACCAACTTCCATGTGTTTTTCCGTAAC AACGACAACTCTATCAAAAACGATTATAACGACCAGACCCATTTT ACCCCGACGTGGGGCAACTACTGGCGTGATGGCTTTCACCGCT TCGGTGTTTATTGGAAATCCCCGACCGATGTCACGTTCTACATC GACGGCCAGAAAACCACGAAAGGTGGCTGGAGTCAAGTGGTTAT GAAAGATAAAGACTATACCGGCGCCATTCTGGATAAATCCCGTT ACAATATGGACCAGGAAGCATTTATTATCATTGATACCGAAGACC ATACGTGGCGCTCTGAAGCGGGTCACATCGCGACGGATGCCGA CCTGGCAGATTCAGACAAAAACAAAATGTACGTCGATTGGATTC GTGTGTACAAACCGACCGGCGGTTCGACCACGCCGCCGACCGG TGATATTACGCCGCCGAGTGGTTATACGAATCTGCAGCTGGCTC ATTCCAACCGTTGCGTCGATGTGATTAATGGCGCGCTGTGGAAC GGTTCAACCTATCAGCAATACTCGTGTAATACGGGTAACAATAAC CAGCGCTTTAAATTCACCAAAATCGCTAATAACCAGTACAGCATT	This study

	AACGCGAAAGTCTCTCAACTGTGCATGGAACTGGCTAGCGGCTC ATCGGCTAATGGTGCGAAAGTTCAGCAATGGATCTGTAACCACG CAAATAGTAACCAGACCTGGTCCCTGGAAGATAAAGGCTCAAAC ACGTTCGAAATCCGTAACAAACAATCGGGTAAATGCCTGGAAGT GGCTAACAGCTCTAATGCGAACGGCGGTCAGATTCGTCAGTGG GCGTGTACGGGTGCGACCAACCAGCGTTTCAAATTCCTGTAA	

Table of Primers Used

Name	Sequence	Use
AH1	TAGGATCGCATTTTTAACCAACGGTTTCCCTCTAGAAATAA	PHB c3 FWD
AH2	TCGTCTTTGGTACCGAGTTAttataggtttaaaactattgatttatgcc	PHB C3 RV
AH3	tcaatagttttaaacctataaTAACTCGGTACCAAAGACGA	PHB bp16 FWD
AH4	TATTTCTAGAGGGAAACCGTTGGTTAAAAATGCGATCCTAAC	PHB BP16 RV
AH5	CAaaagaggagaaatactagATGAAAGGTTTTACGAAACATTC	Agarase FWD
AH6	TCGTCTTTGGTACCGAGTTATTACAGGAATTTGAAACGCTG	Agarase RV
AH7	AGCGTTTCAAATTCCTGTAATAACTCGGTACCAAAGACGA	CcaSR for agarase FWD
AH8	TGTTTCGTAAAACCTTTCATctagtatttctcctctttTGGTTAA	CcaSR for agarase RV
AH9	CAaaagaggagaaatactagcctaggaggaaaaaacatatgg	Digitaliser insert FWD
AH10	TCGTCTTTGGTACCGAGTTAtttatcaaaaagagtgttgacttg	Digitalizer insert RV
AH11	tcaacactctttttgataaaTAACTCGGTACCAAAGACGA	Digitaliser BP16 FWD
AH12	atatgttttttcctcctaggctagtatttctcctctttTGGTTAA	Digitaliser BP16 RV
AH13	ttaggatggtggtgatgataATGGAACATGTTGCATTTGGTAG	TdFAST2 insert Digitalizer FWD
AH14	gatccccgggtaccgagctcAACGCGTTTCACGAACACCC	TdFAST2 insert Digitalizer RV
AH15	GGGTGTTCGTGAAACGCGTTgagctcggtacccggggatc	Digitalizer for TdFAST2 FWD
AH16	CCAAATGCAACATGTTCCATtatcatcaccaccatcctaatgatgg	Digitalizer for TdFAST2 RV

Derivation of Equation 2.1

We start with the equations for the change in active and ground state photoreceptors over time (Eqns. A1.1-A1.2).

$$\frac{dS_a}{dt} = K_g S + k_2 S_a - k_1 S_g \quad \text{(Eqn. A1.1)}$$

$$\frac{dS_a}{dt} = K_1 S_g - k_2 S_a \quad \text{(Equation A1.2)}$$

We solve for η = the ratio of active to total photoreceptors (Eqns. A1.3-A1.5).

$$\eta = \frac{S_a}{S_a + S_g} \quad \text{(Equation A1.3)}$$

$$\frac{d\eta(t)}{dt} = \frac{S_g \frac{dS_a}{dt} - S_a \frac{dS_g}{dt}}{(S_a + S_g)^2} \quad \text{(Equation A1.4)}$$

$$\frac{d\eta(t)}{dt} = \frac{k_1 S_g^2 - K_2 S_a S_g - k_g S S_a - k_1 S_g^2}{S^2} \quad \text{(Equation A1.5)}$$

Substitute for η.

$$\frac{d\eta(t)}{dt} = k_1(1 - \eta^2) - k_2\eta^2 - k_g\eta + \frac{S_a S_g (k_1 - k_2)}{S^2} \quad \text{(Equation A1.6)}$$

$$\frac{d\eta(t)}{dt} = k_1 - \eta(k_1 + k_2 + k_g) \quad \text{(Equation A1.7)}$$